Novel Architectures for MEMS Inertial Sensors and Resonators Targeting Above-IC Integration

Mohannad Y. Elsayed
Electrical and Computer Engineering Department
McGill University, Montreal
August, 2015

A thesis submitted to
McGill University in partial fulfillment of the requirements of the degree of
Doctor of Philosophy

Table of Contents

Abstract

The importance of micromachined sensors and resonators is continuously increasing as they get more widespread in a broad variety of applications ranging from handheld consumer electronics to more sophisticated applications as robotics and space applications. This is pushing research in all aspects of microsystems to produce higher performance lower cost devices to cope with the increasing demand. In this work, architectures for improving the performance of different types of MEMS inertial, magnetic sensors (targeting inertial combos) and resonators (targeting MEMS oscillators) are presented. Also, a low temperature surface micromachining technology featuring independently controlled lateral and vertical gaps targeted for the fabrication of capacitive sensors and resonators above-IC is illustrated.

A novel method for enhancing the sensitivity of bulk mode gyroscopes and resonators is presented. It is based on adding parallel plate comb drives with tuned stiffness to the points of maximum vibration amplitude for optimal driving and sensing of the disk's vibrational modes. Fabricated Prototypes were measured to operate at frequencies of ~1.5 MHz, with quality factors of up to ~33,000, and exhibit a rate sensitivity of 0.43 aF/°/s/electrode, two orders of magnitude higher than a similar design without combs that was also fabricated in the same technology.

A combined magnetometer / accelerometer design based on the Lorentz force is introduced, where an electrical current is switched between two orthogonal directions on the device structure to achieve a 2D in-plane magnetic field measurement. The device can concurrently serve as a 1D accelerometer for out-of-plane acceleration, when the current is switched off. The device is fabricated using a low temperature SiC surface micromachining technology, which is fully adapted for above-IC integration on standard CMOS substrates. Measurement results from the fabricated device show a magnetic field sensitivity of 1.57 pF/T and an acceleration sensitivity of 1.02 fF/g.

A wine-glass bulk mode disk resonator based on a novel transverse piezoelectric actuation technique, which does not require any DC voltage for operation, to achieve bulk mode resonance of the single crystalline silicon disk structure is presented. The device is fabricated in a commercial MEMS process and thus combines reasonable quality factor

and superior motional resistance in a low-cost technology. External capacitive electrodes are used for optional electrostatic tuning of the frequency. Fabricated devices were measured to have resonance frequencies of ~15 MHz and quality factors as high as ~5,000.

The first surface micromachining technology based on amorphous silicon carbide (a-SiC) for above-IC integration of capacitive devices featuring independently controlled submicron lateral and vertical transduction gaps is presented. Processing is optimized for full compatibility with commercial CMOS processes, with the lowest reported fabrication temperature (<200 ^{o}C) amongst comparable technologies. DC sputtered a-SiC structural layers with superior mechanical properties are used. Two polymer-based sacrificial layers define the vertical and sub-micron lateral gaps, without requiring high resolution photolithography, and are ultimately dry released to prevent stiction, a challenging issue with wet methods. Devices including disk resonators and disk gyroscopes were fabricated and resonance frequencies up to 25 MHz with quality factors up to 1,200 were measured.

By combining our low-temperature CMOS compatible micromachining technology with the novel MEMS architectures for sensors and resonators presented, fully-integrated high-performance batch fabricated systems can be brought to market.

Sommaire

Les capteurs micro-usinés et ainsi que les micro-résonateurs génèrent de plus en plus d'intérêt car ceux-ci deviennent de plus en plus répandus dans une large variété d'applications, allant des systèmes électroniques portables, de la robotique ou dans des applications spatiales. Cette demande croissante pousse la recherche dans tous les aspects des microsystèmes pour produire des dispositifs plus performants à moindre coûts. Dans ce travail, des architectures pour améliorer la performance des différents types de microsystèmes électromécaniques (MEMS) inertiels, des capteurs magnétiques (ciblant les capteurs combinant plusieurs capteurs inertiels) et des résonateurs (ciblant les oscillateurs MEMS) sont présentés. En outre, une technologie de micro-fabrication de surface à basse température avec des interstices latéraux et verticaux fixés indépendamment et ciblée pour la fabrication de capteurs et résonateurs capacitifs intégrés est illustrée.

De plus, ce travail introduit une nouvelle architecture pour augmenter la sensibilité des micro-gyroscopes. La structure est basée sur l'ajout de peignes à plaques parallèles aux points d'amplitude maximale de vibration, ce qui augmente l'efficacité du gyroscope. Les prototypes ont été mesurés fonctionnant à des fréquences d'environ 1.5 MHz, avec des facteurs de qualité allant jusqu'à ~ 33,000, et présentant une sensibilité à la rotation de 0.43 aF/°/s/électrode, deux ordres de grandeur supérieurs aux dispositifs conventionnels fabriqués dans la même technologie.

Une conception d'un magnétomètre / accéléromètre combiné basé sur la force de Lorentz est faite, où un courant électrique est commuté entre deux directions orthogonales sur la structure pour mesurer le champ magnétique dans le plan. Le dispositif peut mesurer l'accélération hors-plan en même temps, lorsque le courant est coupé. Le dispositif est fabriqué en utilisant une technologie de micro-fabrication de surface en carbure de silicium (SiC) à basse température et qui est tout à fait adaptée pour l'intégration sur des substrats CMOS standard. Les résultats de mesure des dispositifs fabriqués montrent une sensibilité de champ magnétique de 1.57 pF/T et une sensibilité à l'accélération de 1.02 fF/g.

De plus, un résonateur novateur en forme de disque de type wine-glass est présenté. Celui-ci est basé sur une technique novatrice d'actionnement transversal piézo-électrique permettant d'obtenir une résonance de la structure en mode massique sans nécessiter de

tension DC pour le fonctionnement. Le dispositif est fabriqué dans un processus MEMS commercial et combine un facteur de qualité raisonnable et une résistance d'insertion plus faible et ce, dans une technologie à bas coût. Des électrodes capacitives externes sont utilisées pour le réglage électrostatique de la fréquence de résonance. Une fréquence de résonance de ~ 15 MHz et un facteur de qualité de ~5000 ont été mesurés.

Est aussi présentée la première technologie de micro-fabrication de surface à base de carbure de silicium amorphe (a-SiC) pour intégration avec des circuits intégrés pour l'implémentation de dispositifs capacitifs comportant des interstices submicroniques verticaux et latéraux contrôlés de façon indépendante. Le procédé de fabrication est optimisé pour être compatible avec les procédés commerciaux de fabrication CMOS. Cela est possible car la température de fabrication du procédé présentée (<200 ºC) est la plus basse rapportée parmi les technologies comparables. Une technique de pulvérisation DC des couches structurelles de a-SiC possédant des propriétés mécaniques supérieures sont utilisées. Deux couches sacrificielles de polymère définissent les interstices verticaux et latéraux, sans nécessiter de photolithographie à haute résolution et les structure sont finalement libérées avec un procédé à sec pour éviter un collage des couches relâchées, un problème difficile à pallier avec des méthodes de relâche liquides. Plusieurs dispositifs y compris des résonateurs et gyroscopes en forme de disques ont été fabriqués et des fréquences de résonance jusqu'à 25 MHz avec des facteurs de qualité jusqu'à 1200 ont été mesurés.

En combinant notre technologie de micro-fabrication avec les nouvelles architectures de MEMS présentés, des systèmes à haute performance entièrement intégrés peuvent être mis sur le marché.

Acknowledgements

First, I would like to thank my supervisor Prof. Mourad El-Gamal for his continuous support. His vision, technical advice, and financial support were very important pillars for the success of this work. I would really like to express my deep gratitude to him and I wish we can have more research collaboration in the future.

I also wish to thank Prof. Frederic Nabki. His continuous guidance was very important during the different stages of the project starting from creating the designs to their fabrication and testing.

There are many other people who contributed to the success of this work. I wish to thank Paul-Vahe Cicek. First, Paul helped me a lot in using the cleanroom tools in McGill's micro-fabrication facility. Then, we have been struggling together to develop the MEMS fabrication process for the past five years. Paul has recently joined the department of computer science at the Université du Québec à Montréal (UQAM) as an Assistant Professor. I wish him all the success in his career.

I thank the rest of my colleagues in the Wireless Integrated Circuits and MEMS laboratory especially Karim Allidina for his support on preparing the electrical test setups of the MEMS devices. Also, I would like to thank Qing Zhang for her advice on the fabrication process.

I wish to thank Don Pavlasek the shop supervisor at the mechanical design and machining facility for his help on designing and creating the mechanical and vacuum test setups.

I wish to thank Matthieu Nannini, Don Berry, Jun Li, Lino Eugene, and Sasa Ristic of the McGill Nanotools micro-fabrication facility for assisting with equipment and MEMS processing problems.

Also, I would like to thank CMC Microsystems for their support. The fabrication of the gyroscope and the piezoelectric disk resonator was enabled through them by providing design kits and access to fabrication runs. Also, some testing tools were borrowed from CMC.

This work was supported in part by McGill University, in part by the Natural Sciences and Engineering Research Council of Canada (NSERC), in part by the Quebec

Fund for Research in Nature and Technology (FRQNT), and in part by the Microsystems Strategic Alliance of Quebec (ReSMiQ). These financial supports are greatly appreciated.

List of Abbreviations

2DEG	2 dimensional electron gas
AC	alternating current
ADS	advanced design system
AMR	anisotropic magneto resistance
ASIC	application specific integrated circuit
CMOS	complementary metal oxide semiconductor
CVD	chemical vapour deposition
DC	direct current
DIP	dual in-line package
DOF	degree of freedom
DRIE	deep reactive ion etching
DTG	dynamically tuned gyroscope
DUT	device under test
ESC	electronic stability control
FBAR	film bulk acoustic wave resonator
FOG	fiber-optic gyroscope
FOM	figure of merit
GMI	giant magneto impedance
GMR	giant magneto resistance
GSG	ground signal ground
HF	hydrofluoric acid
HRG	hemispherical resonator gyroscope
IC	integrated circuit
IMU	inertial measurement unit
LGA	land grid array
LPCVD	low pressure chemical vapour deposition
LSB	least significant bit
MCM	multi-chip module
MEMS	micro-electro-mechanical systems

MTJ	magnetic tunnel junction
MUMPs	multi-user MEMS process
PAN	phosphoric acetic nitric acid
PCB	printed circuit board
PECVD	plasma enhanced chemical vapour deposition
PSG	phosphosilicate glass
RF	radio frequency
RIE	reactive ion etching
RLG	ring laser gyroscope
SAW	surface acoustic wave
SCS	single-crystalline silicon
SEM	scanning electron microscope
SOI	silicon-on-insulator
SQUID	superconducting quantum interference device
TIA	trans-impedance amplifier
USB	universal serial bus
VNA	vector network analyzer

Chapter 1 Introduction

1.1. Preface and Motivation

MEMS is the acronym for Micro-Electro-Mechanical Systems. As the name implies, MEMS is the technology that combines both the electrical and mechanical parts of a system at a microscale. The MEMS most important and attracting feature is that it allows building movable microstructures on a substrate using photolithography. This feature enabled the fabrication of the complex microstructures of sensors and actuators such as masses, flexures, actuators, detectors, levers, linkages, gears, dampers, and many other functional building blocks on the same chip together with the electronic parts of the system. Thanks to MEMS, complete sensors and systems, both the electronic circuits and the mechanical components can be fabricated on the same chip which significantly helped in reducing the size, cost and power consumption.

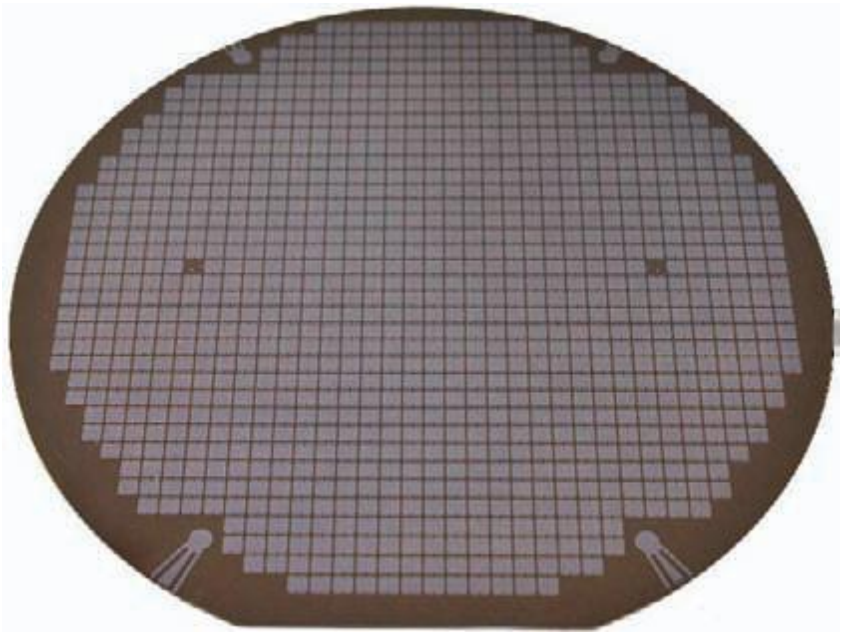

Figure 1.1: A 150mm wafer from a gyroscope prototyping run. In a production process, it is common to have well over 2000 devices on a 150 mm wafer [1].

The importance of micromachined sensors and resonators is continuously increasing as they get more widespread in a broad variety of applications ranging from handheld consumer electronics to more sophisticated applications as robotics and space applications, as shown in Figure 1.2 [2] , and various innovative MEMS devices are emerging in the different fields of application, e.g., resonators as in [3, 4], variable capacitors as in [5, 6], inertial sensors as in [7, 8], pressure sensors as in [9, 10], etc. This is pushing research in all aspects of microsystems to produce higher performance lower cost devices to cope with the increasing demand. Figure 1.3 illustrates the forecasted market growth for the different types of MEMS devices. Combo inertial sensors and MEMS oscillators are expected to have significant growth (43.4 % and 58.5 % respectively) to be in the top 3 growing markets. In this work, architectures for improving the performance of different types of MEMS inertial, magnetic sensors (targeting inertial combos) and resonators (targeting MEMS oscillators) are presented. Also, our work on a low temperature surface micromachining technology featuring independently controlled lateral and vertical gaps targeted for the fabrication of bulk mode sensors and resonators above-IC is illustrated. This technology is expected to bring highly integrated superior performance batch fabricated MEMS inertial measurement units and oscillators to market.

1.2. Thesis Organization

This thesis describes the novel architectures we devised to enhance the performance of different types of MEMS devices, presents the fabricated prototypes, the measurement

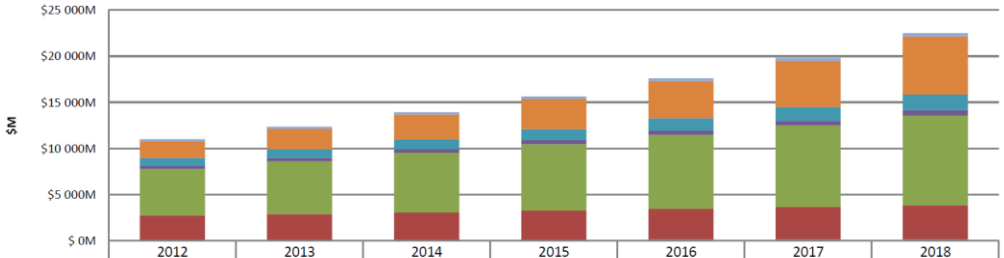

	2012	2013	2014	2015	2016	2017	2018	
Telecom	$ 188M	$ 210M	$ 239M	$ 265M	$ 297M	$ 329M	$ 364M	11,7%
Medical	$1 835M	$2 205M	$2 688M	$3 277M	$4 021M	$4 981M	$6 304M	22,8%
Industrial	$ 874M	$ 963M	$1 069M	$1 203M	$1 339M	$1 495M	$1 676M	11,5%
Defense	$ 297M	$ 335M	$ 379M	$ 421M	$ 470M	$ 525M	$ 583M	11,9%
Consumer	$5 048M	$5 752M	$6 487M	$7 216M	$7 999M	$8 833M	$9 776M	11,6%
Automotive	$2 639M	$2 760M	$2 934M	$3 115M	$3 322M	$3 503M	$3 643M	5,5%
Aeronautics	$ 107M	$ 115M	$ 124M	$ 134M	$ 143M	$ 152M	$ 156M	6,4%

Figure 1.2: Forecast for the MEMS market growth for the different applications [Yole Development, March 2013].

Figure 1.3: Expected market growth for different types of MEMS devices [Yole Development, 2013].

results illustrating the concepts, and finally presents the surface micromachining fabrication technology we developed targeting above-IC integration of capacitive MEMS resonators and sensors, especially bulk-mode devices. This chapter describes the motivation of the work and the main contributions. The thesis is composed of four main parts. Part I (chapters 2 and 3) describes a novel architecture for enhancing the sensitivity of bulk mode gyroscopes and resonators. Chapter 2 includes an overview about MEMS gyroscopes, their types, applications, and operation principles. Chapter 3 details our sensitivity enhancement architecture for bulk mode devices, presents the fabricated prototype, and the measurement results. Part II (chapters 4 and 5) focuses on MEMS magnetometers. An overview about this type of devices is presented in chapter 4. Chapter 5 details our combined magnetometer/ accelerometer sensor. It presents the fabricated devices and the measurement results. Part III (chapters 6 and 7) is focused on resonators. Chapter 6 is a brief introduction about them including their different types, transduction methods, recent advancements, and challenges. Chapter 7 presents our novel design for a wine-glass disk resonator with a novel transverse piezoelectric actuation technique and capacitive frequency tuning fabricated in a commercial of-the-shelf technology. Part IV (chapter 8) focuses on the fabrication technology. It first describes state-of-the-art

advancements in the fabrication technologies used for realizing bulk mode devices. Then, it presents the surface micromachining technology developed through our work, targeting above-IC integration. Chapter 9 presents the conclusion of the thesis, highlighting the main contributions, and discusses the potential future developments.

1.3. Contributions

The following presents the four main contributions of the work presented in this thesis:

1.3.1. A Novel Architecture for Enhancing the Sensitivity of Bulk Mode Devices

The architecture is based on adding parallel plate comb drives to the points of maximum vibration amplitude, and tuning the stiffness of these combs. This increases the drive strength and results in significant improvement in the sensitivity. In this work, the idea was implemented in a commercial relatively large gap technology (SOIMUMPs) in order to outline the sensitivity improvement possible through the proposed method in a widely available standard bulk micromachining technology. The design is composed of a central dodecagon disk structure with added parallel plate comb drives. Adding combs connected to the central disk structure increases the drive strength and results in two orders of magnitude higher sensitivity than a similar design without combs [11], as measured using a custom built electrical vacuum test platform. This enables the fabrication of potentially high performance bulk-mode gyroscopes in standard commercial MEMS technologies. Furthermore, the architecture is well-suited for technologies with ~100 nm transducer gaps in order to achieve very high performance devices. The concept was introduced briefly in [12-13]. I am the main contributor for these publications. Prof. Nabki provided guidance and supervised the design. Also, this novel architecture generated a patent application [14].

1.3.2. A Combined Magnetometer/ Accelerometer Sensor Based on a Novel Current Switching Technique

A Lorentz force based magnetometer / accelerometer combined sensor, made from a low temperature, above-IC-compatible fabrication process is presented. The proposed sensor relies on switching an electrical current between two perpendicular directions on

the device structure to achieve a 2D in-plane magnetic field measurement. Concurrently, the device serves as a 1D accelerometer for out-of-plane acceleration, by switching the current off and by monitoring the structure's capacitive changes in response to acceleration. The design can thus separate magnetic and inertial force measurements, utilizing a single compact device. The proposed sensor supports static operation at atmospheric pressure to avoid the need for complex vacuum packaging. Alternatively, it is also capable of operating at resonance under vacuum for enhanced sensitivity. The device is fabricated using a silicon carbide (SiC) surface micromachining technology as in [15-17], which is fully adapted for above-IC integration on standard CMOS substrates. The device was presented briefly in [18]. I am the main contributor for this article. Mr. Cicek helped in the fabrication and in writing the paper. Prof. Nabki provided guidance throughout the work. Also, a patent was filed about this original design [19].

1.3.3. Bulk Mode Disk Resonator with Transverse Piezoelectric Actuation and Electrostatic Tuning

This work demonstrates the first use of transverse piezoelectric actuation to excite a bulk-mode silicon resonator in the wine-glass mode to offer a desirable combination of reasonably high quality factor and the lowest motional resistance, amongst comparable disk resonators. The device of this work is also the first demonstrated wine-glass bulk-mode disk resonator built using a commercially available low-cost MEMS fabrication process. The device is measured to have a resonance frequency of ~15 MHz and, a quality factor of ~2,000 at atmospheric pressure improving to ~5,000 in a 100 mTorr vacuum, while exhibiting a temperature coefficient of ~ -40 ppm/^{o}C. External capacitive electrodes were also successfully used to adjust the frequency of resonance through the DC voltage tuning. This work is currently under review in [20]. I am the main contributor for this publication. Mr. Cicek helped in the layout and Prof. Nabki supervised the design.

1.3.4. Above-IC Compatible Silicon Carbide Technology with Sub-Micron Lateral Gaps

Surface micromachining is a very important micro-fabrication process, as it allows for more fabrication flexibility, especially for integrating micromachined devices with electronic circuits. This is very advantageous in order to reduce parasitics between the

devices and their interface circuitry, compared to side-by-side co-fabrication approaches. This consequently would allow for improved performance. It is usually a challenge to get good structural material properties, while abiding by the processing temperature constraints for post-processing above standard ICs. Former members of our team have developed a surface micromachining technology based on silicon carbide for above-IC integration, discussed in details in [15-17]. The process utilizes DC sputtered amorphous silicon carbide as it provides superior mechanical properties, namely high Young's modulus, high acoustic velocity, and low stress compared to materials used for micromachining technologies utilized in the literature. This is achieved while maintaining the lowest processing temperature, which makes it ideally suited for post-processing above standard CMOS substrates. The process featured vertical gaps using a sacrificial polyimide layer between a bottom metal layer and a SiC structural layer on top. In this thesis, our work in augmenting the capabilities of our low temperature silicon carbide surface micromachining technology by adding sub-micron lateral gap capability is presented. The process steps are designed carefully so as to make the vertical and lateral gaps independently controllable. Several process issues were resolved while maintaining the lowest reported processing temperature, which makes it ideally suited for post-processing above standard CMOS substrates.

All aforementioned contributions are explained in the subsequent chapters detailing the designs, implementations, test setups, measurement, and characterization results.

1.4. References

[1] C. Acar and A. Shkel, "*MEMS Vibratory Gyroscopes: Structural Approaches to Improve Robustness,*" Springer, 2009.

[2] "*Status of the MEMS Industry*," Yole Development, 2013.

[3] Y. -W. Lin, S. Lee, S. -S. Li, Y. Xie, Z. Ren, and C. Nguyen, "Series-Resonant VHF Micromechanical Resonator Reference Oscillators", *IEEE Journal of Solid-State Circuits*, vol. 39, no. 12, pp. 2477-2491, December 2004.

[4] F. Nabki, K. Allidina, F. Ahmad, P. -V. Cicek, and M. N. El-Gamal, "A Highly Integrated 1.8 GHz Frequency Synthesizer Based on a MEMS Resonator," *IEEE Journal of Solid-State Circuits*, vol. 44, no. 8, pp. 2154-2168, August 2009.

[5] A. Elshurafa and E. El-Masry, "Design Considerations in MEMS Parallel Plate Variable Capacitors," *Proceedings of the IEEE Midwest Symposium on Circuits and Systems*, pp. 1173-1176, August 2007.

[6] A. Elshurafa and E. El-Masry, "Finite Element Modeling of Low-Stress Suspension Structures and Applications in RF MEMS Parallel-Plate Variable Capacitors," *IEEE Transactions on Microwave Theory and Techniques*, vol. 54, no. 5, pp. 2211-2219, May 2006.

[7] N. Yazdi, F. Ayazi, and K. Najafi, "Micromachined Inertial Sensors," *Proceedings of the IEEE*, vol. 86, no. 8, pp. 1640-1659, August 1998.

[8] A. Trusov, A. Schofield, and A. Shkel, "Gyroscope Architecture with Structurally Forced Anti-Phase Drive-Mode and Linearly Coupled Anti-Phase Sense-Mode," *Proceedings of the IEEE International Conference on Solid-State Sensors, Actuators and Microsystems*, pp. 660-663, June 2009.

[9] P. Pattnaik and V. Neeharika, "Novel Optical MEMS Pressure Sensors Incorporating Waveguide Bragg Gratings on Diaphragms", *Proceedings of the IEEE International Conference on Sensors*, pp. 1908-1911, November 2014.

[10] M. Schwerter, M. Leester-Schadel, S. Buttgenbach, A. Dietzel, C. Behr, M. Sinapius, and P. Wierach, "MEMS Pressure Sensors Embedded into Fiber Composite Airfoils," *Proceedings of the IEEE International Conference on Sensors*, pp. 531-534, November 2014.

[11] M. Y. Elsayed, F. Nabki, and M. N. El-Gamal, "A 2000 ^{o}/sec Dynamic Range Bulk Mode Dodecagon Gyro for a Commercial SOI Technology," *Proceedings of the IEEE International Conference on Electronics, Circuits, and Systems*, pp. 264-267, December 2011.

[12] M. Y. Elsayed, F. Nabki, and M. N. El-Gamal, "A Combined Comb/Bulk Mode Gyroscope Structure for Enhanced Sensitivity," *Proceedings of the IEEE International Conference on Microelectromechanical Systems*, pp. 649-652, January 2013.

[13] M. Y. Elsayed, F. Nabki, and M. N. El-Gamal, "A Novel Comb Architecture for Enhancing the Sensitivity of Bulk Mode Gyroscopes," *Journal of Sensors,* vol. 13, no. 12, pp. 16641-16656, December 2013.

[14] M. Elsayed, P.-V. Cicek, F. Nabki, and M. N. El-Gamal, "Microelectromechanical Bulk Acoustic Wave Devices and Methods," *US Patent Application US20140230547 A1*, August 2014.

[15] F. Nabki, T. Dusatko, S. Vengallatore, and M. El-Gamal, "Low-Temperature (<300°C) Low-Stress Silicon Carbide Surface Micromachining Fabrication Technology," *Technical Digest of the Hilton Head Solid-State Sensors, Actuators and Microsystems Workshop*, pp. 216 - 219, June 2008.

[16] F. Nabki, T. Dusatko, S. Vengallatore, and M. El-Gamal, "Low Stress CMOS-Compatible Silicon Carbide Surface-Micromachining Technology - Part I: Process Development and Characterization," *Journal of Microelectromechanical Systems*, vol. 20, no. 3, pp. 720-729, June 2011.

[17] F. Nabki, P. Cicek, T. Dusatko, and M. El-Gamal, "Low Stress CMOS-Compatible Silicon Carbide Surface-Micromachining Technology - Part II: Beam Resonators for MEMS above IC," *Journal of Microelectromechanical Systems*, vol. 20, no. 3, pp. 730-744, June 2011.

[18] M. Y. Elsayed, P. -V. Cicek, F. Nabki, and M. N. El-Gamal, "Surface Micromachined Combined Magnetometer/ Accelerometer for Above-IC Integration," *Journal of Microelectromechanical Systems*, December 2014.

[19] M. Elsayed, P.-V. Cicek, F. Nabki, and M. N. El-Gamal, "Combined Magnetometer Accelerometer MEMS Devices and Methods," *US Provisional Patent Application*, filed November 2014.

[20] M. Y. Elsayed, P. -V. Cicek, F. Nabki, and M. N. El-Gamal, "Bulk Mode Disk Resonator with Transverse Piezoelectric Actuation and Electrostatic Tuning," *Journal of Microelectromechanical Systems*, submitted July 2015.

Part I: MEMS Gyroscopes

Chapter 2 Overview about MEMS Gyroscopes

The importance of measuring the angular rotation rate is continuously increasing day after day. This is a result of the growing need for products that require autonomous navigation as well as accurate orientation measurement. These products include consumer products such as digital cameras, computer games, and automotive applications as shown in Figure 2.1 (a), as well as more sophisticated applications such as robotics, aerospace and military applications as shown in Figure 2.1 (b), (c) and (d). This stimulated research to develop low-cost, light weight angular rate sensors (gyroscopes) to cope with this increasing demand.

(a) Automotive applications <Google Inc.>

(b) Robotics <Honda Motor Co.>

(c) Aerospace applications <NASA>

(d) Unmanned air vehicles <General Atomics Aeronautical Systems Inc.>

Figure 2.1: Examples of gyroscope applications.

This chapter discusses briefly an overview about MEMS gyroscopes including their history, operation principles, types, sensing techniques, and applications. It also constitutes a brief market review and discusses some examples of commercial MEMS gyroscopes.

2.1. Historical Review

A gyroscope is the sensor that measures the rate of rotation of an object. The name "gyroscope" originated from Léon Foucault, combining the Greek word "skopeein" meaning to see and the Greek word "gyros" meaning rotation, during his experiments to measure the rotation of the Earth as shown in Figure 2.2 [1]. The gyroscope principle of operation depends on the Coriolis Effect as will be discussed in section 2.2.

Figure 2.2: The Foucault pendulum, invented by Jean Bernard Léon Foucault in 1851 as an experiment to demonstrate the rotation of the earth. The swinging direction of the pendulum rotates with time at a rate proportional to the sine of the latitude, due to earth's rotation [2].

Figure 2.3: One of the first examples of the gyrocompass, developed in the early 1800s [1].

In the early eighteenth century, spinning devices were being used for sea navigation in foggy conditions. Traditional spinning gyroscopes were invented in the early nineteenth century. Figure 2.3 shows a picture of an early gyrocompass. The gyrocompass gained popularity, especially in steel ships, since steel blocked the ability of magnetic compasses to detect magnetic north [1].

Spinning gyroscopes utilize a rotating wheel attached to a gimbal structure. The main disadvantages of rotating wheel gyroscopes are bearing friction and wear. For this reason, vibratory gyroscopes, such as the Hemispherical Resonator Gyroscope (HRG) and Tuning-Fork Gyroscopes are more attractive as they solve the bearing problems because they do not contain rotating parts. Vibratory gyroscopes depend in the operation on the Coriolis effect as explained in section 2.2. Alternative high-performance technologies such as the Fiber-Optic Gyroscope (FOG) and Ring Laser Gyroscope (RLG) based on the Sagnac effect have also been developed as shown in Figure 2.4. These devices send two laser beams around a circular path in opposite directions. If the path spins, a phase shift can be detected. The rings are usually triangular or rectangular shaped with mirrors at each corner. Optical gyroscopes have many advantages over the conventional spinning mass

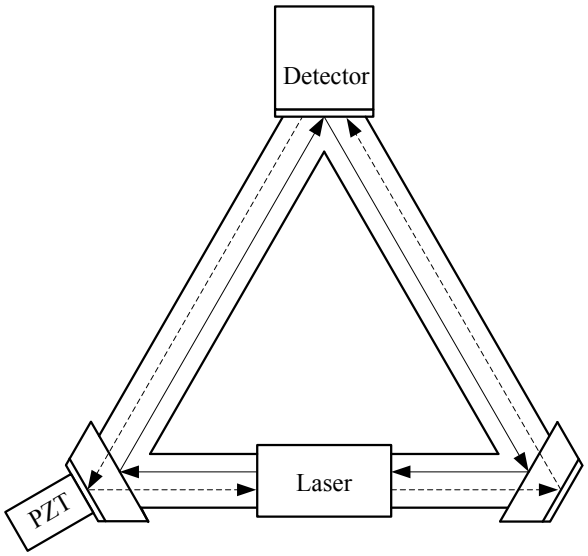

Figure 2.4: General Ring Laser Gyroscope.

gyroscopes which are: no wear, higher reliability, better performance, smaller size, and weight, but they have higher cost due to the complicated process of the whole device assembly and the high cost of the fiber [3]. Due to their advantages, these optical gyroscopes were very attractive for many high-end applications despite their high costs.

2.2. The Coriolis Effect

Any mass that spins at a relatively high speed will conserve the spinning direction. When an external force is applied in a perpendicular direction to that of spinning, the spinning mass will move in a well determined direction which is orthogonal to both the spinning direction and the external applied force. Such phenomenon has been observed since thousands of years. Ancient Egyptians used to have a popular toy spinning top shown in Figure 2.5, which was found in the tomb of Tutankhamun and is currently at the Egyptian Museum. This toy was one of the most beloved toys of Egyptian children in ancient times. When the top is thrown on the ground and the string that is wrapped around it is pulled, it turns like a balanced whirl with a fixed and well defined spinning orientation, irrespective of any external perturbation [1, 4].

Gaspard Gustave Coriolis studied such behavior in his paper “Mémoire sur les équations du mouvement relatif des systémes de corps” where he was investigating moving

Figure 2.5: A wooden, cone-shaped, decorated spinning top from the 14th century BC found in the tomb of Tutankhamun, currently at the Egyptian Museum [4].

particles in rotating systems in 1835 [5]. In his work, Coriolis managed to derive a mathematical expression that describes such phenomenon and has been named after him as "Coriolis effect".

The Coriolis effect is explained as follows: if a body of mass (m) is moving with a velocity (υ) in a certain direction and is acted upon by a rotation rate (Ω) around another direction, a force is generated that will move the body in a direction perpendicular to both the direction of the original motion and the axis of rotation, as demonstrated in Figure 2.6. This force is called the Coriolis force (F_c) and is given by [6]

$$F_c = 2m\,(\upsilon \times \Omega)\,. \tag{2.1}$$

The Foucault pendulum shown in Figure 2.7 is a very good demonstration of the Coriolis effect. The experimental apparatus consists of a long pendulum free to oscillate in any vertical plane. The direction along which the pendulum swings rotates with time because of Earth's daily rotation. This is because the plane of the pendulum's swing, like a gyroscope, tends to keep a fixed direction in space, while the Earth rotates under it. The first public exhibition of a Foucault pendulum took place in February 1851 in the Meridian

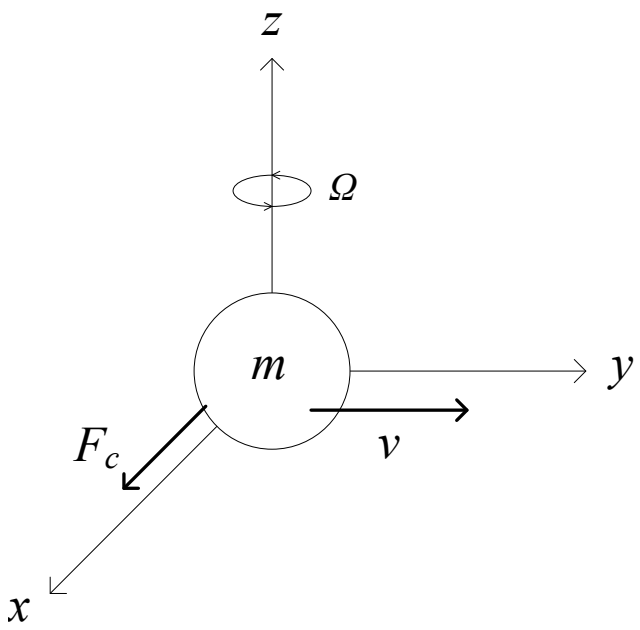

Figure 2.6: Schematic illustrating the Coriolis effect.

Room of the Paris Observatory. A few weeks later, Foucault made his most famous pendulum when he suspended a 28 kg bob with a 67 meter long wire from the dome of the

Figure 2.7: Foucault's Pendulum in the Panthéon, Paris [7].

Panthéon, Paris. The plane of the pendulum's swing rotated clockwise 11° per hour, making a full circle in 32.7 hours. The precession of the pendulum can only be explained by including the Coriolis force in the equations of motion [7].

2.3. The MEMS Gyroscope

By merging electrical and mechanical systems at a micro scale, MEMS led to a revolution in the fabrication of inertial sensors. Since the first micromachined gyroscope (shown in Figure 2.8) was introduced by the Draper Laboratory in 1991, various micromachined gyroscope designs have been reported using a variety of fabrication techniques including surface micromachining, bulk micromachining, and hybrid surface-bulk micromachining technologies. Extensive research efforts towards commercial micromachined gyroscopes led to several innovative gyroscope topologies, fabrication, integration approaches, and detection techniques. Even though an extensive variety of micromachined gyroscope designs and operation principles exist, the majority of the reported micromachined gyroscopes use vibrating mechanical elements to sense angular rate based on sensing the motion due to the Coriolis force, as will be explained in section 2.2. Using vibrating elements exhibits many advantages over utilizing spinning parts by involving no rotating parts and thus, eliminating the need for bearings and

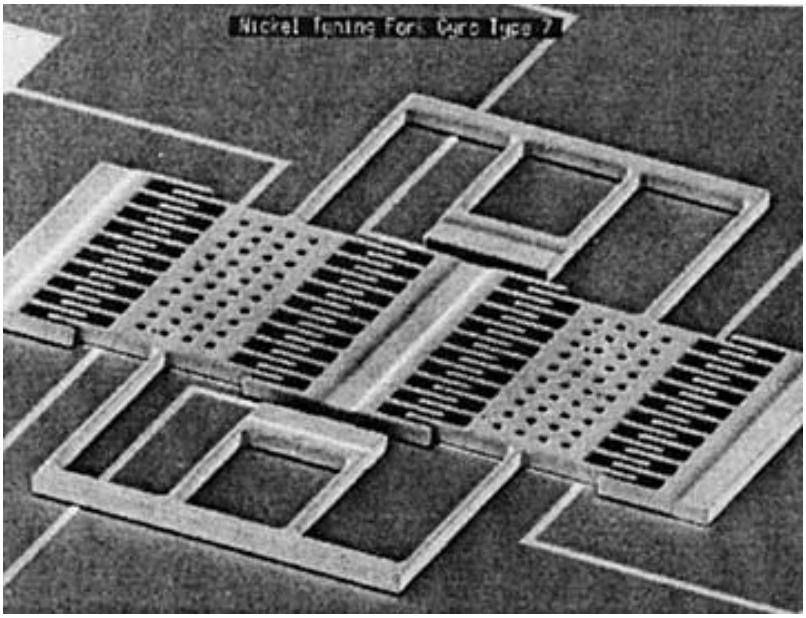

Figure 2.8: The first working prototype of the Draper Lab comb drive tuning fork gyroscope [8].

mitigating friction and wear. That is the primary reason for vibratory gyroscopes being successfully miniaturized using MEMS technologies and becoming an attractive alternative to their macro-scale counterparts.

The fundamental operation principle of micromachined vibratory gyroscopes relies on the Coriolis effect. The proof mass is driven by a sinusoidal electrostatic force (drive mode). When a rotation rate is applied, the Coriolis force affects the proof mass moving it in a direction normal to both the driving direction and the rotation axis (sense mode). By sensing the motion in the sense direction, the rotation rate can be measured. The proof mass is generally suspended above the substrate by a suspension system consisting of flexible beams. The overall system is typically a two degrees of freedom (2 DOF) mass-spring-damper system, where the Coriolis effect causes energy transfer from the drive to the sense mode proportional to the angular rate input. Ideally, it is desirable to utilize resonance in both the drive and the sense modes in order to attain the maximum possible response gain and sensitivity. This is achieved by designing and tuning the drive and sense resonant frequencies to match. Alternatively, the sense-mode is designed to be slightly shifted from the drive-mode to improve robustness and thermal stability, while intentionally sacrificing gain and sensitivity. Even though increasing the spacing between the drive and sense frequencies reduces the impact of variations in oscillatory system parameters that shift the natural frequencies and damping values, the resulting errors still require compensation by

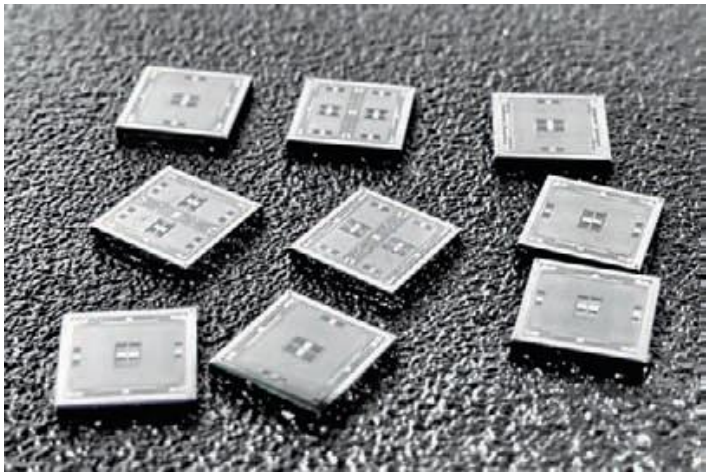

Figure 2.9: Micromachined gyroscope dies designed and fabricated at the University of California at Irvine Microsystems Laboratory [1].

advanced control and signal processing architectures [1]. Examples of fabricated MEMS gyroscope dies (fabricated at the University of California at Irvine Microsystems Laboratory) are shown in Figure 2.9.

2.4. Applications of MEMS Gyroscopes

Based on their performance, gyroscopes can be classified into three categories which are: inertial grade, tactical grade, and rate grade devices. The specifications of each of these categories are shown in Table 2.1 [6, 9, 10].

Due to the continuous improvement in the performance of MEMS gyroscopes, their low costs and small sizes, they are replacing other types of sensors in a wide variety of applications. Other high performance angular rate sensors such as fiber-optic gyroscopes which are mainly used for tactical grade applications, ring laser gyroscopes and hemispherical resonator gyroscopes [11] which are mainly used for inertial grade applications are usually too expensive and too large for use in some emerging applications such as micro-satellites and micro-robotics. Moreover, these high performance sensors are very costly.

MEMS technology allowed batch fabrication of sensors on a chip similar to integrated circuits and furthermore allowed merging the electronic circuits and the mechanical components on the same chip. This led to a significant reduction in the sensor's

Table 2.1: Specifications for different gyroscope grades.

Parameter	Rate Grade	Tactical Grade	Inertial Grade
Angle random walk ($^o/\sqrt{Hr}$)	>0.5	0.5-0.05	<0.001
Bias drift (^{o}/Hr)	10-1000	0.1-10	<0.01
Scale factor accuracy (%)	0.1-1	0.01-0.1	<0.001
Full scale range (^{o}/sec)	50-1000	>500	>400
Max. shock in 1 msec (g)	10^3	10^3-10^4	10^3
Bandwidth (Hz)	>70	≈100	≈100

cost than any other technology. Figure 2.10 shows the iMEMS ADXRS angular rate sensor by Analog Devices as an example of sensors in which the angular rate sensing element and signal processing electronics are integrated on the same die. Raising the performance of MEMS sensors to reach tactical and inertial grade performance is a very difficult task and has gained lots of attention over the last decades. Reaching theses grades requires improving the performance of both the gyroscope mechanical parts and the sensing electronic circuits which is very challenging for both MEMS and circuit designers.

Due to their dramatically reduced cost, size, and weight, MEMS gyroscopes potentially have a wide application spectrum in the aerospace industry, military, automotive, and consumer electronics markets. The automotive industry applications are diverse, including advanced automotive safety systems such as electronic stability control (ESC), high performance navigation and guidance systems, ride stabilization, roll-over detection and prevention, and airbag and brake systems. A wide range of consumer electronics applications with very high volumes include image stabilization in digital cameras and camcorders, virtual reality products, inertial pointing devices, and computer

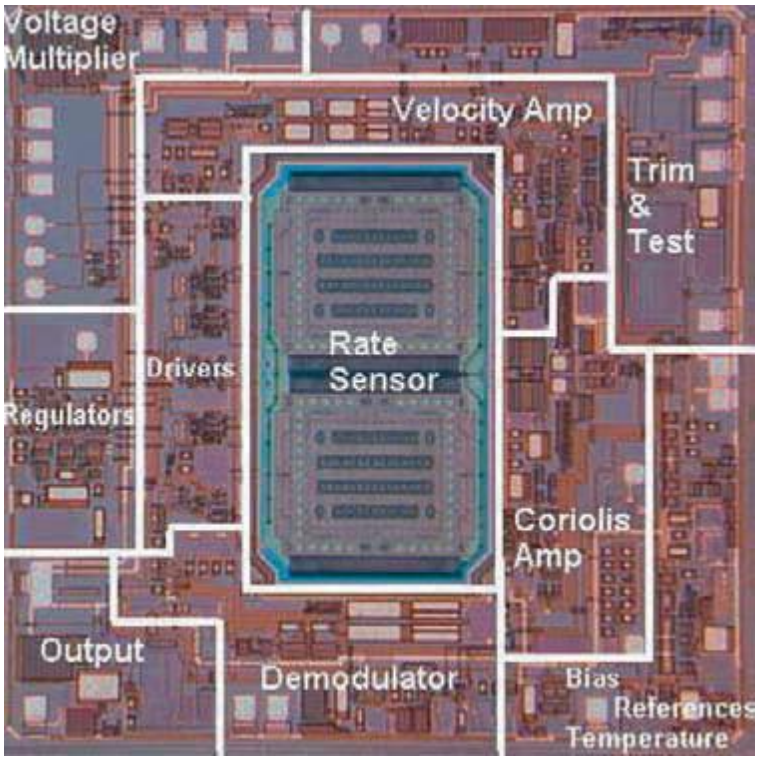

Figure 2.10: iMEMS ADXRS angular rate sensor by Analog Devices [1].

gaming industry. Miniaturization of gyroscopes also enables higher end applications such as micro-satellites, micro-robotics, and even implantable devices to cure vestibular disorders [1].

2.5. Principle of Operation of Vibratory Gyroscopes

Generally, any vibratory gyroscope structure has two resonance modes inclined on each other. The first is called the drive mode and the second is called sense mode. The structure with proof mass of mass *M* is forced to resonate in the drive resonance mode with a velocity *v*. When an external angular rate Ω is applied, the structure is affected by a Coriolis force, as described earlier by (2.1). This force excites the sense mode and therefore the structure starts vibrating in the sense mode as well. The angular rate can be inferred by measuring the sense mode displacement. This principle is illustrated in Figure 2.11.

The drive force frequency must be as close as possible to the drive mode resonance frequency in order to achieve the highest displacement possible. To explain this, the gyroscope will be modeled as a spring mass damper system as shown in Figure 2.12.

The system can be described by

$$F - kx(t) - c\dot{x}(t) = m\ddot{x}(t), \tag{2.2}$$

where *F* is the external force acting on the system, *k* is the spring constant, *m* is the mass, *c* is the damper constant, and *x(t)* is the displacement of the proof mass.

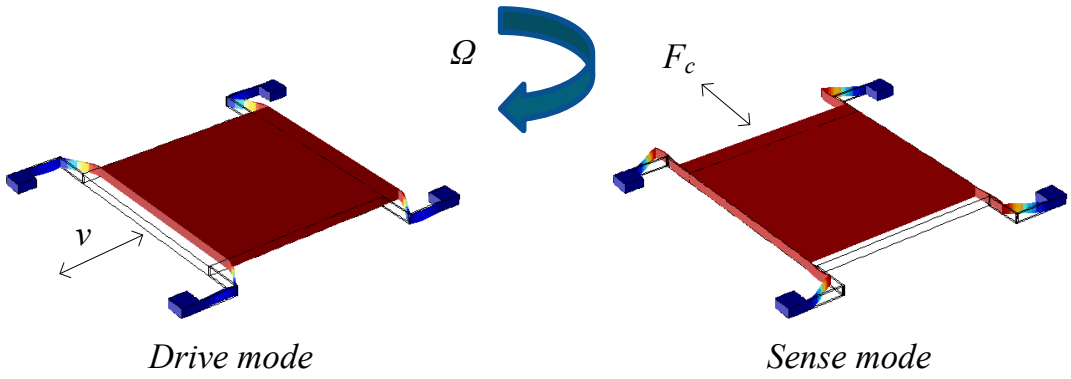

Figure 2.11: Operation principle of vibratory gyroscopes.

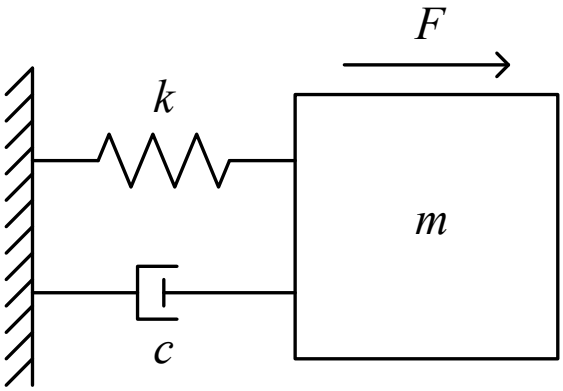

Figure 2.12: Resonant spring-mass-damper system model.

And therefore, the transfer function of the system can be expressed as

$$\frac{X(S)}{F(S)} = \frac{1}{mS^2 + cS + k} = \frac{1/m}{S^2 + (\omega_0/Q)S + \omega_0^2}, \tag{2.3}$$

where ω_0 is the resonance frequency of the system defined as $\sqrt{k/m}$ and Q is the quality factor of resonance defined as $\omega_0 m/c$.

It is clear from (2.3) that if the drive force frequency is the same as the drive mode frequency, a factor of Q will be gained in the transfer function, compared to the static transfer function as shown by

$$\left|\frac{X(j\omega_0)}{F(j\omega_0)}\right| = Q\left|\frac{X(0)}{F(0)}\right|. \tag{2.4}$$

This is usually achieved by driving the gyroscope in a closed loop configuration using a high gain transimpedance amplifier (TIA) as shown in Figure 2.13.

The same effect exactly happens on the sense side. Therefore, in order to gain the best sensitivity, the sense and drive mode frequencies need to be matched. This is ensured by proper design through symmetric architectures and carefully selecting the dimensions of the structures. However, due to process non-idealities some mismatch error is usually inevitable which necessitates the use of electronic mode matching schemes, which complicates the design of the interfacing circuitry. Alternatively, the sensor can be used in

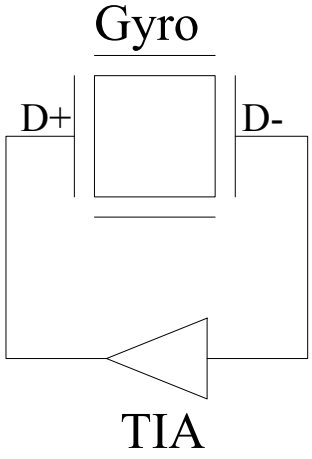

Figure 2.13: Closed loop configuration for gyroscope drive.

the mismatched mode (i.e. drive and sense mode frequencies mismatched) at the cost of degraded sensitivity.

2.6. Sensing Techniques

There are several sensing techniques for MEMS vibratory gyroscopes. The most famous techniques are piezoelectric, piezoresistive, and capacitive sensing techniques.

Numerous piezoelectric vibratory gyroscopes were introduced in the early 1980's. Examples of these devices are fused quartz hemispherical resonator gyroscope introduced by Delco [11], quartz tuning forks [12] like the Quartz Rate Sensor by Systron Donner [13], and the piezoelectric vibrating disc gyro [14]. Quartz vibratory gyroscopes can achieve very high quality factors at atmospheric pressure. However, their fabrication is not compatible with IC fabrication technology.

Another sensing technique is the piezoresistive technique. This technique is based on the idea that the stress induced due to the Coriolis force generated as a result of the rotation rate results in changing the resistance of certain piezoresistors in the design. By sensing this resistance change, the rotation rate can be measured. For example the tuning fork gyroscope introduced by researchers at Daimler Benz for automotive applications [15]. This gyroscope measures the rotation rate by piezoresistively sensing the rotation

induced shear stress in the stem of the tuning fork device. Another example for piezoresistive rate sensors is the sensor presented by researchers at the University of Neuchatel, Switzerland. They demonstrated a tuning fork design based on two isolated vibrating proof masses, each supported by a four beam bridge-type suspension [16]. These proof masses are electromagnetically vibrated in-plane and antiphase, and the out-of-plane motion induced by the rotation is then detected by four piezoresistors connected in a Wheatsone bridge configuration. Although piezoresistive devices are easier to fabricate and require a simpler electronic interface due to their lower output impedance compared to capacitive devices, they have large temperature sensitivity and poor resolution.

Capacitive conversion methods are the most widely used sensing technique in gyroscopes. Capacitive sensing is based on the fact that the rotation induced Coriolis force leads to the motion of the proof mass in the sense direction and consequently leads to the change in the capacitance between the sense mode electrodes. By sensing this capacitance change, the rotation rate can be deduced. Capacitive sensing is also widely employed in other MEMS sensors such as accelerometers, pressure sensors, and also in micro actuators [17]. This is because of its compatibility with the electronic circuit fabrication which leads to the ease of integrating the MEMS components and their interfacing circuitry on the same chip. This consequently leads to less parasitics and better signal to noise ratio. Because of these advantages capacitive sensing is the most abundant sensing technique.

2.7. Types of Vibratory Gyros Based on Vibration Mode

Vibratory gyros and resonators generally can be classified according to their mode of vibration to two main categories: flexural mode and bulk mode devices. Flexural mode devices are usually composed of a proof mass suspended over the substrate by means of some sort of suspensions that are anchored to the substrate. Figure 2.14 shows examples of both types from the literature.

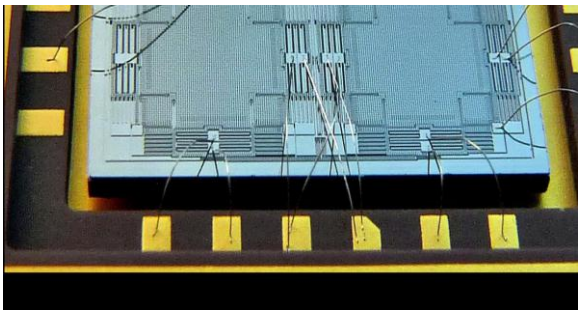

Trusov et al. [18]

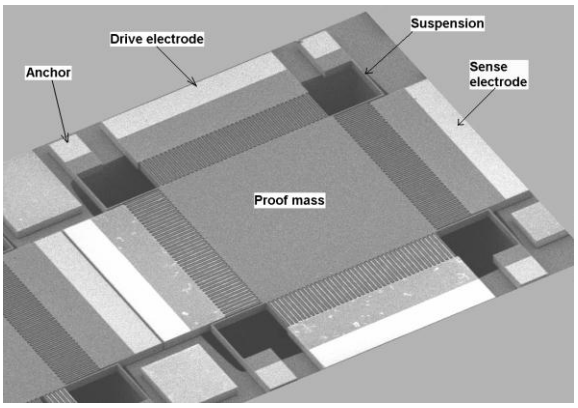

Elsayed et al. [19].

(a)

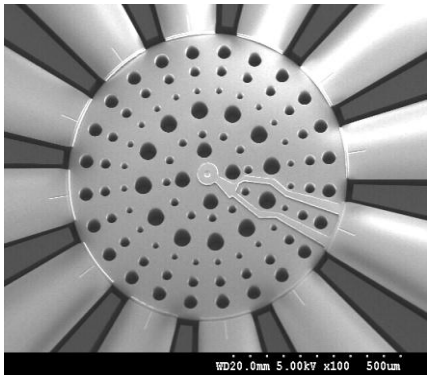

Johari et al. [20].

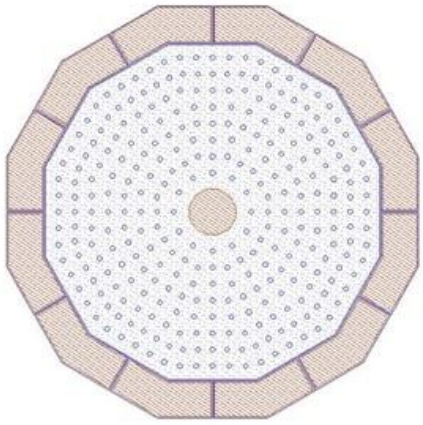

Elsayed et al. [21].

(b)

Figure 2.14: Examples of the different types of vibratory gyroscopes based on their mode of vibration: (a) flexural mode devices, and (b) bulk mode devices.

In flexural mode devices, the resonance usually occurs by vibrating the proof mass and flexing the suspensions. This is where the name flexural mode devices come from. Due to this flexing action, the resonance mode is usually prone to thermoelastic damping, which limits the quality factor of the resonance mode. On the other hand, bulk mode devices are usually composed of very stiff structures vibrating throughout their bulk, as shown in Figure 2.14, which illustrates examples of bulk mode gyros and resonators. Due to their relatively high stiffness, they have much higher resonance frequencies and suffer much less from thermoelastic damping [20-23]. Also, they experience lower motion amplitude and therefore experience less air damping. This consequently avoids the need for expensive

vacuum packaging, which is usually important for flexural mode devices to obtain good quality factors.

As highlighted in [20], bulk mode gyroscopes are capable of achieving superior performance compared to flexural mode ones. These gyros operate in higher order resonant modes, and thus their operating frequencies are generally in the MHz range—three orders of magnitude higher than flexural mode gyros. Notably, higher order modes experience less thermoelastic damping than flexural modes. Moreover, they can achieve very high quality factors (~50,000) even in atmospheric pressure, as air damping has little impact on their operation due to the high stiffness of their structures. Also, bulk mode gyroscopes exhibit orders of magnitude higher bandwidths than flexural mode ones, thus relaxing the need for drive-sense mode matching and expensive vacuum packaging, which are both mandatory for the operation of flexural mode gyroscopes.

In addition, bulk mode gyroscopes generally exhibit lower mechanical noise than flexural ones. The mechanical noise of a vibratory gyroscope is given by [6]:

$$\Omega_{z(Brownian)} \propto \frac{1}{q_{drive}} \sqrt{\frac{4k_B T}{\omega_0 M Q_{effect-sense}}}, \tag{2.5}$$

where q_{drive} is the drive mode vibration amplitude, k_B is the Boltzmann constant, T is the absolute temperature, ω_0 is the resonance frequency, M is the mass, and $Q_{effect\text{-}sense}$ is the effective quality factor. Today, state-of-the-art vibratory gyroscopes operating at lower frequencies (<100 kHz) rely on increasing the proof mass or the vibration amplitude to improve their noise performance. They require low vacuum operation (<10 mTorr) to achieve high quality factors (<10,000) that are ultimately limited by thermoelastic damping. Enhancing the noise performance of gyros without the need for increasing the mass or vibration amplitude is of great interest, as these parameters are limited mainly by design area and power concerns. From Equation (2.5), it is clear that raising the resonance frequency and the quality factor, as allowed by bulk mode architectures, improves the noise performance of a gyroscope significantly.

Different bulk mode gyroscopes that take advantage of these improved characteristics have recently been published. In [20, 22], a circular disk architecture was introduced in (100) and (111) silicon, and a circular disk gyro with spokes was suggested in [23] – it combined flexural and bulk modes, and achieved a large dynamic range. Bulk mode gyros (e.g., [20, 22, 23]) and resonators (e.g., [24-27]) typically utilize very small transducer gaps (e.g., 200 nm) between the center resonating element and the electrodes. In [21], a 3 μm gap dodecagon bulk mode gyroscope design utilizing a commercial MEMS fabrication technology (SOIMUMPs), was reported. This device's sensitivity was significantly less than the previously mentioned devices due to its relatively large transducer gap, mainly dictated and limited by the technology used. In the next chapter, a novel architecture for increasing the sensitivity of bulk mode gyroscopes is presented (as explained in [28, 29]). It is based on adding parallel plate comb drives to the points of maximum vibration amplitude, and tuning the stiffness of the combs. This increases the drive strength and results in a significant sensitivity improvement. In this work, this sensitivity enhancement concept was implemented in SOIMUMPs, the same technology used in [21]. The device exhibits a rate sensitivity, two orders of magnitude higher than the similar design without combs, presented in [21].

2.8. Market Review

Micromachined gyroscopes are receiving increasing attention in the sensing community. This is due to their small size, which enable their use in numerous consumer electronics applications. Mature applications still represent a significant market (gaming, camera stabilization, etc.). Furthermore, a wide range of new applications is emerging. Examples include sports (e.g., gesture monitoring), fitness (e.g., posture monitoring), healthcare (e.g., fall detection), toys (e.g., robotic devices), and remote controls (e.g., pointing for digital set top boxes) [30]. They have also become standard components in several handheld electronic devices (e.g., smart phones and tablets). Furthermore, gyros are used in navigation systems for robotic, military, aeronautic and space applications, providing a significant opportunity for the growth of their micro-machined implementations. However, these high end applications require demanding performance

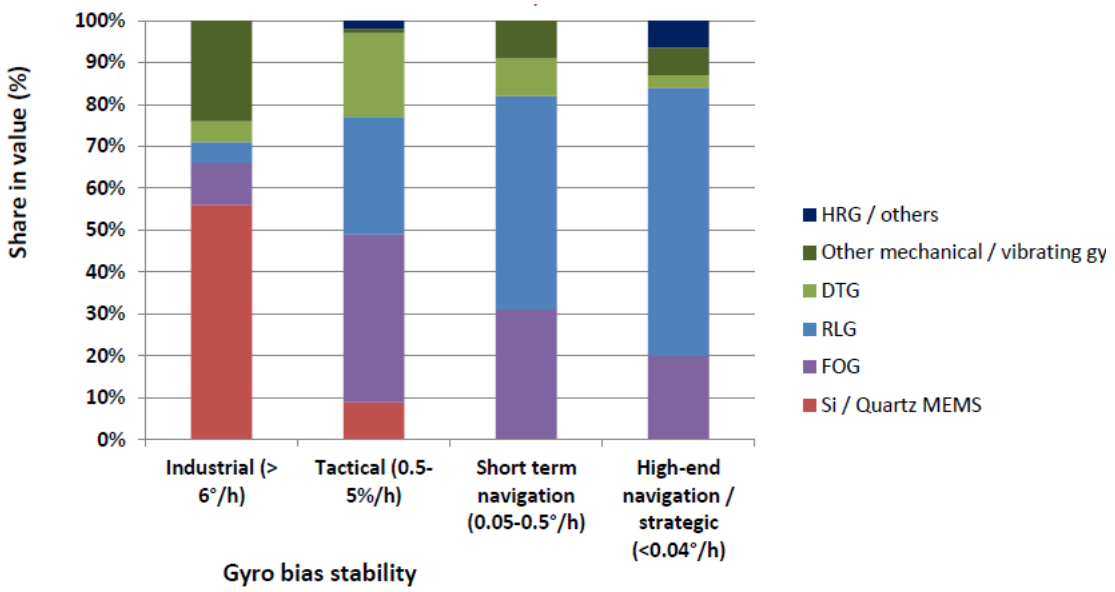

Figure 2.15: Market shares for different gyro types based on their performance grades.
[Yole Development, August 2012]

(tactical and inertial or navigation grade sensors) and therefore are dominated by more bulky and more expensive gyros (e.g.: HRG, FOG, RLG, and others), as shown in Figure 2.15. Thanks to continuous research, MEMS gyros are experiencing continuous development and would hopefully replace the other gyro types in advanced applications. Figure 2.16 shows the significant growth of the MEMS gyroscope market from 2011 through 2017 as it dominates the consumer electronics market. In the next section, some examples for state-of-the-art commercial MEMS gyros available in the market are presented together with their key performance parameters.

2.9. Examples of Commercial Gyros

2.9.1. ST Microelectronics L3G3200D

This is one of the latest gyroscopes by ST Microelectronics [32]. It is a 3-axis discrete gyro with 16 bit digital output. The sensor is available in a 16 pin LGA package and its footprint is 3×3.5×1 mm. The device operates from a 2.5 V DC supply and draws 6.1 mA of current. The full scale rate output is programmable to either ±250, ±500, or ±2000 °/s (dps) and the sensitivity is programmable to 8.75, 17.5, 70 mdps/LSB for the

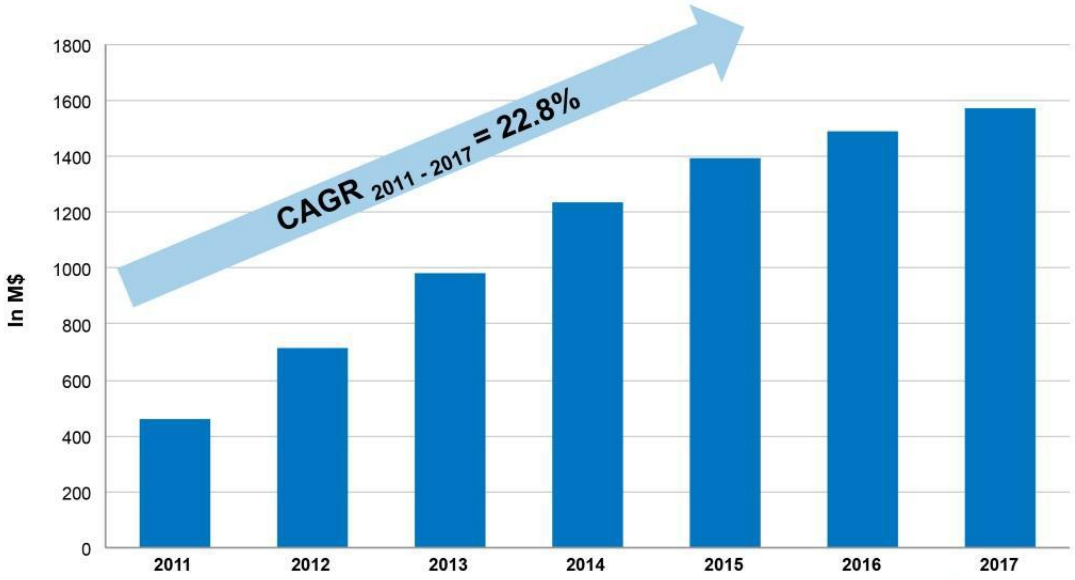

Figure 2.16: Consumer market size growth of 3-axis gyros and gyro-based combos.
[Yole Development, October 2012]

different settings, respectively. The device also exhibits a rate noise density of 0.03 $\text{dps}/\sqrt{\text{Hz}}$. They also provide similar gyros with analog output rather than digital.

2.9.2. Invensense IMU-9250

This is one of the latest 9-axis IMUs from Invensense [33]. MPU-9250 is a multi-chip module (MCM) consisting of two dies integrated into a single 3 mm×3 mm×1 mm QFN package. One die houses the 3-Axis gyroscope and the 3-Axis accelerometer. The other die houses the 3-Axis magnetometer. It operates on a 2.5 V supply and the gyro draws a current of 3.2 mA. The full scale range is programmable to ±250, ±500, ±1000, or ±2000 dps with a 16 bit digital output and the sensitivity is 7.6, 15.3, 30.5, or 61 mdps/LSB for the different settings, respectively. The device exhibits a rate noise density of 0.01 $\text{dps}/\sqrt{\text{Hz}}$.

2.10. References

[1] C. Acar and A. Shkel, "*MEMS Vibratory Gyroscopes: Structural Approaches to Improve Robustness,*" Springer, 2009.

[2] A. Persson, "The Coriolis Effect A Conflict Between Common Sense and Mathematics," *the Swedish Meteorological and Hydrological Institute*, Norrkping, Sweden, available at: http://retro.met.no/english/topics/nomek_2005/coriolis.pdf.

[3] A. Andronova, V. M. Gelikonov, and G. V. Gelikonov, "All-Fiber Optical Gyroscopes on Orthogonal Polarizations," *Journal of Radiophysics and Quantum Electronics*, Springer, vol. 41, no. 11, November 1998.

[4] Egyptian Museum, Egyptian Center for Documentation of Cultural and Natural Heritage, available at: http:// www.eternalegypt.org.

[5] G. G. Coriolis, "Mémoire sur les équations du mouvement relatif des systémes de corps," *Journal de l'école Polytechnique*, vol. 15, pp. 142-154, 1835.

[6] N. Yazdi, F. Ayazi, and K. Najafi, "Micromachined Inertial Sensors," *Proceedings of the IEEE*, vol. 86, no. 8, pp. 1640-1659, August 1998.

[7] J. B. Hart, R. E. Miller, and R. L. Mills, "A Simple Geometric Model for Visualizing the Motion of a Foucault Pendulum," *American Journal of Physics*, vol. 55, no. 1, pp. 67-70, January 1987.

[8] J. Bernstein, S. Cho, A. T. King, A. Kourepenis, P. Maciel, and M.Weinberg, "A Micromachined Comb-Drive Tuning Fork Rate Gyroscope," *Proceedings of the IEEE International Conference on Microelectromechanical Systems*, pp. 143-148, February 1993.

[9] H. Lefevre, "*The Fiber-Optic Gyroscope,*" Artech House, 1993.

[10] A. Lawrence, "*Modern Inertial Technology: Navigation, Guidance and Control,*" Springer-Verlag, New York, 1993.

[11] D. D. Lynch, "Hemispherical Resonator Gyro," in R. R. Ragan (Editor) "Inertial technology for the future," *IEEE Transactions on Aerospace and Electronic Systems*, vol. AES-20, no. 4, pp. 414-444, July 1984.

[12] J. Soderkvist, "Design of a Solid-State Gyroscopic Sensor Made of Quartz," *Sensors and Actuators A: Physical*, vol. 21, no. 1-3, pp. 293-296, February 1990.

[13] S. D. Orlosky and H. D. Morris, "Quartz Rotation (Rate) Sensor," *Proceedings of Sensor Expo*, pp. 171-177, 1994.

[14] J. S. Burdess and T. Wren, "The Theory of a Piezoelectric Disc Gyroscope," *IEEE Transactions on Aerospace and Electronic Systems*, vol. AES-22, no. 4, pp. 410-418, July 1986.

[15] R. Voss, K. Bauer, W. Ficker, T. Gleissner, W. Kupke, M. Rose, S. Sassen, J. Schalk, H. Seidel, and E. Stenzel, "Silicon Angular Rate Sensor for Automotive Applications with Piezoelectric Drive and Piezoresistive Read-Out," *Proceedings of the IEEE International Conference on Solid-State Sensors, Actuators, and Microsystems*, vol. 2, pp. 879-882, June 1997.

[16] F. Paoletti, M. A. Gretillat, and N. F. de Rooij, "A Silicon Micromachined Vibrating Gyroscope with Piezoresistive Detection and Electromagnetic Excitation," *Proceedings of the IEEE International Conference on Microelectromechanical Systems*, pp. 162-167, February 1996.

[17] G. Nagy, Z. Szucs, S. Hodossy, M. Rencz, and A. Poppe, "Comparison of two Low-Power Electronic Interfaces for Capacitive MEMS Sensors," *Symposium on Design, Test, Integration and Packaging of MEMS/MOEMS*, April 2007.

[18] A. Trusov, A. Schofield, and A. Shkel, "Gyroscope Architecture with Structurally Forced Anti-Phase Drive-Mode and Linearly Coupled Anti-Phase Sense-Mode," *Proceedings of the IEEE International Conference on Solid-State Sensors, Actuators and Microsystems*, pp. 660-663, June 2009.

[19] M. Elsayed, F. Nabki, M. Sawan, and M. El-Gamal, "A 5 V MEMS Gyroscope with 3 aF/^{o}/s Sensitivity, 0.6 ^{o}/√hr Mechanical Noise and Drive-Sense Crosstalk Minimization," *Proceedings of the IEEE International Conference on Microelectronics*, pp. 1-5, December 2011.

[20] H. Johari and F. Ayazi, "High Frequency Capacitive Disk Gyroscopes in (100) and (111) Silicon," *Proceedings of the IEEE International Conference on Microelectromechanical Systems*, pp. 47-50, January 2007.

[21] M. Y. Elsayed, F. Nabki, and M. N. El-Gamal, "A 2000 ^{o}/sec Dynamic Range Bulk Mode Dodecagon Gyro for a Commercial SOI Technology," *Proceedings of the IEEE International Conference on Electronics, Circuits, and Systems*, pp. 264-267, December 2011.

[22] H. Johari and F. Ayazi, "Capacitive Bulk Acoustic Wave Silicon Disk Gyroscopes," *Technical Digest of the IEEE Electron Devices Meeting*, pp. 1-4, December 2006.

[23] W. Sung, M. Dalal, and F. Ayazi, "A 3 MHz Spoke Gyroscope with Wide Bandwidth and Large Dynamic Range," *Proceedings of the IEEE International Conference on Microelectromechanical Systems*, pp. 104-107, January 2010.

[24] Y. Xie, S. Li, Y. Lin, Z. Ren, and C. Nguyen, "1.52-GHz Micromechanical Extensional Wine-Glass Mode Ring Resonators," *IEEE Transactions on Ultrasonics, Ferroelectrics and Frequency Control*, vol. 55, no. 4, pp. 890-907, April 2008.

[25] J. Clark, W. Hsu, M. Abdelmoneum, and C. Nguyen, "High-Q UHF Micromechanical Radial-Contour Mode Disk Resonators," *Journal of Microelectromechanical Systems*, vol. 14, no. 6, pp. 1298-1310, December 2005.

[26] J. Wang, Z. Ren, and C. Nguyen, "1.156-GHz Self-Aligned Vibrating Micromechanical Disk Resonator," *IEEE Transactions on Ultrasonics, Ferroelectrics and Frequency Control*, vol. 51, no. 12, pp. 1607-1628, December 2004.

[27] J. Clark, W. Hsu, and C. Nguyen, "High-Q VHF Micromechanical Contour-Mode Disk Resonators," *Technical Digest of the IEEE Electron Devices Meeting*, pp. 493-496, December 2000.

[28] M. Y. Elsayed, F. Nabki, and M. N. El-Gamal, "A Combined Comb/Bulk Mode Gyroscope Structure for Enhanced Sensitivity," *Proceedings of the IEEE International Conference on Microelectromechanical Systems*, pp. 649-652, January 2013.

[29] M. Y. Elsayed, F. Nabki, and M. N. El-Gamal, "A Novel Comb Architecture for Enhancing the Sensitivity of Bulk Mode Gyroscopes," *Journal of Sensors,* vol. 13, no. 12, pp. 16641-16656, December 2013.

[30] "*3-Axis Consumer Gyroscopes,*" Yole Development, 2012.

[31] "*The Growth of the MEMS Market,*" Yole Development, 2012.

[32] "*L3G3200D, MEMS Motion Sensor: Three-Axis Digital Output Gyroscope,*" rev. 1, ST Microelectronics, available at: http:// www.st.com, December 2011.

[33] "*MPU-9250 Product Specification,*" rev. 1.0, Invensense, available at: http:// www.invensense.com, January 2014.

Chapter 3 A Novel Comb Architecture for Enhancing the Sensitivity of Bulk Mode Gyroscopes

3.1. Introduction

Micromachined gyroscopes are receiving increasing attention in the sensing community, as highlighted in the previous chapter. This is due to their small sizes, which enable their use in numerous consumer electronics applications (e.g., image stabilization in digital cameras, motion sensing, etc.). Gyros are also used in navigation systems for robotic, military, aeronautic and space applications, providing a significant opportunity for the growth of their micromachined implementations.

Vibratory gyros are classified based on their mode of vibration to flexural and bulk mode devices. As highlighted in [1], bulk mode gyroscopes are capable of achieving superior performance compared to flexural mode ones. These gyros operate in higher order resonant modes, and thus their operating frequencies are generally in the MHz range - three orders of magnitude higher than flexural mode gyros. Notably, higher order modes experience less thermoelastic damping than flexural modes. Moreover, they can achieve very high quality factors (~50,000) even in atmospheric pressure, as air damping has little impact on their operation due to the high stiffness of their structures. Also, bulk mode gyroscopes exhibit orders of magnitude higher bandwidths than flexural mode ones, thus relaxing the need for drive-sense mode matching and expensive vacuum packaging, which are both mandatory for the operation of flexural mode gyroscopes.

In addition, bulk mode gyroscopes generally exhibit lower mechanical noise than flexural ones. The mechanical noise of a vibratory gyroscope is given by:

$$\Omega_{z(Brownian)} \propto \frac{1}{q_{drive}} \sqrt{\frac{4k_B T}{\omega_0 M Q_{effect-sense}}}, \tag{3.1}$$

where q_{drive} is the drive mode vibration amplitude, k_B is the Boltzmann constant, T is the absolute temperature, ω_0 is the resonance frequency, M is the mass, and $Q_{effect\text{-}sense}$ is the effective quality factor [1]. Today, state-of-the-art vibratory gyroscopes operating at lower

frequencies (<100 kHz) rely on increasing the proof mass or the vibration amplitude to improve their noise performance. They require low vacuum operation (<10 mTorr) to achieve high quality factors (<10,000) that are ultimately limited by thermoelastic damping. Enhancing the noise performance of gyros without the need for increasing the mass or vibration amplitude is of great interest, as these parameters are limited mainly by design area and power concerns. From Equation (3.1), it is clear that raising the resonance frequency and the quality factor, as allowed by bulk mode architectures, improves the noise performance of a gyroscope significantly.

Different bulk mode gyroscopes that take advantage of these improved characteristics have recently been published. In [1-2], a circular disk architecture was introduced in (100) and (111) silicon, and a circular disk gyro with spokes was suggested in [3] – it combined flexural and bulk modes, and achieved a large dynamic range. Bulk mode gyros (e.g., [1-3]) and resonators (e.g., [4-7]) typically utilize very small transducer gaps (e.g., 200 nm) between the center resonating element and the electrodes. In [8], a 3 μm gap dodecagon bulk mode gyroscope design utilizing the same fabrication technology as here, but without comb drives, was reported. This device's sensitivity was significantly less than the previously mentioned devices due to its relatively large transducer gap, mainly dictated and limited by the technology used.

This chapter introduces a novel architecture for raising the sensitivity of bulk mode gyroscopes. It is based on adding parallel plate comb drives to the points of maximum vibration amplitude, and tuning the stiffness of these combs. This increases the drive strength and results in significant improvement in the sensitivity. In this work, the idea was also implemented in a commercial relatively large gap technology (SOIMUMPs) in order to outline the sensitivity improvement possible through the proposed method in a widely available standard bulk micromachining technology. The design is composed of a central dodecagon disk structure with added parallel plate comb drives. Adding combs connected to the central disk structure increases the drive strength and results in two orders of magnitude higher sensitivity than the design presented in [8]. This enables the fabrication of potentially high performance bulk-mode gyroscopes in standard commercial MEMS technologies. Furthermore, the architecture is well-suited for technologies with ~100 nm transducer gaps in order to achieve very high performance devices. Also, the gyro here is

amenable for fabrication in select above-IC technologies, e.g., [9-11]. The concept was introduced in [12-13]. Full details about the design, fabrication, and testing are presented in this chapter.

The chapter is structured such that the operating principle of the device and its design are first described. Simulation results are then reported, and are followed by measurement results of the fabricated device. The device performance is then discussed, and subsequently a conclusion is presented.

3.2. Operating Principle

Generally, vibratory gyroscopes rely in their operation on the Coriolis effect, where if a body of mass (m) is moving with a velocity (υ) in a certain direction and is acted upon by a rotation rate (Ω) around another direction, a force is generated that will move the body in a direction perpendicular to both the direction of the original motion and the axis of rotation. This Coriolis force, F_c, is given by [14]:

$$F_c = 2m(\upsilon \times \Omega). \tag{3.2}$$

Bulk mode disk devices are composed of a main central disk structure (circular or polygonal), which vibrates in a higher order bulk mode. Outer electrodes are used for electrostatic actuation of the structure in the drive mode. When the device is subject to rotation, the Coriolis force excites a different mode than the drive mode, the sense mode.

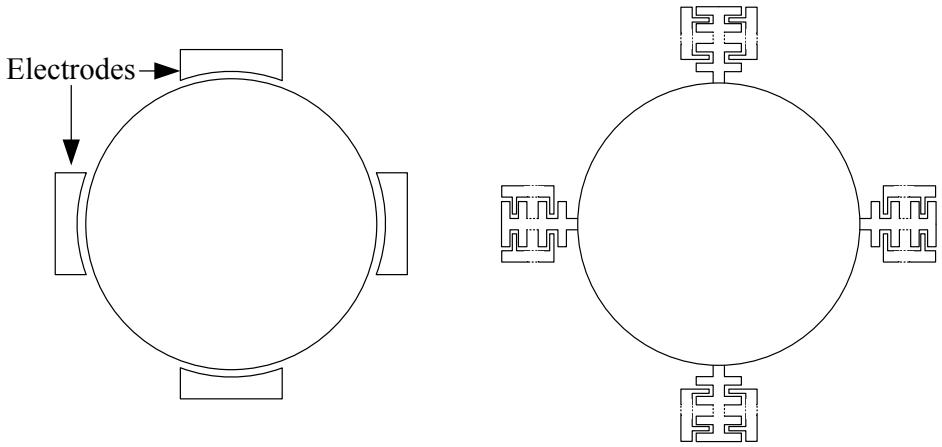

Figure 3.1: Simplified illustration for the (a) typical disk gyroscope, and (b) the proposed combined disk-comb gyroscope (electrodes are positioned symbolically around the disk structure).

The resulting vibration is then detected through the sense electrodes, enabling the gyroscope operation. Traditionally, to drive and sense the disk vibration, electrodes are directly placed at vibrational areas around the disk, as shown in Figure 3.1 (a).

The idea proposed here extends the central resonating disk structure by adding parallel plate comb drives with a variable gap configuration to the parts of the disk which exhibit the maximum vibration amplitude in the drive and sense resonant modes, as shown in simplified form in Figure 3.1 (b). This increases the drive strength and enhances the device sensitivity. This sensitivity improvement is due to the increased electrostatic force and capacitance change that result because of the larger electrode surface area. Equations (3.3) and (3.4) outline the impact of electrode area on the electrostatic force (F_{elec}) and capacitance, in relation to a parallel plate capacitor shown in Figure 3.2 [15]:

$$F_{elec} = \frac{1}{2}\frac{dC}{dx}V^2 = \frac{1}{2}\frac{\varepsilon_0 A}{g^2}V^2, \tag{3.3}$$

$$\Delta C \approx \frac{\varepsilon_0 A}{g^2}\Delta x, \quad \Delta x << g. \tag{3.4}$$

where C is the nominal capacitance between the plates, V is the applied voltage between the plates, ε_0 is the dielectric permittivity of free space, A is the plate area, g is the original gap between the plates, and Δx is the top plate displacement.

Generally, any resonating structure, including the disk resonator and the comb resonating structure, can be modeled with a mass-spring-damper system as shown in Figure 3.3. In order to model the combined resonating system, the mass-spring-damper models for both the disk and the comb resonators are combined to give the double mass-spring-damper system shown in Figure 3.4, which will be used to illustrate the operating

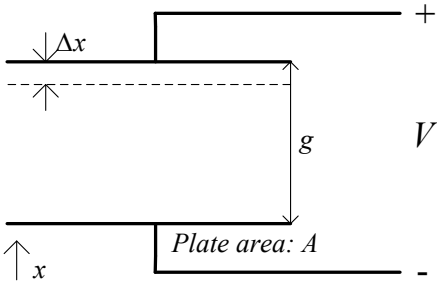

Figure 3.2: Simplified illustration for a parallel plate capacitor.

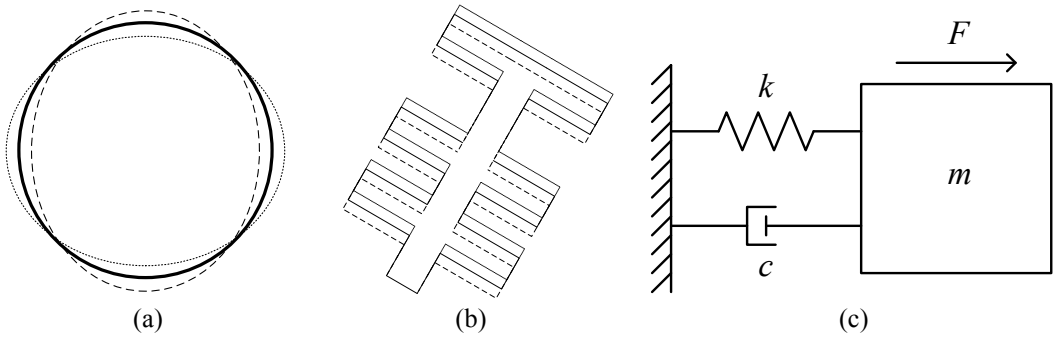

Figure 3.3: (a) Resonating disk structure, (b) resonating comb structure, and (c) resonant mass-spring-damper model.

principle of the combined disk-comb device. k_1 and k_2 are the spring constants of the disk (primary structure) and the comb (secondary structure), respectively; m_1 and m_2 are the masses of the disk and the comb, respectively; and c_1, c_2, and c_3 are the different damping coefficients acting on the system. F_1 is the electrostatic force acting on the disk faces directly, and F_2 is the total electrostatic force of each comb drive. x_1 and x_2 are the displacements of the primary and secondary masses, respectively.

The system can be described as follows:

$$F_1 - k_1 x_1(t) - c_1 \dot{x}_1(t) - k_2\left(x_1(t) - x_2(t)\right) - c_2\left(\dot{x}_1(t) - \dot{x}_2(t)\right) = m_1 \ddot{x}_1(t)\,, \tag{3.5}$$

$$F_2 - k_2\left(x_2(t) - x_1(t)\right) - c_2\left(\dot{x}_2(t) - \dot{x}_1(t)\right) - c_3 \dot{x}_2(t) = m_2 \ddot{x}_2(t)\,. \tag{3.6}$$

These equations can be simplified giving:

$$F_1 - \left(k_1 + k_2\right)x_1(t) + k_2 x_2(t) - \left(c_1 + c_2\right)\dot{x}_1(t) + c_2 \dot{x}_2(t) = m_1 \ddot{x}_1(t)\,, \tag{3.7}$$

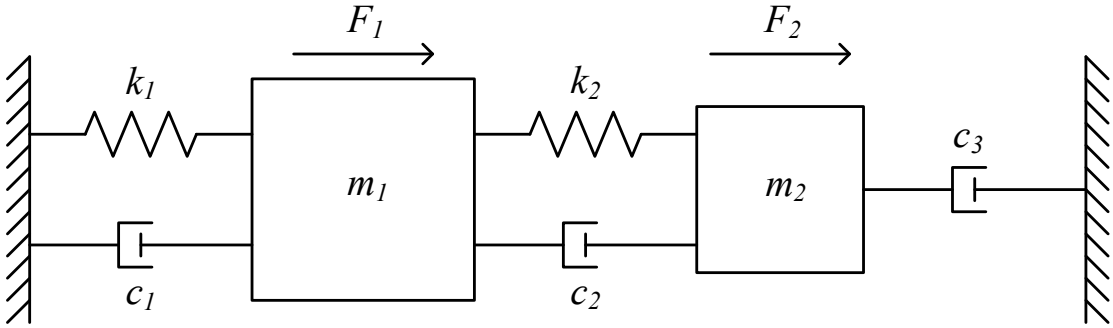

Figure 3.4: Double mass-spring-damper system model for the combined disk-comb structure.

$$F_2 + k_2 x_1(t) - k_2 x_2(t) + c_2 \dot{x}_1(t) - (c_2 + c_3)\dot{x}_2(t) = m_2 \ddot{x}_2(t)\,. \tag{3.8}$$

Since the force of a given comb finger is, by design, equivalent to the force applied onto a disk face, the following relationship between F_1 and F_2 can be written as:

$$F_2 = nF_1\,, \tag{3.9}$$

where n is the number of fingers in each comb drive. By solving Equations (3.7) and (3.8) simultaneously and taking into consideration Equation (3.9), the system transfer function can be reached as given by:

$$\left.\frac{X_1(S)}{F_1(S)}\right|_{double} = \frac{m_2 S^2 + ((n+1)c_2 + c_3)S + (n+1)k_2}{\left[\begin{array}{r} m_1 m_2 S^4 + (m_1 c_2 + m_1 c_3 + m_2 c_1 + m_2 c_2)S^3 + (m_1 k_2 + m_2 k_1 + m_2 k_2 + c_1 c_2 + c_1 c_3 + c_2 c_3)S^2 \\ + (c_1 k_2 + c_2 k_1 + c_3 k_1 + c_3 k_2)S + k_1 k_2 \end{array}\right]} \tag{3.10}$$

Figure 3.5 shows the magnitude of this transfer function versus frequency for different values of k_2, with all other parameters kept constant, and for the mode utilized in our design, where the two masses exhibit in-phase motion. The transfer function of a single mass-spring-damper system (m_1-k_1-c_1) is also plotted for comparison and is given by:

$$\left.\frac{X_1(S)}{F_1(S)}\right|_{single} = \frac{n+1}{m_1 S^2 + c_1 S + k_1}\,. \tag{3.11}$$

The equivalent force of the comb $(n + 1)F_1$ is applied to the single spring-mass-damper system for the comparison. From Figure 3.5, it is clear that when the secondary spring constant is small compared to the primary spring constant, the primary mass displacement at resonance is small, as the force on the secondary mass is not conveyed effectively to the primary mass. As the secondary spring constant is increased, the force is coupled more effectively to the disk and the displacement increases even over the displacement in a single spring-mass-damper system when the same total force is applied directly to the primary mass. Accordingly, the disk drive and sense coupling is increased in this work by carefully designing the spring constant of the comb drive structure so that its driving force (and sensing) enhances optimally the performance of the bulk resonant structure. This enables the fabrication of potentially high performance bulk-mode gyroscopes in standard commercial MEMS technologies, as implemented in this work in a commercial 3 μm gap technology (SOIMUMPs). Furthermore, the architecture is well-suited for technologies with sub-micron lateral transducer gaps (e.g.: ~100 nm), in order to achieve very high performance devices.

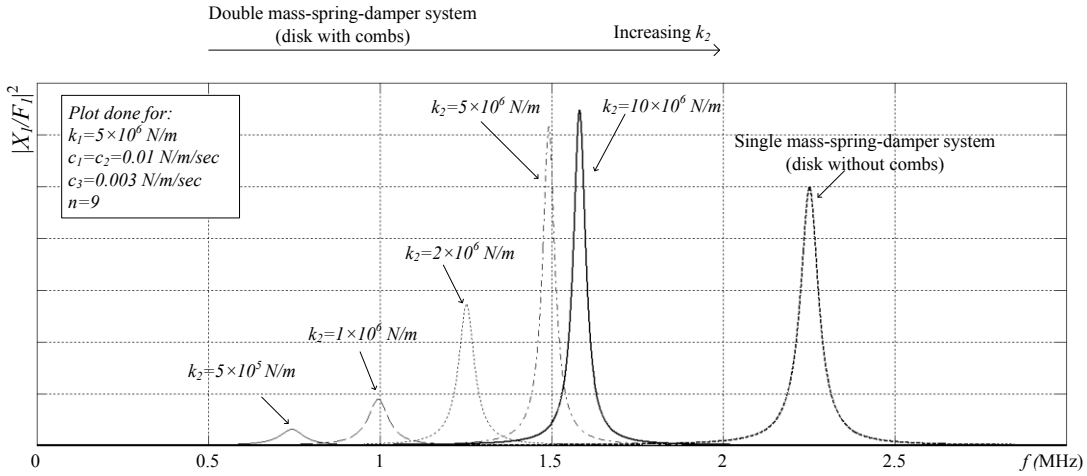

Figure 3.5: $|X_1/F_1|^2$ for the disk-comb combined structure (double spring-mass-damper system for different secondary spring constants), and for the disk structure (single spring-mass-damper system).

3.3. Device Design

The proposed design is shown in Figure 3.6. The structure is composed of a central dodecagon structure with a 730 μm face to face distance and a 25 μm thickness. The reason for choosing a dodecagon structure is that the design is implemented in the SOIMUMPs technology, where the device layer is (100) single crystalline silicon (SCS), which is anisotropic. In a disk with the same central disk dimensions, the first order bulk mode exhibits a 1 MHz split between the drive and sense modes. Therefore, in order to have closer matching of the drive and sense modes, the second order bulk mode of a dodecagon (12 sides) structure is favored, providing a drive-sense mode separation of only 270 Hz. The drive and sense modes for the second order mode are spatially separated by 30°. Therefore, a 12-side structure is selected, in order to have 30° between its vertices, so that the second order maxima coincide with the disk vertices. Comb fingers of 25 μm width were added to the vertices, which are the points that exhibit the largest vibration amplitudes. The dimensions of the fingers were optimized, as discussed in the following section, to ensure a sufficiently large stiffness. As was previously discussed, this allows the forces applied to the fingers to be conveyed efficiently to the disk vertices because of the sufficiently high comb spring constant, and also ensures that the combs vibrate constructively with the disk in the wanted sense/drive modes – not in any spurious modes.

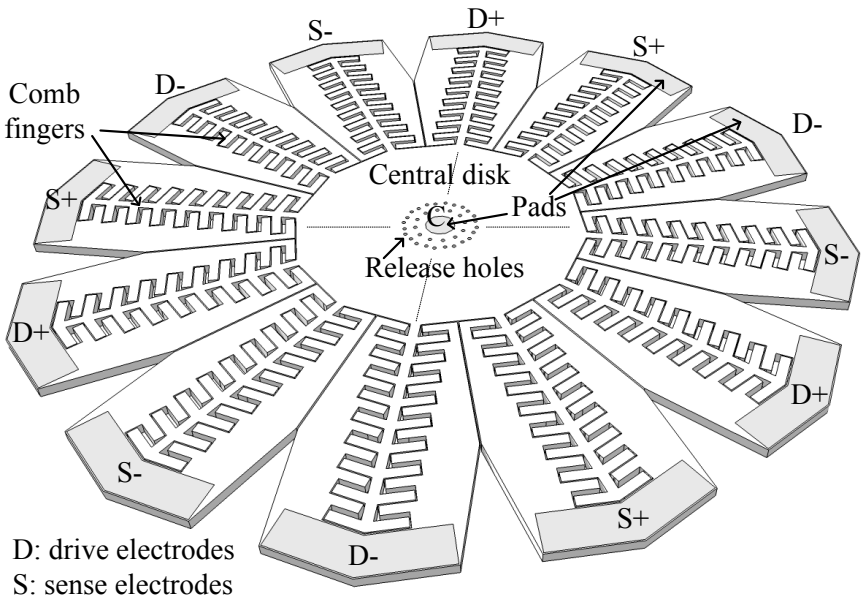

Figure 3.6: Schematic of the proposed gyro design (for clarity, not all the release holes are shown).

As shown in Figure 3.6, the resonating structure is surrounded by electrodes that electrostatically drive the structure (marked as "D") and sense its output signal differentially (marked as "S"). The central pad (marked as "C") is used to connect the necessary DC bias voltage to the disk structure. This precludes the need for suspended upper traces as was used in [1-3] or for a lower metallization – both would result in a more complex fabrication process. In order to release the structure, release holes with 10 μm diameter and spaced out by 25 μm are added. The release holes are distributed around the structure in a symmetric manner, in order to mitigate any frequency splits that may arise due to these holes. In addition, the release holes are distanced from the central pad, in order to ensure that a complete release of the disk can be performed, without etching the sacrificial layer under the central pad. Table 3.1 summarizes the device key design parameters.

Table 3.1: Summary of Device Design Parameters

Parameter	**Value**
Face to face distance	730 μm
Number/ width of comb fingers	9/ 25 μm
Capacitive gap	3 μm
Resonance frequency	~1.5 MHz

The gyroscopes were fabricated in the MEMSCAP SOIMUMPs technology. The fabrication steps of the SOIMUMPs technology are briefly outlined in Figure 3.7 [16]. The gyro is fabricated on a double-side polished silicon-on-insulator (SOI) substrate with a 25 μm (100) SCS structural layer (Figure 3.7 (a)). The top layer is then doped by depositing phosphosilicate glass (PSG) (Figure 3.7 (b)), which is then removed by wet etching. Afterwards, a pad metal layer is deposited and patterned by a liftoff process to form the metal pads for the electrical connections as shown in Figure 3.7 (c). Then, the device layer is lithographically patterned and etched using deep reactive ion etching (DRIE) to form the proof mass and electrodes (Figure 3.7 (d)). Finally, the release was performed in-house by timed hydrofluoric acid (HF) wet etching (Figure 3.7 (e)). An etch rate of 1.6 μm/min is stated in [17] for SOIMUMPs, using 48% aqueous HF and a Triton X-100 surfactant. To validate this etch rate, HF etch tests were performed in-house on similar SOI wafers and an etch rate of ~1 μm/min using 49% aqueous HF was measured. Careful timing is essential so as to avoid etching below the central pad, which may lead to the structural failure of the disk while wire bonding to it later on, but the timed etch must be long enough to release the structure: both the disk and combs. It would be advantageous to make the central

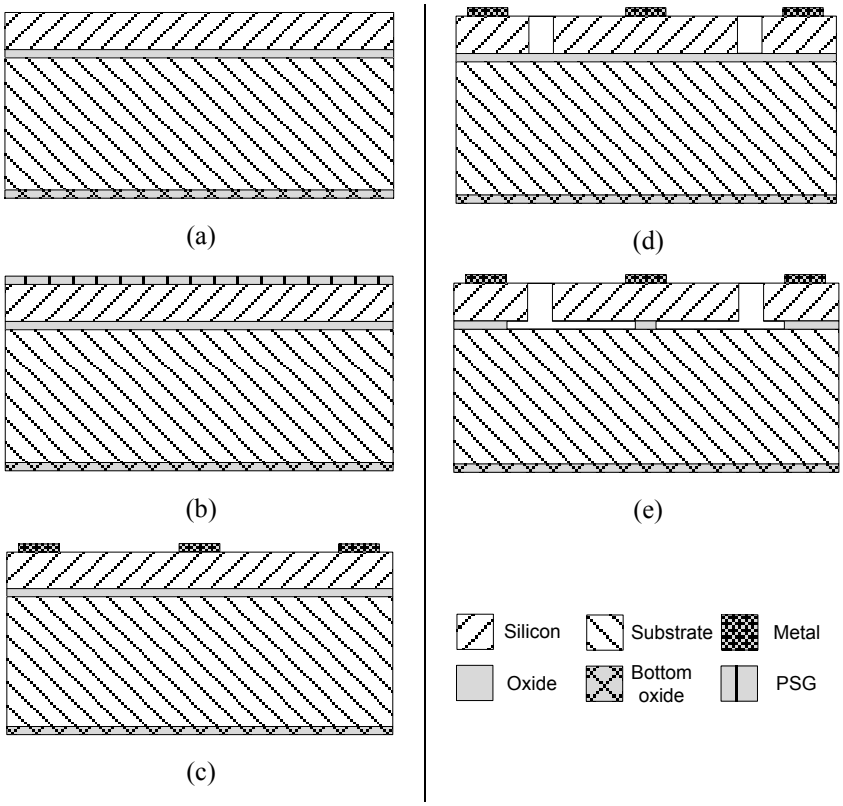

Figure 3.7: Simplified processing steps of the SOIMUMPs technology [16].

support as small as possible in order to reduce the energy losses due to the coupling of vibrations to the substrate through the central support and thus increase the quality factor of the device. However, the size of the central support in the design is limited to the central pad size, as mentioned above, which limits the quality factor of the device.

3.4. Simulation Results

The COMSOL Multiphysics finite element simulation package is used for all simulations. As was previously mentioned, for the device to function properly, the comb fingers should be stiff enough so that the electrostatic force applied to them is coupled to the disk faces, and to ensure that they vibrate constructively with the disk and not in any spurious mode. In order to optimize the width of the comb fingers (w_f), the simplified model for one comb drive shown in Figure 3.8 is used. In this model, the disk is replaced by a spring, with spring constant K acting as the primary spring constant in the model in Figure 3.4, which was obtained to be ~10^6 N/m through stationary simulation, by applying a force to the disk faces and measuring the resulting displacement. Stationary simulation was then performed on the model in Figure 3.8, and the displacement of the comb end which is connected to the spring (point x) was measured and compared to that of the tips of the fingers. The finger width was then tuned such that these displacements were almost the same, and scaled according to the number of fingers on which the force was applied. Table 3.2 shows the stationary displacement of point x normalized with respect to the applied force per unit area using Equation (3.12) for different finger widths.

$$Disp._{normalized} = \frac{Disp.|_x}{force\ per\ unit\ area\ applied} \tag{3.12}$$

Based on this analysis, a width of 25 μm was selected for use in the design. This sizing ensures that the forces applied to the fingers are coupled to the end of the comb, and thus

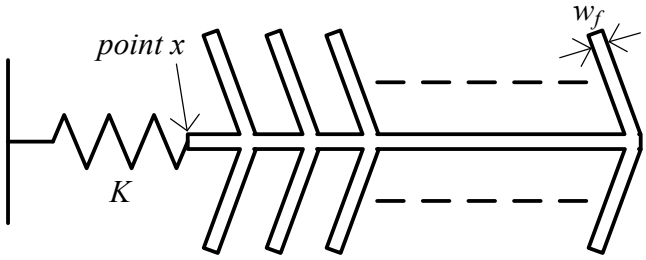

Figure 3.8: Simplified model of a single comb, where the disk is replaced with a spring of constant K.

Table 3.2: Normalized displacement at point *x* for different finger width, w_f.

Number of Finger Pairs	Normalized Displacement (m^3/N) × 10^{14}			
	Finger Width, w_f (µm)			
	5	**10**	***25***	***35***
1	0.35	0.37	0.41	0.44
2	0.68	0.71	0.81	0.88
3	1.01	1.06	1.22	1.32
4	1.34	1.41	1.62	1.76
5	1.67	1.76	2.03	2.2
6	1.99	2.1	2.4	2.64
7	2.32	2.45	2.83	3.08
8	2.65	2.8	3.25	3.52
9	2.98	3.15	3.7	3.96

can actuate the disk effectively, as shown in Figure 3.9. Also, it acts as a good compromise between force coupling and device area.

Eigen frequency simulations were performed for the entire disk and comb structure. The resonance frequencies of the drive and sense modes were found to be 1.499271 MHz and 1.499543 MHz, respectively. The mode shapes of the drive and sense modes are shown in Figure 3.10. It is clear that the combs vibrate constructively with the disk. This was confirmed by performing a frequency analysis for the structures and making sure that the displacement of the disk vertices scale with the number of fingers subject to the face forces.

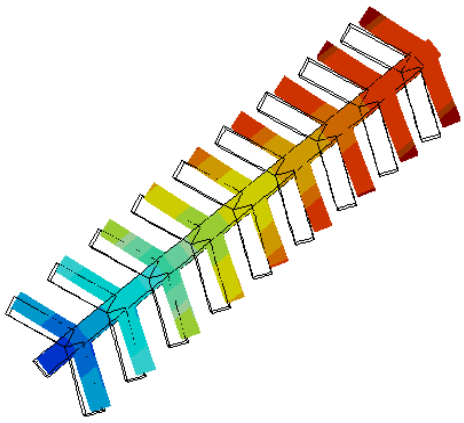

Figure 3.9: Displacement resulting from applying face forces on the comb fingers.

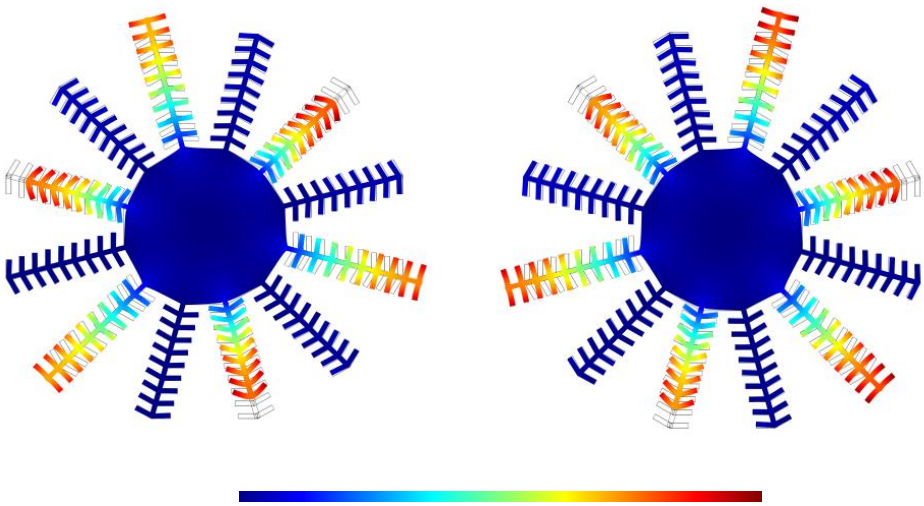

(a) (b)

Figure 3.10: Mode shape of the (a) drive mode at 1.499271 MHz, and (b) sense mode at 1.499543 MHz, obtained by finite element simulations.

3.5. Measurement Results

Devices were fabricated in the SOIMUMPs technology from MEMSCAP. An SEM micrograph of a fabricated device is shown in Figure 3.11.

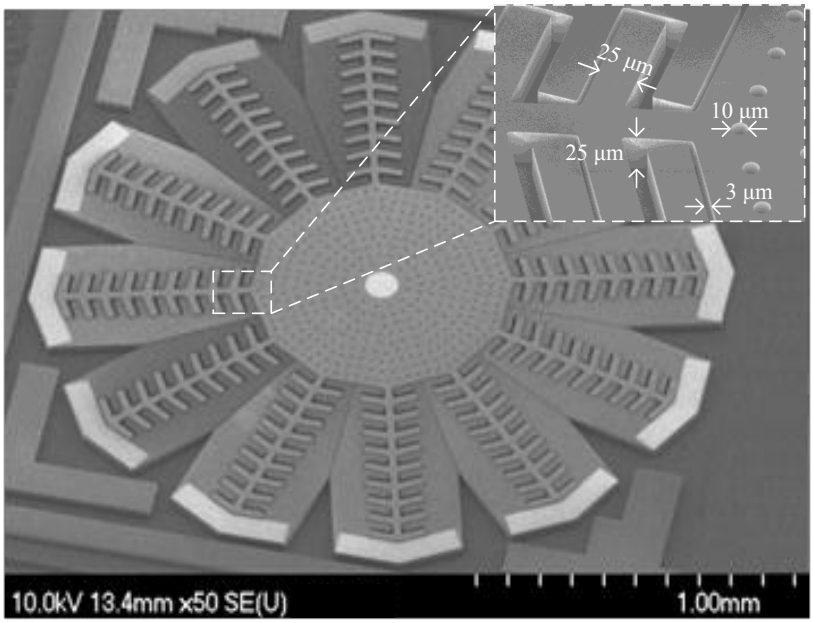

Figure 3.11: SEM micrograph of a fabricated device with zoomed view of the comb structure.

The resonance characteristics of the drive and sense modes were measured under a vacuum level ~10 mTorr. The prototypes were found to resonate in the drive mode with a center frequency of 1.498418 MHz, and a quality factor of 33,000, and in the sense mode with a center frequency of 1.498603 MHz, and a quality factor of 15,000, as shown in

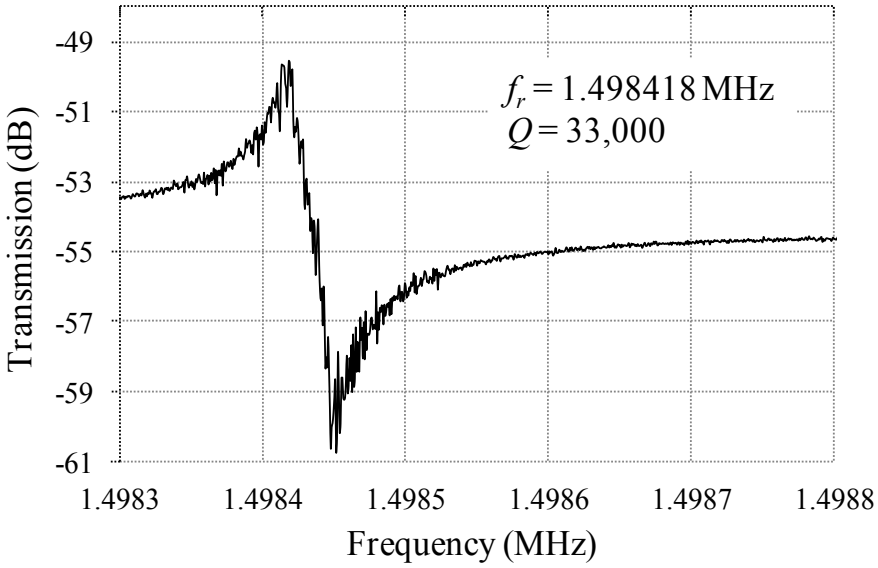

(a)

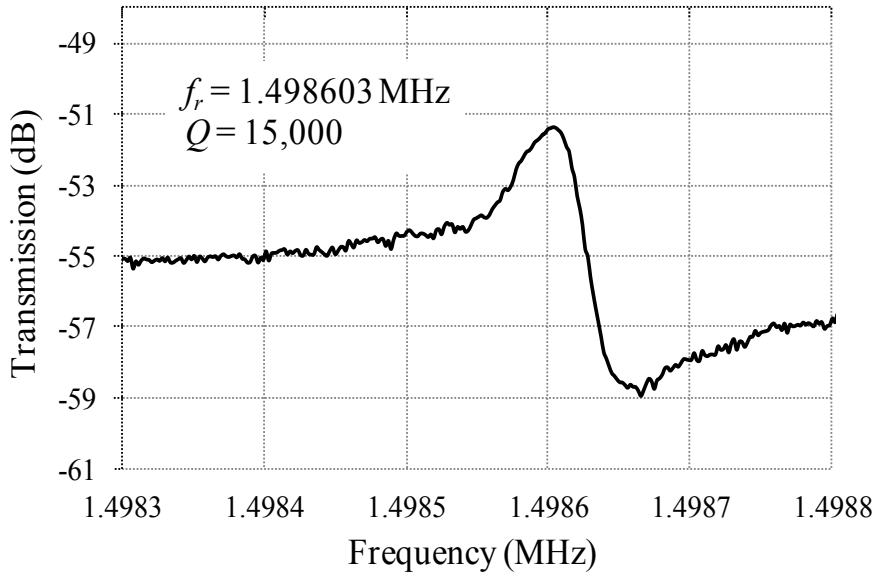

(b)

Figure 3.12: Measured resonance characteristics of the (a) drive mode, and (b) sense mode (10 mTorr vacuum).

Figure 3.12. A DC polarization voltage of 50 V was used. These resonance frequencies are consistent with the simulated results. The difference between the quality factors of the drive and sense modes may be due to the anisotropic elastic properties of the (100) single crystalline silicon structural layer provided by the fabrication technology, as detailed in [18].

The angular rate response of a prototype gyro was measured at a ~10 mTorr vacuum level using discrete electronics, a rate table, and a vacuum chamber, fixed on top of the rate table. A schematic of the test setup is shown in Figure 3.13. The vacuum chamber was designed and custom machined in-house. A hermetic valve was added to it, in order to maintain the vacuum level while rotation after the valve is closed and the pump is disconnected, as shown in Figure 3.14. Bias tees are used to apply the DC voltages required by the drive and sense electrodes. They are built using discrete components on the sensor board. Furthermore, a high gain trans-impedance amplifier board was built using the AD8015 transimpedance amplifier (TIA) chip from Analog Devices [19], in order to amplify the gyro's output signal current. Figure 3.15 shows a photograph of the printed circuit boards (PCBs) that include the gyro and TIA, where the electrodes of the gyro and

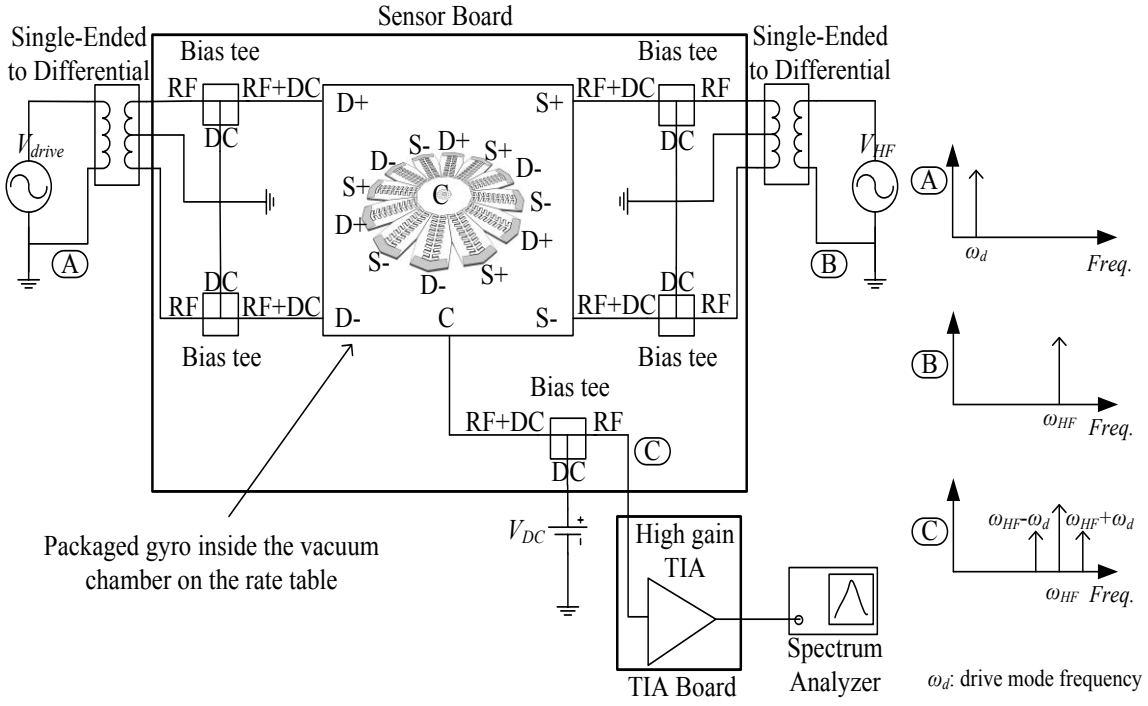

Figure 3.13: Schematic of the test setup showing the signal frequency spectrum at important nodes.

the input and output of the TIA are each connected to an SMA connector to be interfaced within the test setup. The high frequency signal (V_{HF}) is used to modulate the output signal of the gyroscope to a higher frequency, in order to separate it from any feed-through from the drive signal utilizing a mixing configuration similar to that in [5, 6]. Measurements were limited below 50 °/s angular rate input due to the mechanical limitations of the current test setup. The rate sensitivity was measured to be 0.31 μV/°/sec, corresponding to a capacitance sensitivity of 0.43 aF/°/s/electrode. The resulting measured angular rate response is shown in Figure 3.16. These measurement results are limited by the parasitics and noise floor of the discrete test setup. Improved performance could be achieved by using an application specific integrated circuit (ASIC) and wire bonding it to the device within the same package to reduce noise and parasitics (e.g., as demonstrated in [20] for a capacitive accelerometer).

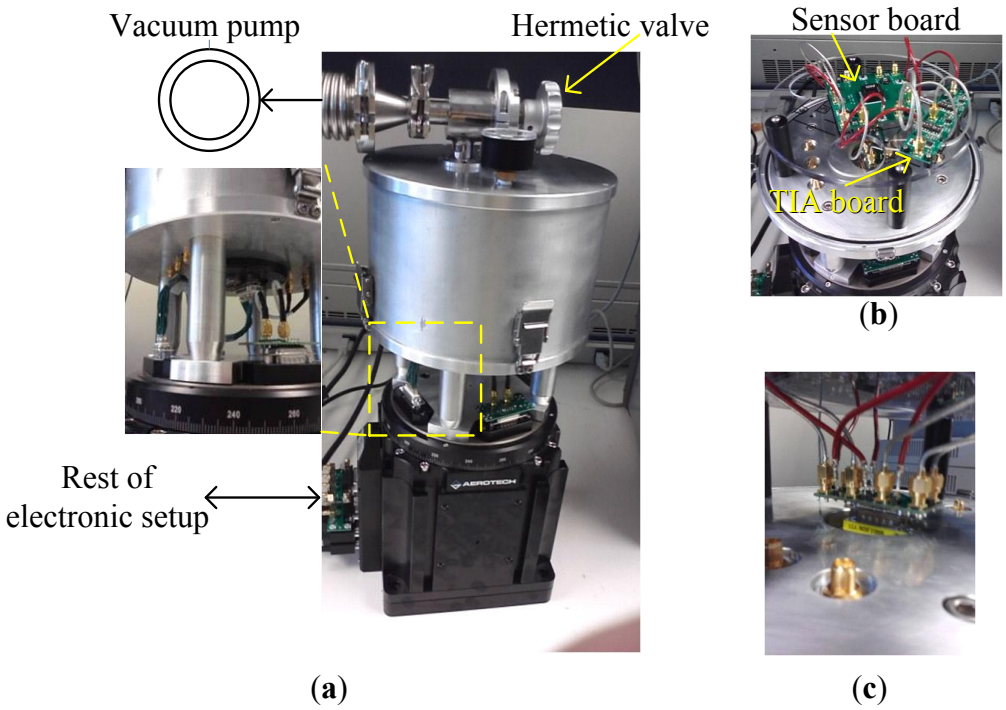

Figure 3.14: (a) Photograph of the test setup, (b) circuits and connections from inside the vacuum chamber, and (c) vacuum sealed electrical feed-throughs.

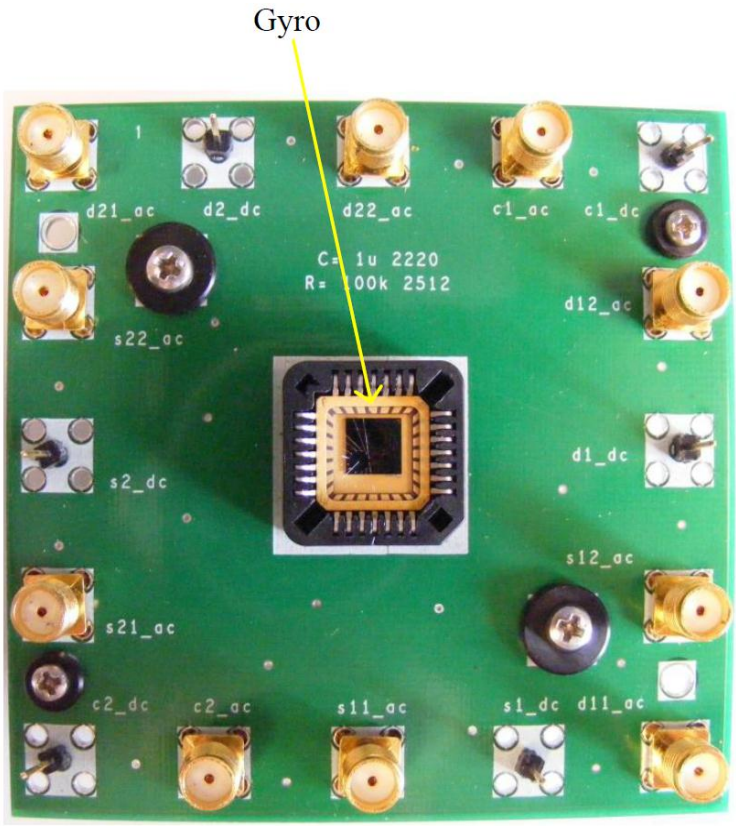

(a)

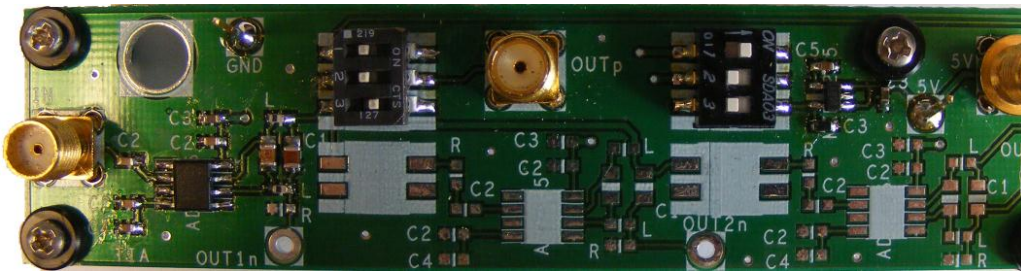

(b)

Figure 3.15: Photographs of (a) PCB with packaged gyro, and (b) PCB with TIA.

3.6. Discussion

A comparison between the design proposed here, and state-of-the-art bulk mode gyros is shown in Table 3.3. The proposed design, with added combs, achieves two orders of magnitude higher sensitivity than the design presented in [8], of similar shape but without combs, and fabricated in the same technology.

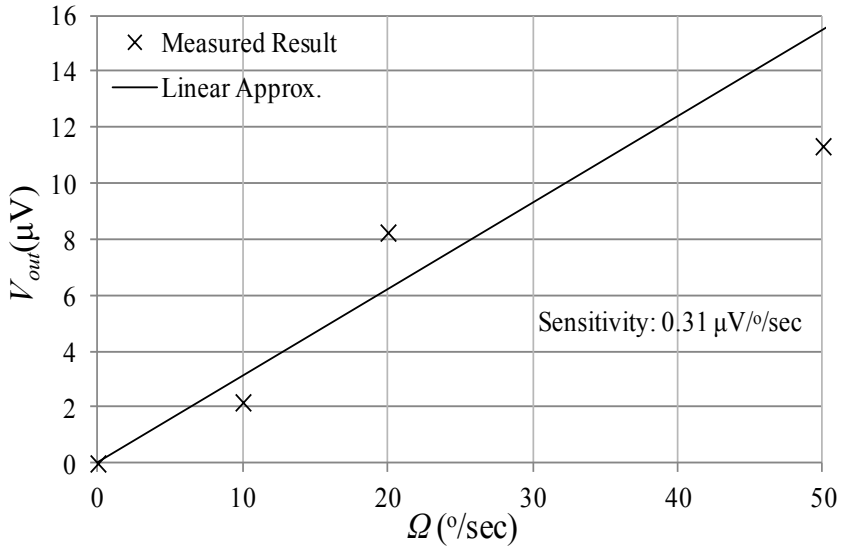

Figure 3.16: Measured angular rate response, and a linear approximation.

Table 3.3: Comparison between the comb/bulk mode gyroscope proposed in this work and state-of-the-art.

	References					
	[1]	**[2]**	**[3]**	**[8]**	**This Work**	
Diameter (mm)	0.8	1.2	1.12	0.73	2.13	
Gap (g) (µm)	0.25	0.18	0.2	3	3	
Thickness (µm)	50	35	60	25	25	
					Drive	Sense
f (MHz)	5.88	2.917	3.12	8.14	Sim. 1.499271 Meas. 1.498418	Sim. 1.499543 Meas. 1.498603
Q (,000)	12	66	1	10	33 (meas.)	15 (meas.)
Meas. Rate Sensitivity (µV/°/s)	190	320	15	-	0.31	
Sensitivity per Electrode (aF/°/s)	-	4.63	-	0.002	0.43	
FOM (µm²·aF/°/s)	**-**	**0.15**	**-**	**0.018**	**3.87**	

The structure exhibits lower sensitivity than the gyros presented in [1-3], due to their comparatively much smaller transducer gaps. However, based on the 3 μm transducer gap results presented in this work, this gyro structure has the potential of yielding higher sensitivities than the devices in [1-3], when implemented in similar ≲200 nm gap technologies. In order to present a meaningful comparison between the different devices, an appropriate figure of merit (FOM) is introduced:

$$FOM = [Sensitivity\ per\ Electrode] \times [g \times 10^6]^2 \tag{3.13}$$

This FOM is used to normalize the sensitivity with respect to the gap size, as the electrostatic driving force and capacitance variation are proportional to $1/g^2$ as shown in Equations (3.3) and (3.4) for the variable gap electrode configuration utilized here, and equal electrostatic drive forces for the devices in comparison. The FOM, as it considers the transducer gap differences between the different presented gyros, shows the potential of the improved design to yield a higher sensitivity than conventional designs when fabricated in a given technology.

3.7. Conclusions

This work introduces a novel method for enhancing the sensitivity of bulk mode gyroscopes. It is based on adding parallel plate comb drives to the points of maximum vibration amplitude, and tuning the stiffness of the combs for optimal driving and sensing of the disk's vibrational modes. This proposed method increases the drive strength and results in significant improvement in the sensitivity of the device. This gyro architecture is well-suited to technologies with ~100 nm-scale transducer gap sizes in order to achieve very high performance devices. Alternatively, the suggested method can also enable the fabrication of high performance bulk-mode gyroscopes that perform adequately in more standard commercial MEMS technologies (e.g., with μm-scale gaps). In this work, the proposed structure was implemented in SOIMUMPs as a proof of concept carried out in a standard large gap size commercial bulk micro-fabrication technology. Prototypes were measured to operate at frequencies of ~1.5 MHz, with quality factors of up to ~33,000, at a 10 mTorr vacuum level. Measurements using discrete electronics show a rate sensitivity of 0.31 μV/°/s, corresponding to a capacitance sensitivity of 0.43 aF/°/s/electrode, two

orders of magnitude higher than a similar design without combs that was also fabricated in the same technology [8]. This improved performance validates the enhancement potential of the proposed combined disk-comb gyroscope structure over traditional implementations of bulk-mode gyros. It can be also applied to bulk-mode resonators generally to improve the signal level.

3.8. References

[1] H. Johari and F. Ayazi, "Capacitive Bulk Acoustic Wave Silicon Disk Gyroscopes," *Technical Digest of the IEEE Electron Devices Meeting*, pp. 1-4, December 2006.

[2] H. Johari and F. Ayazi, "High Frequency Capacitive Disk Gyroscopes in (100) and (111) Silicon," *Proceedings of the IEEE International Conference on Microelectromechanical Systems*, pp. 47-50, January 2007.

[3] W. Sung, M. Dalal, and F. Ayazi, "A 3 MHz Spoke Gyroscope with Wide Bandwidth and Large Dynamic Range," *Proceedings of the IEEE International Conference on Microelectromechanical Systems*, pp. 104-107, January 2010.

[4] Y. Xie, S. Li, Y. Lin, Z. Ren, and C. Nguyen, "1.52-GHz Micromechanical Extensional Wine-Glass Mode Ring Resonators," *IEEE Transactions on Ultrasonics, Ferroelectrics and Frequency Control*, vol. 55, no. 4, pp. 890-907, April 2008.

[5] J. Clark, W. Hsu, M. Abdelmoneum, and C. Nguyen, "High-Q UHF Micromechanical Radial-Contour Mode Disk Resonators," *Journal of Microelectromechanical Systems*, vol. 14, no. 6, pp. 1298-1310, December 2005.

[6] J. Wang, Z. Ren, and C. Nguyen, "1.156-GHz Self-Aligned Vibrating Micromechanical Disk Resonator," *IEEE Transactions on Ultrasonics, Ferroelectrics and Frequency Control*, vol. 51, no. 12, pp. 1607-1628, December 2004.

[7] J. Clark, W. Hsu, and C. Nguyen, "High-Q VHF Micromechanical Contour-Mode Disk Resonators," *Technical Digest of the IEEE Electron Devices Meeting*, pp. 493-496, December 2000.

[8] M. Y. Elsayed, F. Nabki, and M. N. El-Gamal, "A 2000 ^{o}/sec Dynamic Range Bulk Mode Dodecagon Gyro for a Commercial SOI Technology," *Proceedings of the IEEE International Conference on Electronics, Circuits, and Systems*, pp. 264-267, December 2011.

[9] F. Nabki, T. Dusatko, S. Vengallatore, and M. El-Gamal, "Low-Temperature (<300 °C) Low-Stress Silicon Carbide Surface Micromachining Fabrication Technology," *Technical Digest of the Hilton Head Solid-State Sensors, Actuators and Microsystems Workshop*, pp. 216-219, June 2008.

[10] F. Nabki, T. Dusatko, S. Vengallatore, and M. El-Gamal, "Low Stress CMOS-Compatible Silicon Carbide Surface-Micromachining Technology - Part I: Process Development and Characterization," *Journal of Microelectromechanical Systems*, vol. 20, no. 3, pp. 720-729, June 2011.

[11] F. Nabki, P. Cicek, T. Dusatko, and M. El-Gamal, "Low Stress CMOS-Compatible Silicon Carbide Surface-Micromachining Technology - Part II: Beam Resonators for MEMS above IC," *Journal of Microelectromechanical Systems*, vol. 20, no. 3, pp. 730-744, June 2011.

[12] M. Y. Elsayed, F. Nabki, and M. N. El-Gamal, "A Combined Comb/Bulk Mode Gyroscope Structure for Enhanced Sensitivity," *Proceedings of the IEEE International Conference on Microelectromechanical Systems*, pp. 649-652, January 2013.

[13] M. Y. Elsayed, F. Nabki, and M. N. El-Gamal, "A Novel Comb Architecture for Enhancing the Sensitivity of Bulk Mode Gyroscopes," *Journal of Sensors,* vol. 13, no. 12, pp. 16641-16656, December 2013.

[14] N. Yazdi, F. Ayazi, and K. Najafi, "Micromachined Inertial Sensors," *Proceedings of the IEEE*, vol. 86, no. 8, pp. 1640-1659, August 1998.

[15] C. Acar and A. Shkel, "*MEMS Vibratory Gyroscopes: Structural Approaches to Improve Robustness*," Springer, 2009.

[16] "*SOIMUMPs Design Handbook*," 4th edition, MEMSCAP, available at: http:// www.memscap.com, 2004.

[17] D. Miller, B. Boyce, M. Dugger, T. Buchheit, and K. Gall, "Characteristics of Commercially Available Silicon-on-Insulator MEMS Material," *Journal of Sensors and Actuators A: Physical*, vol. 138, no. 1, pp. 130-144, July 2007.

[18] M. Hopcroft, W. Nix, and T. Kenny, "What is the Young's modulus of silicon?" *Journal of Microelectromechanical Systems*, vol. 19, no. 2, pp. 229-238, 2010.

[19] "*AD8015, Wideband Differential Output Transimpedance Amplifier,*" rev. A, Analog Devices, available at: http:// www.analog.com, 1996.

[20] A. Alfaifi, K. Allidina, F. Nabki, and M. N. El-Gamal, "A Low Cross-Sensitivity Dual-Axis Silicon-on-Insulator Accelerometer Integrated as a System in Package with Digital Output," *Journal of Analog Integrated Circuits and Signal Processing*, vol. 77, no. 3, pp. 345-354, December 2013.

Part II:

MEMS Magnetometers

Chapter 4 Overview about MEMS Magnetometers

4.1. Historical Background

Magnetic field sensing is not a new subject. Its earliest form is the magnetic compass, which consists of a suspended magnetic structure that aligns itself to the Earth's magnetic field and thus points to the magnetic north. It was invented by the Chinese about 206 BC [1-3]. At this time, compasses were used for geomancy and fortune telling. Then, they started to be used later by the Chinese for navigation purposes around 1000 AD [1]. Figure 4.1 shows a picture of the early form of the Chinese compasses, a south-indicating ladle made of magnetized lodestone, which is a natural magnetic stone.

The first magnetometer was invented by Carl Friedrich Gauss in 1832 to measure the Earth's magnetic field. The device is composed of a permanent bar magnet suspended horizontally. The change in the bar oscillations between its magnetized and demagnetized states allows for the measurement of the strength of the Earth's magnetic field [4].

Figure 4.1: Early Chinese south-indicating ladle (Sinan) [3].

4.2. Common Types of Traditional Magnetometers

Magnetometers are classified to scalar and vector magnetometers. Scalar magnetometers, as the name implies, measure the magnitude of the magnetic field. On the other hand, vector magnetometers are able to detect both the magnitude and direction. There are several types of magnetometers common nowadays. For very small fields, usually biomagnetic, SQUID (superconducting quantum interference device) sensors are mostly used. For fields higher than 0.1 nT, fluxgate and resonance sensors are more dominant. Resonance sensors are mainly two categories which are optical pumping sensors and nuclear resonance sensors. These have superior resolution. However, they are scalar sensors and they are very bulky. Therefore, they are used for specific applications (e.g., geophysical and space applications). Fluxgate sensors offer comparable resolutions, but their design is very challenging. For magnetic fields in the range of the Earth's and higher, magnetoresistive sensors and Hall effect sensors are dominating. Figure 4.2 shows different types of magnetometers and their range of operation [5]. It is worth mentioning that inductive magnetometers have the widest operation range.

In the past few years, with the widespread of handheld electronics (e.g., smart phones and tablets), another type of magnetometers got very popular, which is integrated magnetometers. These magnetometers are now present in numerous electronics, as it is

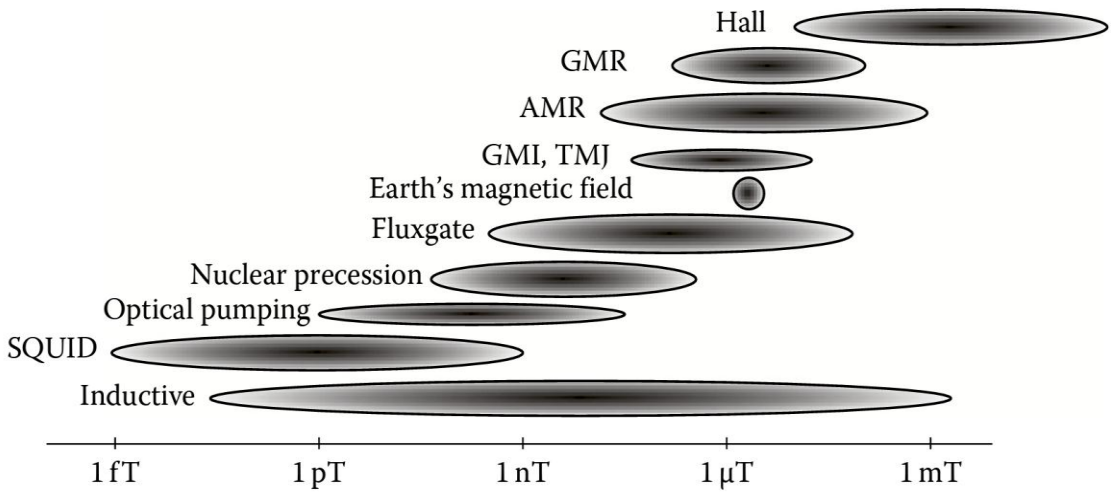

Figure 4.2: Range of operation of common types of magnetometers [5].

used in smart compass applications for navigation. The primary requirement for this type of sensors is to have small size, in order to be able to integrate it within a handheld device. Most of the previously mentioned sensors are bulky and consequently are not suitable, except for Hall and magnetoresistive sensors. Another type of sensors has gained much importance within the integrated sensors regime, which is the Lorentz force magnetometer. Integrated sensors will be discussed in more details in the following section.

4.3. Integrated Magnetometers

As mentioned earlier, integrated magnetometers are split into three main types which are:

- Hall effect
- Magnetoresistive
- Lorentz force

4.3.1. Hall Effect Magnetometers

Hall effect was discovered by Edwin Hall in 1879 [5]. It is explained as follows: If a charged particle with charge q moves in an electric field E and a magnetic field of density B with a velocity v, it is affected by a Lorentz force given by

$$\vec{F}_{Lorentz} = q(\vec{E} + \vec{v} \times \vec{B}). \tag{4.1}$$

Therefore, if a certain voltage V is placed over the length of a specimen of material with length l, width w, and thickness t, the carriers (holes and electrons generally) will be acted upon by an electric field E as shown in Figure 4.3, given by

$$E = V / l. \tag{4.2}$$

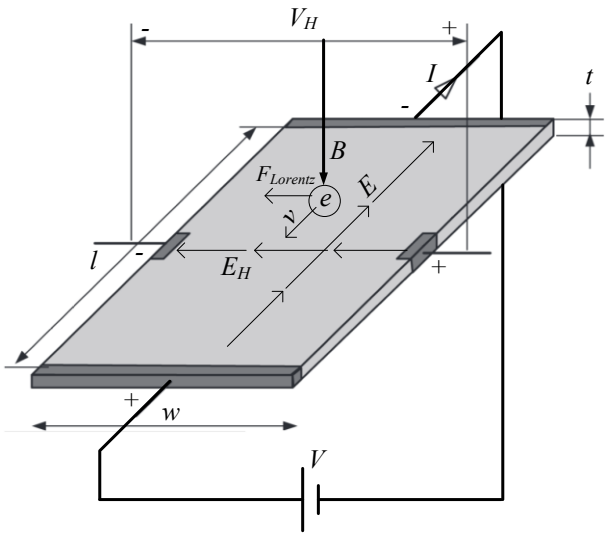

Figure 4.3: Schematic illustrating the Hall effect [5].

Assuming the majority carriers are electrons for this material as an example. The electrons will move with a velocity v creating a current density J along the electric field direction, given by:

$$\vec{v} = -\mu_n \vec{E}, \tag{4.3}$$

$$\vec{J} = -e N \vec{v}, \tag{4.4}$$

where e is the electron charge, N is the carrier density, and μ_n is the electron mobility.

If an out-of-plane magnetic field is introduced to the sample, magnetic force will take effect according to (4.1), deflecting the electrons for their straight line path as shown in Figure 4.4, and creating an accumulation of charges in the transverse direction. Therefore, a balancing electric field E_H is created along the width of the sample in the transverse direction, called the Hall field, given by:

$$\vec{E}_H = -\vec{v} \times \vec{B}, \tag{4.5}$$

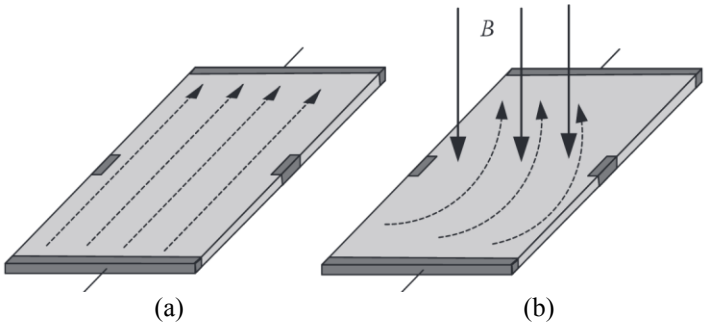

Figure 4.4: Current lines: (a) without magnetic field applied, and (b) with magnetic field applied [5].

where B is the magnetic flux density. This field corresponds to a voltage, called the Hall voltage, which is usually used as the output of the sensor, given by:

$$V_H = w\, E_H = w\, \mu_n\, E\, B = \mu_n \frac{w}{l} V\, B\,. \tag{4.6}$$

Hole carries experience a similar effect, but in reversed polarity. Therefore, the sign of the Hall voltage can be used to detect the material type, whether n-type or p-type.

From (4.6) it is clear that the Hall sensor sensitivity is proportional to the carrier mobility. This creates some limitations on the sensor design. Usually Hall sensors are built using thin film deposition by epitaxial growth to obtain good carrier mobility. Heterostructures can also be used to further enhance mobility, using quantum wells (or 2D electron gas (2DEG)), as in [6]. Table 4.1 shows properties of common semiconductor materials used for Hall sensor design.

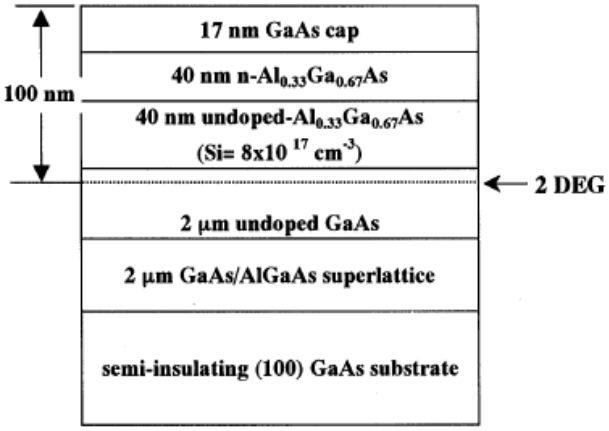

Figure 4.5: 2 DEG GaAs/ AlGaAs heterostructure presented in [6].

Table 4.1: Approximate parameters of the typical materials used in Hall sensors [5].

	μ_n ($cm^2.V^{-1}.s^{-1}$)	μ_p ($cm^2.V^{-1}.s^{-1}$)	E_g (eV)	R_H ($cm^3.A^{-1}.s^{-1}$)	α_T (%/k)
Si	1,400	1,200	1.12	3,000	-0.4
GaAs	8,500	400	1.42	60	-0.2
InAs	33,000	460	0.36	100	-0.17
InSb	80,000	1,250	0.17	380	-0.75

E_g is the band gap, R_H is the Hall coefficient (R_H=1/($N.q$)), and α_T is the temperature coefficient .

Also, it is worth mentioning that the sensitivity is proportional to the applied voltage, which implies some constraints on the power consumption of the sensor. The sensitivity of Hall sensors is relatively low, as clear from Figure 4.2. It is usually enhanced by magnetic flux concentrators, which complicates their fabrication [7], especially if they are targeted for monolithic integration.

Numerous Hall sensors are available in the market from different manufacturers, as F. W. Bell [8-11], Asahi Kasei [12-14], Honeywell [15], etc. Table 4.2 shows the key performance parameters of some examples.

4.3.2. Magnetoresistive Magnetometers

The magnetoresistive (MR) effect is the change of the electrical resistivity of the material in response to the applied magnetic field. This effect is generally present in all materials, but is mostly detectable under extreme conditions of high magnetic field and very low temperature. However, some materials exhibit significant magnetoresistive effect at room temperature, for example: ferromagnetic materials, some semiconductors, and some minerals as bismuth and lanthanum-based oxides [5]. Figure 4.6 shows the relative change in resistance exhibited by different types of magnetoresistors.

Semiconductor magnetoresistors (e.g., indium antimonide (InSb)) rely on their operation on a similar physical principle as the Hall effect. The change in the path of moving carriers in the presence of magnetic field leads to a change in the material

Table 4.2: Key performance parameters of some commercial Hall sensors.

	Sensitivity (V/T)	**Current (mA)**	**Dimensions (mm)**	**Material**
BH-200	0.15	150	5.2×1.75×0.47	Bulk InAs
FH-301	0.1	25	2×1×0.5	InAs
GH-600	0.5	5	4 diameter	GaAs
SH-400	2.9-11.2	5	0.3 diameter	InSb
HG-0711	1.1-1.5	7-9	1.2×0.5×0.3	GaAs
HZ-116C	0.48-0.66	5	2.5×1.5×0.6	InAs
HS-0111	1.04-1.34	2.44-3.85	1.6×0.8×0.45	InSb
SS39ET	14	6	2.9×2.8×1.4	-

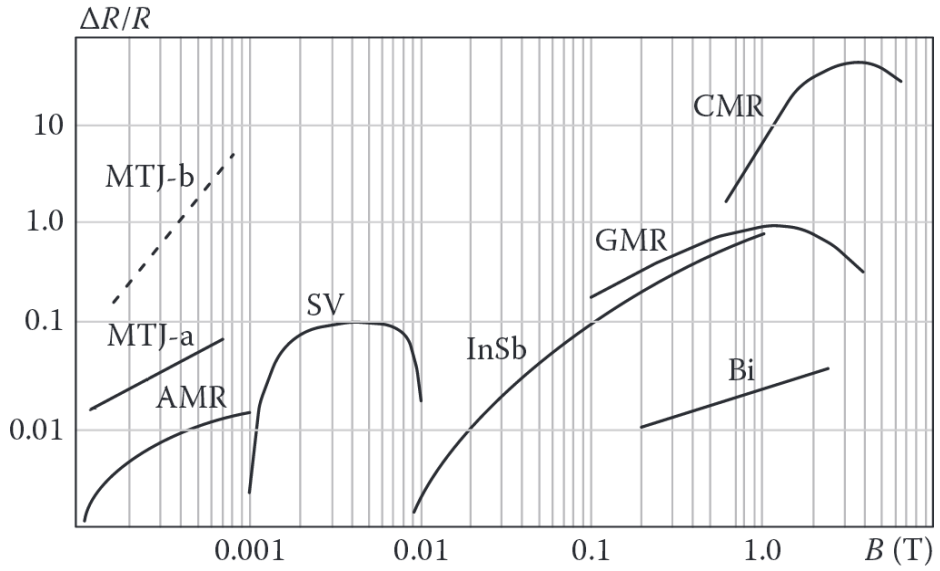

Figure 4.6: The relative change in resistance for different types of magnetoresistors [5].

resistivity. This effect is observable only under relatively large fields. Therefore, semiconductor magnetoresistors are uncommon. In this range, semiconductor Hall effect sensors provide much better performance [5]. On the other hand ferromagnetic magnetoresistors, such as anisotropic magnetoresistors (AMR) and magnetic tunnel junction magnetoresistors (MTJ) offer superior sensitivity. However, they are not very suitable for monolithic integration with CMOS integrated circuits as they require special materials (ferromagnetic) and the processing of such materials often require process steps that are not compatible with CMOS circuitry, for example high temperature steps that would degrade or melt the aluminum tracks. Furthermore, magnetic materials suffer from magnetic hysteresis which complicates the sensor design [7].

4.3.3. Lorentz Force Magnetometers

The principle of operation of a Lorentz force magnetometer can be explained as illustrated in Figure 4.7. If a magnetic field B is acting on a wire of length l and carrying a current I, the wire will be affected by a Lorentz force ($F_{Lorentz}$) orthogonal to both the wire and the magnetic field. This force is given by

$$\vec{F}_{Lorentz} = i(\vec{l} \times \vec{B}). \tag{4.7}$$

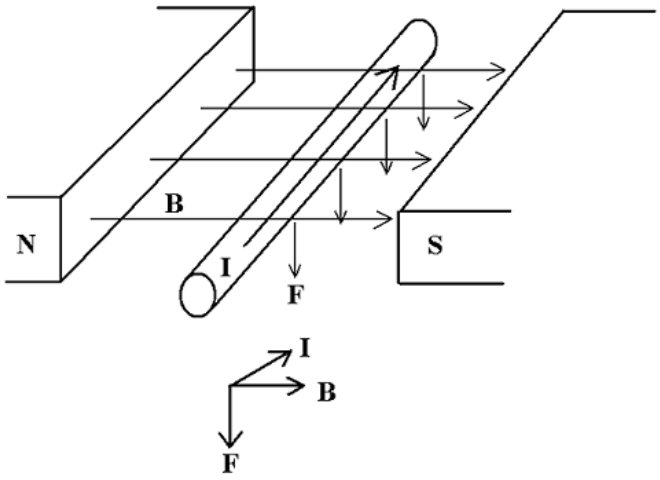

Figure 4.7: Schematic illustrating Lorentz force.

As such, by measuring the displacement caused by the force, while knowing the current and length, the magnetic field can be inferred. Micromachined Lorentz force magnetometers are receiving considerable attention in the sensing community, as they can be fabricated without requiring any custom magnetic materials [16]. This allows for their co-fabrication alongside other MEMS sensors on the same chip, for augmented functionality with minimum impact on form factor. Such integration is highly attractive for consumer electronics applications, where MEMS sensors are playing an increasing role each day. In such cost-sensitive applications, exotic magnetic materials often do not justify the added costs and fabrication complexity, and limit the compatibility of magnetometers with other MEMS sensing structures and integrated circuits (ICs). There are two disadvantages with Lorentz force magnetometers. If these issues are solved, this type of sensors will be an ideal candidate for integrated magnetometers. First, from (4.7), it is clear that the sensitivity of the sensor is proportional to the applied current. However, competitive performance can be reached by proper design of the sensors in order to minimize the needed current. Second, they comprise moving suspended structures. Therefore, they are prone to external inertial forces (e.g., applied acceleration and external shocks). To eliminate this problem, the acceleration needs to be measured and used to cancel out its effect from the magnetometer measurements. This is the main motivation for the work presented in the next chapter, which is to create a combined magnetometer / accelerometer sharing a single surface micromachined structure. The device utilizes

electrical current switching between two perpendicular directions on the structure to achieve a 2D in-plane magnetic field measurement based on the Lorentz force. The device can concurrently serve as a 1D accelerometer for out-of-plane acceleration, when the current is switched off. Accordingly, the proposed design is capable of separating magnetic and inertial force measurements, achieving higher accuracy through a single compact device.

4.4. Latest Advancements in Integrated Magnetometers

As highlighted earlier, micromachined magnetometers are receiving increasing attention in the research community due to their widespread of handheld electronics comprising e-compass functionality, where MEMS magnetometers play an important role. In this section, the latest developments in micromachined magnetometer fabrication will be discussed.

In [17], a novel 3-axis MEMS-based vector magnetometer with integrated magnets and piezoresistive detection using silicon nano-gauges is presented. Sensitivities of 9 V/T and resolutions below 10 $\mathrm{nT}/\sqrt{\mathrm{Hz}}$ are reported. The operation principle is illustrated in Figure 4.8. It is based on nanometer sized piezoresistive gauges which are connected to a silicon mass, as shown in Figure 4.9. This allows for achieving high sensitivities while maintaining reduced size. The silicon mass is used as carrier structure for a magnetic material. If the structure is acted upon by an external magnetic field of flux density *B*, and has a magnetization *M* (provided by the ferromagnetic layer), it will be affected by a magnetic dipole moment *Γ*, given by:

$$\vec{\Gamma} = V\,(\vec{M} \times \vec{B}), \tag{4.8}$$

where *V* is the magnetic volume. This moment induces a rotation of the silicon carrier structure around its fulcrum and leads to a deformation of the nano-gauges, in which high mechanical stresses are generated. Figure 4.10 illustrates the rotation of the structure as a result of in-plane and out-of-plane magnetic fields. Due to piezoresistive effect, a measurable resistance change is generated inside the gauges. The proposed device consumes a power as low as 10 μW.

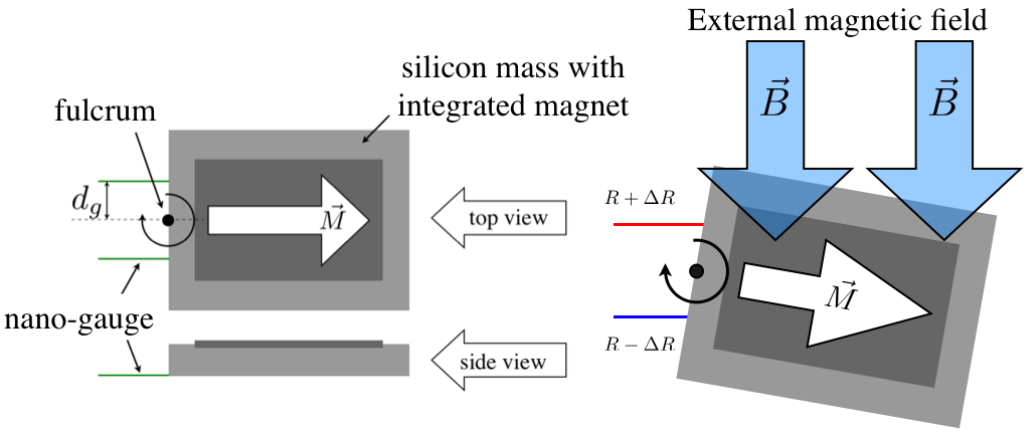

Figure 4.8: Schematic illustrating the sensing mechanism of the device in [17].

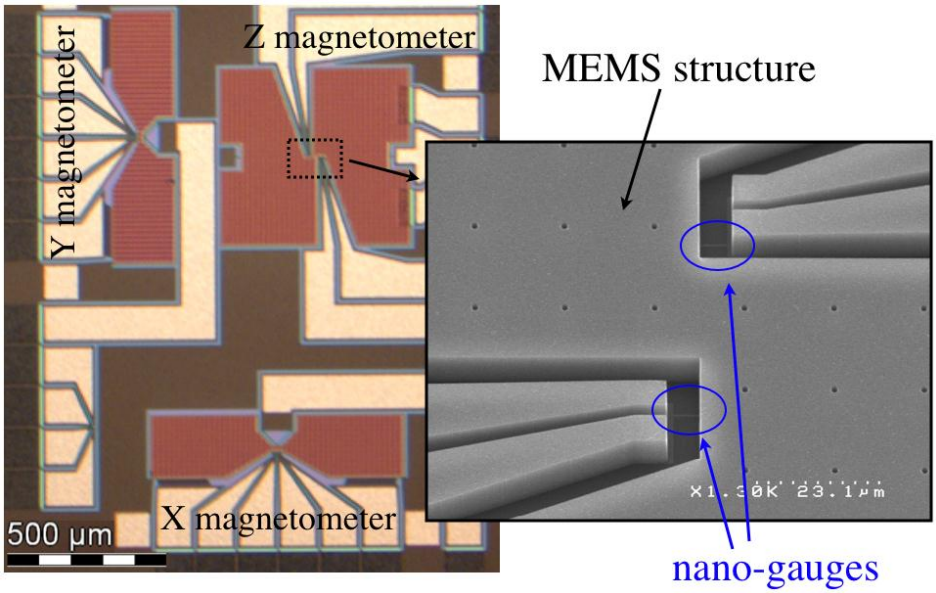

Figure 4.9: SEM micrographs of the device presented in [17].

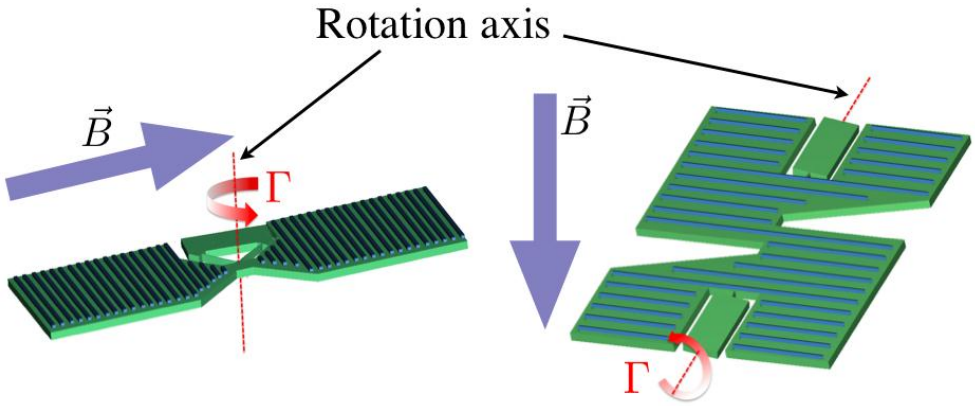

(a) (b)

Figure 4.10: Schematic illustrating the structure rotation for: (a) in-plane magnetic field, and (b) out-of-plane magnetic field [17].

Table 4.3: Summary of performance parameters of the devices presented in [17].

	NdFeB In plane/ Out of Plane	PtMn/ CoFe In plane/ Out of Plane
Sensitivity (V/T)	9.1/ 8.3	1.4/ 0.4
Resolution ($nT/\sqrt{Hz}$)	9.7/ 7.2	66/ 250

The design utilizes two approaches, both requiring exotic materials (one approach utilizes a bilayer of PtMn and CoFe, while the other utilizes NdFeB). These materials would impose severe constraints on monolithic integration with CMOS circuitry for handheld electronics applications, if not make it impossible. It would also probably result in higher fabrication costs due to the use of these special materials. Table 4.3 shows briefly the performance of the two sensing approaches presented.

In [18], an out-of-plane Lorentz force magnetometer and a ferromagnetic in-plane nickel magnetometer are presented. Figure 4.11 explains the operation principle briefly. The deflection experienced as a result of the Lorentz force for the out-of-plane sensor or the magnetic torque moment for the in-plane sensor is measure using n-type monocrystalline silicon piezoresistors set up in a Wheatstone bridge, as shown by the SEM micrographs in Figure 4.12. The fabrication technology comprises steps requiring high temperature (e.g., 800 ^{o}C for silicon nitride low pressure chemical vapour deposition LPCVD and 625 ^{o}C for polysilicon plasma enhanced chemical vapour deposition PECVD). Such high temperatures introduce limitations on the sensor's integration with low thermal budget integrated circuit fabrication technologies in order to avoid affecting the aluminum metal tracks [19]. The sensors exhibit a sensitivity of 0.15 V/T for currents ranging from 10 mA to 50 mA.

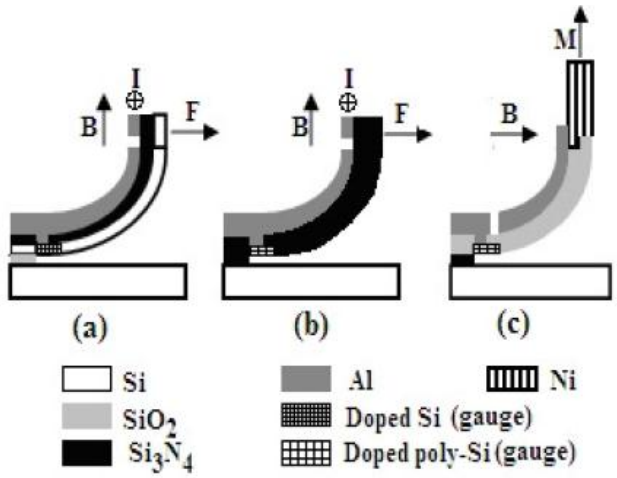

Figure 4.11: Cross section views of the devices presented in [18] illustrating their operation principle: (a), (b) Lorentz force out-of-plane magnetic field sensing, and (c) ferromagnetic sensing for in-plane field.

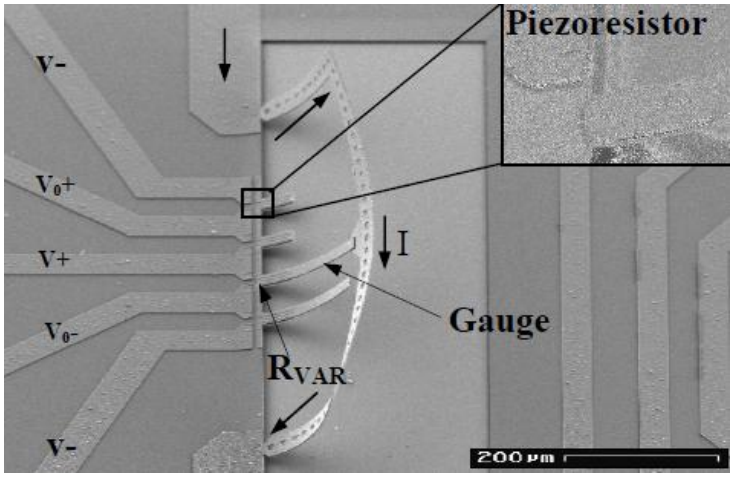

(a)

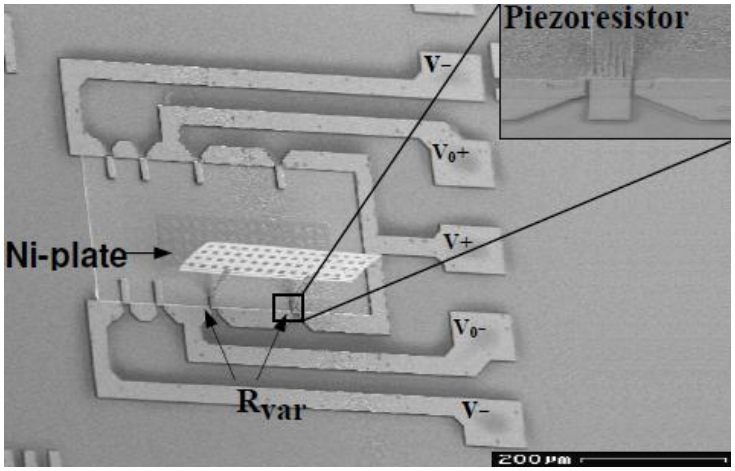

(b)

Figure 4.12: SEM micrographs of devices presented in [18].

In [20, 21], a Lorentz force-based resonant sensor for in-plane or out-of-plane magnetic fields is built using SOI technology. The device utilizes two pairs of parallel-plate electrodes for in-plane motion capacitive sensing and one z-axis sense pick-off electrode for out-of-plane motion sensing. Two similar orthogonal structures could be used for 3D sensing. These devices are not suitable for post-CMOS monolithic integration as they are built using SOI bulk micromachining. The design utilizes a chip level vacuum seal, in order to achieve high quality factors for the resonant mode of operation utilized. The device achieves sensitivities of 0.78 V/T, 12.98 V/T, resolutions of 444 $\mathrm{nT}/\sqrt{\mathrm{Hz}}$, 137 $\mathrm{nT}/\sqrt{\mathrm{Hz}}$, quality factors of 1400 and 10000, for in-plane and out-of-plane sensors, respectively. The dissipated power was measured to be 0.58 mW. Figure 4.13 shows an SEM micrograph of the fabricated device and Figure 4.14 shows FEM simulation results for the resonance mode shapes. Devices were measured to resonate with frequencies of 20.55 kHz and 46.96 kHz for the in-plane and out-of-plane modes, respectively. Two similar orthogonal structures could be used for 3D sensing. However, these devices are not suitable for post-CMOS monolithic integration, as mentioned earlier.

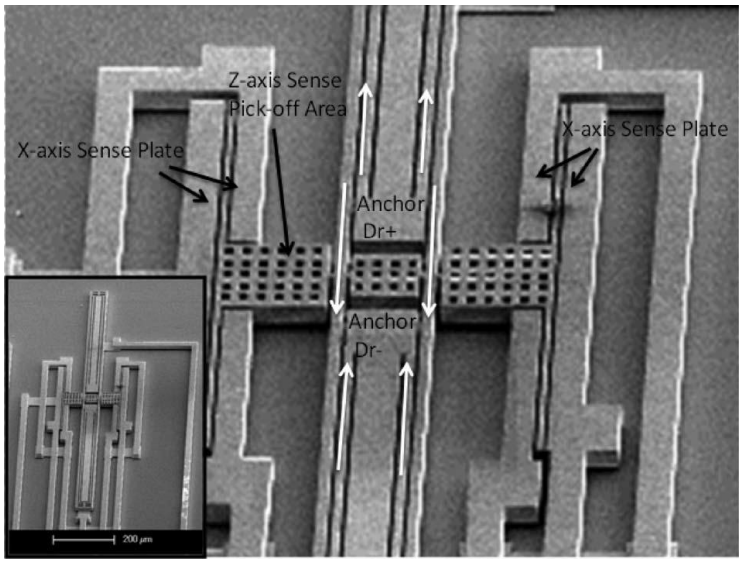

Figure 4.13: SEM micrograph of the Lorentz force sensor presented in [21], where the current flow direction is indicated by the white arrows. The full 1 mm × 0.2 mm structure is shown in the inset.

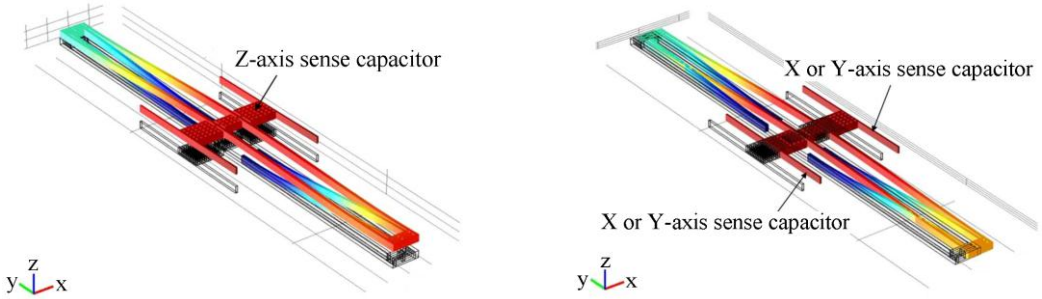

(a) (b)

Figure 4.14: FEM mode shapes for: (a) out-of-plane mode and (b) in-plane mode [21].

In [22], a 3D CMOS-MEMS magnetic sensor has been proposed and demonstrated based on the standard TSMC 0.35 μm 2P4M process utilizing the stacking of metal/tungsten layers to realize a magnetic-coil, which could respectively generate Lorentz and electromagnetic forces by out-of-plane and in-plane magnetic fields for multi-axes magnetic field detection. Figure 4.15 shows the sensor structure and principle of operation and Figure 4.16 shows an SEM micrograph of the fabricated devices. At atmospheric pressure, the sensor exhibits resolutions of 319.9 $\text{nT}/\sqrt{\text{Hz}}$, 296.5 $\text{nT}/\sqrt{\text{Hz}}$, and 121.6 $\text{nT}/\sqrt{\text{Hz}}$ for the *x*, y, and *z*-axis respectively. The sensitivities of the sensor were characterized to be 0.13 V/T, 0.14 V/T, and 1.51 V/T for the three axes respectively. Table 4.4 shows the key performance parameters of the sensor. The sensitivity and resolution could be improved by vacuum packaging, in order to raise the resonance quality factor of the device. The MEMS structure was co-fabricated with the sensing circuitry. This co-fabrication technique restricts the MEMS to the materials and constraints inherent to that semiconductor process node. Alternatively, sensors that are amenable to above-IC integration present lower parasitics to the associated readout circuitry, resulting in an improved overall sensitivity. Furthermore, the area sharing made possible by overlaying the sensors with the electronics allows for smaller overall chip size, compared to the side-by-side co-fabrication approach. Accordingly, this is the main focus of our work explained in the next chapter, which presents a Lorentz force based magnetometer / accelerometer combined sensor, made from a low temperature, above-IC-compatible fabrication process.

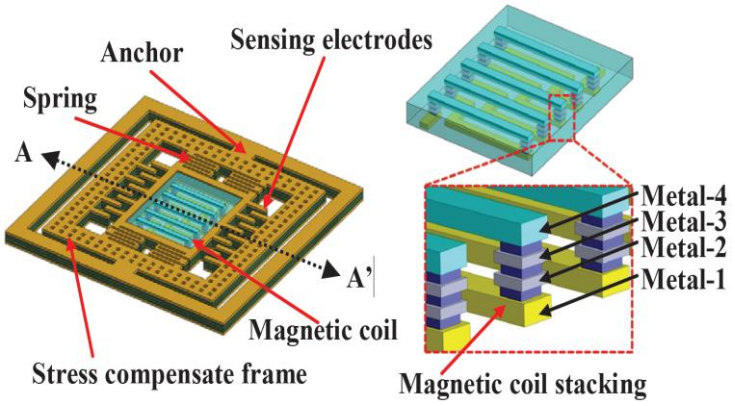

(a)

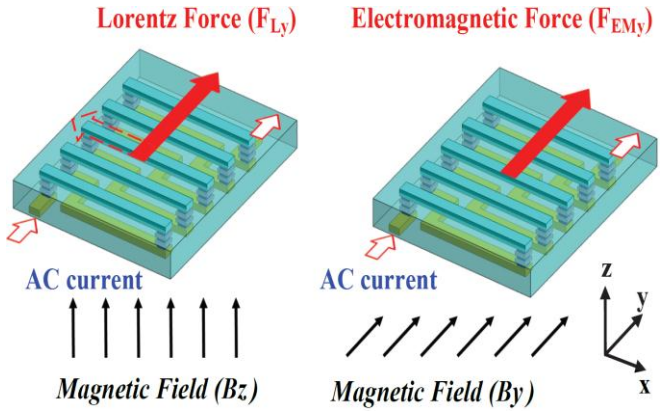

(b)

Figure 4.15: (a) Schematic of the device structure and (b) illustration of the forces affecting the structure resulting from magnetic fields along *y* and *z* axes [22].

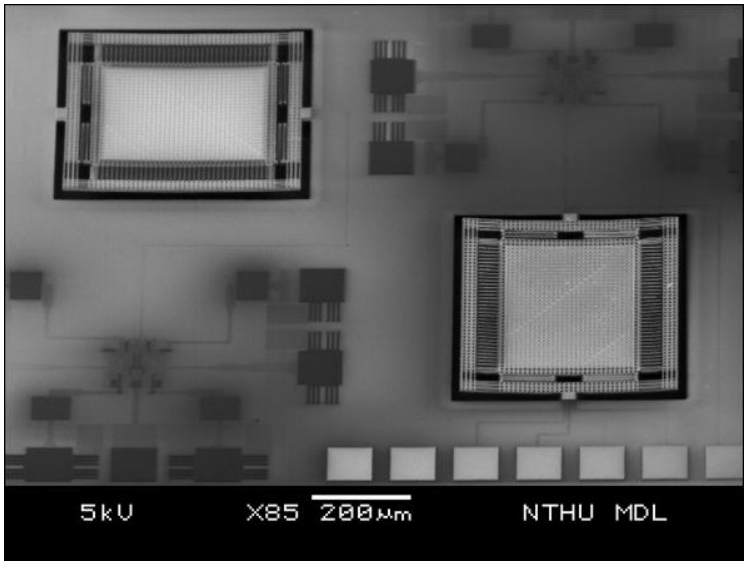

Figure 4.16: SEM micrograph of the device proposed in [22].

Table 4.4: Key performance parameters of the device presented in [22].

	x	*y*	*z*
Current (mA)	4.18	4.02	4.02
Sensitivity (V/T)	0.13	0.14	1.51
Resolution ($nT/\sqrt{Hz}$)	319.9	296.5	2.24
Nonlinearity (%)	2.27	3.27	2.24
Size (μm×μm)	1800×1500 (MEMS+IC)		

4.5. Applications of Integrated Magnetometers

Magnetometers generally have a very wide range of application including space, geographical surveying, military, archaeological, magnetic imaging, automotive, e-compass, and medical applications. Certain range of applications is dominated by integrated magnetometers, where size and cost are critical, and when integrated magnetometers provide adequate performance. This range is in a continuous increase as the performance of the sensors improves due to non-stopping research. Below are some examples of the key applications:

4.5.1. E-Compass

This is one of the main applications for integrated magnetometers as they are becoming one of the essential sensors present in any smart phone or tablet. They are also present in many speciality watches and other handheld electronics. In such application reducing sensors size and cost is very crucial, which makes integrated sensors indispensable.

(a) (b)

Figure 4.17: Examples of e-compasses integrated in: (a) cell phone <Apple>, (b) watches <left: Casio, right: Timex> [5].

4.5.2. Position Sensing

Magnetometers are often used in linear and angular displacement sensing. This is based on placing either the sensor or a permanent magnet on the moving object, whose displacement needs to be measured, while keeping the other at a fixed position. Then, the magnetometer reading will vary according to the relative position between them. An example product available in the market for this application is the magnetic position sensing solution developed by ZMDI [23]. It is utilized in automotive applications to measure the angular displacement of shafts.

4.5.3. Magnetic Imaging

By scanning an object by a magnetometer and detecting the variation of the sensor's reading, an image of the object can be formed. Alternatively, magnetic sensors can be arranged in a matrix to form the image faster without the need for scanning the sensors on the object. Figure 4.18 shows examples of an extremely small (50 nm) Hall effect sensor

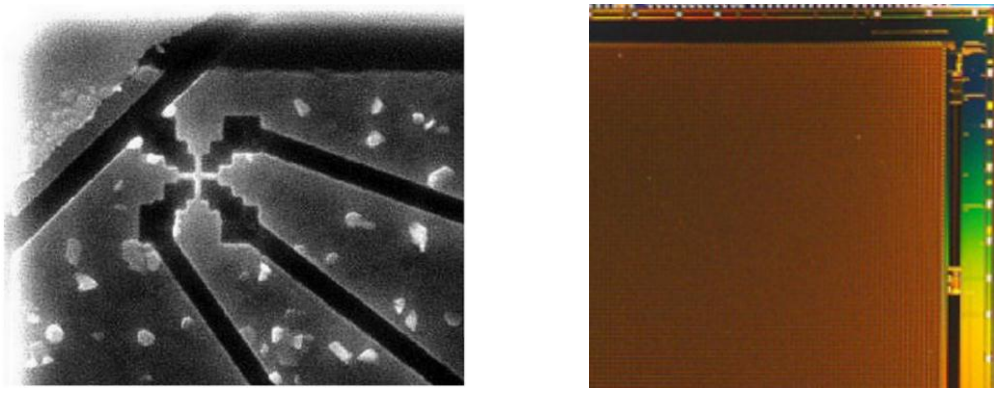

(a) (b)

Figure 4.18: (a) 50 nm Hall Sensor developed by Nanomagnetics Instruments for their scanning Hall microscope [24] and (b) part of the Hall sensor matrix developed by MagCam [25].

developed by Nanomagnetics Instruments for imaging purposes [24] and a 2D Hall sensor (128×128) camera array developed by MagCam [25].

Magnetometer based imaging devices have been reported in several application including reading hard disk data, checking welding quality, and even DNA analysis [5].

4.6. Market and Examples of Commercial Integrated Magnetometers

As mentioned earlier, integrated magnetometers have become standard components present in handheld electronics. They are also used significantly in the automotive sector and others. Figure 4.19 shows the market trend for different MEMS devices through the upcoming years in the handheld smart electronics sector.

It is worth mentioning that discrete magnetometers are expected to become less popular with the widespread of more integrated solutions as 6-axis e-compasses and 9-axis combos. However, the overall market of magnetometers (discrete and combos) is expected to increase significantly. This general inclination towards integration and combos opens the doors for novel structures that serve as multiple sensors in order to further reduce size, cost and allow for even more integration. Some examples of commercially available magnetometers, both discrete and in combo inertial measurement units (IMUs), are shown below.

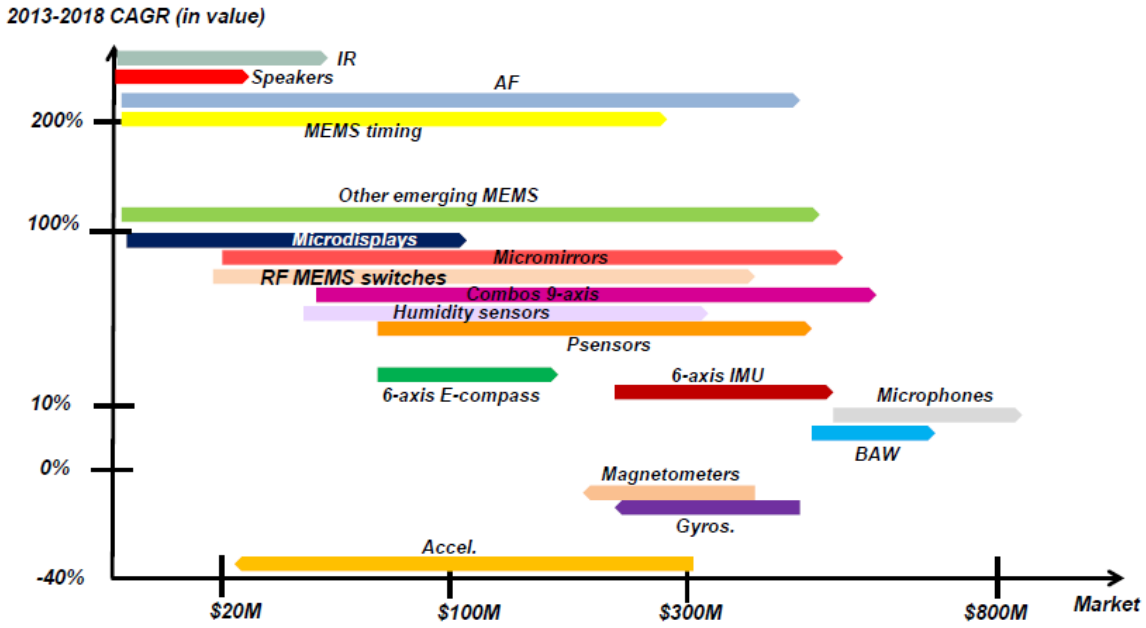

Figure 4.19: Market trends for MEMS devices in cell phones and tablets [Yole Development, 2013].

4.6.1. ST Microelectronics LSM303D

This is the latest e-compass from ST Microelectronics [27]. It comprises a 3D accelerometer and a 3D magnetometer in a 3 mm×3 mm×1 mm LGA-16 package. The measurements are supplied in a 16 bit digital format. The magnetometer provides a programmable full scale of ±200, ±400, ±800, or ±1200 µT with a sensitivity of 0.008 µT/LSB for the smallest full scale setting, while the measurement full scale of the accelerometer is programmable to ±2, ±4, ±6, ±8, or ±16 g with sensitivity of 0.061 mg/LSB for the smallest full scale setting. The sensor operates from a supply voltage of 2.5 V and draws a current of 0.3 mA. Figure 4.20 shows an image of the sensor.

Figure 4.20: LSM303D e-compass by ST Microelectronics [27].

ST Microelectronics also offers another similar sensor without an accelerometer, which is LIS3MDL.

4.6.2. Kionix KMX61G

This sensor from Kionix is a magnetometer accelerometer combo with an embedded emulated gyro function [28]. This leads to lower power consumption compared to adding physical gyro to make it a 9-axis combo. It has a 3 mm×3 mm×0.9 mm footprint. It offers a 12 bit output and operates from a 2.5 V supply. The magnetometer has a full scale of ±1200 μT and a sensitivity of 0.146 μT/LSB. While the accelerometer's full scale is programmable to ±2, ±4, or ±8 g, and its sensitivity is 0.98 mg/LSB.

4.6.3. Invensense IMU-9250

This is one of the latest 9-axis IMUs from Invensense [29]. MPU-9250 is a multi-chip module (MCM) consisting of two dies integrated into a single 3 mm×3 mm×1 mm QFN package. One die houses the 3-Axis gyroscope and the 3-Axis accelerometer. The other die houses the AK8963 3-Axis magnetometer from Asahi Kasei Microdevices Corporation, which is a 3-axis silicon monolithic Hall effect magnetic sensor with magnetic concentrator. It offers a 14 or 16 bit output and operates from a 2.5 V supply. The magnetometer has a full scale of ±4800 μT and a sensitivity of 0.6 μT/LSB and 0.15 μT/LSB for the two output settings, respectively. As for the accelerometer, it provides a programmable full scale of ±2, ±4, ±8, or ±16 g with a 16 bit output, and its sensitivity is 0.06 mg/LSB for the lowest full scale setting. The current required for the IMU without the gyro (as it is not the focus of this section) is 730 μA.

The mentioned examples and all other magnetometer/ accelerometer combos available are based on separate sensors solution stacked or bonded with the electronics in the same package. It would be very beneficial if the two sensors can be fabricated using the same structure. This would lead to further size and cost reduction. Furthermore, if the fabrication was done in a technology compatible with standard CMOS substrates, this would lead to even more integration capabilities and would allow for the sensors to be fabricated above the circuits which would result in reducing the parasitics and lead to

improved performance. This is the main goal of our work as will be discussed in details in the next chapter.

4.7. References

[1] W. Lowrie, "*Fundamentals of Geophysics*," 2nd edition, Cambridge University Press, 2007.

[2] L. Yongxiang (Editor), "*A History of Chinese Science and Technology*," vol. 2, Springer, 2014.

[3] H. Selin (Editor), "*Encyclopaedia of the History of Science, Technology, and Medicine in Non-Western Cultures*," Springer, 2008.

[4] C. Gauss, "The Intensity of the Earth's Magnetic Force Reduced to Absolute Measurement," Translated by S. Johnson, *Treatises of the Royal Scientific Society*, vol. 8, pp. 3-44, December 1832.

[5] S. Tumanski, "*Handbook of Magnetic Measurements*," CRC Press, 2011.

[6] A. Sandhu, H. Masuda, A. Oral, and S. Bending, "Room Temperature Magnetic Imaging of Magnetic Storage Media and Garnet Epilayers in the Presence of External Magnetic Fields Using a Sub-Micron GaAs SHPM," *Journal of Crystal Growth*, vol. 227-228, pp. 899-905, July 2001.

[7] M. Thompson and D. Horsley, "Parametrically Amplified Z-Axis Lorentz Force Magnetometer," *Journal of Microelectromechanical Systems*, vol. 20, no. 3, pp. 702-710, June 2011.

[8] "*BH-200 Series Hall Effect Sensors Datasheet,*" F. W. Bell, available at: http:// www.fwbell.com.

[9] "*FH Series Hall Effect Sensors Datasheet,*" F. W. Bell, available at: http:// www.fwbell.com.

[10] "*GH-600 Series Hall Effect Sensors Datasheet,*" F. W. Bell, available at: http:// www.fwbell.com.

[11] "*SH Series Hall Effect Sensors Datasheet,*" F. W. Bell, available at: http:// www.fwbell.com.

[12] "*HG-0711 GaAs Hall Element Datasheet,*" Asahi Kasei Microdevices, available at: http:// www.akm.com, February 2013.

[13] "*HZ-116C InAs Hall Element Datasheet,*" Asahi Kasei Microdevices, available at: http:// www.akm.com, February 2013.

[14] "*HS-0111 InSb Hall Element Datasheet,*" Asahi Kasei Microdevices, available at: http:// www.akm.com, February 2013.

[15] "*SS39ET/SS49E/SS59ET Series Linear Hall-effect Sensor ICs Datasheet,*" Honeywell International Inc., available at: http:// www.honeywell.com, February 2015.

[16] M. Y. Elsayed, P. -V. Cicek, F. Nabki, and M. N. El-Gamal, "Surface Micromachined Combined Magnetometer/ Accelerometer for Above-IC Integration," *Journal of Microelectromechanical Systems*, December 2014.

[17] D. Ettelt, G. Dodane, M. Audoin, A. Walther, G. Jourdan, P. Rey, P. Robert, and J. Delamare, "A Novel Microfabricated High Precision Vector Magnetometer," *Proceedings of the IEEE Conference on Sensors*, pp. 2010-2013, October 2011.

[18] M. El Ghorba, N. André, S. Sobieski, and J. -P. Raskin, "CMOS Compatible Out-of-Plane and In-Plane Magnetometers," *Proceedings of the IEEE Conference on Solid-State Sensors, Actuators and Microsystems*, pp. 2373-2376, June 2007.

[19] S. Sedky, A. Witvrouw, H. Bender, and K. Baert, "Experimental Determination of the Maximum Post-Process Annealing Temperature for Standard CMOS Wafers," *IEEE Transactions on Electron Devices*, vol. 48, no. 2, pp. 377-385, February 2001.

[20] M. Thompson, M. Li, and D. Horsley, "Low Power 3-Axis Lorentz Force Navigation Magnetometer," *Proceedings of the IEEE Conference on Microelectromechanical Systems*, pp. 593-596, January 2011.

[21] M. Li, V. Rouf, M. Thompson, and D. Horsley, "Three-Axis Lorentz Force Magnetic Sensor for Electronic Compass Applications," *Journal of Microelectromechanical Systems*, vol. 21, no. 4, pp. 1002-1010, August 2012.

[22] C. -I. Chang, M. -H. Tsai, Y. -C. Liu, C. -M. Sun, and W. Fang, "Development of Multi-Axis CMOS-MEMS Resonant Magnetic Sensor Using Lorentz and Electromagnetic Forces," *Proceedings of the IEEE Conference on Microelectromechanical Systems*, pp. 193-196, January 2013.

[23] "*Magnetic Position Sensing Solutions*," Zentrum Mikroelektronik Dresden AG (ZMDI), available at: http:// www.zmdi.com.

[24] "*LT-SHPM Low Temperature Scanning Hall Probe Microscope*," Nanomagnetic Instruments, available at: http:// www.nanomagnetics-inst.com.

[25] "*MagCam Advanced Magnet Inspection*," MagCam, available at: http:// www.magcam.com.

[26] "*Status of the MEMS Industry*," Yole Development, 2013.

[27] "*LSM303D, Ultra-Compact High-Performance E-Compass Module*," rev. 2, ST Microelectronics, available at: http:// www.st.com, November 2013.

[28] "*KMX61G Mag-Accel Combo*," Kionix, available at: http:// www.kionix.com, 2013.

[29] "*MPU-9250 Product Specification,*" rev. 1.0, Invensense, available at: http:// www.invensense.com, January 2014.

Chapter 5 Surface Micromachined Combined Magnetometer / Accelerometer for Above-IC Integration

5.1. Introduction

As highlighted in the previous chapter, micromachined Lorentz force magnetometers are receiving considerable attention in the sensing community, as they can be fabricated without requiring any custom magnetic materials (e.g., integrated permanent magnets in [1]). This allows for their co-fabrication alongside other MEMS sensors on the same chip, for augmented functionality with minimum impact on form factor. Such integration is highly attractive for consumer electronics applications, where MEMS sensors are playing an increasing role each day. In such cost-sensitive applications, exotic magnetic materials often do not justify the added costs and fabrication complexity, and limit the compatibility of magnetometers with other MEMS sensing structures and integrated circuits (ICs). In [2], an out-of-plane Lorentz force magnetometer and a ferromagnetic in-plane nickel magnetometer are presented, requiring high temperature fabrication steps (e.g., 800 ^{o}C), while, in [3, 4], a Lorentz force-based resonant sensor for in-plane or out-of-plane magnetic fields is built using SOI technology. While two similar orthogonal structures could be used for 3D sensing, these devices are not suitable for post-CMOS monolithic integration. In [5], a co-fabricated CMOS-MEMS magnetometer is presented in a TSMC 0.35 μm technology, but is restricted to the materials and constraints inherent to that semiconductor process node.

Alternatively, sensors that are amenable to above-IC integration present lower parasitics to the associated readout circuitry, resulting in an improved overall sensitivity. Furthermore, the area sharing made possible by overlaying the sensors with the electronics allows for smaller overall chip size, compared to the side-by-side co-fabrication approach. Accordingly, our work presented in this chapter focuses on a Lorentz force based magnetometer / accelerometer combined sensor, made from a low temperature, above-IC-compatible fabrication process. The proposed sensor relies on switching an electrical

current between two perpendicular directions on the device structure to achieve a 2D in-plane magnetic field measurement. Concurrently, the device serves as a 1D accelerometer for out-of-plane acceleration, by switching the current off and by monitoring the structure's capacitive change in response to acceleration. The design can thus separate magnetic and inertial force measurements, utilizing a single compact device. The proposed sensor supports static operation at atmospheric pressure to avoid the need for complex vacuum packaging. Alternatively, it is also capable of operating at resonance under vacuum for enhanced sensitivity. The device is fabricated using a silicon carbide (SiC) surface micromachining technology as in [6-8], which is fully adapted for above-IC integration on standard CMOS substrates. The device was presented earlier in [9]. This chapter explains it in more details.

This chapter first describes the device design, and then presents finite-element simulation results. The process flow for the fabrication technology is then detailed, and measurement results are presented and discussed.

5.2. Device Design

The principle of operation for a Lorentz force magnetometer can be explained as follows. If a magnetic field B is acting on a wire of length l and carrying a current I, the wire will be affected by a Lorentz force ($F_{Lorentz}$) orthogonal to both the wire and the magnetic field. This force is given by

$$\vec{F}_{Lorentz} = i(\vec{l} \times \vec{B}) . \tag{5.1}$$

As such, by measuring the displacement caused by the force, while knowing the current and length, the magnetic field can be inferred.

An SEM micrograph of the fabricated device is shown in Figure 5.1. Bowing is apparent in the device due to its relatively large area, and the residual stresses present in the film stack. This can be mitigated by tuning the deposition recipes and/or adjusting the structure dimensions. The sensor is composed of: *i*) a 2 µm-thick 500 µm-wide square suspended silicon carbide (SiC) structure acting as the current carrying element for magnetometer operation and concurrently serving as the proof mass for the accelerometer; *ii*) four 250 µm-long and 9 µm-wide suspension beams, anchored from their ends, holding the proof mass and allowing for its free motion; *iii*) a sensing electrode underneath the

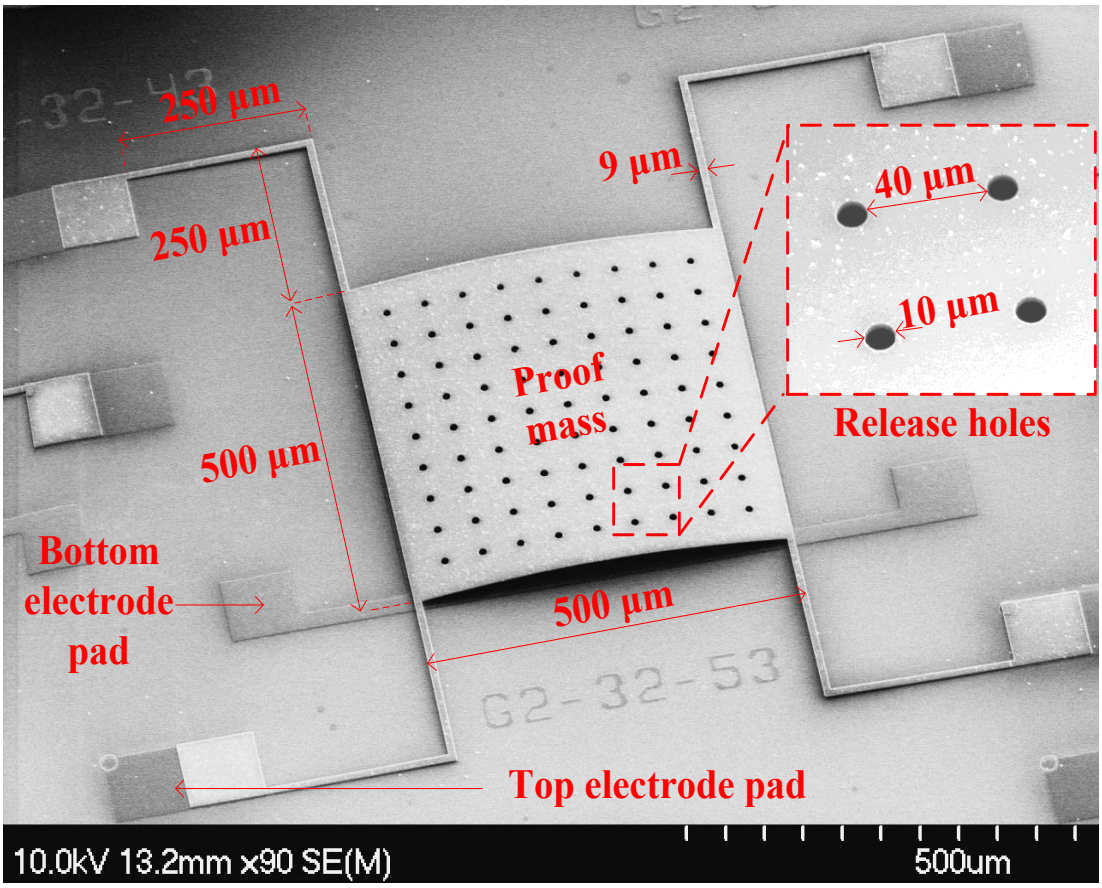

Figure 5.1: SEM micrograph of a fabricated device.

structure used for the capacitive detection of the out-of-plane motion resulting from Lorentz or inertial forces; and *iv*) a metallic layer underlying the SiC structure in order to serve as a low resistivity path for the current, thus helping to reduce electrical noise.

The beam dimensions are chosen to adjust the stiffness of the supports in order to provide adequate sensitivity and ensure the structural integrity of the device. The spring constant k of a simple cantilever beam is given by [10]

$$k_{simplebeam} = E\frac{wt^3}{4l^3}, \tag{5.2}$$

where E is the Young's Modulus of the beam material (amorphous SiC in this case), w is the beam width, t is the structure thickness, and l is the beam length. A summary of the device design parameters is given in Table 5.1.

Table 5.1: Summary of Device Design Parameters

Parameter	Value
Proof mass	500 μm × 500 μm
Structure thickness	2 μm
Suspension dimensions	250 μm × 9 μm
Capacitive gap	0.5 μm
Spring constant (k_{eq})	1.07 N/m
Resonance frequency	4.03 kHz

During device operation, the sensing cycle is divided into three successive phases, as illustrated in Figure 5.2:

1) The current is driven along the *x*-axis, from left to right, causing the resulting Lorentz force to induce a displacement along the *z*-axis, due to any magnetic field in the *y*-axis. This displacement is detected capacitively by the sense electrode, and can be used to infer the *y*-axis component of the magnetic field.
2) The current is directed along the *y*-axis, from bottom to top. The resulting Lorentz force then causes a displacement along the *z*-axis, due to any magnetic field along the *x*-axis. Capacitive detection at the sense electrode is used to determine the *x*-axis component of the magnetic field. Notably, measurements in phases 1 and 2 are sensitive to external *z*-axis inertial force.
3) The current is switched off so that the motion due to the *z*-axis inertial force is detected and used to cancel out its effect on the magnetic field measurements in phases 1 and 2, achieving a high accuracy combined 2D magnetometer / 1D accelerometer.

In order to increase the number of operation axes of the device, lateral electrodes could eventually be added at the perimeter of the proof mass as suggested in [11] to enable in-plane motion detection and achieve a 3D magnetometer / 3D accelerometer.

5.3. Casimir Force

The Casimir force is an attractive force that acts between two close parallel uncharged conducting plates. It is due to quantum vacuum fluctuations of the electromagnetic field. As the device presented here has a large electrode area and a relatively small gap, this force must be considered. In addition to the Casimir force, the suspended top plate of the device is affected by several other forces, namely the gravitational force, the applied Lorentz and inertial forces, and the suspension spring forces such that

$$F_{total} = F_{Casimir} + F_{gravity} + F_{Lorentz} + F_{inertial} + F_{spring}. \tag{5.3}$$

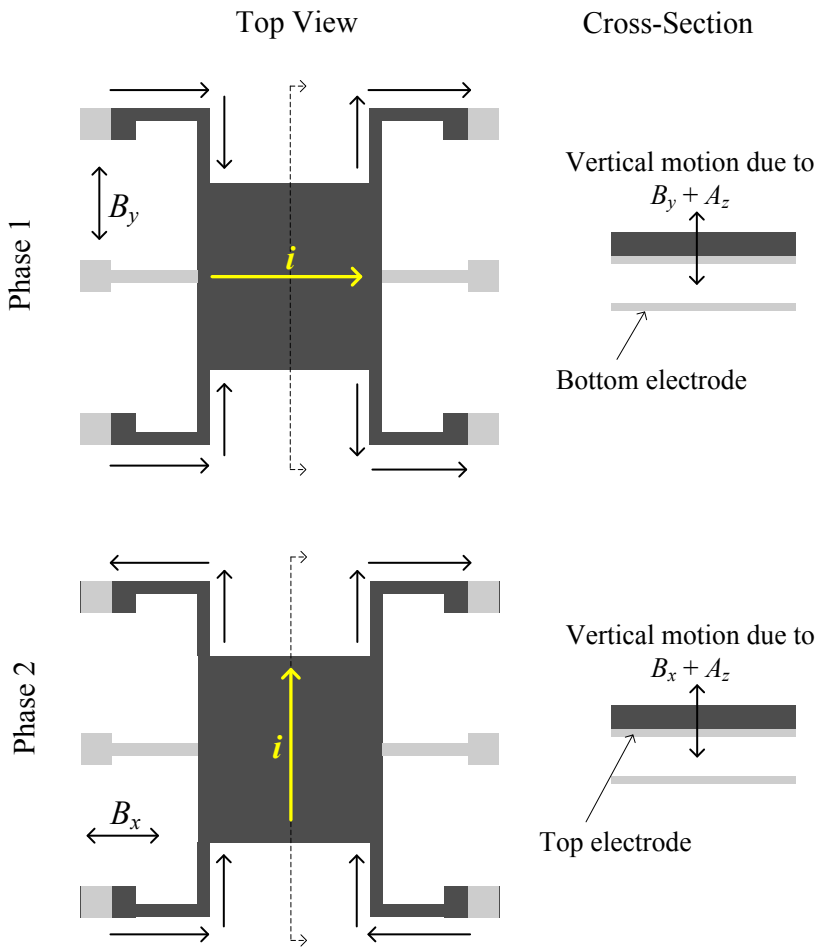

Figure 5.2: First two phases of the sensing cycle showing the current direction together with a side cross-section view illustrating the device displacement.

The Casimir force is proportional to the electrode area and is inversely proportional to the fourth power of the distance between the two electrodes. It is given by [12]

$$F_{Casimir} = \frac{\pi \hbar c w_{PM} L_{PM}}{480(d-z)^4}, \tag{5.4}$$

where h is Planck's constant, c is the speed of light in vacuum, w_{PM} is the width of the proof mass (top electrode), and L_{PM} is its length, d is the nominal capacitive gap between the electrodes, and z is the displacement of the top electrode. It is worth mentioning that Equation 5.4 is neglecting the finite conductivity of aluminum as well as its finite cut-off frequency. A more general approach, as in [13], can used for more accurate results.

The force related to the weight of the structure is given by

$$F_{gravity} = \rho_{SiC} g w_{PM} L_{PM} t, \tag{5.5}$$

where ρ_{SiC} is the density of the SiC structural material, and g is Earth's gravitational acceleration.

The balancing spring force is given by

$$F_{spring} = -k_{eq} z, \tag{5.6}$$

where k_{eq} is the equivalent spring constant of the structure.

At equilibrium, the resultant force must be zero (i.e., $F_{total} = 0$), as illustrated in Figure 5.3, where all the forces are plotted along with that of the restorative spring force.

Furthermore, a necessary condition is that the first derivative of total force (i.e., dF_{total}/dz) be negative at the point of equilibrium, such that

$$\frac{dF_{total}}{dz} = \frac{\pi \hbar c w_{PM} L_{PM}}{120(d-z)^5} - k_{eq} < 0. \tag{5.7}$$

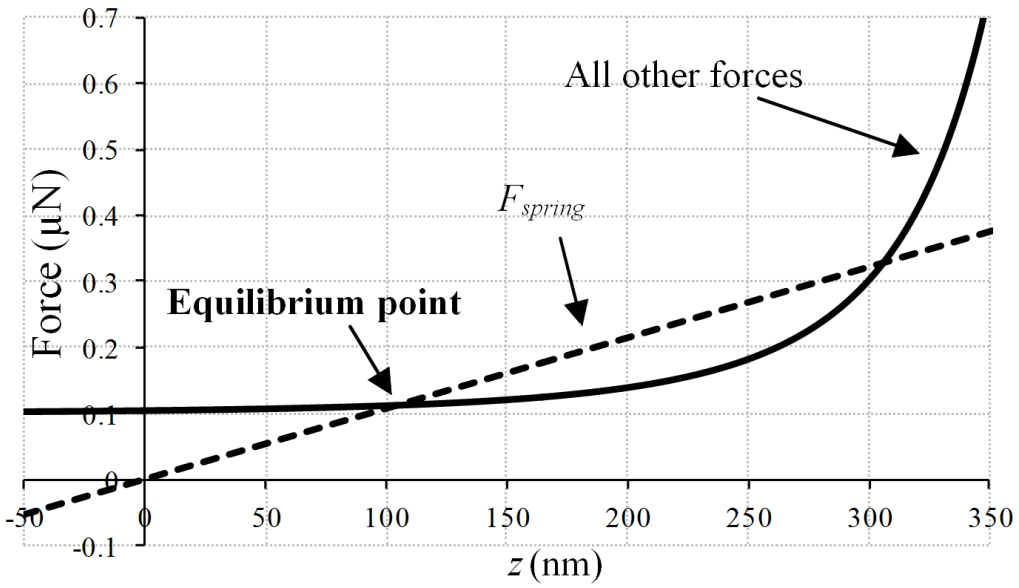

Figure 5.3: Forces affecting the structure versus vertical displacement.

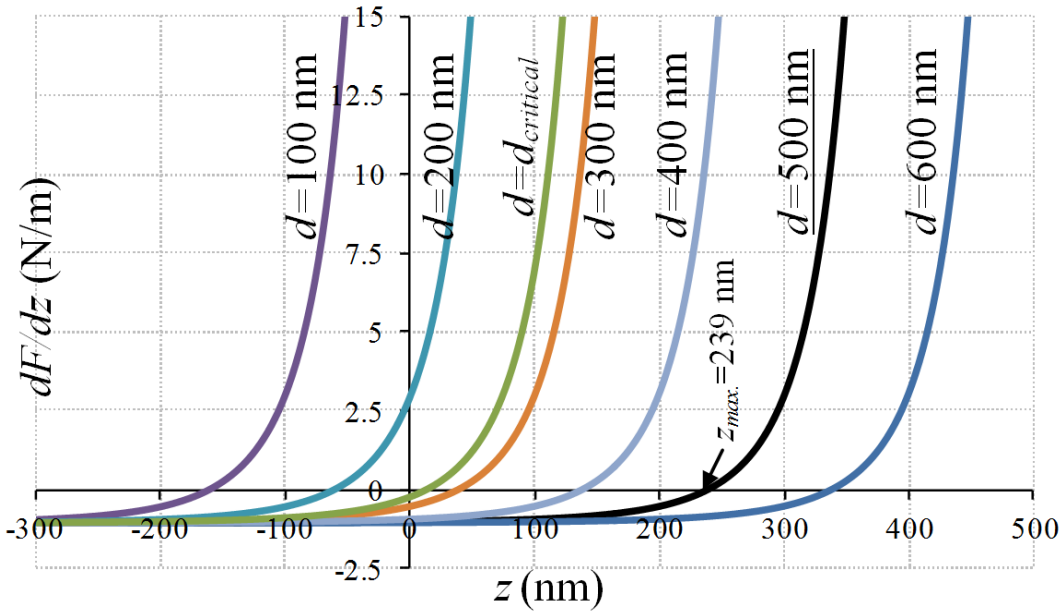

Figure 5.4: First derivative of the total force (dF_{total}/dz) vs the displacement (z) for different values of the inter-electrode gap (d). The selected inter-electrode gap is underlined and the resulting maximum displacement ($z_{max.}$) is shown.

Figure 5.4 shows dF_{total}/dz for different values of the gap between the electrodes (d). For small values of d, dF_{total}/dz is always positive for all positive displacement (z) values. This means that the top electrode would always be pulled-in by the Casimir force

directly after release such that there is no stable equilibrium state. As d increases beyond a certain value, $d_{critical}$, a stable equilibrium range, where the derivative is negative for positive z, is reached. This equilibrium ensures that the structure will not collapse as a result of Casimir force after release. In order to calculate $d_{critical}$, the Casimir force for small values of z can be neglected as it is very small, and will otherwise complicate the solution due to its $1/(d\text{-}z)^4$ dependence. For a critically stable condition without pull-in after release, the spring force should balance the weight, such that

$$k_{eq} z_{PI} = \rho_{SiC} g w_{PM} L_{PM} t \,, \tag{5.8}$$

where z_{PI} is the displacement in this critically stable situation. By combining (5.7) and (5.8), $d_{critical}$ can be calculated using

$$d > d_{critical} = \sqrt[5]{\frac{\pi hcw_{PM} L_{PM}}{120 k_{eq}}} + \frac{\rho_{SiC} g w_{PM} L_{PM} t}{k_{eq}} \,. \tag{5.9}$$

Using (5.9), the value for $d_{critical}$ is calculated to be of 275 nm. The maximum possible displacement (z_{max}) of the structure before pull-in collapse due to the Casimir force is expressed as

$$z_{\max} = d - \sqrt[5]{\frac{\pi hcw_{PM} L_{PM}}{120 k_{eq}}} \,. \tag{5.10}$$

Accordingly, a sacrificial layer thickness (gap between the electrodes) of 500 nm is selected in order to ensure structural integrity of the device after release, and to allow sufficient displacement before a pull-in collapse occurs. The derivative of the total force vs the displacement for this selected gap size is shown in Figure 5.4, yielding a stable equilibrium region for displacements below 239 nm. This allowable displacement range allows for a good dynamic range of the device.

Note that at all times the electrical potential difference between the electrodes must be kept well below the electrostatic pull-in voltage given by [10]

$$V_{PI} = \sqrt{\frac{8 k_{eq} d^3}{27 \varepsilon_0 L_{PM} w_{PM}}} \,, \tag{5.11}$$

where ε_0 is the free space permittivity. The pull-in voltage value is calculated from (5.11) to be ~130 mV. Accordingly, careful attention needs to be given to this issue during the sensing circuit design, in order to avoid electrostatic pull-in and collapsing of the structure, as will be discussed in section 5.6. Notably, this calculated pull-in value is expected to be below the actual value, because of the bowing observed in Figure 5.1.

5.4. Simulation Results

A finite-element simulation illustrating the displacement of the structure as a result of a force along the *z*-axis is shown in Figure 5.5.

Figure 5.6 (a) shows simulation results for the displacement Δd relative to F_z, the external force applied along the *z*-axis. In order to calculate ΔC_{actual}, the resulting change in capacitance for the device, a parallel plate capacitor approximation is used, fringing fields and other non-ideal effects such as surface roughness and non-uniform bending of the top plate are neglected:

$$\Delta C_{actual} = C_{new} - C_{nominal} = \frac{\varepsilon_0 A}{d - \Delta d} - \frac{\varepsilon_0 A}{d}, \tag{5.12}$$

where A is the area of the capacitor plate and d is the nominal gap size, defined by the thickness of the sacrificial polyimide.

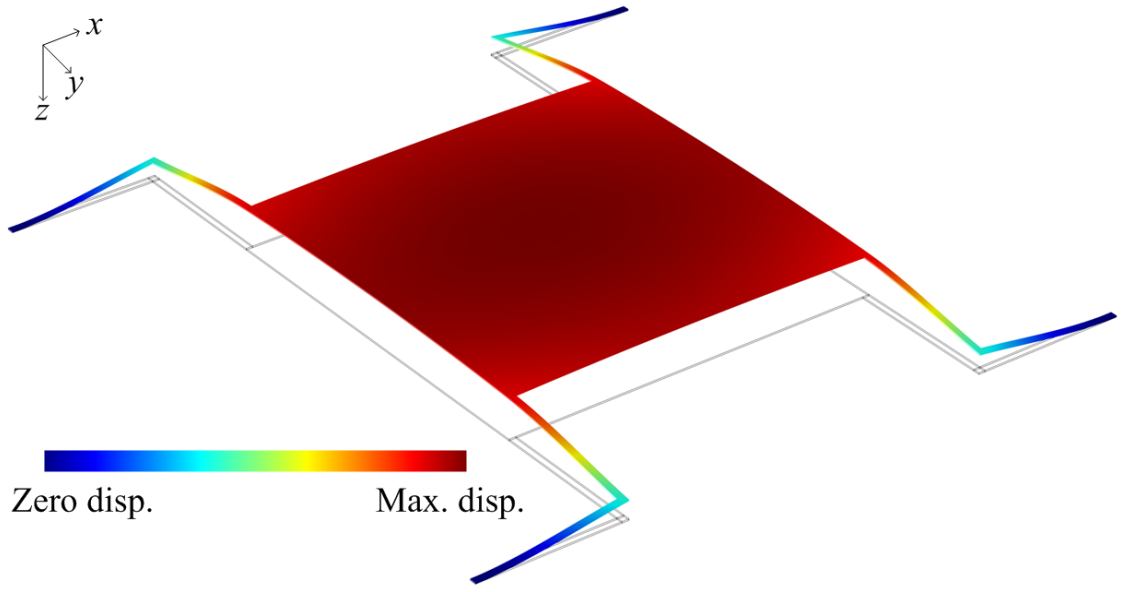

Figure 5.5: FEM simulation showing the structure displacement as a result of a force along the *z*-axis.

From Taylor series expansion, a linear approximation for the change in capacitance can be made for $\Delta d << d$ such that

$$\Delta C_{linear} = \frac{\varepsilon_0 A}{d}\left(\left(1-\frac{\Delta d}{d}\right)^{-1}-1\right) \approx \frac{\varepsilon_0 A}{d^2}\Delta d\,, \tag{5.13}$$

Figure 5.6 (a) shows the sensor response calculated using (5.12) as well as the linear approximation given in (5.13). Accordingly, the spring constant $k_{eq.}$ of the structure can be calculated to be of 1.07 N/m, which corresponds to a capacitance sensitivity of 8.24 μF/N. This translates to a magnetic field sensitivity of 8.24 nF/A/T for a structure length of 1 mm in which current flows to generate the Lorentz force, as deduced from (5.1), and an acceleration sensitivity of 121 fF/g, stemming from (5.5). The percentage error between the actual and linear capacitance changes is shown in Figure 5.6 (b), and is expressed as

$$\%Error = \left|\frac{\Delta C_{actual} - \Delta C_{linear}}{\Delta C_{linear}}\right| \times 100\,. \tag{5.14}$$

The actual change in capacitance coincides well with the linear approximation for small displacements, but starts to differ for larger motion. By limiting the worst-case linearity error to 10%, the dynamic range of the device is found to be ±50 nN. This value corresponds either to a detected magnetic field of ±50 mT with a driving current of 1 mA, or to a detected acceleration of ±3.4 g.

Furthermore, in order to determine the maximum shock the device can survive before collapsing, a step input acceleration is considered. The damping ratio (ζ) is calculated to be ~0.0167 from the measured value of the quality factor (Q), given in section 5.6. Therefore, as shown in [14], the system's step response experiences an overshoot percentage (M_p) of 95%, according to

$$M_p = 100.e^{-\pi\zeta/\sqrt{1-\zeta^2}}\,. \tag{5.15}$$

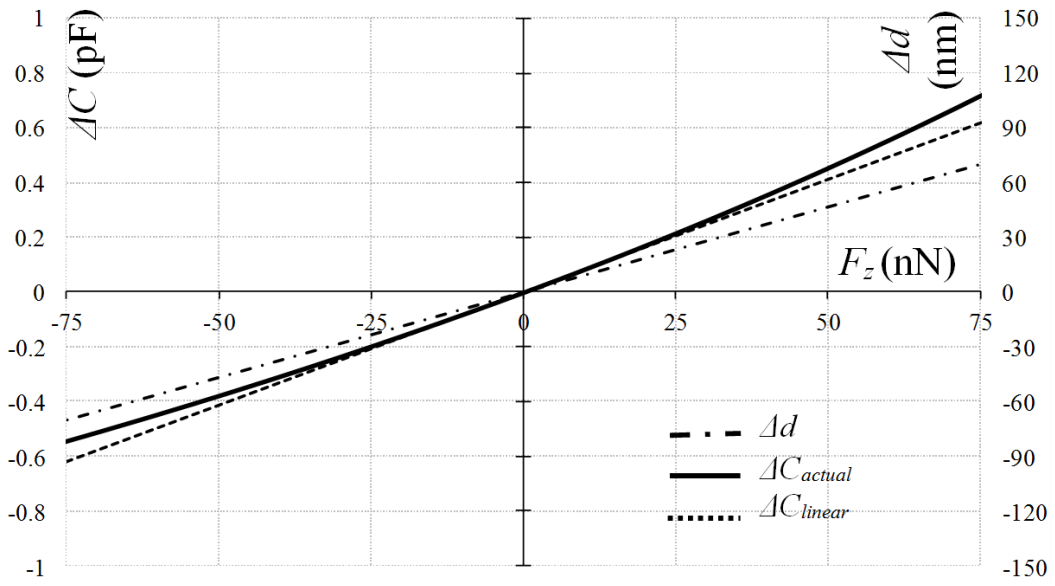

(a)

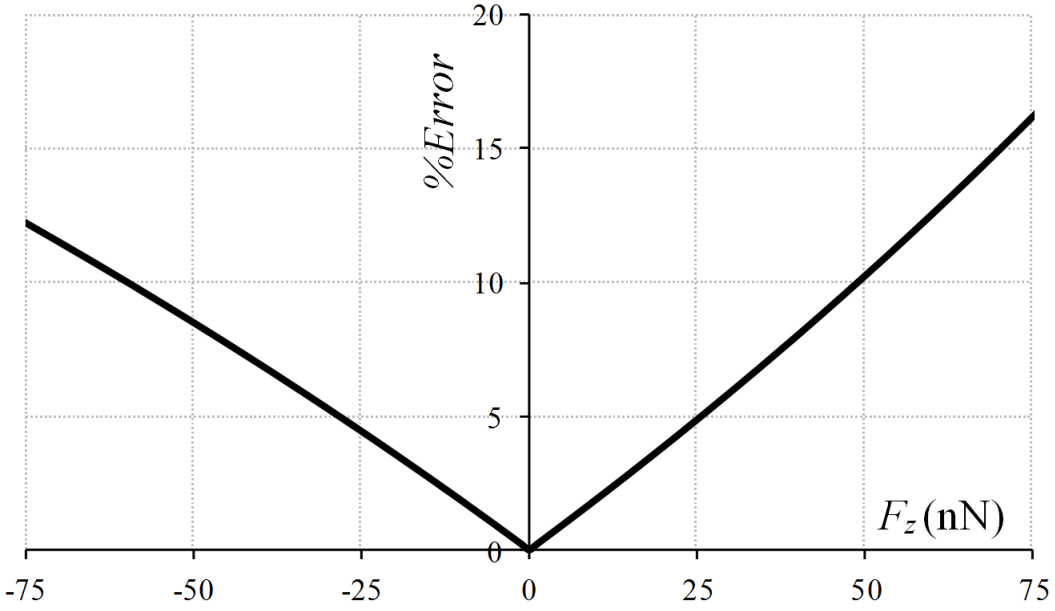

(b)

Figure 5.6: (a) Change in capacitance (linear approximation, actual) and displacement vs. external force applied, and (b) percentage error of capacitance linear approximation.

By limiting the maximum displacement overshoot to 239 nm ($z_{max.}$ before Casimir pull-in, calculated in section 5.3), determining the displacement step input yielded by the overshoot percentage, and calculating the required acceleration to generate this step, the maximum shock the device can survive is calculated to be ±9 g.

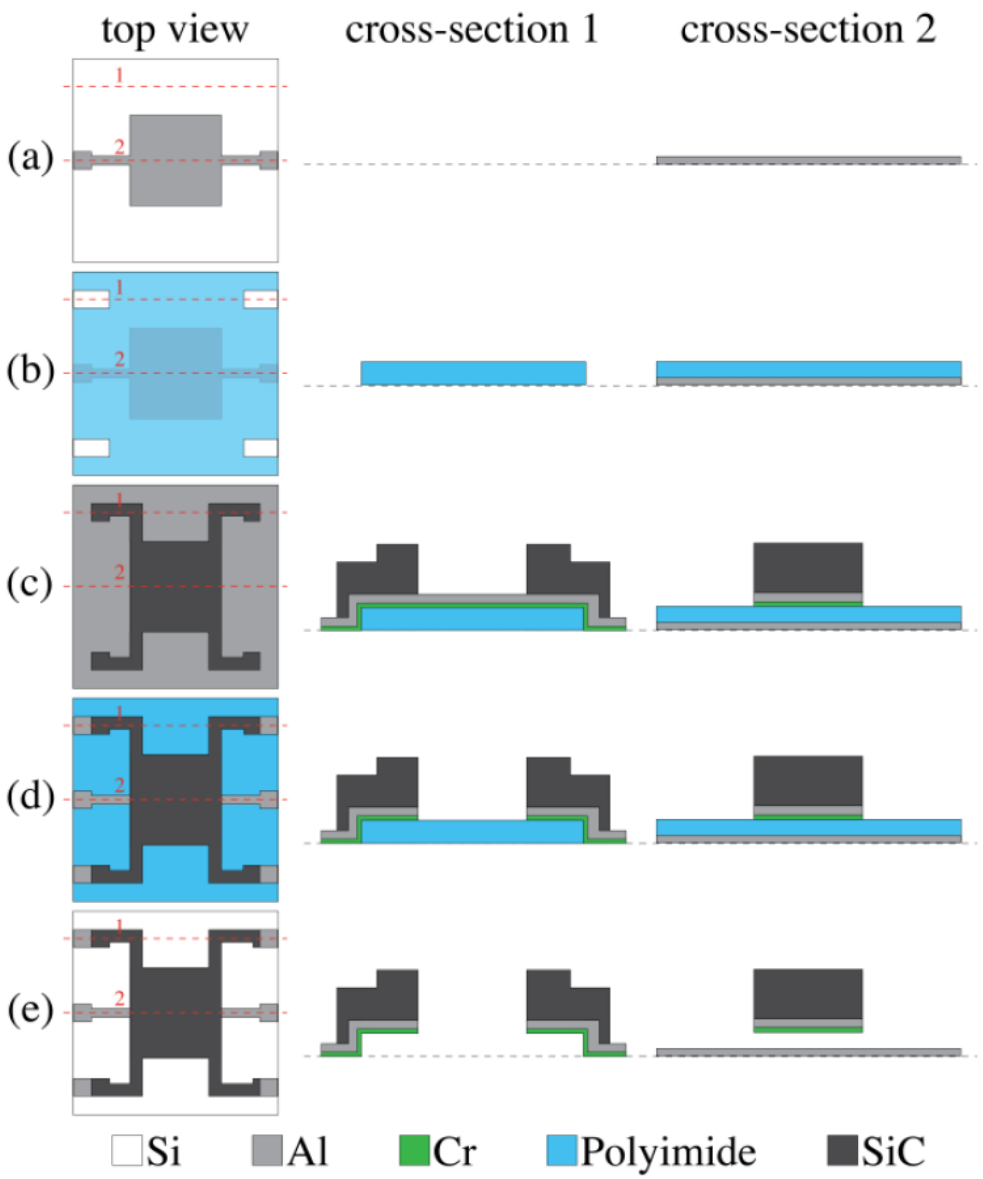

Figure 5.7: Simplified device fabrication process flow.

5.5. Fabrication Process

The fabrication process sequence is illustrated in Figure 5.7. A silicon substrate covered with a layer of thermal oxide is used for this prototype. The process is designed to be fully compatible with monolithic integration on standard CMOS substrates.

First, a 200 nm layer of aluminum is deposited onto the substrate by DC sputtering. The aluminum is then patterned and wet etched using phosphoric-acetic-nitric acid (PAN)

etchant to form the bottom electrode and the pads, as shown in Figure 5.7 (a). A 0.5 μm sacrificial polyimide layer is then spin coated. Then, the polymer is oven cured at 200°C to form the vertical gaps for the sense capacitor. An oxygen reactive ion etch patterns the polyimide to allow for the eventual anchoring of the structural supports to the substrate, as shown in Figure 5.7 (b). Afterwards, the structural stack is deposited, including the following layers, ordered from top to bottom: *i*) a 2 μm amorphous SiC layer, which is the main structural layer; *ii*) a 200 nm aluminum (Al) layer to form the low resistance path for the current, reducing the electrical noise; and *iii*) a 20 nm layer of chromium acting as an etch stop layer during the second aluminum etch.

The stack is covered by a 600 nm chromium (Cr) layer to act as a hard mask while etching the SiC layer. The deposition of the four layers is performed using DC sputtering, after which the chromium hard mask is patterned and wet etched. The SiC is then dry etched using nitrogen trifluoride (NF_3) reactive ion etching, stopping onto the underlying aluminum layer. Subsequently, the chromium hard mask is wet stripped as shown in Figure 5.7 (c), and the underlying aluminum and chromium layers are patterned using wet etching, as shown in Figure 5.7 (d). During this step, the chromium layer acts as an etch stop, protecting the exposed regions of the first aluminum layer from the etch of the second aluminum layer. Finally, the process is completed by dry release of the sacrificial polyimide using oxygen plasma, as shown in Figure 5.7 (e). A dry release mitigates the risk of stiction, compared to the more common wet release methods. Release holes with 10 μm diameter and 40 μm spacing are incorporated within the suspended structure to facilitate the release process.

5.6. Measurement Results

5.6.1. Resonance Characteristics

The resonance characteristics of the fabricated devices are measured under vacuum using the test setup shown in Figure 5.8. Bias tees are used to decouple the high frequency measurement signals from the DC signals, and apply the DC voltages to the device, which are necessary for electrostatic actuation. Measurement results for devices with 200 μm support beam length are shown in Figure 5.9. They exhibit a resonance frequency (f_r) of

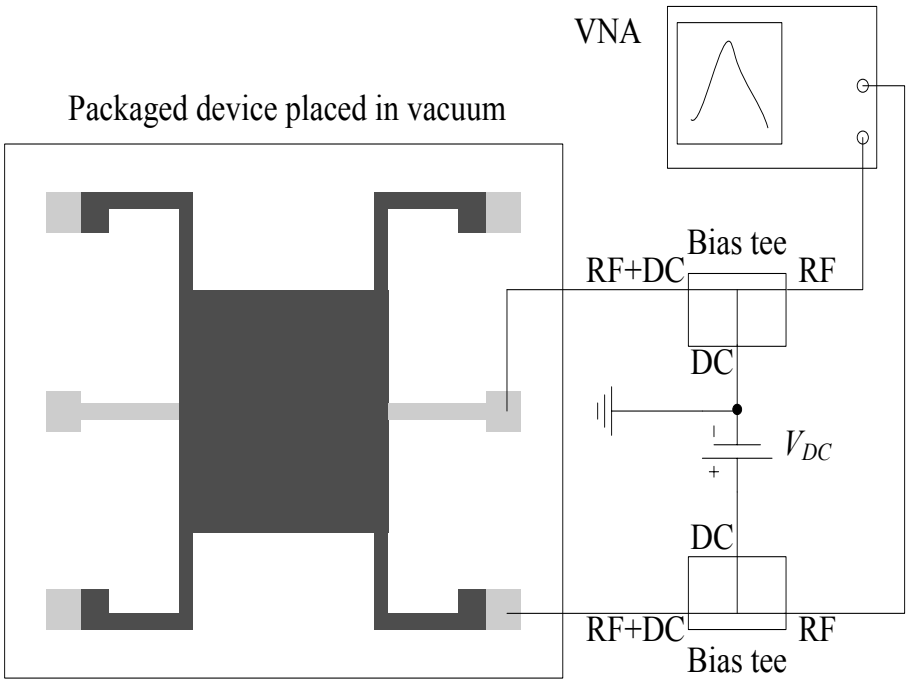

Figure 5.8: Simplified schematic of the test setup used for resonance characterization.

6.53 kHz and a quality factor (Q) of 30 under 10 mTorr vacuum level and using a 4 V DC polarization voltage. This Q value is calculated based on the 3-dB bandwidth inferred in Figure 5.9.

Note that the actual measured peak is slightly lower than 3-dB. However, this method is used to ascertain a worst case value. Alternatively, considering the resonance curve as symmetric and calculating the bandwidth using the right side of the curve only, a Q of 125 is obtained. Finite-element Eigen frequency simulation indicates a resonance frequency of 4.03 kHz. The difference between the simulated and measured values can most likely be attributed to the residual stress also at play in the bowing of the structure.

5.6.2. Magnetic Field Response

The magnetic field response of the fabricated devices was characterized using a variable electromagnet and discrete electronics. The schematic of the test setup used is shown in Figure 5.10, where DC current is generated by a variable current source and flows through the top structure of the device from pad T_1 to pad T_2. This current serves to generate a Lorentz force when the device is subjected to an in-plane magnetic field normal to the current. The resulting capacitance change between the top (T) and bottom (B) electrodes

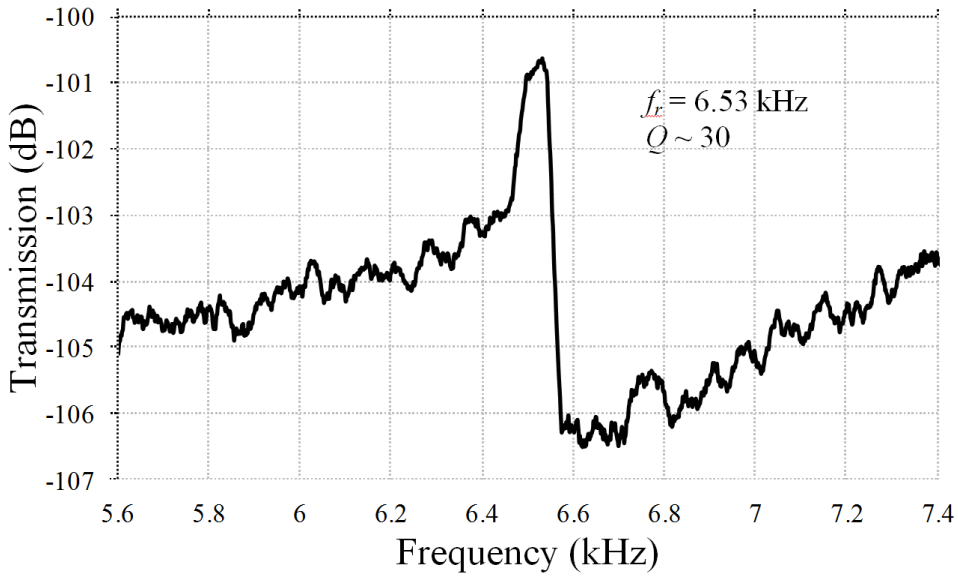

Figure 5.9: Measured resonance characteristics of fabricated devices (10 mTorr vacuum).

of the device is monitored and used to acquire the magnetic field. The ZMDI ZSSZ3123 capacitance to digital converter chip [15] is configured to measure the capacitance of the device relative to an internal reference capacitor. This chip outputs a 1 MHz 1.8 V square wave excitation signal for the capacitance measurement. As the bowing that the fabricated structure exhibited has widened the gap to ~5 μm, the corresponding electrostatic pull-in voltage has increased to 4.23 V. Accordingly, electrostatic pull-in will not occur during sensing. Coupling capacitors (C_c) of 22 μF are used to couple the AC signal between the device and the capacitance readout chip, as well as prevent any DC current leakage from the current source circuit to the chip. A large resistor of 10 MΩ is connected between the top and bottom electrodes of the device to make sure that they stay at the same DC potential in order to avoid any electrostatic force between them. The capacitance readout chip communicates the digital words for the measured capacitance through an I^2C interface to the USB interface circuit using the two pull-up resistors R_{PU} (2.2 kΩ). A Microchip PIC18LF2550 microcontroller [16] serves to accept the digital data from the capacitance readout circuit through the I^2C interface and then transmits it to the host PC via USB. The microcontroller is also used for configuration of the capacitance readout chip.

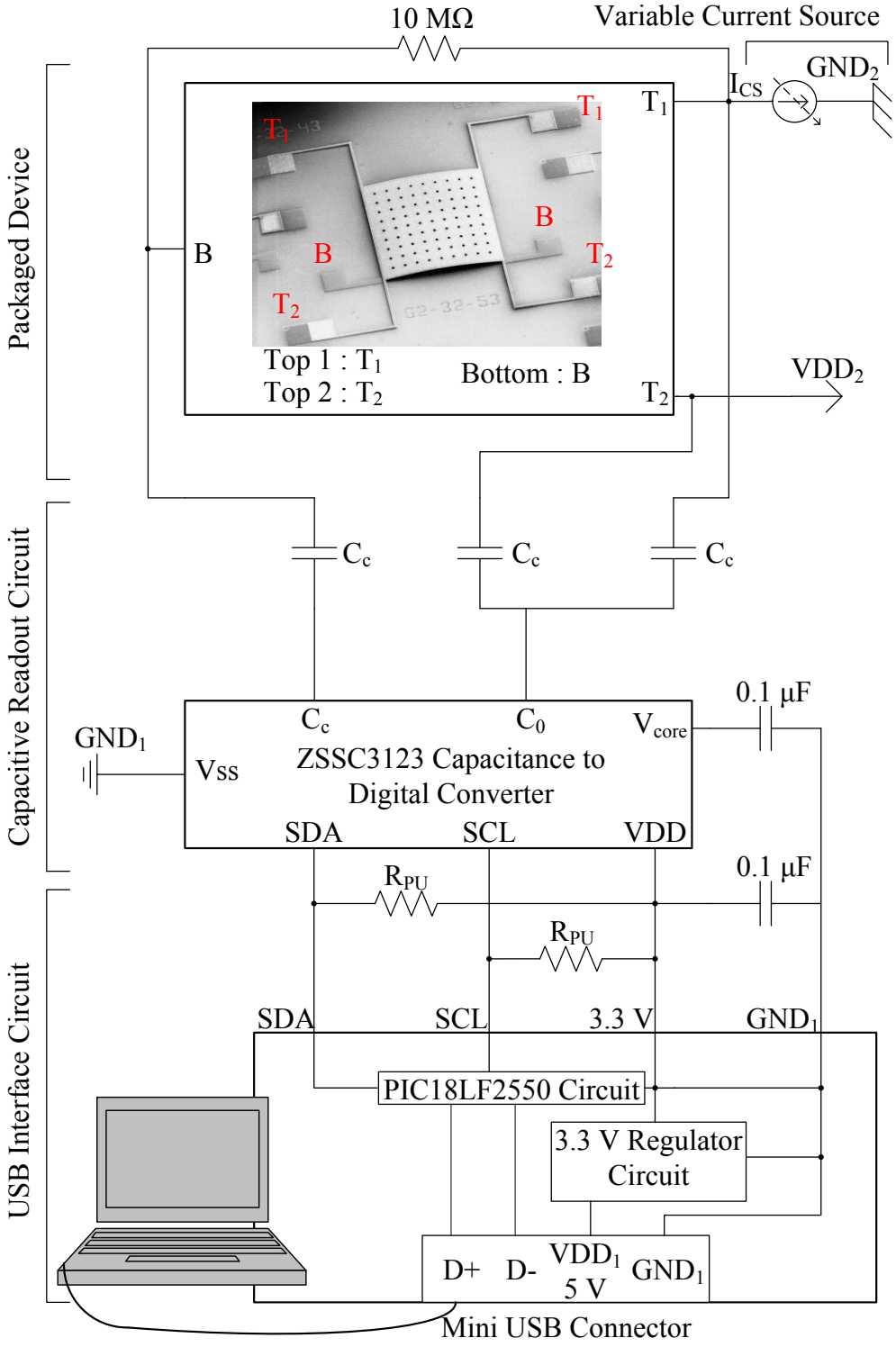

Figure 5.10: Schematic of the test setup used for the magnetic characterization of the device.

The schematic of the current source circuit is shown in Figure 5.11, utilizing the Analog Devices MAT14 matched monolithic quad transistor chip [17]. One transistor is connected in a diode configuration with two resistors (R_{limit} and R_{tune}) at the collector, generating the reference current. R_{limit} serves as a current-limiting resistor to protect the chip by ensuring that the current does not exceed the maximum current rating for the minimum value of the tuning resistor R_{tune}. R_{limit} is set to 200 Ω, limiting the current to a maximum of 14.5 mA, well below the rated maximum. A 2 MΩ trimmer variable resistor is used for R_{tune}, due to its large number of turns, enabling fine current tuning, with a range from 1.4 μA to 14.5 mA. The remaining three transistors in the chip are connected in a basic current mirror configuration. A DIP switch is used to select the number of transistors driving the output current, thus tripling the tuning range.

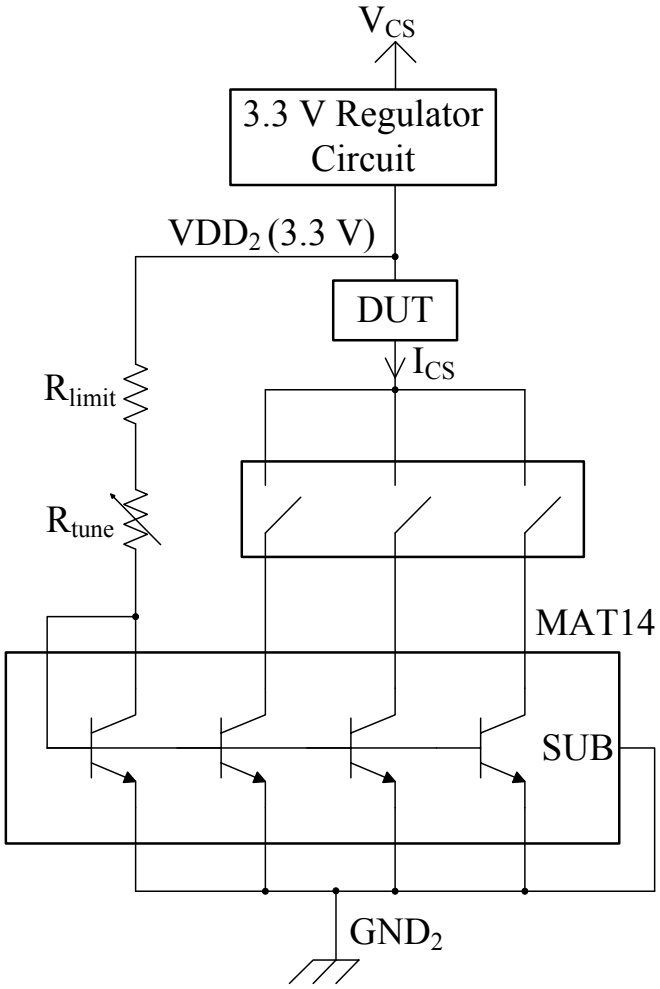

Figure 5.11: Schematic of the variable current source circuit.

The capacitive readout and interface circuits are powered through the 5 V USB supply from the host PC, while the current source circuit is powered through a distinct 4.5 V battery pack feeding a 3.3 V regulator. The grounds are also kept separate as illustrated on the schematics in order to avoid any crosstalk or feedthrough between the different sections of the circuit.

A photograph of the printed circuit boards used in the testing is shown in Figure 5.12, illustrating the different functional sections. The measured magnetic field response of the device is presented in Figure 5.13. The sensor exhibits a magnetic field sensitivity of 1.57 pF/T under static operation at a 10 mA current. The measured response shows a non-linearity of less than 6 % for the whole ±3 mT measurement range, where the non-linear error is calculated using

$$\%Error_{meas.} = \left| \frac{measured\ result - linear\ \ fit}{linear\ \ fit} \right| \times 100\,. \qquad (5.16)$$

The measured non-linear error is a bit higher than the simulation results due to the non-linearity of the readout circuitry.

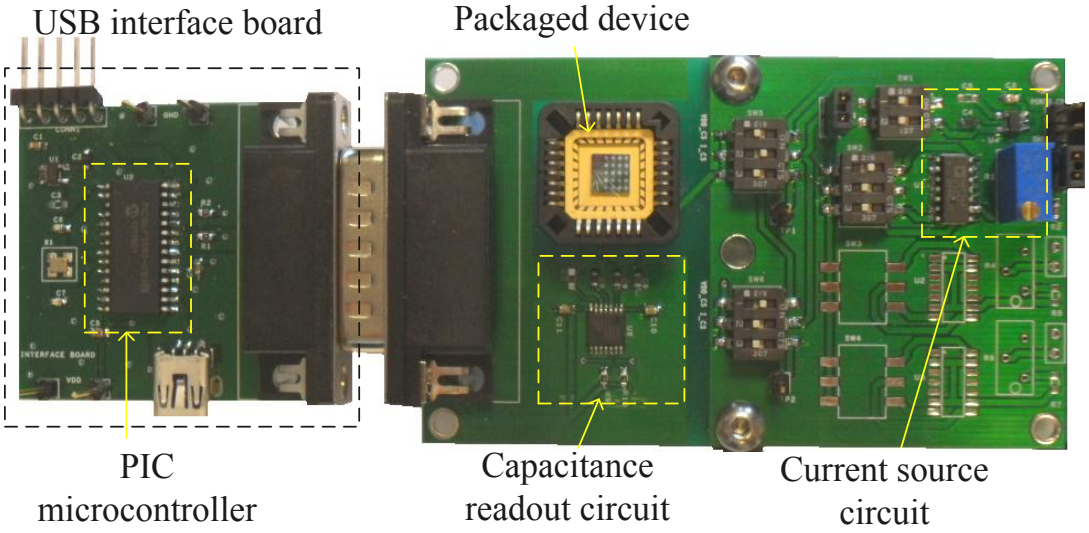

Figure 5.12: Photograph of the printed circuit boards used in the testing.

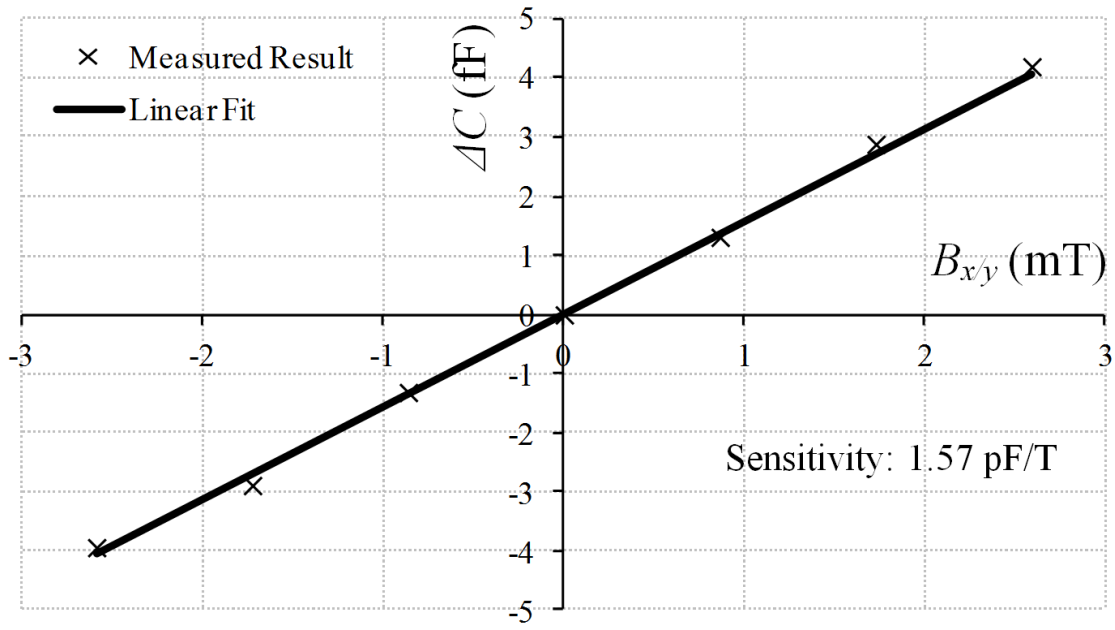

Figure 5.13: Measured device response to magnetic field ($B_{x/y}$), shown along with a linear fit.

The current test setup is limited to one axis being tested at a time. As such, different axis measurements can currently be achieved only by interfacing the test setup manually to the different pads of the device. The test setup could be augmented with an automated switching mechanism to allow for sequential testing of both axes without intervention.

5.6.3. Acceleration Response

The inertial response of the fabricated devices is characterized by the same test circuitry used for magnetic field response, but with the current source circuit switched off. A picture of the test setup used is shown in Figure 5.14.

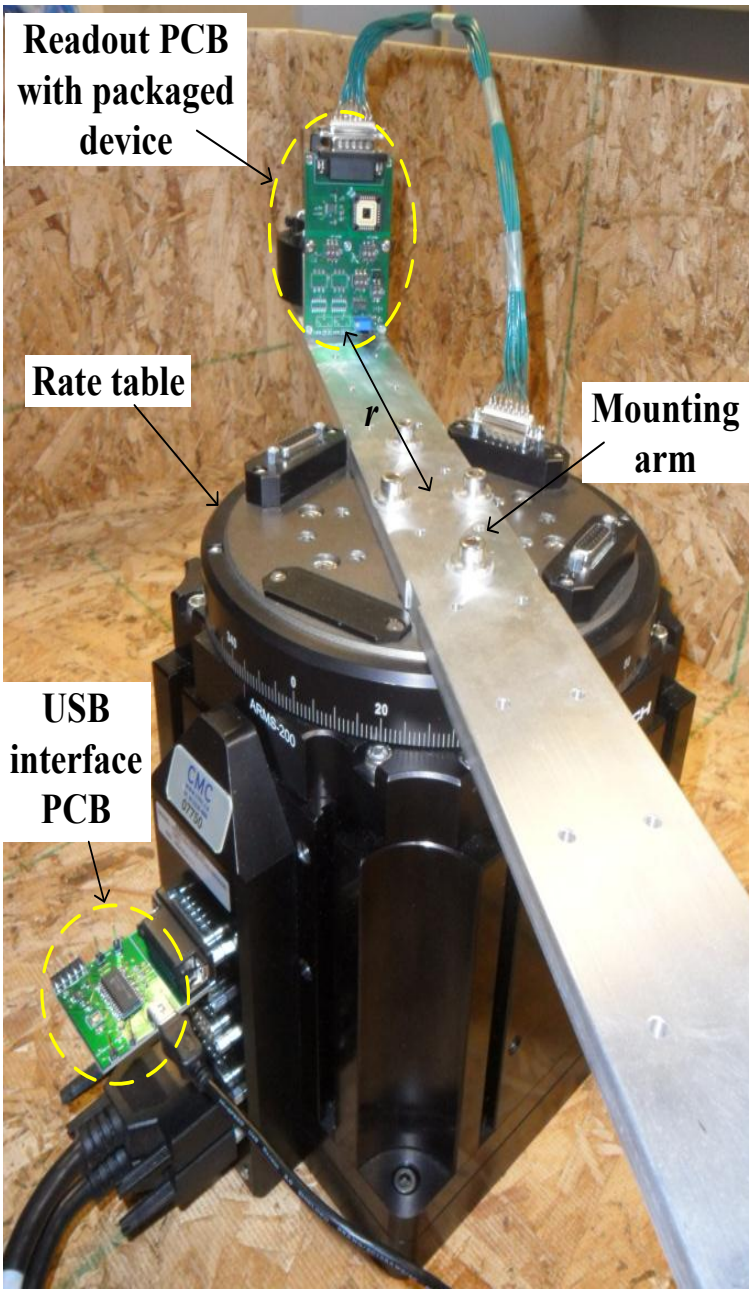

Figure 5.14: Picture of the test setup used for acceleration response characterization.

An Aerotech ARMS-200 rate table [18] is used for the test, where the packaged device is placed, along with the capacitive readout circuit, vertically using a right angle mount on the mounting arm at a distance r from the rate table center. The centrifugal acceleration generated by rate table rotation is utilized to measure the response of the device. The rate table angular speed, ω, is varied to generate the different acceleration steps for the test using (5.17) [19]. The centrifugal acceleration, A_c, is given by

$$A_c = mr\omega^2, \tag{5.17}$$

where m is the proof mass. The digital capacitance data is then transmitted to the interface microcontroller circuit through the I^2C interface via a 15 pin D-SUB cable and the rate table slip rings, which maintain the electrical connectivity throughout rotation.

The measured acceleration response of the device is shown in Figure 5.15. The sensor exhibits an acceleration sensitivity of 1.02 fF/g for static operation, with a non-linear error less than 10% in the range of ±2g.

5.7. Discussion

Table 5.2 compares the proposed device to state-of-the-art. The different units used to report the sensitivities are a result of the different readout schemes utilized. Piezoresistive readout is used in [1, 2], while insufficient information is provided in [4, 5] to extract the capacitance change.

In this work, the measurement results for sensitivity are lower than the simulated results mainly due to the bowing of the structure, as clear from the SEM micrograph in Figure 5.1. This bowing causes an increase of the effective gap between the electrodes of

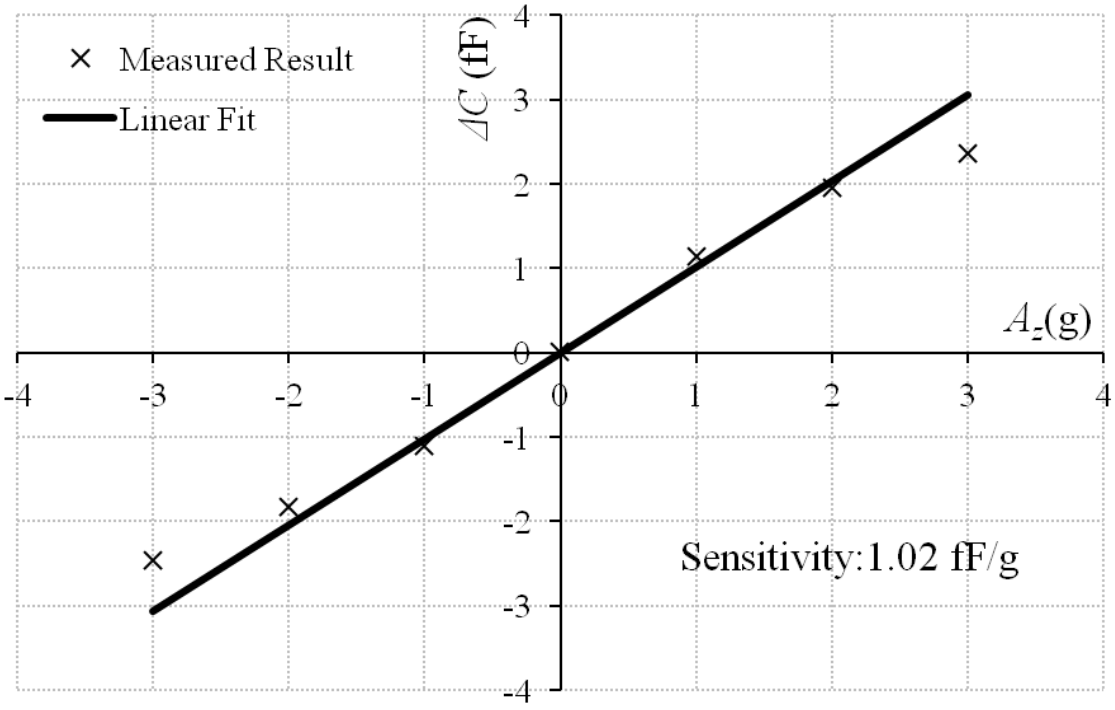

Figure 5.15: Measured device response to out-of-plane acceleration (A_z), shown along with a linear fit.

the capacitor by a factor of ~10 and consequently reduces the capacitance variation and sensitivity by a factor of ~100. The bowing could be reduced by optimizing the device and suspension dimensions, and further tuning the stress profile of the material stack. Another cause for the sensitivity reduction lies in interconnect parasitics between the device and the readout circuitry, as discrete components were used for measurements. Fabricating the sensor directly above a full-fledged CMOS ASIC, as made possible by the fabrication process, is expected to allow for significant sensitivity improvements. Alternatively, wire bonding the device and the interface circuit within the same package could be used to reduce noise and parasitics (e.g., as demonstrated in [20] for a capacitive accelerometer). The metallic track below the structure leads to a low resistive path for the current (~20 Ω), which results in power dissipation and electrical noise reduction. Measurements were performed at a 10 mA current, which corresponds to 2 mW power dissipation. These values can be lowered, while maintaining good sensitivity, by reducing the bowing, and parasitics, as discussed earlier. They can also be significantly improved by using resonant operation. Based on the static operation measurements and a resonant mode with Q-factor of 30 (measured), the current required to keep the same sensitivity level will be reduced to ~330 μA, and the power consumption of the device is expected to be ~1 μW.

Table 5.2: Comparison between the combined magnetometer/ accelerometer proposed in this work and the state-of-the-art

	Axis	Sensitivity	Linearity		Resistance (Ω)	Current (µA)	Power (µW)	Area (mm^2)	Features
			Dymanic range	Non-linearity					
[1]	*z* *x/y*	164 mV/T 1.82 V/T	N/A	N/A	N/A	N/A	10	N/A	- Uses permanent magnets
[2]		0.15 V/T	N/A	N/A	N/A	10,000-50,000	N/A	N/A	- Utilizes Nickel - High temperature steps (e.g. 800 ˚C)
[4]	*z* *x/y*	12.98 V/T 0.78 V/T	Results up to 0.44 mT	1 %	5900	400 200	460 120	0.2 × 1 MEMS	- Chip level vacuum seal (~1 mBar) - SOI technology
[5]	*x* *y* *z*	0.13 V/T 0.14 V/T 1.51 V/T	Results up to 1.2 mT	2.27 % 3.27 % 2.24 %	N/A	~4000	N/A	1.8 × 1.5 MEMS + IC	- TSMC 0.35 µm technology - 3D measurement achieved using two perpendicular structures
This work	$B_{x/y}$	Simulation	Simulation		20 (metallic path)	Static operation		1 × 1 MEMS	- Low temperature surface micromachining - Above-IC compatible - Atmospheric pressure operation with vacuum operation capability - Can measure out-of-plane acceleration
		82 pF/T	±50 mT ±5 mT	10 % 1 %		10,000	2,000		
		Measurement	Measurement			Resonant operation			
		1.57 pF/T	±3 mT	6 %		330*	1*		
	A_z	Simulation	Simulation			0**	0**		
		121 fF/g	±3.4 g	10 %					
		Measurement	Measurement						
		1.02 fF/g	±2g	10 %					

*Values estimated based on static operation measurements, while maintaining the same sensitivity.

**No average current or power is consumed by the device for accelerometer operation, due to the capacitive detection scheme utilized.

5.8. Conclusion

This work introduced a combined magnetometer / accelerometer design based on the Lorentz force, where an electrical current is switched between two orthogonal directions on the device structure to achieve a 2D in-plane magnetic field measurement. The device can concurrently serve as a 1D accelerometer for out-of-plane acceleration, when the current is switched off. The design is therefore capable of separating the magnetic and inertial force measurements, achieving higher accuracy with a single compact device. The proposed sensor supports static operation at atmospheric pressure, precluding the need for costly vacuum packaging. It can alternatively operate at resonance under vacuum for enhanced sensitivity. The device is fabricated using a low temperature SiC surface micromachining technology, which is fully adapted for above-IC integration on standard CMOS substrates. Measurement results from the fabricated device, using a discrete electronics interface, show a magnetic field sensitivity of 1.57 pF/T and an acceleration sensitivity of 1.02 fF/g for static operation. The device could be further enhanced by adding lateral electrodes around the proof mass to allow for more axes of operation.

5.9. References

[1] D. Ettelt, G. Dodane, M. Audoin, A. Walther, G. Jourdan, P. Rey, P. Robert, and J. Delamare, "A Novel Microfabricated High Precision Vector Magnetometer," *Proceedings of the IEEE Conference on Sensors*, pp. 2010-2013, October 2011.

[2] M. El Ghorba, N. André, S. Sobieski, and J. -P. Raskin, "CMOS Compatible Out-of-Plane and In-Plane Magnetometers," *Proceedings of the IEEE Conference on Solid-State Sensors, Actuators and Microsystems*, pp. 2373-2376, June 2007.

[3] M. Thompson, M. Li, and D. Horsley, "Low Power 3-Axis Lorentz Force Navigation Magnetometer," *Proceedings of the IEEE Conference on Microelectromechanical Systems*, pp. 593-596, January 2011.

[4] M. Li, V. Rouf, M. Thompson, and D. Horsley, "Three-Axis Lorentz Force Magnetic Sensor for Electronic Compass Applications," *Journal of Microelectromechanical Systems*, vol. 21, no. 4, pp. 1002-1010, August 2012.

[5] C. -I. Chang, M. -H. Tsai, Y. -C. Liu, C. -M. Sun, and W. Fang, "Development of Multi-Axis CMOS-MEMS Resonant Magnetic Sensor Using Lorentz and Electromagnetic Forces," *Proceedings of the IEEE Conference on Microelectromechanical Systems*, pp. 193-196, January 2013.

[6] F. Nabki, T. Dusatko, S. Vengallatore, and M. El-Gamal, "Low-Temperature (<300ºC) Low-Stress Silicon Carbide Surface Micromachining Fabrication Technology," *Technical Digest of the Hilton Head Solid-State Sensors, Actuators and Microsystems Workshop*, pp. 216 - 219, June 2008.

[7] F. Nabki, T. Dusatko, S. Vengallatore, and M. El-Gamal, "Low Stress CMOS-Compatible Silicon Carbide Surface-Micromachining Technology - Part I: Process Development and Characterization," *Journal of Microelectromechanical Systems*, vol. 20, no. 3, pp. 720-729, June 2011.

[8] F. Nabki, P. Cicek, T. Dusatko, and M. El-Gamal, "Low Stress CMOS-Compatible Silicon Carbide Surface-Micromachining Technology - Part II: Beam Resonators for MEMS above IC," *Journal of Microelectromechanical Systems*, vol. 20, no. 3, pp. 730-744, June 2011.

[9] M. Y. Elsayed, P. -V. Cicek, F. Nabki, and M. N. El-Gamal, "Surface Micromachined Combined Magnetometer/ Accelerometer for Above-IC Integration," *Journal of Microelectromechanical Systems*, December 2014.

[10] S. D. Senturia, "*Microsystem Design*," Springer, 2001.

[11] M. El-Gamal, P. -V. Cicek, and F. Nabki, "Low Temperature Ceramic Microelectromechanical Structures," WO Patent 2010003228, 2010.

[12] W.-H. Lin and Y.-P. Zhao, "Casimir Effect on the Pull-in Parameters of Nanometer Switches," *Microsystem Technologies*, vol. 11, no. 2-3, pp. 80-85, February 2005.

[13] I. Dzyaloshinskii, E. Lifshitz, and L. Pitaevskii, "General Theory of Van Der Waals' Forces," *Soviet Physics Uspekhi*, vol. 4, no. 2, 1961.

[14] K. Ogata, "*Modern Control Engineering*," 5th edition, Prentice Hall, 2010.

[15] "*ZSSC3123 cLiteTM Capacitive Sensor Signal Conditioner Datasheet*," rev. 1.61, Zentrum Mikroelektronik Dresden AG (ZMDI), available at: http:// www.zmdi.com, 2013.

[16] "*PIC18F2455/2550/4455/4550 Datasheet*," Microchip Technology Inc., available at: http:// www.microchip.com, 2009.

[17] "*MAT14 Matched Monolithic Quad Transistors Datasheet*," Analog Devices Inc., http:// www.analog.com, 2010.

[18] "*ARMS Series Stage User Manual*," rev. 1.01.00, Aerotech Inc., http:// www.aerotech.com, 2011.

[19] J. R. Taylor, "*Classical Mechanics*," University Science Books, 2005.

[20] A. Alfaifi, K. Allidina, F. Nabki, and M. El-Gamal, "A Low Cross-Sensitivity Dual-Axis Silicon-On-Insulator Accelerometer Integrated as a System In Package with Digital Output," *Analog Integrated Circuits and Signal Processing*, vol. 77, no. 3, pp. 345-354, October 2013.

Part III: MEMS Resonators

Chapter 6 Overview about MEMS Resonators

6.1. Historical Background

Timekeeping in general has been very important to humans since the very early ages. This importance is probably due to our curiosity to visualize and interpret the surrounding world and its different phenomena. Its importance further increased as an important part of humans' living when the need for cooperation between members of their expanding groups increased. In fact, there are existing devices which are believed to be made by the Ancient Egyptians six thousand years ago for the purpose of telling time from the stars [1]. The evolution of timekeeping devices may be divided into three main epochs, depending on the method used for timekeeping. These epochs are: continuous flow epoch, aperiodic control epoch, and resonance control epoch [1]. Figure 6.1 illustrates this evolution, indicating the three main epochs of development, and the accuracy of the main measurement methods used.

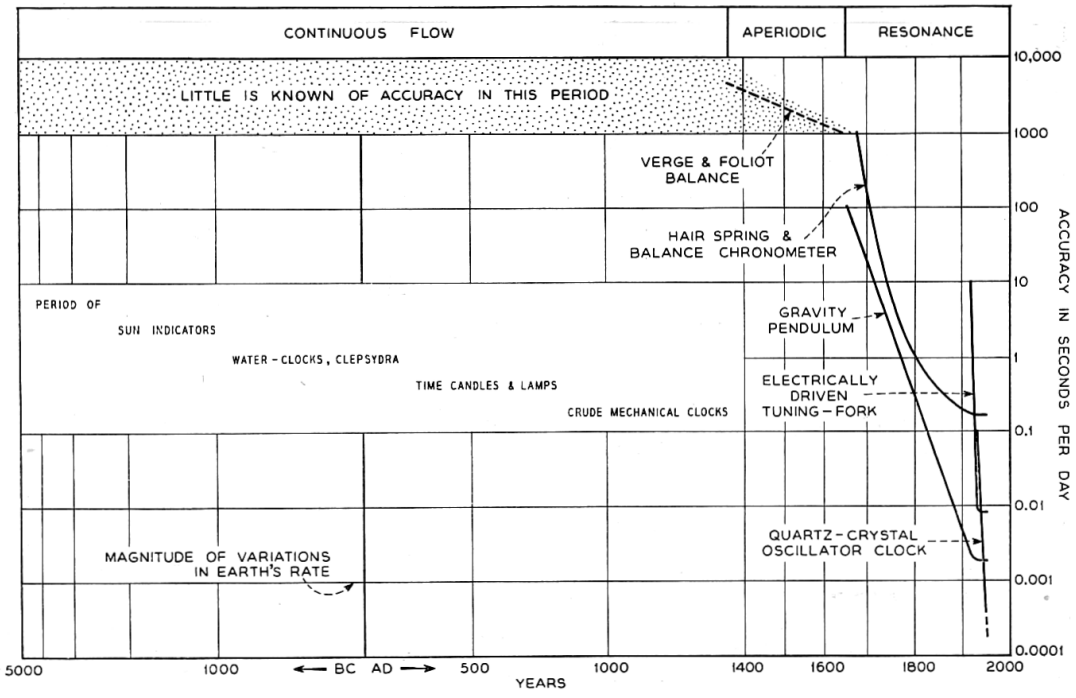

Figure 6.1: Accuracy of timekeeping through history [1].

The continuous flow epoch extended till about 1000 A.D. The time measurements then relied on the time required for filling or emptying certain containers with water or sand for example. Many devices operating on this principle were constructed and used. Some of the earliest are as old as 3500 years, made by the Babylonians and the Egyptians [1]. The hour glass is a well-known example of the timekeeping devices from this epoch.

The aperiodic epoch extends from about 1000 to about 1675. One of the most important findings of this time is the invention of an escapement mechanism in about year 1360. It is based on controlling an alternating motion from a steady motive power, such as a suspended weight or a balance spring. This invention is known to be the first really important step in the history of precision clock development, and marks the beginning of the second major epoch in timekeeping evolution [1]. The escapement in one form or another is still used in clocks and watches till now. A clock constructed based on this mechanism by Henry De Vick about 1360 is still in use till now in the Palais de Justice in Paris. Figure 6.2 illustrates some of the early escapement mechanisms. Then, the rest of this epoch was mainly modifications of the De Vick clock in various sizes and forms.

The third major epoch is the resonance control epoch extending from about 1675 till now. This epoch has seen the use of resonance in its numerous forms for timing control.

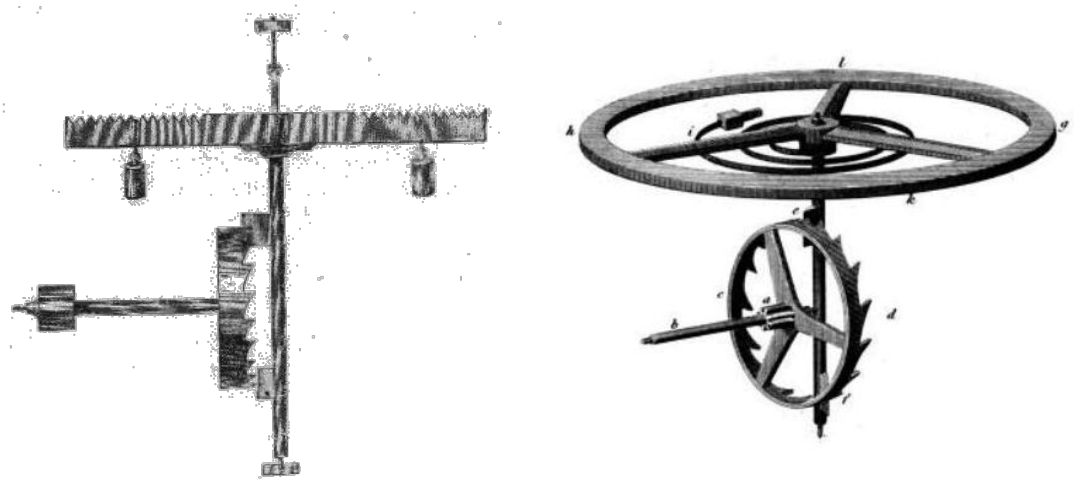

(a) (b)

Figure 6.2: (a) Escapement mechanism used De Vick clock [2], and (b) 3D view of an early escapement mechanism [3].

A resonator is basically a device which exhibits oscillatory behavior at certain frequencies called natural or resonant frequencies. At these frequencies the device exhibits higher vibration amplitude than other frequencies. This resonant behavior can occur in any form of energy, for example: mechanical, electrical, acoustic, electromagnetic, etc. This behavior has been known for a very long time. One of its simplest forms is the oscillation exhibited by strings of musical instruments, such as guitars violins, and pianos, where the vibration is in the audible range and the resonance frequency is varied based on the tension in the strings and their lengths. Pendulum and spring mass systems are also examples of early resonators.

One of the early resonators which is the basis of many forms of modern resonators is the tuning fork resonator. It is an acoustic resonator in the form of a two-pronged fork. It was invented in 1711 by British musician John Shore [4]. Conventional tuning forks are still used as references for tuning musical instruments. The tuning fork resonates at a specific constant frequency by striking it against another object, and emits a pure musical tone. The frequency that a particular tuning fork generates depends on the dimensions of the two prongs and the properties of the fork material as given by [5]

$$f_r = \frac{1.875^2}{2\pi l^2}\sqrt{\frac{EI}{\rho A}}, \tag{6.1}$$

where l is the prong length, A is the cross-sectional area of the prong, I is the moment of inertia of the prong, E is Young's modulus of the material, and ρ is the density of the material.

Based on the same resonance principle, crystal resonators were developed, which are the most common resonators used nowadays. They utilize mechanical resonance of piezoelectric materials to create electrical signals with very precise frequencies. Piezoelectric effect (discovered by Jacques and Pierre Curie in 1880 [6, 7]) is used as means of electromechanical transduction. The first crystal based oscillator, using a crystal of Rochelle salt, was built in 1917 by Alexander M. Nicholson at Bell Telephone Laboratories while the first quartz crystal oscillator was built in 1921 by Walter Guyton Cady [1, 8]. Crystal resonators are commonly used as timing references for numerous applications including watches, digital integrated circuits (as in computer processors), and RF transceivers (as in radios and cell phones). The most common material used in crystals is

quartz, but other piezoelectric materials including ceramics are used as well. Quartz crystals are manufactured for frequencies from a few tens of kHz to hundreds of MHz depending of the crystal cut, dimensions, and resonance mode.

6.2. Micromachined Resonators

In the past few decades, another type of resonators started emerging which is micromachined resonators. They are receiving continuously increasing attention due to their small sizes compared to conventional crystal resonators as well as their potential for integration with other MEMS sensors and circuits on the same chip, which can be especially advantageous for handheld electronic applications (e.g., smart phones and tablets), where weight, size, and cost are particularly critical parameters.

Micromachined resonators can be operated through two main widespread actuation mechanisms: piezoelectric or electrostatic, each method having its specific advantages and drawbacks as explained below in more details.

6.2.1. Piezoelectric Resonators

This type of resonators utilizes the piezoelectric effect (discovered by Jacques and Pierre Curie in 1880 [6, 7]) for electromechanical transduction (i.e., as a relation between the electrical and mechanical domains). This effect can be explained briefly as follows. For certain materials with the proper atomic structure and crystal orientation, electric charge accumulates in response to applied mechanical stress, as well as the reverse effect. This relationship can be quantified, with the electric field and stress expressed as independent variables, by [9]

$$D = \varepsilon E + d\sigma , \tag{6.2}$$

$$\xi = d^T E + S\sigma , \tag{6.3}$$

where D is the electric displacement vector, ε is the dielectric constant matrix, E is the electric field intensity vector, d is the piezoelectric coefficient matrix, σ is the stress tensor, ξ is the strain tensor, and S is the compliance matrix. Piezoelectric devices such as surface acoustic wave (SAW) and film bulk acoustic resonators (FBAR) are already widely used in timing applications [10]. Piezoelectric FBARs generally exhibit a very low signal loss,

resulting in low motional resistance, which is very advantageous as it simplifies the design constraints of the associated electronic circuitry.

6.2.2. Electrostatic Resonators

Electrostatic resonators, as the name implies, utilize electrostatic force as a method for actuation and sensing. The electrostatic force (F_{elec}) between electrodes of a capacitor of any geometry can generally be expressed as the gradient of the electrical co-energy (W^*) stored in the capacitor [9, 11]

$$F_{elec}(r,t) = \nabla W^*(r,t). \tag{6.4}$$

The electrical co-energy can be expressed as

$$W^*(r,t) = \frac{C_a(r)V_a{}^2(r,t)}{2}, \tag{6.5}$$

where V_a is the applied voltage across the electrodes and C_a is the actuation capacitance.

Therefore, since the voltage is independent of the position, the electrostatic force can be expressed as

$$F_{elec}(r,t) = \frac{V_a{}^2(t)}{2}\nabla C_a(r), \tag{6.6}$$

The voltage is usually split to its DC and AC components as

$$V_a(t) = V_{DC} + V_{AC}(t), \tag{6.7}$$

and therefore the electrostatic force can be reformulated as

$$F_{elec}(r,t) = \frac{V_{DC}^2 + V_{AC}^2(t) + 2V_{DC}V_{AC}(t)}{2}\nabla C_a(r). \tag{6.8}$$

The DC voltage is usually much higher than the amplitude of the AC voltage. Therefore, the electrostatic force can be approximated as

$$F_{elec}(r,t) \approx \frac{V_{DC}^2 + 2V_{DC}V_{AC}(t)}{2}\nabla C_a(r). \tag{6.9}$$

The electrostatic force is used as the actuation mechanism by converting the applied electrical voltage to a mechanical displacement between the actuation electrodes according to (6.9). On the sense side, the displacement induced between the sense electrodes is converted back to electrical current, as given by

$$i_{out}(r,t) = \frac{dQ(r,t)}{dt} = \frac{d[C_s(r,t)V_s(r,t)]}{dt}, \tag{6.10}$$

where Q is the charge on the sense capacitor electrode, C_s is the capacitance between the sense electrodes, and V_s is the voltage applied between the sense electrodes.

Electrostatic actuators have two configurations which are variable gap and variable area configurations as shown in Figure 6.3. In order to explain them briefly, a parallel plate capacitor is considered. Its capacitance can be approximated, while neglecting the fringing capacitance, as

$$C = \frac{\varepsilon_0 A}{g} = \frac{\varepsilon_0 lw}{g}, \tag{6.11}$$

where ε_0 is the permittivity of free space, A is the plate area, l is the plate length, w is the plate width, and g is the gap between the plates.

If one of the electrodes is allowed only to move laterally, while maintaining the same gap, this will lead to changing the overlap area, and hence comes the name variable area configuration. Based on (6.6), the electrostatic force can then be expressed as

$$F_{elec}\big|_{var.area} = \frac{V_a^2}{2}\frac{dC}{dy} = \frac{V_a^2 \varepsilon_0 w}{2g}, \tag{6.12}$$

which is constant with respect to the plate displacement.

On the other hand, if one of the electrodes is allowed only to move vertically, while maintaining the same overlap area, this will lead to changing the gap size, and hence comes the name variable gap configuration. Based on (6.6), the electrostatic force can then be expressed as

$$F_{elec}\big|_{var.gap} = \frac{V_a^2}{2}\frac{dC}{dz} = -\frac{V_a^2 \varepsilon_0 wl}{2(g+z)^2}. \tag{6.13}$$

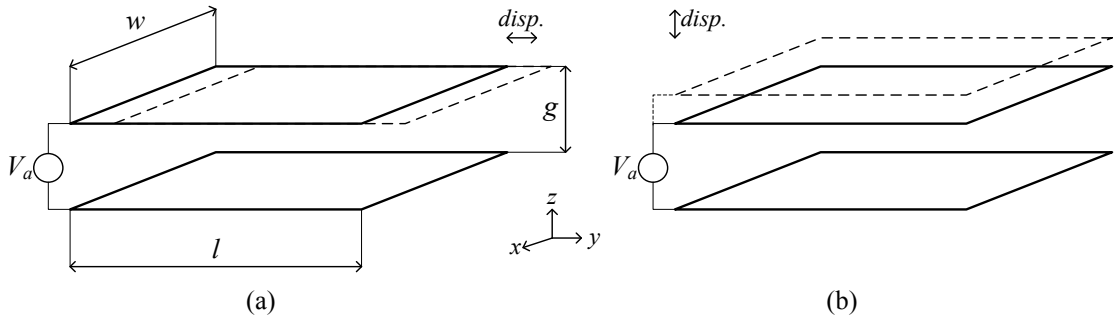

Figure 6.3: Simplified diagram of parallel plate capacitor with: (a) variable area configuration, and (b) variable gap configuration.

By comparing (6.12) and (6.13), it can be noted that the electrostatic force is constant with respect to the displacement for the variable area configuration while it is proportional to $1/(g+z)^2$ for the variable gap configuration. This makes variable area advantageous in terms of linearity. On the other hand, variable gap requires lower voltage for actuation as the electrostatic force is proportional to $1/g^2$ as opposed to $1/g$ for the variable area configuration.

Electrostatic resonators rely mostly on vibratory resonance, either in a flexural or bulk mode. Bulk-mode devices exhibit a very high stiffness, and are consequently less prone to thermoelastic damping, compared to flexural devices, allowing them to achieve large quality factors (>10,000), even at atmospheric pressure [12-23]. However, they suffer from significant signal loss which leads to higher motional resistance than typical piezoelectric devices. This can however be mitigated by increasing the applied DC polarization voltage and utilizing sophisticated technologies to realize very thin lateral transduction gaps (<100 nm). Electrostatic resonators with variable gap configuration can also benefit from the electrostatic spring softening phenomenon to allow for tuning the resonant frequency by varying the polarization voltage, as explained in section 6.4. This effect cannot be replicated for typical piezoelectric devices.

6.3. Resonator Modeling

Generally, a resonator can be modeled with a spring-mass-damper system as shown in Figure 6.4. Newton's equation of motion for the system can be written as

$$F(t) - kx(t) - c\dot{x}(t) = m\ddot{x}(t) . \tag{6.14}$$

By getting Laplace transform, the equation can be written as

$$F(S) - kX(S) - cSX(S) = mS^2X(S) . \tag{6.15}$$

Then, the system transfer function can be deduced as

$$\frac{X(S)}{F(S)} = \frac{1}{mS^2 + cS + k} . \tag{6.16}$$

Figure 6.5 shows the magnitude of the transfer function. At a certain frequency called resonance frequency (ω_0), given by

$$\omega_0 = \sqrt{\frac{k}{m}}\ radian/s , \tag{6.17}$$

the response exhibits a peak, where the transfer function is increases by a factor, called the quality factor (Q), which is given by

$$Q = \frac{\omega_0 m}{c} , \tag{6.18}$$

relative to the static response (response at zero frequency).

The transfer function can be reformulated in terms of ω_0 and Q as

$$\frac{X(S)}{F(S)} = \frac{1}{m}\frac{1}{S^2 + \frac{\omega_0}{Q}S + \omega_0^2} . \tag{6.19}$$

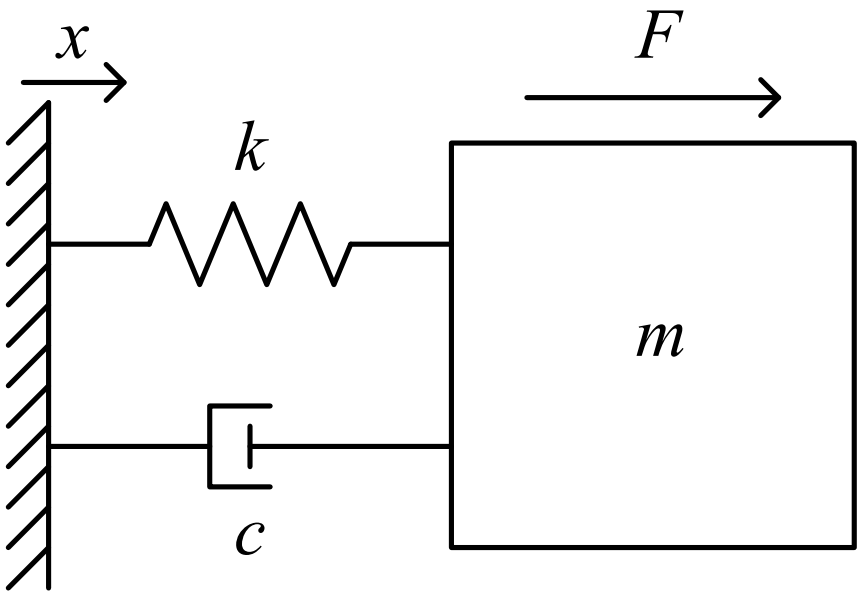

Figure 6.4: Spring-mass-damper resonator model

6.4. Frequency Tuning for Variable Gap Electrostatic Resonators

As clear from (6.13), the electrostatic force is in the opposite direction compared to the displacement. Therefore, it impedes the motion of the resonator and consequently it is equivalent to reducing the equivalent spring constant of the structure by a certain value, $k_{elec.}$, expressed as [11]

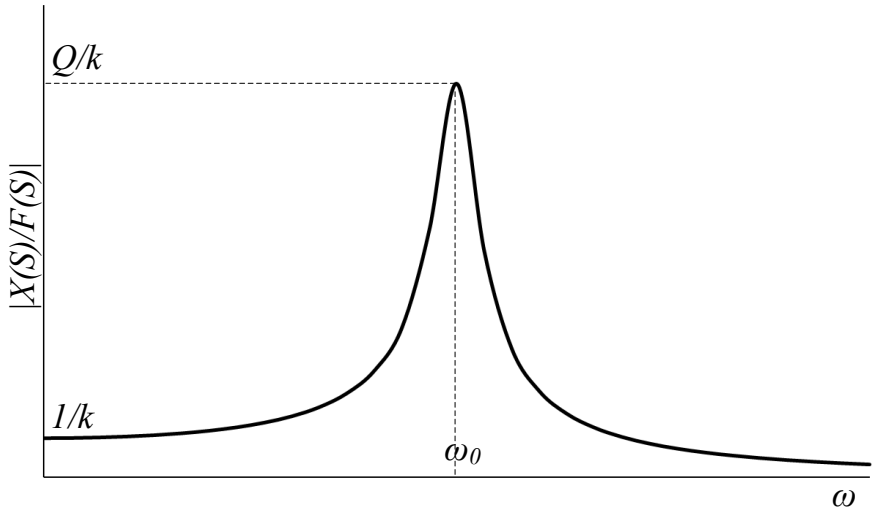

Figure 6.5: Magnitude of the transfer function of a simple spring-mass-damper system vs the angular frequency (ω).

$$k_{elec} = -\frac{dF_{elec}\big|_{var.gap}}{dx} \approx \frac{\varepsilon_0 wl}{g^3} V_a^2 \ , \ x << g \ . \tag{6.20}$$

This spring softening effect alters the resonance frequency of the structure from its original value to

$$\omega_r = \sqrt{\frac{k - k_{elec}}{m}} = \omega_0 \sqrt{1 - \frac{k_{elec}}{k}} = \omega_0 \sqrt{1 - \frac{\varepsilon_0 wl}{kg^3} V_a^2} \ . \tag{6.21}$$

Such tuning is typically limited to capacitive-based resonators, as the piezoelectric does not readily allow for a similar softening effect. In our work however, the design presented makes use of this electrostatic tuning method in order to allow for frequency tuning of the resonance induced via piezoelectric actuation, as explained in the next chapter.

6.5. Review of State-of-the-Art Resonators

In [13], a disk resonator resonating in the wine-glass mode was presented. The device is anchored to the substrate through beams at the mode nodal points as shown in Figure 6.6. The devices operate at ~60 MHz with a quality factor of ~145,000 and a motion resistance of ~ 32 kΩ at a 3 V DC polarization voltage. The motional resistance can be reduced to 3.2 kΩ by increasing the voltage to 12 V, but at the expense of reducing the quality factor to 48,000. Figure 6.7 shows an SEM micrograph of a fabricated device.

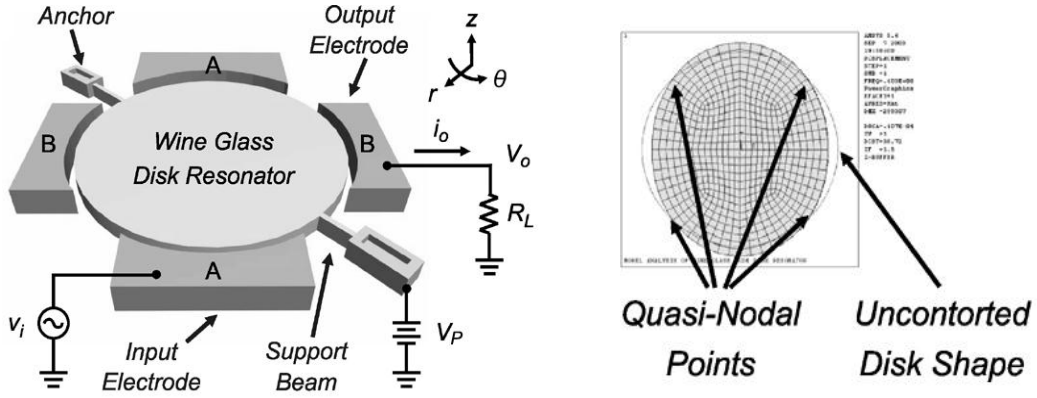

(a) (b)

Figure 6.6: (a) Simplified schematic of the device presented in [13], and (b) wine-glass mode utilized.

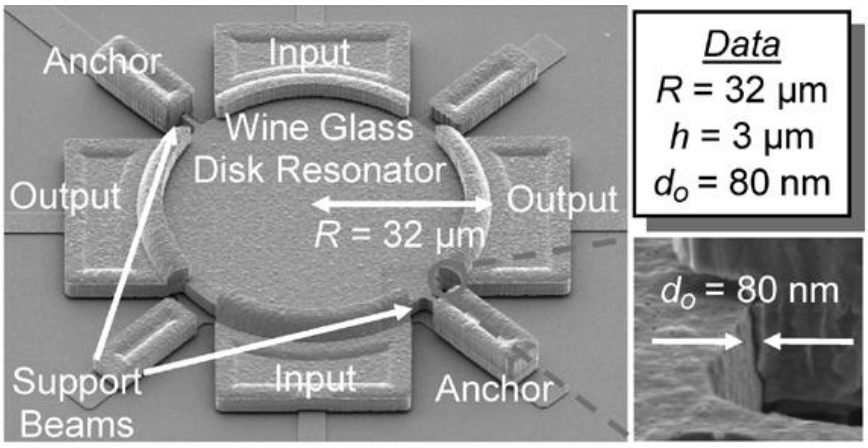

Figure 6.7: An SEM micrograph of the device presented in [13].

In [14], disk resonator vibrating in the radial contour mode was presented. It was fabricated using a technology combining polysilicon surface micromachining and metal electroplating to attain submicron lateral capacitive gaps. Devices were measured to operate at frequencies as high as 829 MHz and with quality factors as high as 23,000 at 193 MHz. The disk resonating structure is anchored at its center to the substrate as shown in Figure 6.8, which illustrates the design and the resonance mode utilized. Figure 6.9 shows the fabrication process and an SEM micrograph of a fabricated resonator.

In [16], a new fabrication methodology that allows self-alignment of a micromechanical structure to its center anchor has been used to achieve radial contour mode polysilicon disk resonators, as shown in Figure 6.10. Devices were demonstrated to resonate at frequencies up to 1.156 GHz with a quality factor of 2,650. Devices operating at lower frequencies (e.g., ~735 MHz) were demonstrated to operate with higher quality

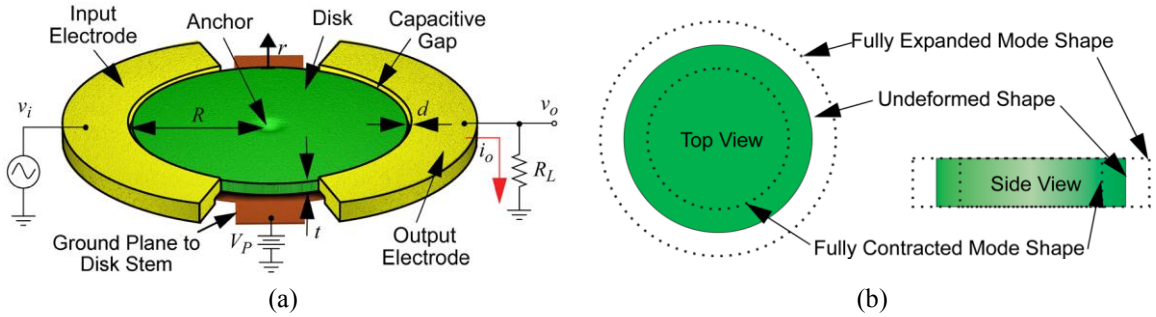

Figure 6.8: (a) Schematic of the resonator presented in [14], and (b) radial contour mode shape used.

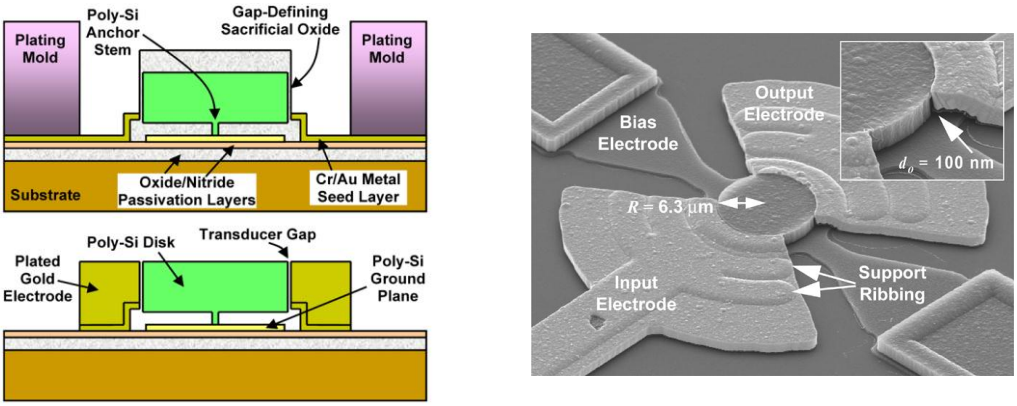

(a) (b)

Figure 6.9: (a) A simplified schematic of the cross section of a device illustrating the fabrication process, and (b) an SEM micrograph of a fabricated device [14].

factors (~7890). This self-alignment method utilizes the same mask to define the structure and the anchors, and therefore allows for better balancing of the structure compared to devices without self-alignment (e.g.: [14, 15]). This allows the device to achieve higher quality factors.

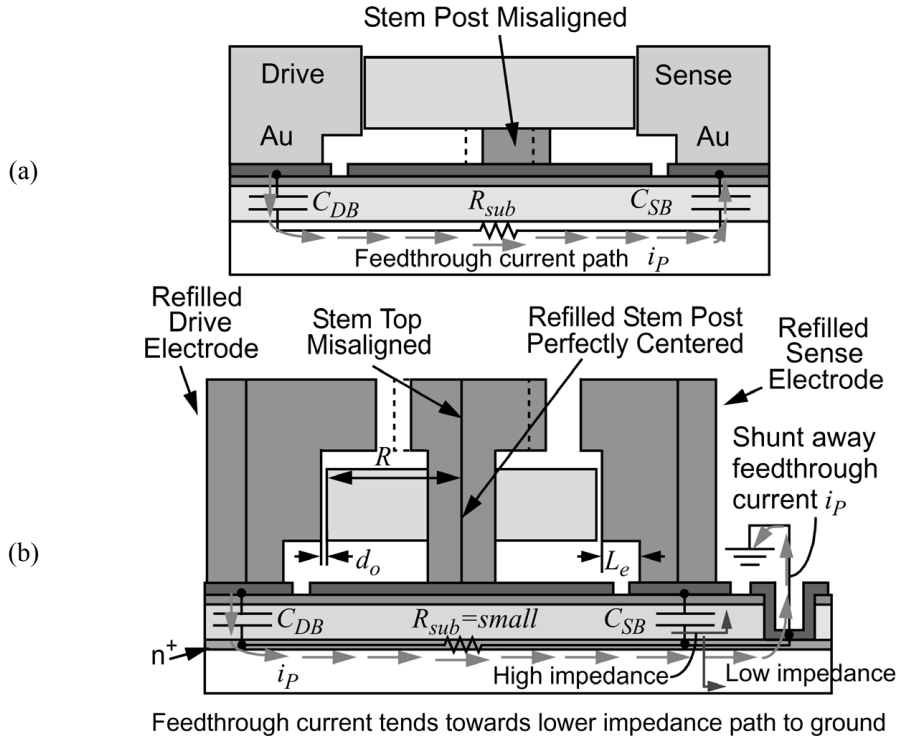

Figure 6.10: Comparison between: (a) the non-self-aligned structure presented in [15], and (b) the self-aligned structure presented in [16].

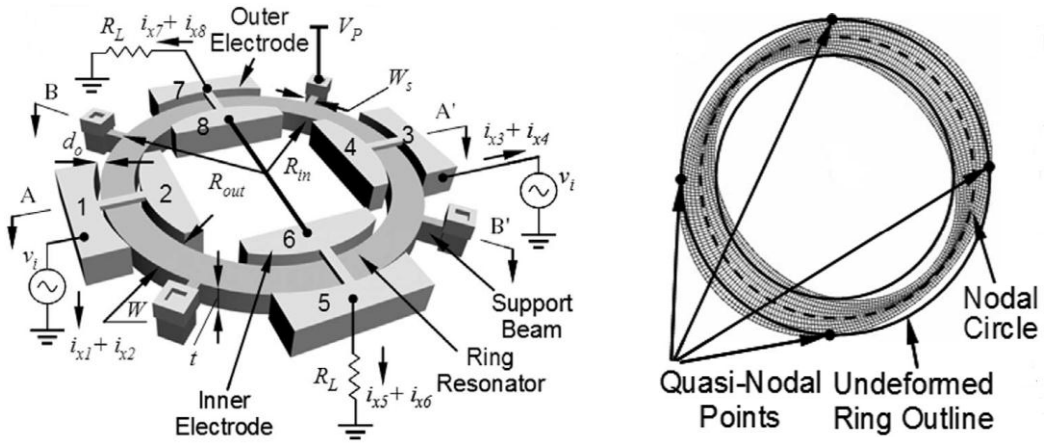

(a) (b)

Figure 6.11: (a) Schematic of the ring resonator proposed in [17], and (b) the extensional wine-glass mode utilized.

In [17], polysilicon micromechanical ring resonators, using the extensional wine-glass mode are presented. Figure 6.11 shows a schematic of the proposed device and the utilized mode shape. They were measured to operate at frequencies as high as 1.2 GHz with a quality factor of 3,700, and 1.52 GHz with a quality factor of 2,800. The 1.2 GHz resonator exhibits a measured motional resistance of 1 MΩ with a DC bias voltage of 20 V. Using the ring architecture the device can achieve more drive and sense and consequently lower motional resistance due to the increased capacitance resulting from the increased area. Figure 6.12 shows SEM micrographs of some of the fabricated devices. Notably, all

(a)

(b)

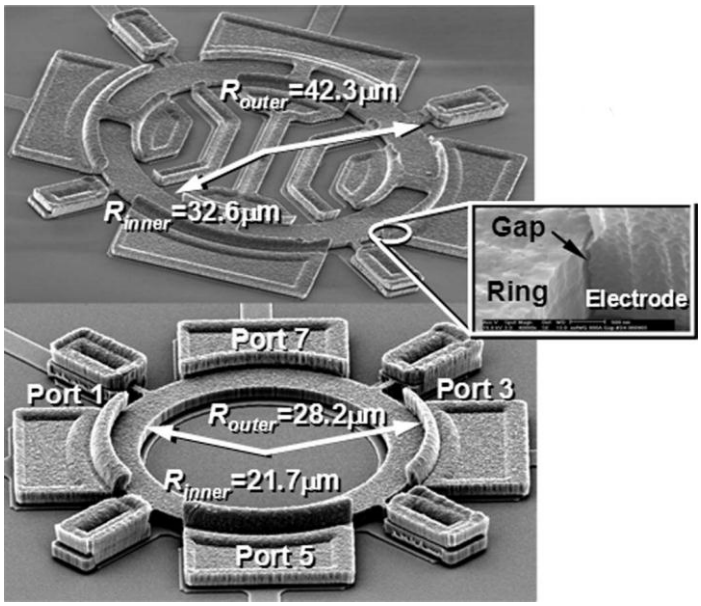

Figure 6.12: SEM micrographs for fabricated devices presented in [17] with: (a) both inner and outer electrodes, and (b) outer electrodes only.

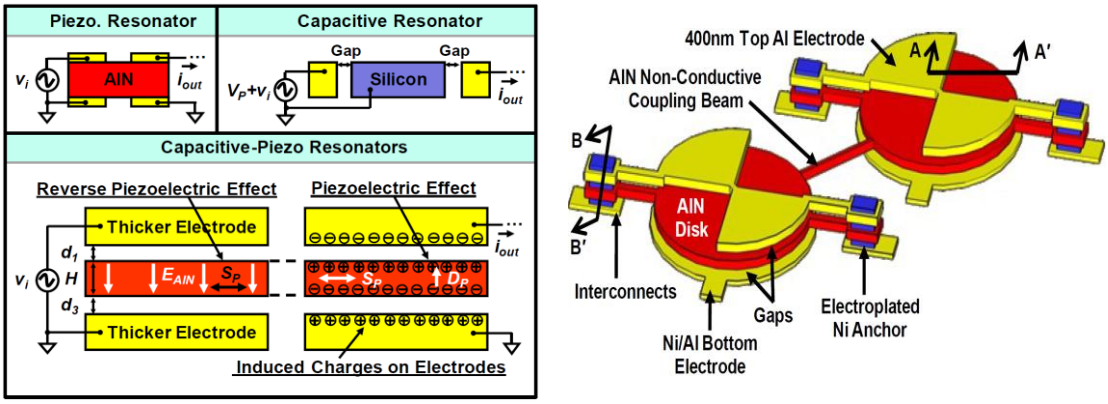

(a) (b)

Figure 6.13: (a) Schematic illustrating the combined capacitive piezoelectric actuation mechanism of the device presented in [18], and (b) schematic of a resonator array presented in [18].

aforementioned devices can benefit from electrostatic tuning which is a characteristic of parallel plate capacitive actuation, as discussed in section 6.4.

In [18], actuation and sensing of a bulk-mode wine-glass mode disk resonator made of AlN is performed by a combination of piezoelectric and capacitive methods as illustrated in Figure 6.13. The device resonates at 51 MHz with quality factor of ~13,000 and a loss of ~-34 dB, which corresponds to a motional resistance of ~4.9 kΩ. However, no tuning capability is reported.

In [19], a switchable AlN contour mode disk resonator is presented. It employs a similar combination of piezoelectric and capacitive schemes for actuation and sensing using electrodes above and beneath the disk structure, as shown in Figure 6.14 (a). The

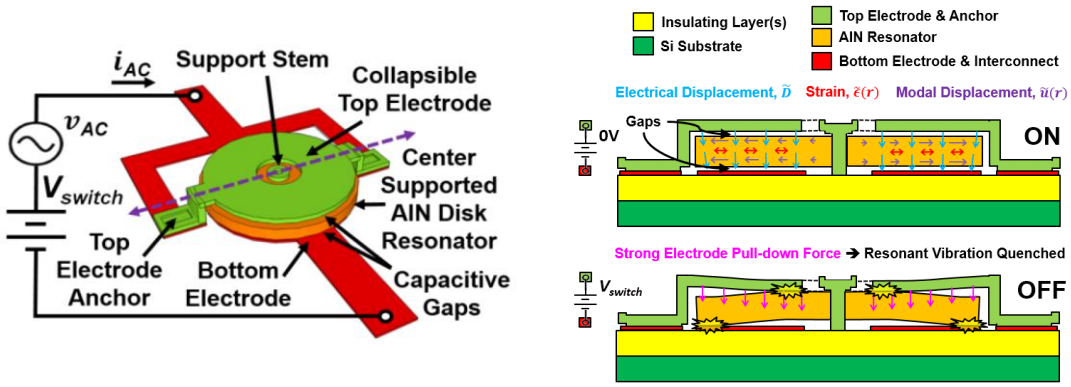

(a) (b)

Figure 6.14: (a) Simplified schematic of the switchable resonator presented in [19], and (b) cross-sections illustrating the device's operation in both the ON and OFF states.

same capacitive electrodes are used to pull the disk down to the substrate and consequently power it off by introducing more loss mechanisms when a high DC voltage is applied as shown in Figure 6.14 (b). Devices were demonstrated to resonate at frequencies around 300 MHz with quality factors as high as 8,800, and motional resistances as low as 3 kΩ. However, no tuning capability is reported. Notably, all the aforementioned designs require complex fabrication process steps to realize submicron lateral gaps in order to avoid excessive motional resistances.

Electrostatic resonating bulk structures using commercial micromachining technologies were reported before (e.g., [20, 21]). In [20], a Lamé mode resonator was presented. The devices were measured to operate at frequencies around 6 MHz with quality factors of about 1,000,000. However, the devices needed to operate at high voltages (>50 V) in order to overcome the dimension limitations on the transducer gap imposed by the technology. Figure 6.15 shows an SEM micrograph of the device as well as the mode utilized.

In [22, 23], combs were added to the bulk-resonating structure in order to improve overall sensitivity and allow for operation at a lower voltage, at the expense of increased area, as detailed in Chapter 3. The structure was designed to operate at the secondary

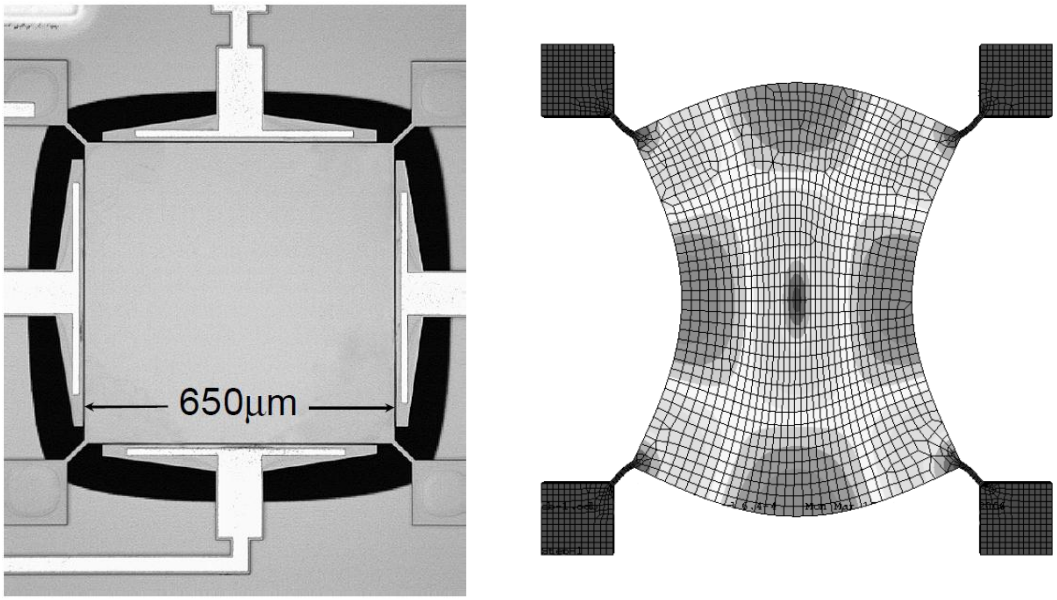

(a) (b)

Figure 6.15: (a) An SEM micrograph of the Lamé mode resonator presented in [20], and (b) the resonance mode shape of the device.

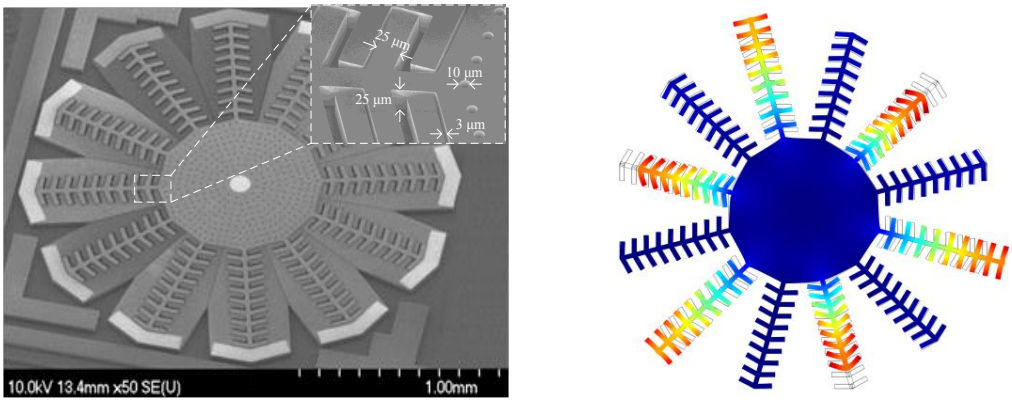

(a) (b)

Figure 6.16: (a) An SEM micrograph of the design proposed in [22, 23], and (b) the resonance mode shape utilized.

elliptic mode and devices were measured to resonate at ~ 1.5 MHz with a quality factor of ~33,000. Figure 6.16 shows an SEM micrograph of the design as well as the mode shape utilized.

6.6. Market Overview

As noted earlier, MEMS resonators are receiving continuously increasing attention due to their small sizes compared to conventional crystal resonators as well as their potential for integration with other MEMS sensors and circuits on the same chip, which

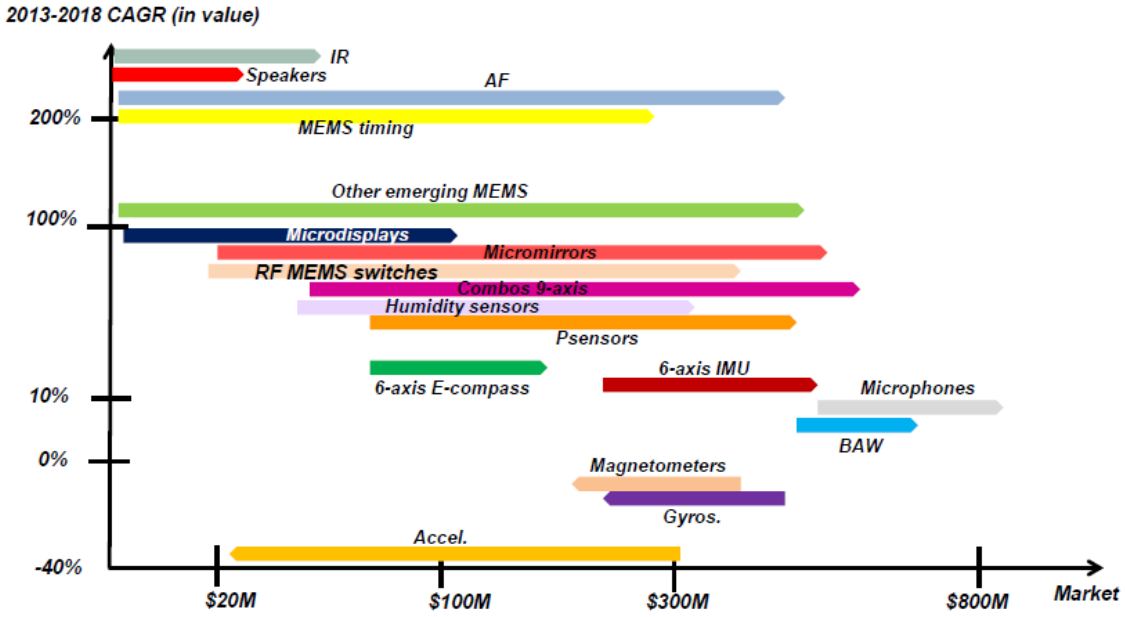

Figure 6.17: Market trends for MEMS devices in cell phones and tablets [Yole Development, 2013]

can be especially advantageous for handheld electronic applications (e.g.: smart phones and tablets), where weight, size, and cost are particularly critical parameters. Figure 6.20 shows the significant expected increase in the market size of MEMS timing devices.

In this work, as detailed in the next chapter, we focused on combining the advantages of the two main micromachined resonator actuation schemes, electrostatic and piezoelectric. A silicon bulk mode disk resonator in a commercially available MEMS process (MEMSCAP PiezoMUMPs) is presented. The device combines transverse piezoelectric actuation and sensing with bulk mode operation and electrostatic tuning in order to achieve a reasonable quality factor, low motional resistance, as well as frequency tunability using this affordable technology.

6.7. References

[1] W. Marrison, "The Evolution of the Quartz Crystal Clock," *The Bell System Technical Journal*, vol. 27, pp. 510-588, 1948.

[2] P. Dubois, "*Histoire de L'Horlogerie*," Le Moyen Âge et La Renaissance, 1849.

[3] A. Rees, "*The Cyclopaedia, or Universal Dictionary*," vol. 2, Longman, Hurst, Rees, Orme, and Brown, 1820.

[4] H. Feldmann, "The History of the Tuning-Fork - Part 1: The Invention of the Tuning-Fork, its Course in Music and Natural Science. Pictures from the History of Otorhinolaryngology, High-lighted bx Exhibits of the Deutsche Medizinhistorische Museum Ingolstadt," *Laryngo-Rhino-Otol*, vol. 76, no. 2, pp. 116-122, 1997.

[5] S. Han, H. Benaroya, and T. Wei, "Dynamics of Transversely Vibrating Beams Using Four Engineering Theories," *Journal of Sound and Vibration*, vol. 225, no. 5, pp. 935-988, 1999.

[6] J. Curie and P. Curie, "Développement par compression de l'électricité polaire dans les cristaux hémièdres à faces inclinées," *Bulletin de la Société Minérologique de France*, vol. 3, pages 90-93, 1880.

[7] J. Curie and P. Curie, "Développement par pression de l'électricité polaire dans les cristaux hémièdres à faces inclinées," *Bulletin de la Société Minérologique de France*, vol. 91, pages 294-295, 1880.

[8] A. Nicholson, "*Generating and Transmitting Electric Currents*," U.S. Patent 2,212,845, filed April 10, 1918, granted August 27, 1940.

[9] S. D. Senturia, *Microsystem Design*, Springer, 2001.

[10] Q. -X. Su, P. Kirby, E. Komuro, M. Imura, Q. Zhang, and R. Whatmore, "Thin-Film Bulk Acoustic Resonators and Filters Using ZnO and Lead–Zirconium–Titanate Thin Films," *IEEE Transactions on Microwave Theory and Techniques*, vol. 49, no. 4, pp. 769-778, April 2001.

[11] C. Acar, and A. Shkel, "MEMS Vibratory Gyroscopes *Gyroscopes: Structural Approaches to Improve Robustness,*" Springer, 2009.

[12] H. Johari and F. Ayazi, "High Frequency Capacitive Disk Gyroscopes in (100) and (111) Silicon", *Proceedings of the IEEE Conference on Microelectromechanical Systems*, pp. 47-50, January 2007.

[13] Y. -W. Lin, S. Lee, S. -S. Li, Y. Zie, Z. Ren, and C. Nguyen, "Series-Resonant VHF Micromechanical Resonator Reference Oscillators", *IEEE Journal of Solid-State Circuits*, vol. 39, no. 12, pp. 2477-2491, December 2004.

[14] J. Clark, W.-T. Hsu, M. Abdelmoneum, and C. Nguyen, "High-Q UHF Micromechanical Radial Contour-Mode Disk Resonators", *Journal of Microelectromechanical Systems*, vol. 14, no. 6, pp. 1298-1310, December 2005.

[15] J. Clark, W.-T. Hsu, and C. Nguyen, "High-*Q* VHF Micromechanical Contour-Mode Disk Resonator," *Technical Digest of the* IEEE International Electron Devices Meeting, pp. 493-496, December 2000.

[16] J. Wang, Z. Ren, and C. Nguyen, "1.156-GHz Self-Aligned Vibrating Micromechanical Disk Resonator", *IEEE Transactions on Ultrasonics, Ferroelectrics and Frequency Control*, vol. 51, no. 12, pp. 1607-1628, December 2004.

[17] Y. Xie, S. Li, Y. Lin, Z. Ren, and C. Nguyen, "1.52-GHz Micromechanical Extensional Wine-Glass Mode Ring Resonators", *IEEE Transactions on Ultrasonics, Ferroelectrics and Frequency Control*, vol. 55, no. 4, pp. 890-907, May 2008.

[18] L. -W. Hung and C. Nguyen, "Capacitive-Piezoelectric AlN Resonators with Q>12,000," *Proceedings of the IEEE Conference on Microelectromechanical Systems*, pp. 173-1766, January 2011.

[19] R. Schneider and C. Nguyen, "On/Off Switchable High-Q Capacitive-Piezoelectric AlN Resonators," *Proceedings of the IEEE Conference on Microelectromechanical Systems*, pp. 1265-1268, January 2014.

[20] L. Khine, M. Palaniapan, and W. -K. Wong, "6 MHz Bulk-Mode Resonator with Q Values Exceeding One Million", *Proceedings of the IEEE Conference on Solid-State Sensors, Actuators and Microsystems*, pp. 2445-2448, June 2007.

[21] M. Elsayed, F. Nabki, and M. El-Gamal, "A 2000 °/sec Dynamic Range Bulk Mode Dodecagon Gyro for a Commercial SOI Technology", *Proceedings of the IEEE Conference on Electronics, Circuits, and Systems*, pp. 264-267, December 2011.

[22] M. Elsayed, F. Nabki, and M. El-Gamal, "A Combined Comb/Bulk Mode Gyroscope Structure for Enhanced Sensitivity", *Proceedings of the IEEE Conference on Microelectromechanical Systems*, pp. 649-652, Jan. 2013.

[23] M. Elsayed, F. Nabki, and M. El-Gamal, "A Novel Comb Architecture for Enhancing the Sensitivity of Bulk Mode Gyroscopes", *Sensors*, vol. 13, pp. 16641-16656, December 2013.

[24] "*Status of the MEMS Industry*," Yole Development, 2013.

Chapter 7 Bulk Mode Disk Resonator with Transverse Piezoelectric Actuation and Electrostatic Tuning

7.1. Introduction

Micromachined resonators are receiving continuously increasing attention due to their small sizes compared to conventional crystal-based resonators as well as their potential for integration with other MEMS resonators and circuits on the same chip (e.g., [1]), which can be especially advantageous for handheld electronic applications (e.g., smartphones and tablets) where weight, size, and cost are particularly critical parameters.

Micromachined resonators can be operated through two main widespread actuation mechanisms: piezoelectric or electrostatic, each method having its specific advantages and drawbacks. Piezoelectric devices such as surface acoustic wave (SAW) and film bulk acoustic resonators (FBAR) are already widely used in timing applications [2]. Piezoelectric FBARs generally exhibit low signal losses, resulting in low motional resistances, which is very advantageous as it simplifies the design constraints of the associated electronic circuitry and results in lower power consumption. Also, piezoelectric devices do not require any DC voltage for operation. However, they generally suffer from lower quality factors [3, 4] and their resonance frequencies are limited by the piezoelectric layer thickness, which makes it impractical to achieve more than one frequency on the same chip [5]. As for electrostatic resonators, they rely mostly on vibratory resonance, either in a flexural or bulk mode. Bulk-mode devices typically exhibit high stiffness, and are consequently less prone to thermoelastic damping, compared to flexural devices, allowing them to achieve large quality factors (>10,000), even at atmospheric pressure [6-14]. However, electrostatic actuation makes these resonators suffer from significant signal loss which leads to higher motional resistance than typical piezoelectric devices. This can however be mitigated by increasing the applied DC polarization voltage and utilizing sophisticated technologies to realize very thin lateral transduction gaps (<100 nm). Electrostatic resonators can also benefit from the electrostatic spring softening

phenomenon to allow for tuning the resonance frequency by varying the polarization voltage. This effect cannot be replicated for typical piezoelectric devices. In [7-10], capacitive bulk-mode disk resonators exhibiting quality factors of 2,000-150,000 and motional resistances of 1.5 k-1 MΩ using polarization voltages <20 V are demonstrated. In [3], actuation and sensing of a bulk-mode disk resonator made of AlN is performed by a combination of piezoelectric and capacitive methods. The device resonates at 51 MHz with quality factor of ~13,000 and a loss of ~ -34 dB. However, no tuning capability is reported. In [4], a radial mode AlN resonator is presented. It employs a capacitive-piezoelectric actuation scheme similar to [3], using metal electrodes above and beneath the disk structure. The electrostatic electrodes beneath the disk structure are also used to pull it down to the substrate and consequently power the resonator off upon the application of a switching DC voltage. Notably, all the aforementioned designs require complex fabrication process steps to realize submicron lateral gaps in order to avoid excessive motional resistances. In [15], a flexural (out-of-plane) piezoelectric resonator is presented. The device employs a metal electrode beneath the suspended structure for electrostatic tuning. However, it operates at a relatively low frequency of ~ 32 kHz due to the low stiffness flexural mode of operation. Electrostatic resonating bulk structures using commercial micromachining technologies were fabricated before (e.g., [11, 12]). In [11], the devices had to operate at high voltages (>50 V) in order to overcome the dimension limitations on the transducer gap imposed by the technology. In [13, 14], combs were added to the bulk-resonating structure in order to improve overall sensitivity and allow for operation at lower voltage, at the expense of increased area.

Due to the limitations of the aforementioned designs, the motivation behind this work is to combine transverse piezoelectric actuation with bulk mode resonance in order to achieve low motional resistance without requiring any DC voltage, reasonable quality factor (also in air), and a relatively high resonance frequency. This is achieved without requiring any DC voltage for operation, and thus the design brings together the advantages of piezoelectric actuation and bulk-mode resonators. The work also presents optional electrostatic tuning of the device and implements it in a relatively simple and low resolution technology, MEMSCAP PiezoMUMPs.

The design was presented briefly in [16]. In this chapter, it is explained in more details. The chapter begins with a description of the device design, followed by finite-elements simulation results. The process flow for the fabrication technology is then detailed, and measurement results are presented and discussed.

7.2. Design

Figure 7.1 shows a simplified schematic of the proposed design. The device is composed of a single-crystalline silicon central disk structure acting as the wine-glass resonator. This disk is 10 µm thick and has a 200 µm diameter. It is covered by a 0.5 µm layer of aluminum nitride, the piezoelectric material used for transduction and to bring the resonator into its wine-glass mode of resonance. The aluminum nitride covers the disk completely in one design, and in another it is patterned into four distinct quadrants. Both designs exhibit similar performance. The disk structure is supported by four suspension beams having a 10 µm width (the minimum allowed by the design rules of the technology) with 90° angular spacing, so as to correspond with the nodal points of the wine-glass resonance mode. The support beams are anchored to the substrate at their ends and mechanically connected to the electrical pads. Each of these supports is associated with a

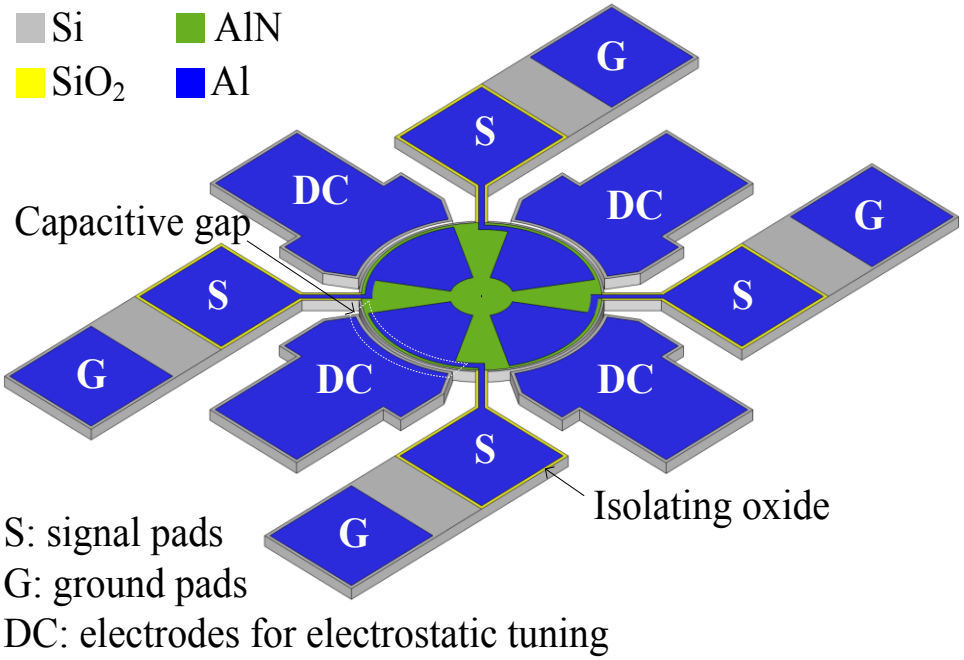

Figure 7.1: Simplified diagram of the disk resonator outlining the pads used for piezoelectric actuation and electrostatic tuning.

pair of pads, one for the signal routed above the piezoelectric layer, and the other for the ground, routed through the underlying silicon structural layer. For this purpose, an aluminum layer above the disk structure is patterned into four distinct quadrants, each electrically connected to a distinct signal pad by an aluminum track routed above its respective suspension beam. The conductive structural silicon layer itself acts as the ground plane for the device, and connects with each ground pad while remaining electrically insulated from the signal track by a layer of silicon dioxide. Aluminum nitride is not present on the supports to avoid any unintended transduction which would alter the resonance mode and possibly lead to undesirable spurious modes of vibration.

The disk structure is also surrounded by four capacitive electrodes which are separated from it by a lateral transduction gap of 2.5 μm, the critical spacing imposed by the fabrication process. These electrodes are intended for electrostatic tuning of the resonance frequency through the electrostatic spring softening effect, as detailed in section 7.4. Table 7.1 summarizes the design parameters of the resonator device fabricated here. A finite-element simulation illustrating the mode-shape of the resonator in the wine-glass mode is shown in Figure 7.2. The resonance frequency of the disk in the wine-glass mode is simulated to be of 17.54 MHz.

Table 7.1: Summary of Resonator Device Design Parameters

Parameter	Value
Disk diameter (μm)	200
Structure thickness (μm)	10
Support width (μm)	10
Capacitive gap (μm)	2.5
AlN layer thickness (μm)	0.5
Simulated resonance frequency (MHz)	~17

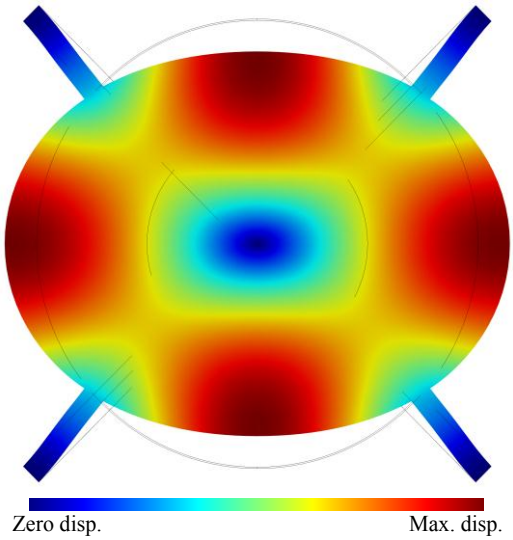

Figure 7.2: Wine-glass mode shape of the resonator.

7.3. Piezoelectric Actuation

Operation of the proposed device relies on the piezoelectric effect, a relationship across the electrical and mechanical domains. For certain materials with the proper atomic structure and crystal orientation, a mechanical stress results from electric charge accumulating across the material. This effect can also be used in reverse where a charge results from a mechanical stress. This relationship can be quantified, with the electric field and stress expressed as independent variables, by [17]

$$D = \varepsilon E + d\sigma , \tag{7.1}$$

$$\xi = d^T E + S\sigma , \tag{7.2}$$

where D is the electric displacement vector, ε is the dielectric constant matrix, E is the electric field intensity vector, d is the piezoelectric coefficient matrix, σ is the stress tensor, ξ is the strain tensor, and S is the compliance matrix.

For this device, the vertical electric field resulting from the input voltage between the input electrodes on top of the disk and the ground plane is converted to an in-plane mechanical stress in the aluminum nitride layer through its transverse piezoelectric coefficient, d_{31}, based on

$$|\sigma_{in-plane}| = \left| \frac{\varepsilon_{33} v_{in}}{d_{31} t} \right| , \tag{7.3}$$

where v_{in} is the input voltage, ε_{33} is the vertical dielectric constant of the piezoelectric layer (AlN for this design), and t is the piezoelectric layer thickness, i.e. the distance between the signal electrodes and the ground plane. The quadrant subdivision of the electrodes was selected for the induced stress pattern to force a mechanical actuation of the disk in the wine-glass mode shape. Based on its structural and dimensional properties, the disk filters this mechanical perturbation to favor strain at frequencies close to its resonance, in an identical fashion to usual electrostatically-actuated disk resonators. The reverse piezoelectric effect serves to convert this piezoelectrically-induced and mechanically-filtered strain back into an electrical output voltage based on (7.2).

7.4. Electrostatic Tuning

Generally, any resonator can be modeled as a spring-mass-damper system. Its resonance frequency can be expressed as [17]

$$f_0 = \frac{1}{2\pi}\sqrt{\frac{k_{eq}}{m_{eq}}}, \tag{7.4}$$

where k_{eq} and m_{eq} are the equivalent spring constant and mass of the structure respectively.

The capacitance between the electrodes and disk, based on a parallel-plate approximation, can be calculated as

$$C \approx \frac{\varepsilon_0 A}{g + x}, \tag{7.5}$$

where ε_0 is the free space permittivity, A is the overlap area of the electrostatic electrodes, g is the gap between the electrodes, and x is the lumped displacement of the disk.

When a DC voltage, V_{tuning}, is applied between the tuning electrodes and the grounded disk, an electrostatic force ($F_{elec.}$) is generated as given by [17]

$$F_{elec} = \frac{1}{2}\frac{dC}{dx}V^2 \approx -\frac{\varepsilon_0 A}{2(g+x)^2}V_{tuning}^2. \tag{7.6}$$

This force impedes the motion of the resonator and therefore is equivalent to reducing the equivalent spring constant of the structure by a certain value, k_{elec}, expressed as [18]

$$k_{elec} = -\frac{dF_{elec}}{dx} \approx \frac{\varepsilon_0 A}{g^3} V_{tuning}^2, \; x << g \,. \tag{7.7}$$

This spring softening effect alters the resonance frequency of the structure from its original value to

$$f_r = \frac{1}{2\pi}\sqrt{\frac{k_{eq} - k_{elec}}{m_{eq}}} = f_0\sqrt{1 - \frac{k_{elec}}{k_{eq}}} = f_0\sqrt{1 - \frac{\varepsilon_0 A}{k_{eq} g^3} V_{tuning}^2} \,. \tag{7.8}$$

Such tuning is typically limited to capacitive-based resonators, as the piezoelectric devices do not readily allow for a similar softening effect. In this work however, the design presented makes use of this electrostatic tuning method in order to allow for frequency tuning of the resonance induced via piezoelectric actuation.

7.5. Fabrication Process

The resonators in this work were fabricated in the PiezoMUMPs technology from MEMSCAP. The fabrication process sequence, as detailed in [19], is illustrated in Figure 7.3 for the devices fabricated here. The process begins with 150 mm n-type double-side polished silicon on insulator (SOI) wafers, as shown in Figure 7.3 (a). The top silicon surface is doped using phosphosilicate glass (PSG) in order to increase its conductivity. This layer constitutes the main structural layer that will be used to form the device, and that is connected to the electrical ground. A 200 nm-thick thermal silicon dioxide is then grown, patterned and etched using reactive ion etching (RIE), as illustrated in Figure 7.3 (b). This thermal oxide serves to isolate the signal pads and interconnects from the ground plane in the areas without aluminum nitride (e.g., the signal pads or the top of supports). A 0.5 μm thick layer of aluminum nitride is then deposited, patterned, and wet etched, as shown in Figure 7.3 (c). This piezoelectric layer is used for transduction. A metal stack composed of 20 nm of chrome and 1 μm of aluminum is subsequently deposited and patterned through a lift-off process to form the electrical interconnects and pads, as illustrated in Figure 7.3 (d). At this stage, silicon is lithographically patterned, and etched using deep reactive ion etching (DRIE) to form the structural disk and the tuning electrodes, as shown in Figure 7.3 (e). Afterwards, a protective material is applied to the frontside of the substrate, to serve as a cover during subsequent backside etch steps.

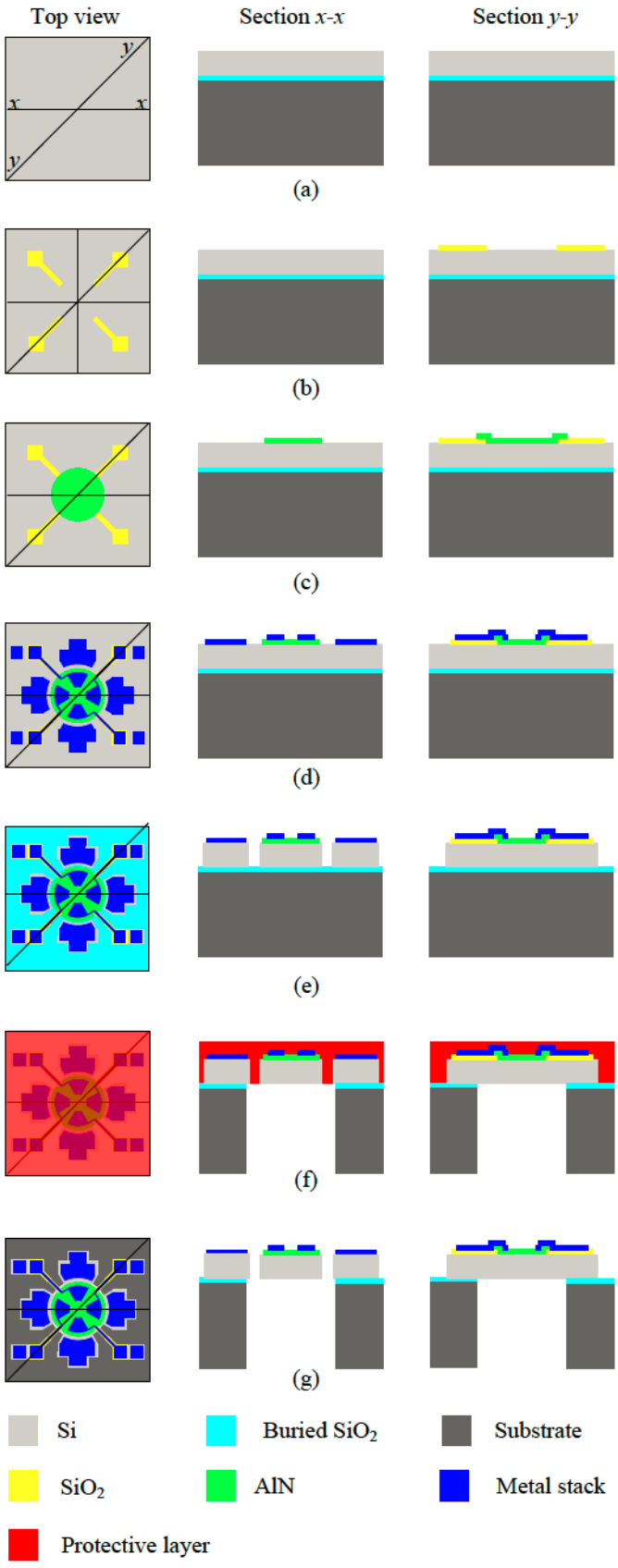

Figure 7.3: Simplified PiezoMUMPs fabrication process flow [19].

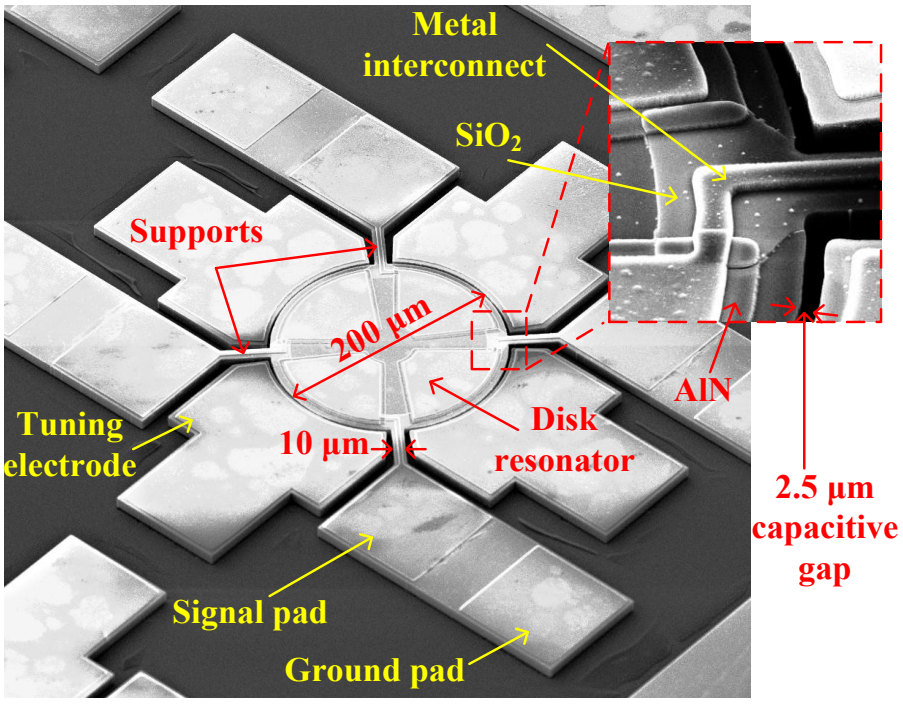

Figure 7.4: SEM micrograph of one fabricated resonator.

The substrate layer is then lithographically patterned and etched from the backside using DRIE to form release trenches that stop at the oxide layer. Wet oxide etch then removes the now-exposed buried oxide layer in the trench regions, as shown in Figure 7.3 (f). The frontside protection material is finally stripped by dry plasma etching, which completes the release of the disk structure and allows for its free motion, as illustrated in Figure 7.3 (g). Figure 7.4 shows an SEM micrograph of one of the fabricated devices.

7.6. Measurement Results

7.6.1. Resonance Configurations and Characteristics

The structure was intentionally designed with four independent signal electrodes to enable its use within both single-ended and differential configurations, making it possible to directly connect to different amplifier types without the need for extra components or converters such as baluns. The dies of the tested devices were wire bonded directly onto a gold-plated PCB, as shown in Figure 7.5. This direct bonding approach was preferred to packaging in order to avoid added parasitics. The resonance characteristics of the devices

were measured using the test setups shown in Figure 7.6, both at atmospheric pressure and in ~100 mTorr vacuum. Measurement results for the devices are shown in Figure 7.7. The device exhibits a resonance frequency, f_r, of 14.63 MHz and quality factor, Q, of ~ 2,000 and ~ 4,900 under atmospheric pressure and 100 mTorr vacuum level, respectively. Although modal analysis in simulations projected a resonance frequency of 17.54 MHz, the difference between the simulated and measured values can reasonably be attributed to the residual stress of the different layers, to the discrepancies between the structural material parameters used for simulation and their actual values, and to dimension variations of the fabricated device. The resonator exhibits a transmission of -32 dB (i.e., an insertion loss of 32 dB) for the single-ended configuration in a 100 mTorr vacuum level, which corresponds to a motional resistance of ~ 3.9 kΩ. In the differential configuration, the transmission is higher at -22.6 dB in vacuum, corresponding to a motional resistance of

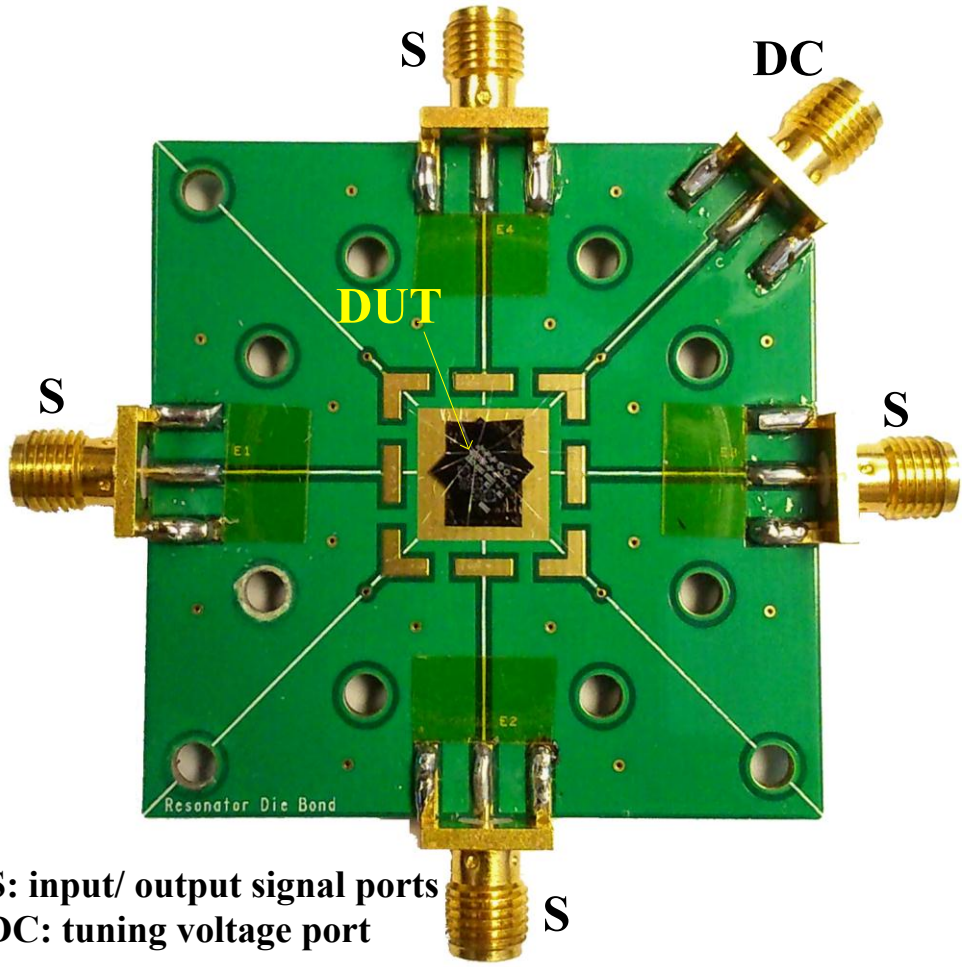

Figure 7.5: Printed circuit board used for testing the resonator. A resonator die is directly wire bonded onto the board.

~1.2 kΩ. This increase in transmission is expected because of the additional drive and sense electrodes used in the differential configuration.

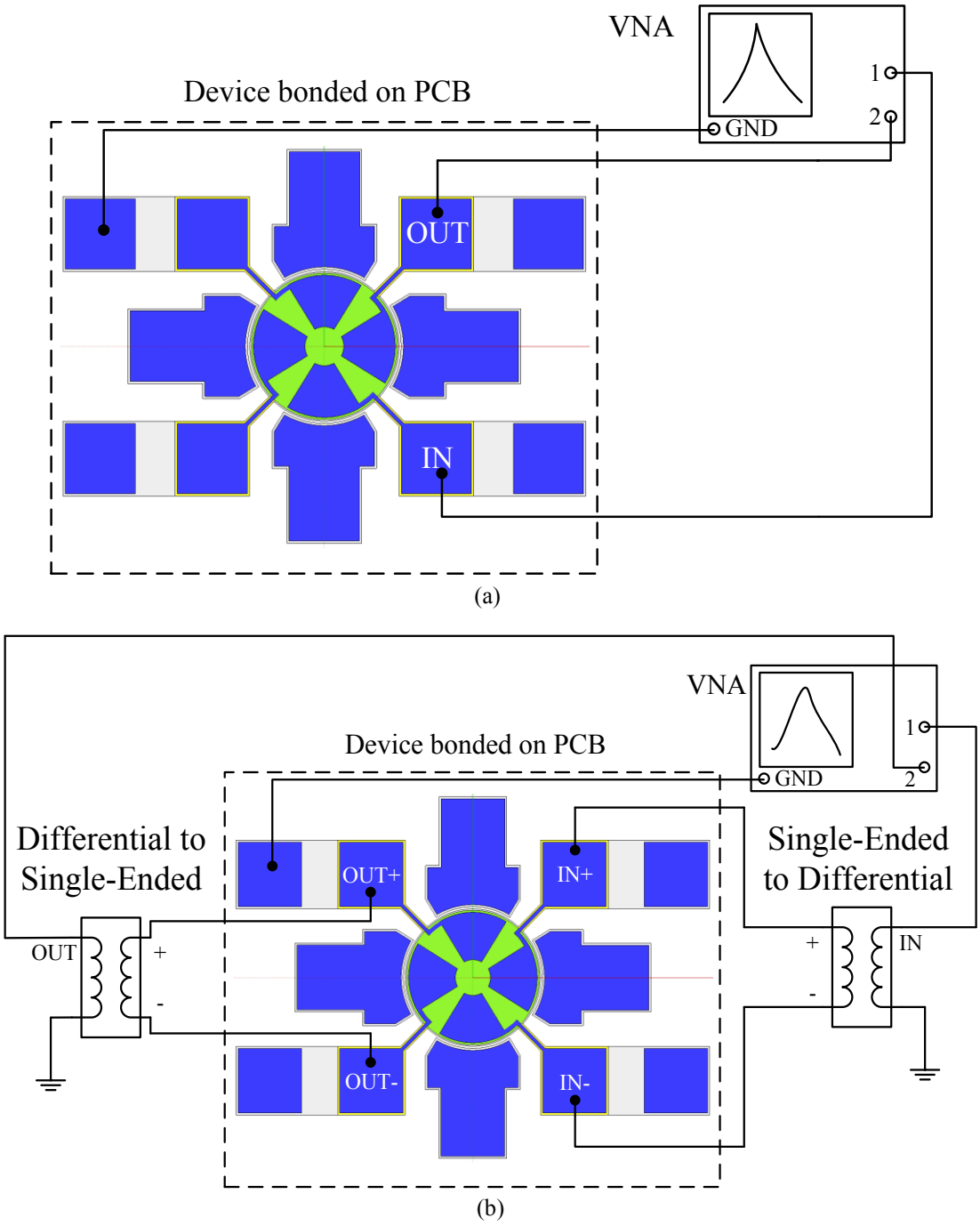

Figure 7.6: Different resonance testing configurations: (a) single-ended, and (b) differential.

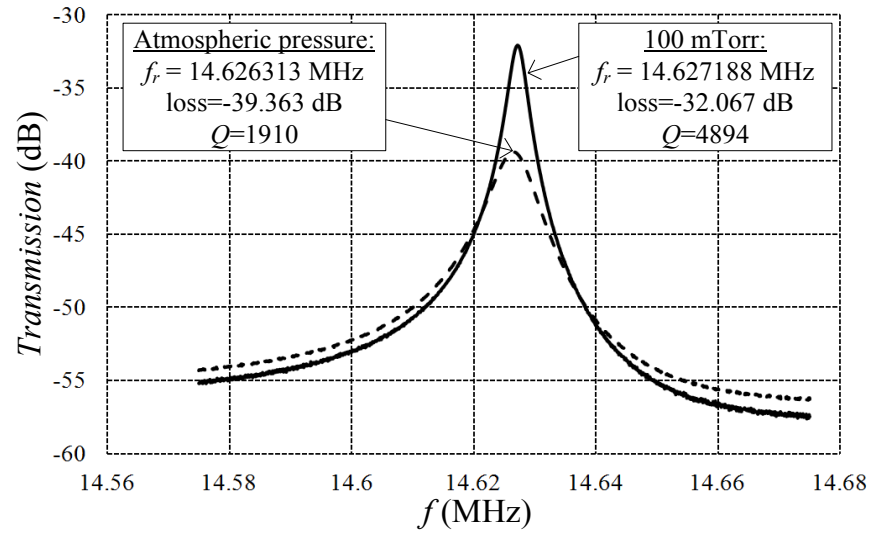

(a)

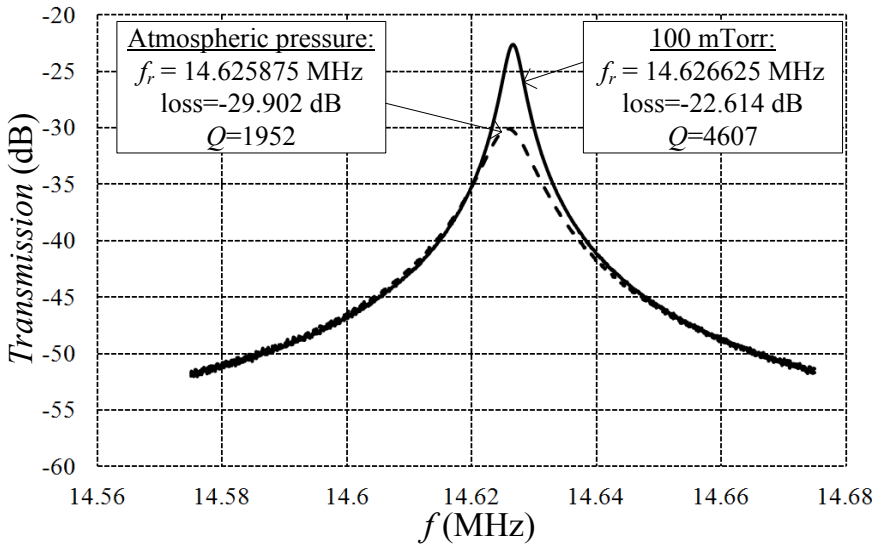

(b)

Figure 7.7: Measured resonance characteristics of the resonators at atmospheric pressure (dashed line) and in vacuum (solid line) in: (a) single-ended configuration, and (b) differential configuration.

Figure 7.8 illustrates the effect of the ambient pressure level on the resonance quality factor. Air damping has relatively little impact on the device performance, as the quality factor varies only by a factor of ~2.5 over the full range of the studied pressures. The quality factor approaches its maximum at pressures below 5 Torr. Two main reasons were considered as potential causes for the limited quality factor measured since the structural silicon layer is crystalline and should not be a limiting factor, namely i) damping from the top AlN layer, and ii) anchor loss. AlN damping was ruled out as the cause as two fabricated versions of the devices, one with AlN covering the disk completely, and the

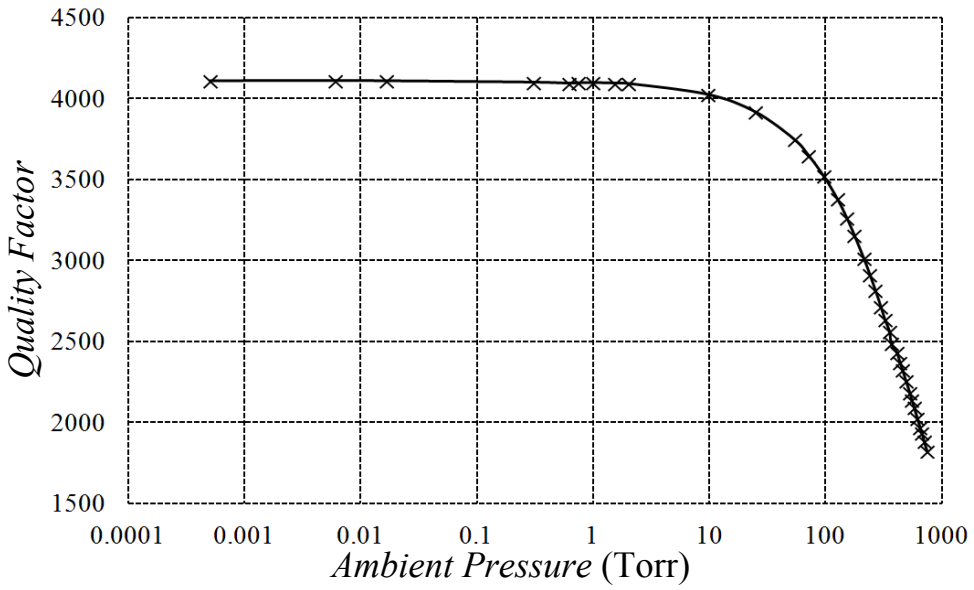

Figure 7.8: Resonator quality factor vs ambient pressure.

other with AlN patterned into four distinct quadrants under the electrodes, exhibit nearly the same quality factor despite the varying AlN disk coverage percentage. This is in-line with the results presented in [3], which confirmed that AlN is a high-Q material. The maximum quality factor is therefore limited by anchor loss through the supports. These supports are relatively wide due to fabrication technology constraints (10 μm). However, the design would be capable of reaching higher quality factors if the supports could be made narrower, as noted in [3], where changing the supports by 1 μm, from 2 μm to 1 μm, led to a quality factor increase of ~ 80 %. Notably, the silicon supports of the proposed device could potentially be narrowed by a post-process timed isotropic etch. Xenon di-fluoride (XeF_2) vapor is a promising candidate to perform this etch, as it has already been successfully used to release MEMS structures (e.g. [3]) and is highly selective to silicon.

7.6.2. Effect of Operating Temperature

The effect of ambient temperature on the frequency response of the resonator at atmospheric pressure was determined using the single-ended test setup of Figure 7.6 (a) over the temperature range of -40 to 90 ºC. The temperature coefficient of frequency (TC_f) was found to be ~ -40 ppm/°C, as a consequence mainly of thermal expansion of the structure. The TC_f is slightly higher than devices presented in the literature (e.g., [7, 9]),

which is probably due to the differences between the properties of the structural materials used. Figure 7.9 presents the effects of temperature on the resonance frequency, the quality factor, and the transmission of the resonator.

The device's quality factor is limited by two main damping mechanisms, namely, anchor loss due to the supports, and air damping resulting from the squeeze film damping between the resonating disk structure and the electrodes. At low temperatures, the anchor loss is the dominant mechanism, and therefore the quality factor is constant. As the temperature increases, the air damping effect increases due to the increase of the air viscosity [20, 21], as illustrated in Figure 7.9 (b). Expectedly, the transmission curve follows the same pattern of the quality factor curve, as shown in Figure 7.9 (c).

7.6.3. Electrostatic Tuning

The electrostatic tuning capability of the resonator was characterized using the single-ended test setup of Figure 7.6 (a), with an external DC source used to set the tuning voltage. The ground nodes of the source and network analyzer were connected together to ensure a common reference voltage between the ground plane of the disk and the applied tuning voltage, and thus ensure the intended voltage difference between the tuning electrodes and the disk. Figure 7.10 presents the measured fractional change in the resonance frequency with respect to the tuning voltage applied, along with the theoretical variation expected based on (7.8). The device exhibits a tuning factor of ~ -1 ppb/V^2 that could serve to compensate for minor variations in operating conditions (e.g., temperature), or for implementing tunable high frequency synthesizers, as in [1], where a frequency multiplier could be used to increase the absolute frequency change.

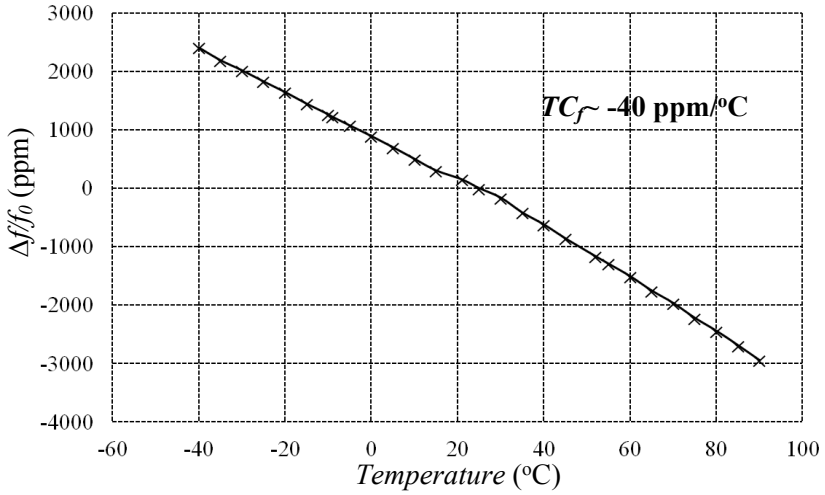

(a)

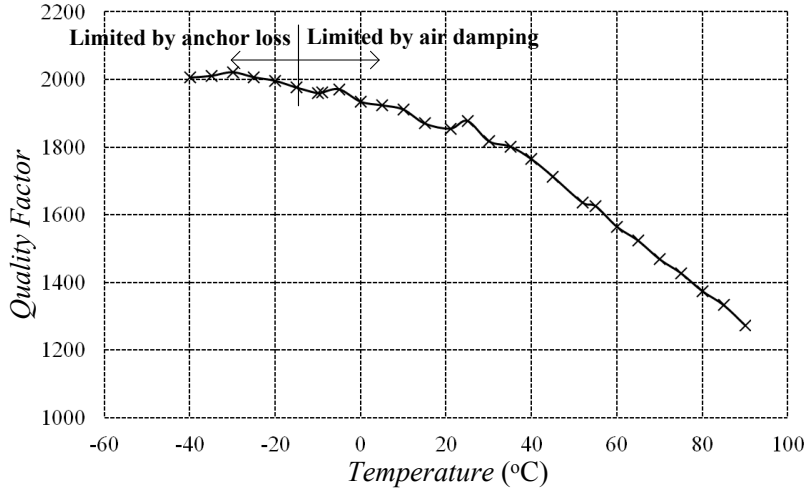

(b)

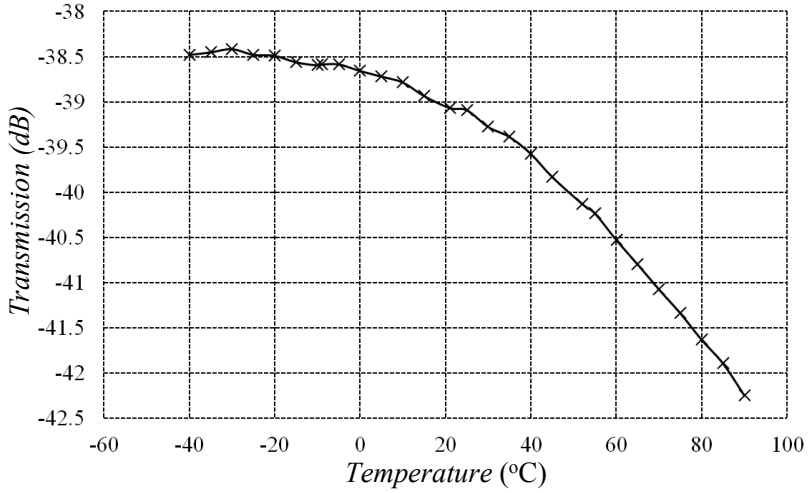

(c)

Figure 7.9: Temperature dependence of the resonator's (a) resonance frequency, (b) quality factor, and (c) transmission.

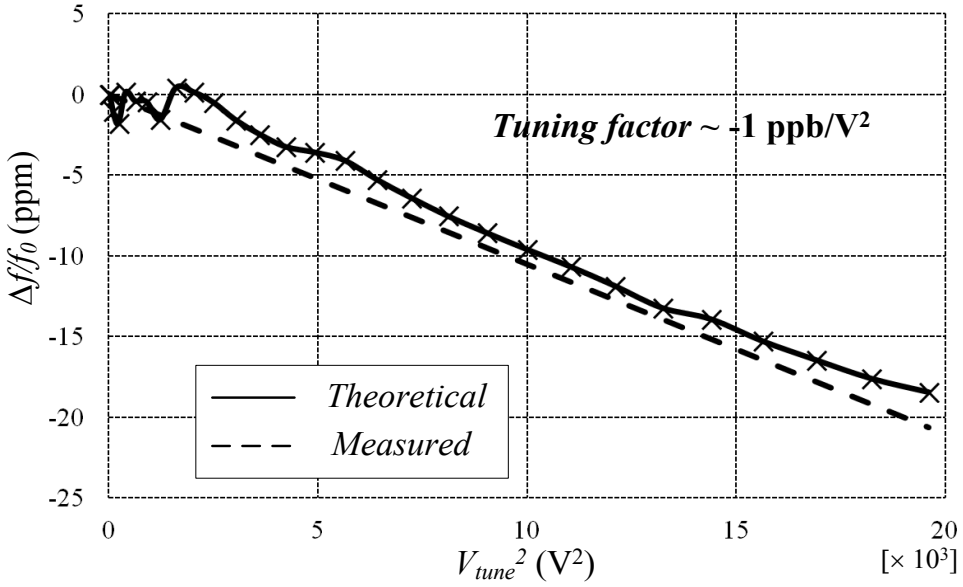

Figure 7.10: Fractional change in the resonance frequency vs (tuning voltage)^2.

7.7. Discussion

Table 7.2 compares the device proposed here and implemented in a low-cost commercial MEMS technology to other state-of-the-art bulk-mode resonators. The table highlights its reasonable quality factor, limited by the anchor loss dictated by the technology, and its superior motional resistance. The device achieves the lowest signal loss and motional resistance amongst the devices in comparison. The achieved motional resistance is a key advantage for the device presented in this work, as it results in significant simplification of the associated electronics for realizing complete systems (e.g., oscillator and phase locked loop in [1]) resulting in lower power consumption and phase noise. The performance demonstrated here is achieved without the need for submicron lateral gaps, as in [3, 4, 6-10], or high DC polarization voltages, as in [11-14]. In fact, the device requires no DC voltage for its operation. The quality factor can be further improved by decreasing the width of the suspension beams to reduce the anchor losses, either by post-processing as explained in section 7.6.1, or by using another technology with smaller critical dimensions. Compared to other piezoelectric disk resonators (e.g., [3, 4]), the proposed design adds tuning functionality to piezoelectric resonators by employing separate electrostatic electrodes. Although the tuning range of the proposed design is relatively low due to the large gap imposed by the fabrication technology, it could be significantly

improved by using a technology with narrower lateral gaps. The structure also allows for various frequency devices to be fabricated concurrently, unlike FBARs. It is worth mentioning that the present structure is achieved in a relatively simple commercial MEMS technology, and that its performance could be enhanced by implementation in a technology with smaller critical dimensions.

7.8. Conclusion

This work demonstrates the first use of transverse piezoelectric actuation to excite a bulk-mode silicon resonator in the wine-glass mode to offer a desirable combination of reasonably high quality factor and frequency, along with the lowest motional resistance amongst comparable disk resonators without requiring any DC voltage for operation. The device of this work is also the first demonstrated wine-glass bulk-mode disk resonator built using a commercially available low-cost MEMS fabrication process. The device is measured to have a resonance frequency of ~15 MHz and, a quality factor of ~2,000 in atmospheric pressure increasing to ~5,000 in a 100 mTorr vacuum, while exhibiting a temperature coefficient of ~ -40 ppm/^{o}C. External capacitive electrodes were also successfully used to optionally adjust the frequency of resonance through DC voltage tuning and thus combine the advantages of both electrostatic and piezoelectric actuation.

Table 7.2: Comparison between the resonator proposed in this work and state-of-the-art

	Type	Mode	Freq. (MHz)	Quality factor	Transmission (dB)	R_x* (Ω)	V_{DC} (V)	Freq. tuning	Features
[3]	Cap./ piezo.	Wine-glass	51	1 µm wide supports			-	×	AlN disk resonators with capacitive-piezoelectric actuation/ sensing electrodes above/ below the structure with 260 nm gap and anchor beams of 1-2 µm width
				12,748	-34	4.9 k			
				2 µm wide supports					
				7,076	-40	9.9 k			
[4]	Cap./ piezo.	Radial	300	250 nm gap and 1.2 µm anchor			-	×	AlN capacitive-piezoelectric disk resonators with ON/ OFF switching capability utilizing capacitive electrodes above / below the structure with 120-250 nm gap and center anchors
				8,800 (vacuum)	-40	9.9 k			
				120 nm gap and 1.8 µm anchor					
				6,600 (vacuum)	-30	3.01 k			
[6]	Cap.	1ary elliptic 2ary elliptic	2.9 5.9	66,000 (1 mTorr) 100,000 (1 mTorr)	-53 -31	44.6 k 3.4 k	10	✓	Bulk-mode disk gyros in 111 and 100 single-crystalline Si with 180-250 nm capacitive gaps
[7]	Cap.	Wine-glass	210 1520	7,700 (200 µTorr) 3,000 (200 µTorr)	-	9.16 k 791.6 k	15 5	✓	Poly-Si wine-glass mode ring resonators with 63-85 nm capacitive gaps and 1.6 µm wide anchor beams
[11]	Cap.	Lamé	6.35	1.6 M (36 µTorr) 5,100 (atm.)	-40	9.9 k	50	✓	Square Lamé-mode capacitive resonator with Si structural layer
[12]	Cap.	2ary elliptic	8.14	-	-	-	25	✓	Dodecagon disk gyro with Si structural layer
[13-14]	Cap.	2ary elliptic	1.5	33,000 (10 mTorr)	-50	31.5 k	50	✓	Dodecagon disk gyro with combs utilizing a Si structural layer
This work	Piezo	Wine-glass	14.63	10 µm wide supports			-	✓	Si wine-glass disk resonators using piezoelectric actuation / sensing and electrostatic frequency tuning and anchor beams of 10 µm width
				4,894** (100 mTorr)	-22	1.2 k			

*The motional resistance R_x is estimated based on $R_x = 100\ (1/T_{max} - 1)$, if not reported, where T_{max} is the transmission at resonance. This assumes a measurement characteristic impedance of 50Ω.

**The quality factor of the device is limited by the 10 µm support width imposed by the fabrication technology. It could be improved by using another technology which allows for smaller support widths in order to reduce the anchor loss as shown in [3].

7.9. References

[1] F. Nabki, K. Allidina, F. Ahmad, P. -V. Cicek, and M. N. El-Gamal, "A Highly Integrated 1.8 GHz Frequency Synthesizer Based on a MEMS Resonator," *IEEE Journal of Solid-State Circuits*, vol. 44, no. 8, pp. 2154-2168, August 2009.

[2] Q. -X. Su, P. Kirby, E. Komuro, M. Imura, Q. Zhang, and R. Whatmore, "Thin-Film Bulk Acoustic Resonators and Filters Using ZnO and Lead–Zirconium–Titanate Thin Films," *IEEE Transactions on Microwave Theory and Techniques*, vol. 49, no. 4, pp. 769-778, April 2001.

[3] Li. -W. Hung and C. Nguyen, "Capacitive-Piezoelectric AlN Resonators with Q>12,000," *Proceedings of the IEEE International Conference on Microelectromechanical Systems*, pp. 173-1766, January 2011.

[4] R. Schneider and C. Nguyen, "On/Off Switchable High-Q Capacitive-Piezoelectric AlN Resonators," *Proceedings of the IEEE International Conference on Microelectromechanical Systems*, pp. 1265-1268, January 2014.

[5] C. Zuo, N. Sinha, and G. Piazza, "Very High Frequency Channel-Select MEMS Filters Based on Self-Coupled Piezoelectric AlN Contour-Mode Resonators," *Journal of Sensors and Actuators A: Physical*, vol. 160, pp. 132-140, April 2010.

[6] H. Johari and F. Ayazi, "High Frequency Capacitive Disk Gyroscopes in (100) and (111) Silicon", *Proceedings of the IEEE International Conference on Microelectromechanical Systems*, pp. 47-50, January 2007.

[7] Y. Xie, S. Li, Y. Lin, Z. Ren, and C. Nguyen, "1.52-GHz Micromechanical Extensional Wine-Glass Mode Ring Resonators", *IEEE Transactions on Ultrasonics, Ferroelectrics and Frequency Control*, vol. 55, no. 4, pp. 890-907, May 2008.

[8] J. Clark, W.-T. Hsu, M. Abdelmoneum, and C. Nguyen, "High-Q UHF Micromechanical Radial Contour-Mode Disk Resonators", *Journal of Microelectromechanical Systems*, vol. 14, no. 6, pp. 1298-1310, December 2005.

[9] J. Wang, Z. Ren, and C. Nguyen, "1.156-GHz Self-Aligned Vibrating Micromechanical Disk Resonator", *IEEE Transactions on Ultrasonics, Ferroelectrics and Frequency Control*, vol. 51, no. 12, pp. 1607-1628, December 2004.

[10] Y. -W. Lin, S. Lee, S. -S. Li, Y. Zie, Z. Ren, and C. Nguyen, "Series-Resonant VHF Micromechanical Resonator Reference Oscillators", *IEEE Journal of Solid-State Circuits*, vol. 39, no. 12, pp. 2477-2491, December 2004.

[11] L. Khine, M. Palaniapan, and W. -K. Wong, "6 MHz Bulk-Mode Resonator with Q Values Exceeding One Million", *Proceedings of the IEEE International Conference on Solid-State Sensors, Actuators and Microsystems*, pp. 2445-2448, June 2007.

[12] M. Elsayed, F. Nabki, and M. El-Gamal, "A 2000 °/sec Dynamic Range Bulk Mode Dodecagon Gyro for a Commercial SOI Technology", *Proceedings of the IEEE International Conference on Electronics, Circuits, and Systems*, pp. 264-267, December 2011.

[13] M. Elsayed, F. Nabki, and M. El-Gamal, "A Combined Comb/Bulk Mode Gyroscope Structure for Enhanced Sensitivity", *Proceedings of the IEEE International Conference on Microelectromechanical Systems*, pp. 649-652, January 2013.

[14] M. Elsayed, F. Nabki, and M. El-Gamal, "A Novel Comb Architecture for Enhancing the Sensitivity of Bulk Mode Gyroscopes", *Sensors*, vol. 13, pp. 16641-16656, December 2013.

[15] D. Serrano, R. Tabrizian, and F. Ayazi, "Electrostatically Tunable Piezoelectric-on-Silicon Micromechanical Resonator for Real-Time Clock," *IEEE Transactions on Ultrasonics, Ferroelectrics and Frequency Control*, vol. 59, no. 3, pp.358-365, March 2012.

[16] M. Y. Elsayed, P. -V. Cicek, F. Nabki, and M. N. El-Gamal, "Bulk Mode Disk Resonator with Transverse Piezoelectric Actuation and Electrostatic Tuning," *Journal of Microelectromechanical Systems*, submitted June 2015.

[17] S. D. Senturia, "*Microsystem Design*," Springer, 2001, pp. 134, 263, 572.

[18] C. Acar and A. Shkel, "*MEMS Vibratory Gyroscopes: Structural Approaches to Improve Robustness*," Springer, 2009, pp. 114.

[19] "*PiezoMUMPs Design Handbook*," rev. 1.3, MEMSCAP, available at: http:// www.memscap.com, 2014.

[20] E. Hosseinian, P. Theillet, and O. Pierron, "Temperature and Humidity Effects on the Quality Factor of a Silicon Lateral Rotary Micro-resonator in Atmospheric Air," *Journal of Sensors and Actuators A: Physical*, vol. 189, pp. 380-389, September 2012.

[21] P. Tsilingiris, "Thermophysical and transport properties of humid air at temperature range between 0 and 100 ºC," *Journal of Energy Conversion and Management*, vol. 49, pp. 1098-1110, November 2007.

Part IV:

Fabrication Process

Chapter 8 Above-IC Compatible Silicon Carbide Technology with Sub-Micron Lateral Gaps

8.1. Introduction

As noted earlier in Chapter 1, surface micromachining is a very important micro-fabrication process, as it allows for more fabrication flexibility, especially for integrating micromachined devices with electronic circuits. This is very advantageous in order to reduce parasitics between the devices and their interface circuitry, compared to side-by-side co-fabrication approaches. This consequently would allow for improved performance. It is usually a challenge to get good structural material properties, while abiding by the processing temperature constraints for post-processing above standard ICs [1-11]. Former members of our team have developed a surface micromachining technology based on silicon carbide for above-IC integration, discussed in details in [9-11]. The process utilizes DC sputtered amorphous silicon carbide as it provides superior mechanical properties, namely high Young's modulus, high acoustic velocity, and low stress compared to materials used for micromachining technologies utilized in the literature, as shown in Table 8.1. This is achieved while maintaining the lowest processing temperature, which makes it ideally suited for post-processing above standard CMOS substrates. The process features vertical gaps using a sacrificial polyimide layer between a bottom metal layer and a SiC structural layer on top.

Submicron lateral transduction gaps are generating high interest by improving actuation / sensing efficiency of micro-resonators and sensors. This is clear from the discussions about the presented designs in the previous chapters, where reducing the gap would result in significant improvement in the sensors' sensitivity as well as the signal level and motional resistance of electrostatic resonators. Furthermore, the capability of creating both lateral and vertical gaps would allow increasing the capacitive sensing capability, for example: increasing the number of sensing axes for the combined/ magnetometer accelerometer presented earlier in Chapter 5, by introducing capacitive electrodes around the main structure.

Table 8.1: Comparison between common structural materials utilized in state-of-the-art surface micromachining technologies

Material	SiC		SiGe	SiN			Our SiC
Type	poly 3C	amorphous	poly				amorphous
Doping	N		P				
Dep. method	LPCVD	PECVD	PECVD	LPCVD	PECVD		DC sputtering
Dep. T. (°C)	775-825	870	450	800	200	300	<200
Dep. Rate (nm/min)			fast	2	6.1		22
Thickness (um)	0.5	0.5	10	0.45	0.5	~0.6	2
Mech. prop.							
Young's mod. (GPa)	280	232	140	260	140	198	260
Poisson's ratio	0.237						
Stress (MPa)	306	-607	<70	200	-400	~200	<50
Fracture Strength (GPa)				7-8	16	22	18
Density (Mg/m^3)	2.2*	4.7*	3-4.5*		2.6	2.8	2.7
Acoustic velocity (km/sec)	~11.25 [9]	~7 [9]	5.6-6.8*	9.81**	7.3	8.4	9.81
Elec. prop.							
Resistivity (Ω.cm)	0.075		0.01				500
CMOS compatible	×	×	✓ ?	×	✓	✓	✓
References	[1, 2]	[2]	[3 ,4]	[5, 6]	[7, 8]	[7, 8]	[9-11]

*Value not found in the references. Therefore, an approximate value obtained from the web to calculate the acoustic velocity/ or calculated based on it.
**Value based on the density of the PECVD material.

Therefore, the focus in this chapter is augmenting the capabilities of our low temperature silicon carbide surface micromachining technology by adding sub-micron lateral gap capability while maintaining the lowest processing temperature, which makes it ideally suited for post-processing capacitive sensors and resonators above standard CMOS substrates. While [3 ,4] claim 0.35 µm CMOS technology integrability, its temperature of 450 °C may raise issues with modern semiconductor nodes, featuring copper interconnects or low-k dielectrics.

8.2. Literature Review about Lateral Gap Fabrication Processes

In [12], extensional wine-glass ring resonators are presented utilizing polysilicon surface micromachining. The process uses two structural polycrystalline silicon layers and a sacrificial oxide layer to achieve phosphorus-doped polysilicon structures with polysilicon side electrodes, and with nano-scale (as low as 63 nm) electrode to resonator lateral gaps. The resonating structures are released using wet hydrofluoric (HF) etching, which limits the yield of the process to 85 %. Figure 8.1 (a) shows SEM micrographs of some of the fabricated devices, illustrating the lateral gap. Cross-sections illustrating the fabrication process of the devices are shown in Figure 8.1 (b). The process includes process steps requiring temperatures as high as 1050 °C (for polysilicon and oxide deposition), which makes it not suitable for above-IC integration.

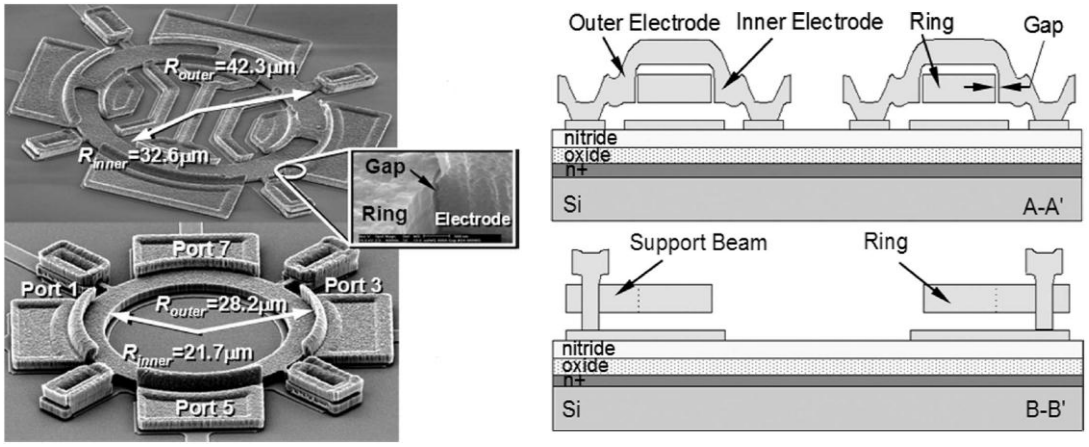

(a) (b)

Figure 8.1: (a) SEM micrographs of devices presented in [12], and (b) cross-sections illustrating the fabrication process.

Similar processes are introduced in [13] and [14], with diamond [13] and polycrystalline-SiC [14] as the structural material respectively, offering superior properties such as high stiffness and acoustic velocity. The processes involve high temperature fabrication steps as well as wet HF release.

While these processes utilize surface micromachining, [15] combines surface and bulk methods, where deep silicon trenches are patterned to form a silicon structure. Then, the trenches are filled with sacrificial oxide and another polysilicon structural layer. The structures finally undergo a wet HF vapor step to etch the sacrificial oxide layer and release the structures, allowing for their free motion. Figure 8.2 illustrates the process flow used on silicon substrates as well as SEM micrographs of a ring gyroscope and a beam resonator fabricated in this process. Alternatively, a similar process flow was used on SOI substrates

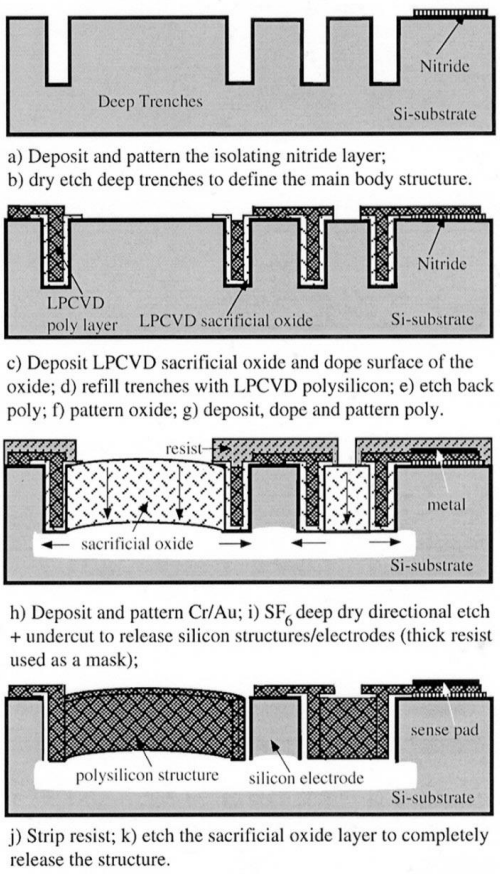

(a)

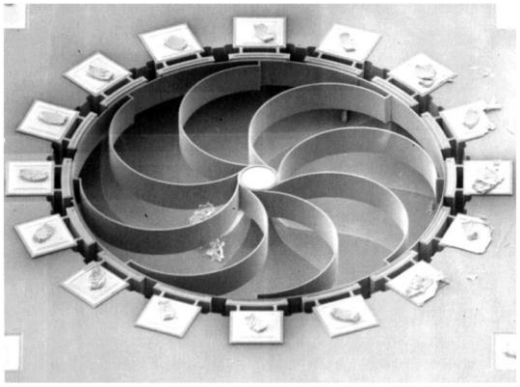

(b)

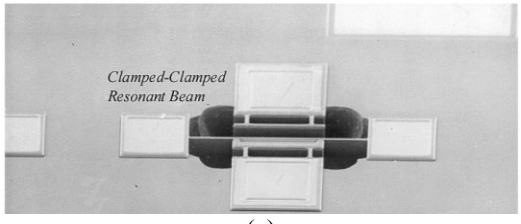

(c)

Figure 8.2: (a) Fabrication process flow presented in [15], SEM micrographs of devices presented: (b) ring gyroscope, and (c) clamped-clamped beam resonator.

to realize bulk mode gyroscopes (e.g., [16, 17]). The modified process flow for SOI substrates is shown in Figure 8.3. Figure 8.4 (a) illustrates an SEM micrograph of one the BAW gyroscopes presented in [16]. The device is composed mainly of a central disk structure with a central oxide anchor. The signal is conducted to the central disk using traces of polysilicon as shown in Figure 8.4 (a). Figure 8.4 (b) illustrates the 250 nm lateral gap realized using the sacrificial oxide layer.

(a) Grow and pattern initial oxide, etch the trenches

(b) Deposit sacrificial oxide, fill with LPCVD polysilicon, and pattern oxide

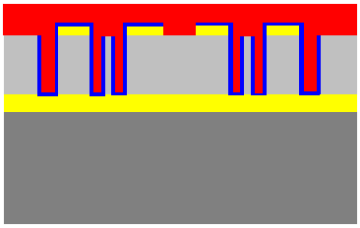

(c) Deposit LPCVD polysilicon, boron doped, and anneal

(d) Pattern polysilicon, etch silicon using Bosch process, and release using HF

Figure 8.3: Fabrication process flow described in [16].

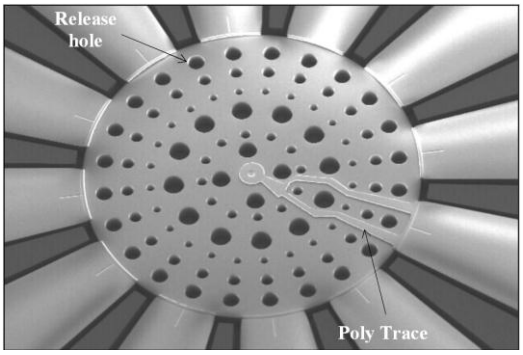

(a)

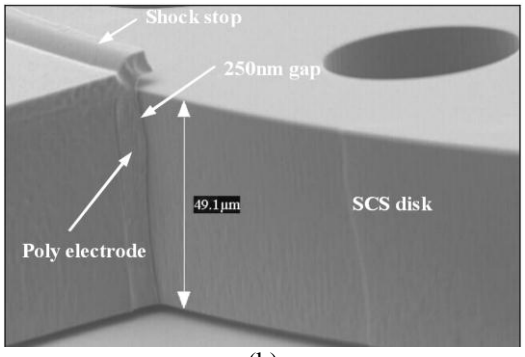

(b)

Figure 8.4: (a) SEM micrograph of the BAW gyroscope presented in [16], and (b) SEM micrograph illustrating the released gap between the polysilicon electrode and the central single-crystalline silicon disk structure.

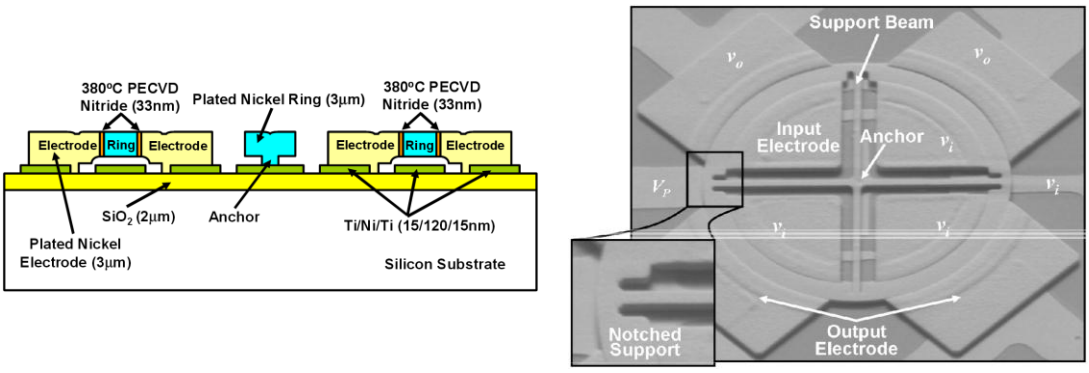

(a) (b)

Figure 8.5: (a) Cross-section illustrating the fabrication process of the ring resonator presented in [18], and (b) SEM micrograph of the device presented.

All aforementioned technologies are incompatible with above-IC integration due to high temperature fabrication steps, which are not compatible with the thermal budget required for above-IC post processing. Furthermore, some of the aforementioned processes feature bulk micromachining steps which are also not compatible with above-IC fabrication.

In [18], ring resonators are presented, where two layers of electroplated nickel are utilized as two structural layers. One for realizing the resonator ring structure and the other for the actuation and sensing electrodes. The two layers are separated by a thin PECVD nitride gap, which remains as a solid gap without being etched. The processing complies with above-IC requirements, but does not allow the implementation of non-solid gaps. Figure 8.5 (a) shows a cross-section illustarting the fabrication process used, and Figure 8.5 (b) shows an SEM micorgraph of one of the fabricated ring resonators.

In [19], bulk mode wine-glass and Lamé mode resonators are presented. They are surface micromachined utilizing boron-doped polycrystalline LPCVD GeSi as a structural layer. A 40 nm thick layer of PECVD oxide is used as a sacrificial layer for realizing the electrode to resonator lateral gap. The oxide is released in the end using an HF wet etch release step. Figure 8.6 illustrates the process flow steps used and Figure 8.7 shows an SEM micrograph of one of the resonators presented. The maximum processing temperature

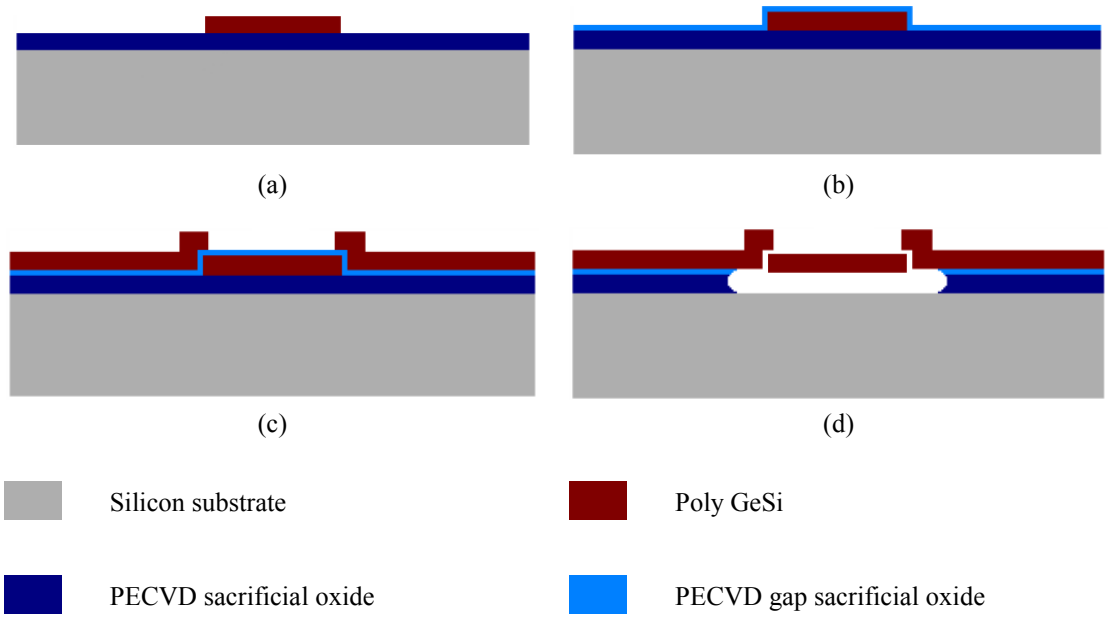

Figure 8.6: Fabrication process flow presented in [19].

of the presented process is 450 °C. However, this temperature may raise issues with modern semiconductor nodes, featuring copper interconnects or low-k dielectrics.

All the previously mentioned lateral processes involve fabrication steps that may prevent them from being used for above-IC integration or make them unideal for this purpose. This is the main motivation for our work, as detailed in the rest of this chapter, to develop a process that achieves nano-scale lateral gaps while maintaining low processing

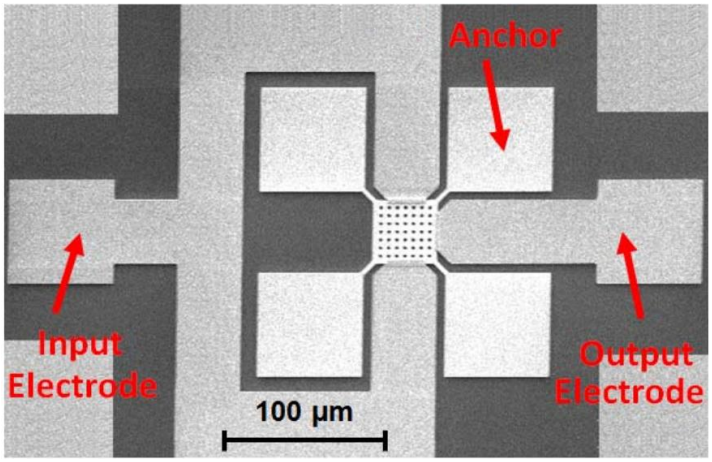

Figure 8.7: SEM micrograph of a Lamé mode resonator presented in [19].

temperature as well as superior mechanical properties. The first surface micromachining technology based on amorphous silicon carbide (a-SiC) for above-IC integration of electrostatic devices, especially bulk mode, featuring submicron lateral transduction gaps is presented. Processing is optimized for full compatibility with commercial CMOS processes, with the lowest reported fabrication temperature amongst comparable technologies. a-SiC structural layers, combining high stiffness and fracture strength, are used, as they have been demonstrated to enable high performance microsystems [9-11]. Two polymer-based sacrificial layers define vertical gaps and sub-micron lateral gaps, without requiring high resolution photolithography, and are ultimately dry released to prevent stiction, a challenging issue with wet release methods.

First, the initial version of the process flow is discussed briefly. Then, the details of the fabrication process challenges are explained, with the optimized solutions that we devised. Afterwards, the final version of the process flow is explained and the measurement results for some early prototype devices fabricated using our technology are discussed in details as well as the test setups used, followed by the conclusion and future works.

8.3. SiC Lateral Gap Initial Fabrication Process

The process starts with dielectric passivated wafers. The wafers can be wafers with electronics already built and passivated (with nitride for example). For process development purposes, silicon wafers covered with a layer of thermally grown oxide are used here. The passivation is necessary to prevent shorts between electrical interconnects on the MEMS side. The process is illustrated in Figures 8.8 and 8.9. First, a 60 nm thick layer of aluminum is deposited by DC sputtering, and wet patterned to form interconnects, as shown in Figure 8.8 (a). A 1 μm sacrificial polyimide layer is then spin coated and cured at 200 °C to define vertical gaps. The polyimide is then patterned and etched using oxygen RIE and photoresist as a mask to allow anchoring of the disk resonator stem, as shown in Figure 8.8 (b). Afterwards, the disk stack layers are deposited through sputtering: a 20 nm chromium layer, a 60 nm thick aluminum bottom conductive layer, a 2 μm a-SiC structural layer, a 60 nm thick layer of aluminum as a top conducting layer, and finally a hard mask of a 600 nm thick chromium layer as shown in Figure 8.8 (c). The chromium and aluminum

are wet patterned. Then, the SiC is etched using RIE in NF_3 utilizing chromium as a hardmask and stopping on the underlying aluminum layer. The underlying aluminum is then wet etched. The 20 nm chromium layer acts as an etch stop for the aluminum etch as well as an adhesion layer. The chromium hard mask is then stripped and the adhesion layer is etched, as shown in Figure 8.8 (d). Next, a 120 nm conformal layer of CVD parylene is deposited to define lateral gaps, as shown in Figure 8.8 (e). The parylene and the underlying polyimide are then patterned to define the anchors of the second SiC structural layer using O_2 RIE, as shown in Figure 8.9 (f). The second structural multi-material stack forming the electrodes is then sputtered, which is composed of a 10 nm thick chromium adhesion layer, a 300 nm thick aluminum metallization layer, a 2 μm a-SiC structural layer, a 60 nm thick aluminum top metallization layer, and a 600 nm thick chromium hardmask layer, as shown in Figure 8.9 (g). The top chromium and aluminum layers are patterned using wet chemical etchants. Then, the a-SiC is etched as previously described in NF_3 RIE to form the suspended electrodes, with the etch stopping at the aluminum. The chromium hardmask is then wet stripped, as shown in Figure 8.9 (h). Afterwards, aluminum is wet patterned to form electrical interconnects and pads, as shown in Figure 8.9 (i). Finally, the devices are released by O_2 plasma isotropic etching, which clears all the remaining polymers, as shown in Figure 8.9 (j).

8.4. Fabrication Challenges

During process development, some issues arose with the initial suggested process flow, explained in the previous section. In this section, the issues are going to be explained in details, as well as the solutions reached.

8.4.1. Polymer Etching Residues

The fabrication process involves two important polymers (polyimide and/ or parylene) patterning steps in order to define the anchors of the two silicon carbide structural layers to the substrate. The original plan was to pattern the polymers through O_2 RIE using standard positive photoresist as a mask. This method was found to work well for thin polymer layers (< 0.5 μm), which require relatively short etch times. The masking resist could then be easily stripped in acetone.

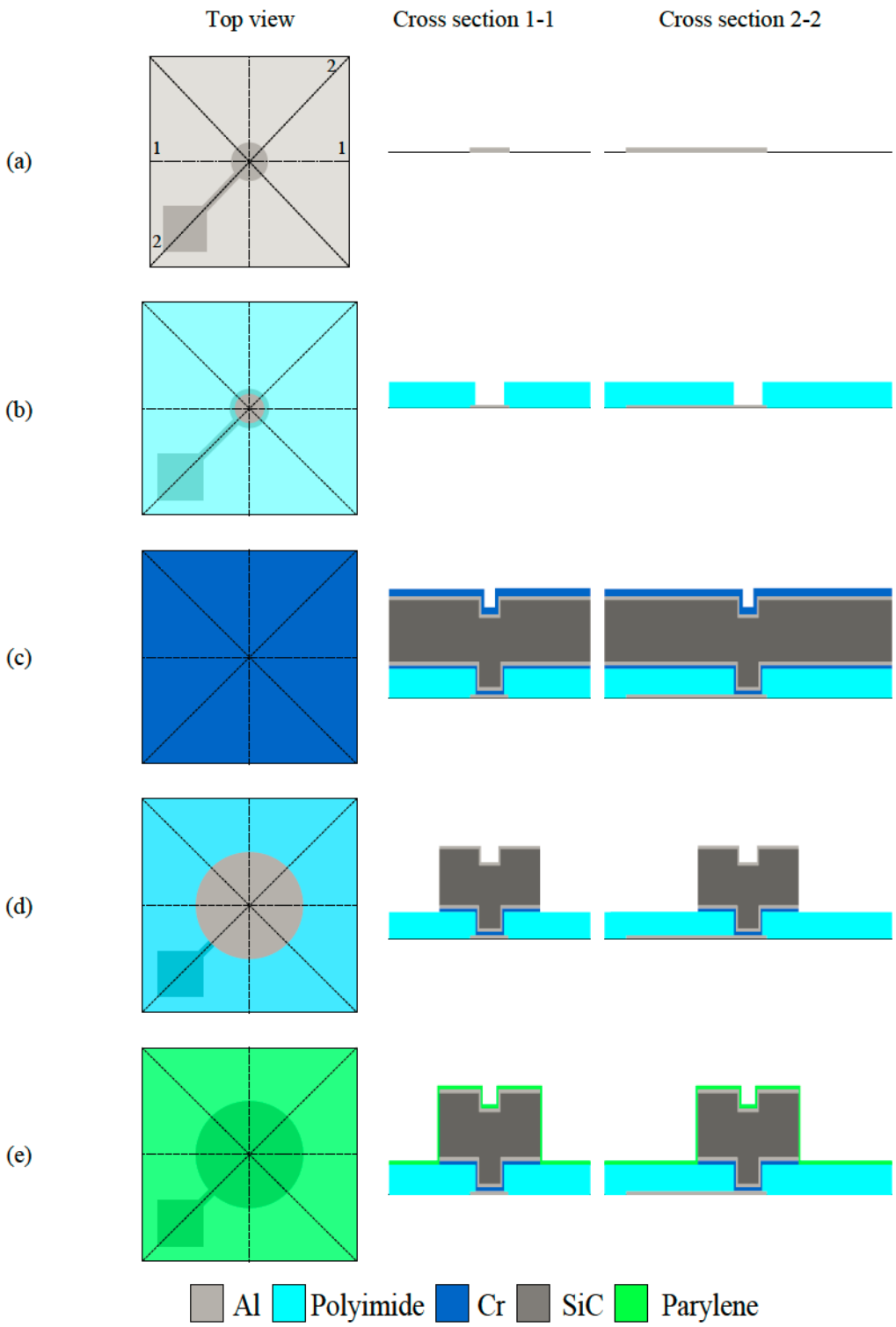

Figure 8.8: Initial process flow of the lateral gap SiC process, shown on a disk resonator as an example (part 1).

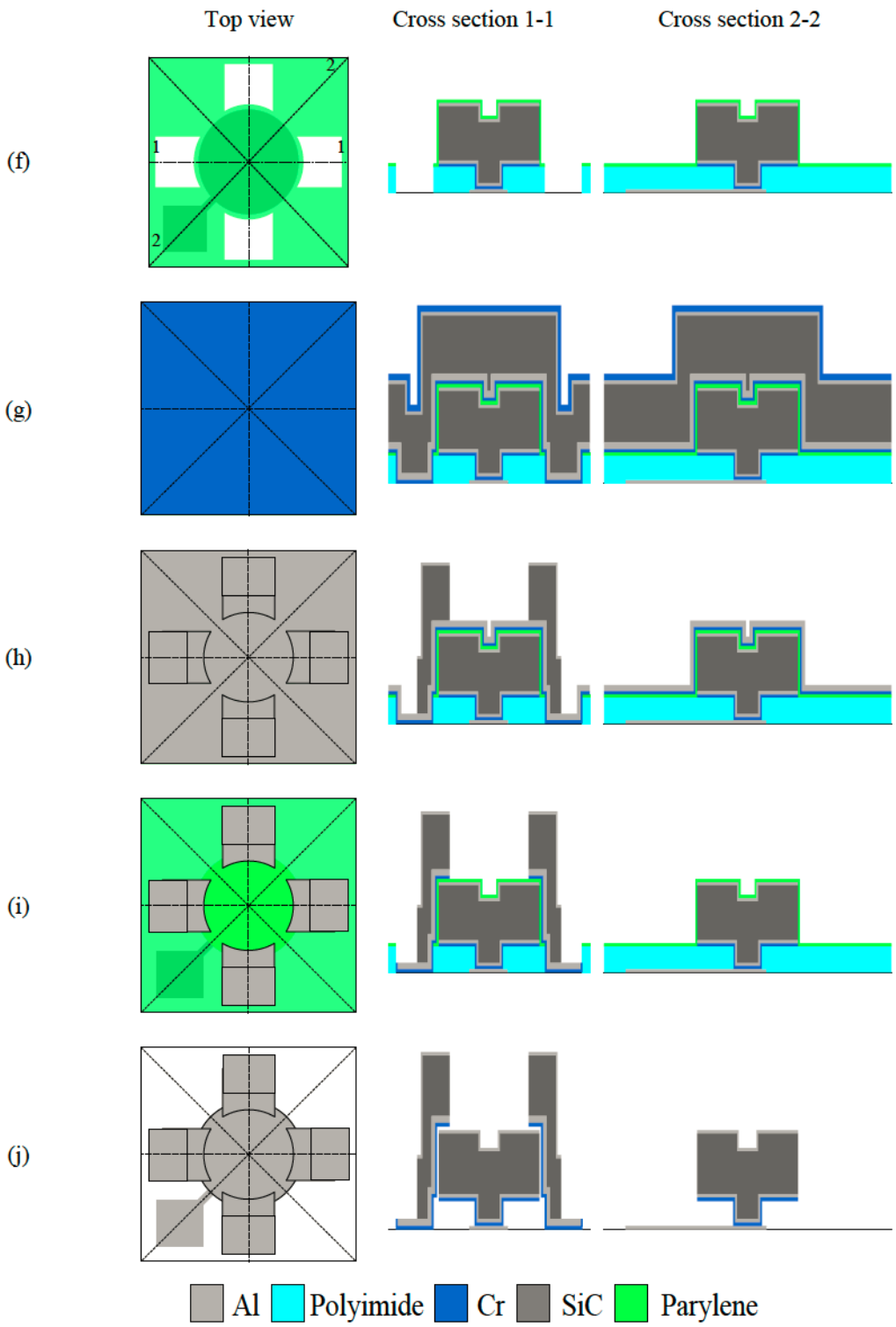

Figure 8.9: Initial process flow of the lateral gap SiC process, shown on a disk resonator as an example (part 2).

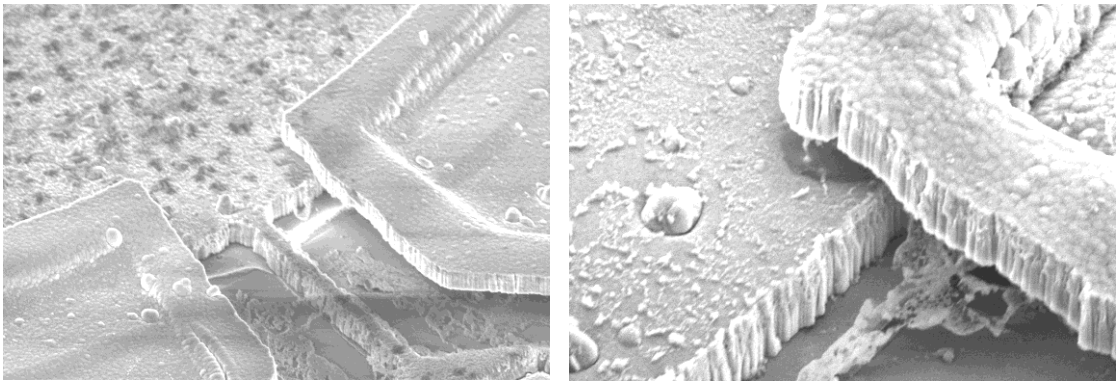

(a) (b)

Figure 8.10: Residues arising from using a photoresist mask during the polymer O_2 RIE: (a) image showing electrodes and support of a wine-glass disk resonator, and (b) zoomed image for the electrode to disk gap.

However, for the 1 μm polyimide used in the process, the RIE etch time, when the photoresist is exposed to oxygen plasma, needed to be longer (~500 sec). This time was enough to burn the masking resist making it difficult to remove afterwards, as well as creating some residues that redeposit on the unmasked areas masking them from further etching. Therefore, the surfaces after the polymer etch and resist stripping was not clean and had significant residues, as shown in Figure 8.10. In order to mitigate these residues, the masking material during this RIE step needed to be changed. For this purpose, a 60 nm DC sputtered aluminum layer is used. First, the aluminum is wet patterned in a PAN etch

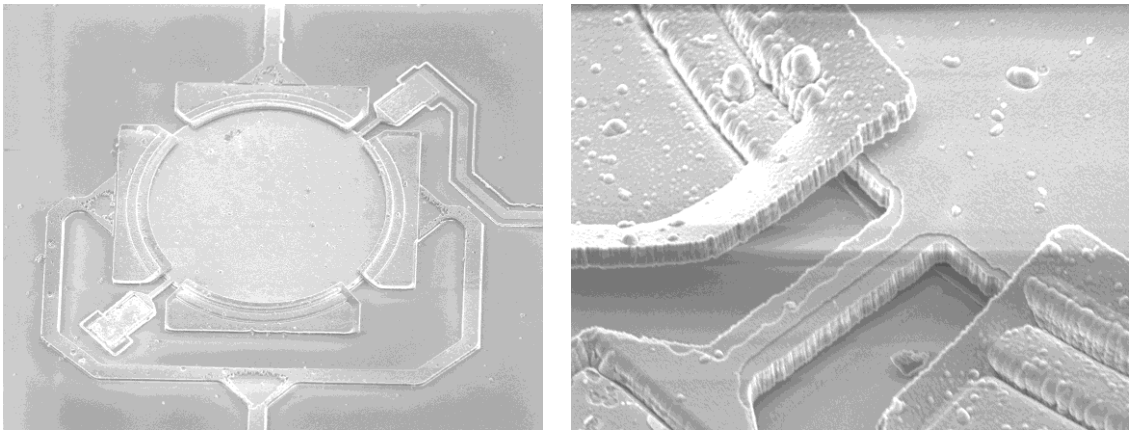

(a) (b)

Figure 8.11: Clean etch results after using an aluminum hard mask instead of a photoresist mask for the polymer O_2 RIE steps: (a) wine-glass disk resonator and (b) zoomed image for the electrodes and support.

solution, using positive photoresist as a mask. Then, the photoresist is stripped in acetone. Afterwards, the aluminum is used as a hard mask during the polymer O_2 RIE step. Finally, the aluminum hard mask is stripped using the same wet etch method. Using an aluminum hard mask leads to very clean results and avoids the residues that used to result from the resist mask before, as shown in Figure 8.11.

8.4.2. Planarization Layer

The process flow involves the deposition of the second structural stack above the first structural layer and then patterning the second structural layer to form the electrodes as shown in Figure 8.9 (g-i). The first structural layer is already patterned, forming the structures. Therefore, when the second structural stack is deposited, it takes the same topography as the first structural layer, and goes into the patterned corners, as shown in Figure 8.12 (a). The SiC is etched using RIE which is highly directional, and therefore when the second SiC is patterned, thin hillocks are left behind in the corners of the first

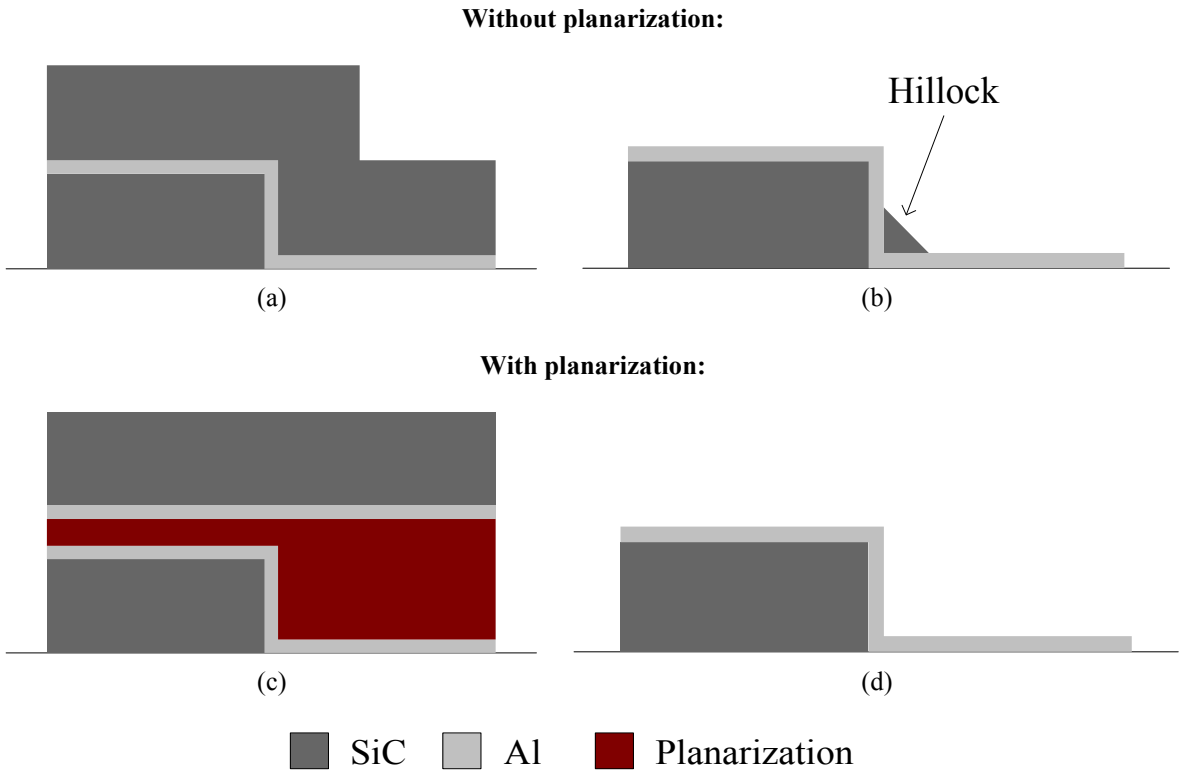

Figure 8.12: Simplified schematic illustrating the SiC hillocks problem: (a), (b) show cross sections before and after the second SiC RIE without planarization, (c) and (d) show cross sections before and after the second SiC RIE with planarization, respectively.

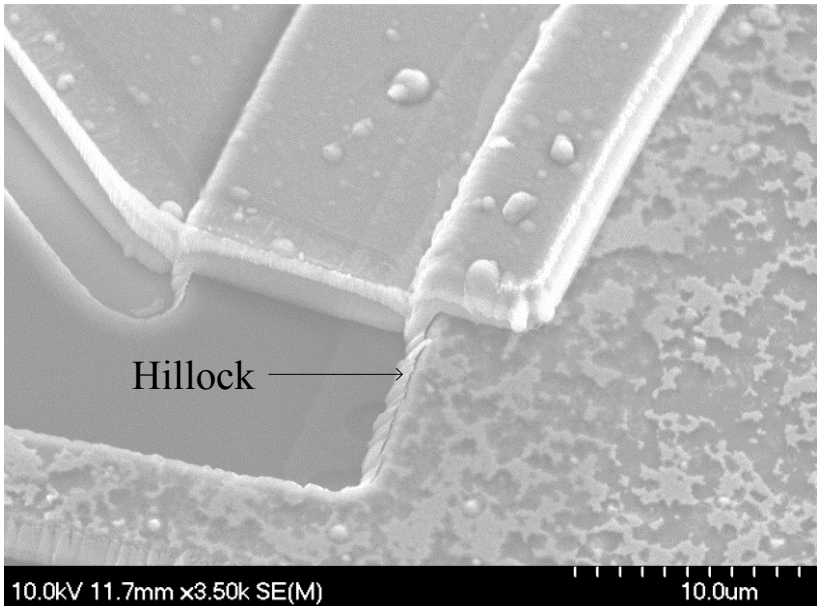

Figure 8.13: SEM micrograph illustrating the SiC hillock problem.

SiC topography, as illustrated in Figure 8.12 (b). These hillocks are metalized and therefore create low resistance paths, shorting the structures together, as illustrated in the SEM micrographs shown in Figure 8.13. The main problem is that the corners of the first structural layer topography get filled with the second SiC layer. This was mitigated by adding a polymer planarization layer in order to fill the sharp corners. The planarization layer is patterned in order to be cleared only in the areas with the second structural layer patterns. The polymer is released in the end without leaving any hillocks, as illustrated in Figure 8.12 (c, d).

Several polymers were tried for the planarization layer, as SU-8 negative photoresist, polyimide, and baked S1813 positive photoresist. SU-8 was found to be very difficult to be clearly removed later for release, as shown in the SEM micrograph in Figure 8.14. Polyimide was found to work fine for planarization. However, its processing further complicates the fabrication process, as it needs an aluminum hard mask, as detailed in the previous section. S1813 was selected for use, as it is easily patterned by lithography and development. The layer requires a hot plate bake at 170 ^{o}C for 30 minutes, in order to withstand the following SiC sputter step. Figure 8.15 shows an SEM micrograph of a fabricated device using S1813 planarization after release showing no hillocks and clean release.

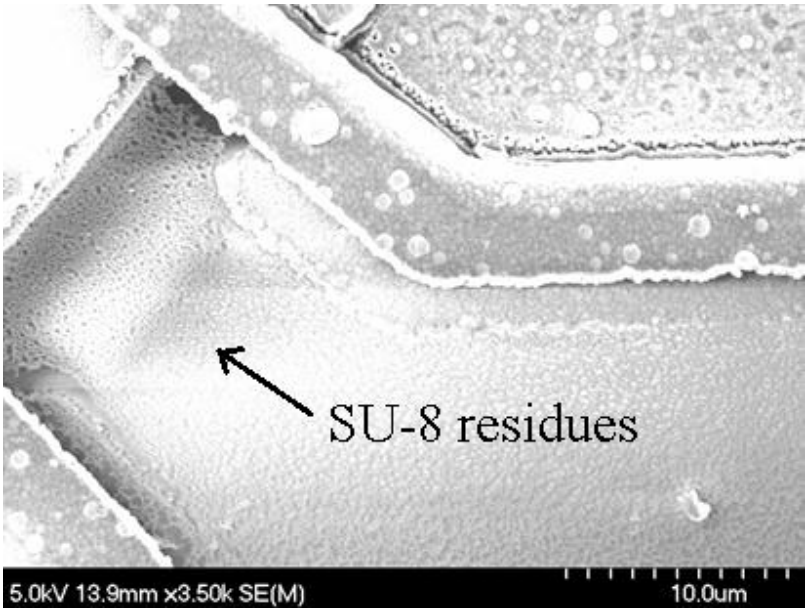

Figure 8.14: SEM micrograph illustrating SU-8 residues after release.

8.4.3. Vertical Spacer Layer

According to the initial process flow presented earlier, the lateral gap sacrificial layer is deposited directly on the structures built in the first structural layer. Then, the second structural layer stack is processed after patterning the anchors. The patterns of the

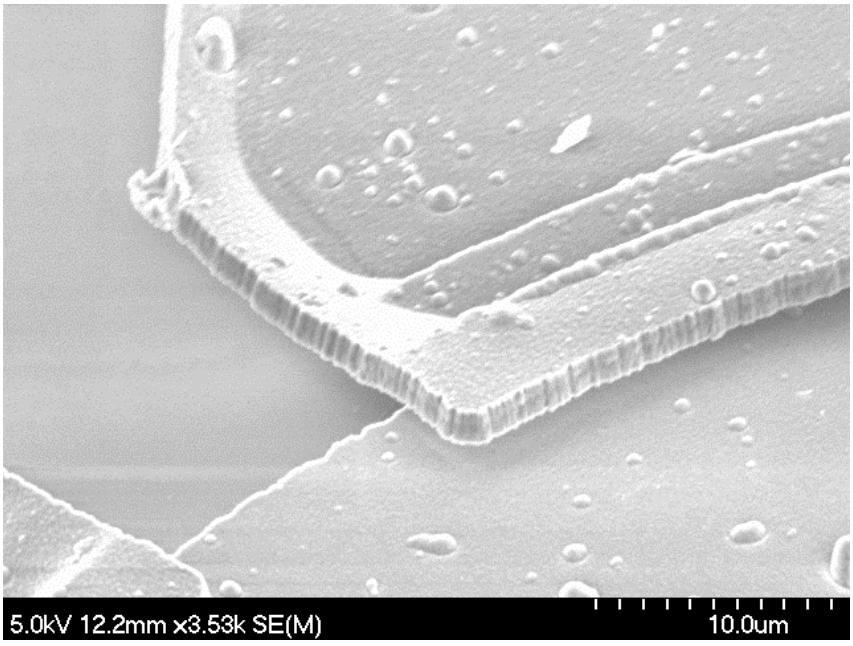

Figure 8.15: SEM micrograph illustrating the surface with no hillocks and clean release after using S1813 planarization.

second structural layer has to overlap and extend over the first structural layer patters in order to account for any misalignment issues. This results in an undesired capacitance (C_v) between the extended part of the electrode and the resonating disk structure, besides the desired capacitance (C_l) across the lateral gap which is used for actuation and sensing, as shown in Figure 8.16.

Bulk mode devices are usually much stiffer in the lateral direction, which is the main direction of actuation and sensing, than the vertical out-of-plane direction. Therefore, upon applying the DC polarization voltage for electrostatic actuation, there is a risk that the electrode and disk will experience electrostatic pull-in vertically in the overlap area. Consequently, for proper operation of the device, the vertical pull-in voltage (V_{PI}) must be lower than the polarization voltage (V_P), as expressed by:

$$V_{PI} < V_P . \tag{8.1}$$

The pull-in voltage can be expressed as [20]

$$V_{PI} = \sqrt{\frac{8k_v g_v^3}{27\varepsilon_0 A_{OL}}}, \tag{8.2}$$

where k_v is the spring constant in the vertical (out-of-plane) direction, g_v is the vertical gap between the extended part of the electrode and the disk top surface, ε_0 is the permittivity of free space, and A_{OL} is the overlap area between the electrode and the disk. Since, bulk mode devices have much lower stiffness in the out-of-plane direction than the in-plane direction. Therefore, it is very difficult to ensure the necessary aforementioned condition regarding the vertical pull-in, expressed in (8.1), while maintaining reasonably low polarization

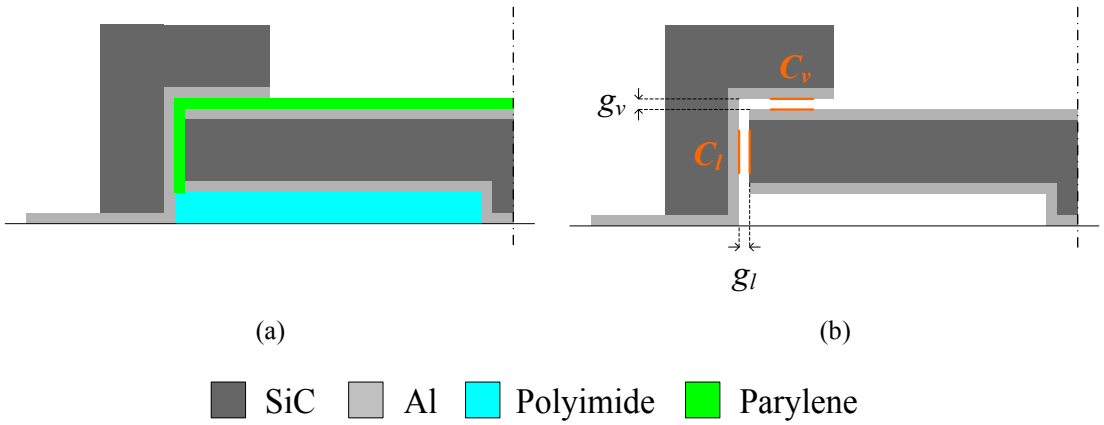

Figure 8.16: Schematic illustrating the lateral and vertical gaps between the electrode and the disk resonator structure: (a) before release, and (b) after release.

voltage if the lateral gap (g_l) and vertical gap (g_v) are equal (defined by the parylene thickness), as in the initial process flow.

This can be solved by applying a vertical spacer layer above the first structural stack and patterning it with the stack using the same mask to avoid any alignment problems. Parylene is then deposited and patterned. Afterwards, the second structural layer is processed, as illustrated in Figure 8.17. This allows for independent control of the lateral and vertical gap thicknesses, by controlling the thicknesses of the parylene and spacer layers, as shown by:

$$g_l = t_p \,, \tag{8.3}$$

$$g_v = t_p + t_s \,, \tag{8.4}$$

where t_p is the parylene thickness, and t_s is the spacer layer thickness. As the planarization material, photoresist was selected as the vertical spacer material. A bake at 170 °C for 30 minutes on a hot plate is necessary, in order to withstand the subsequent SiC sputter step. Polyimide is also a viable option for the spacer layer.

8.4.4. SiC to Aluminum Contact Resistance Optimization

After fabrication and testing of some resonators based on the process flow explained before while applying the process modifications to solve the aforementioned issues, it was found that the devices exhibit significant series resistance which limits the quality factor and increases the transmission loss, as explained in details later in section 8.6.

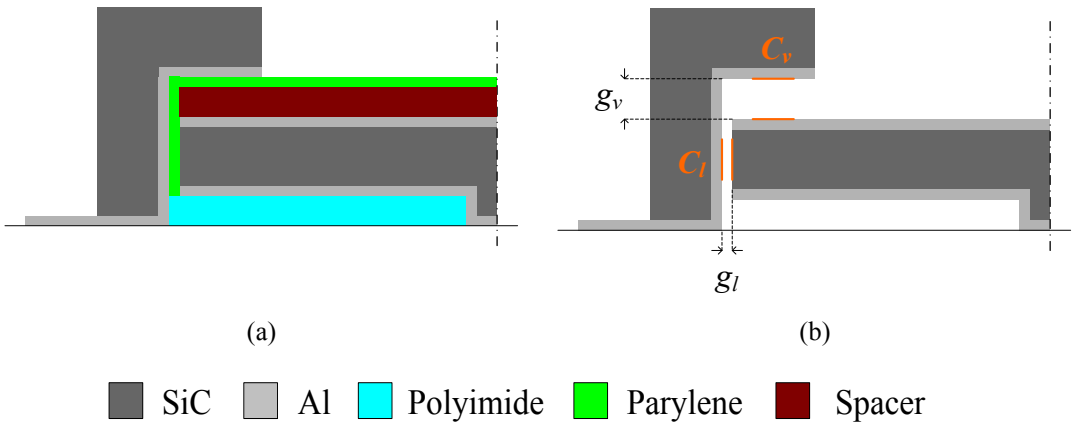

Figure 8.17: Schematic illustrating the lateral and vertical gaps between the electrode and the disk resonator structure after using a vertical spacer layer: (a) before release, and (b) after release.

This arose doubts about the silicon carbide to aluminum interface. Separate tests were performed to characterize the Al-SiC contact resistance.

A schematic illustrating the contact resistance characterization test structure is shown in Figure 8.18. The structure is composed of a silicon carbide serpentine like structure, in contact with the aluminum pads at the ends. Structures with different dimensions were fabricated and the resistance between the aluminum pads was measured. The resistance between the pads can be expressed as

$$R_t = \frac{\rho_{SiC} l}{A_{CS}} + \frac{r_c}{A_c}, \tag{8.5}$$

where ρ_{SiC} is the resistivity of silicon carbide, l is the total length of the serpentine, A_{CS} is the cross section area of the silicon carbide structure, r_c is the normalized contact resistance (for 1 μm^2 contact area), and A_c is the contact (anchor) area. By using measurements from test structures with different dimensions, ρ_{SiC} is estimated to be 4.2 Ω.m, which is in good agreement with the value reported in [9-11], and r_c is estimated to be 5×10^9 Ω.μm^2, which is very high and needs improvement. In order to solve this issue, another thin (10 nm) metal layer is introduced between the aluminum and the silicon carbide at their interface in order to reduce the contact resistance. Different materials were tried for this purpose including chromium, titanium, and tungsten. The same test using serpentine structures was repeated while introducing the contact resistance improvement layer at the interface between silicon carbide and aluminum. First, the aluminum and the contact resistance improvement layer are sputtered on an oxide covered wafer. Then, both are patterned using the same mask. Afterwards, silicon carbide is deposited and patterned. Resistance measurement results shows that tungsten and titanium achieve approximately two orders of magnitude

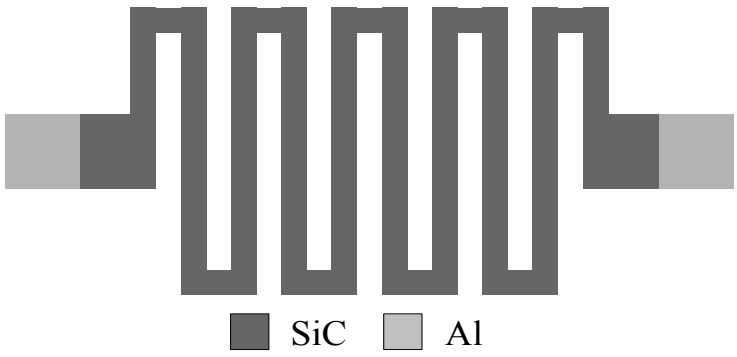

Figure 8.18: Schematic illustrating the contact resistance test structure.

improvement in the contact resistance, while no significant improvement is observed for chromium. Table 8.2 summarizes the contact resistance measurements for the different materials. It is worth mentioning that the contact resistance tests were performed under several biasing voltages ranging from -5 V to 5 V and no change in the measurements was observed.

8.5. SiC Lateral Gap Final Fabrication Process

The process modifications discussed in section 8.4 were introduced to the process to reach the final fabrication process flow, as follows. The process starts with dielectric passivated wafers. The wafers can be wafers with electronics already built and passivated with nitride for example. For process development purposes, silicon wafers covered with a layer of thermally grown oxide are used. The passivation is necessary to prevent shorts between electrical interconnects on the MEMS side. The process is illustrated in Figures 8.19 and 8.20. First, a stack of 60 nm thick layer of aluminum, 20 nm thick layer of chromium, and 60 nm layer of aluminum is deposited by DC sputtering, and wet patterned to form interconnects, as shown in Figure 8.19 (a). A 1 μm sacrificial polyimide layer is then spin coated and cured at 200 °C to define vertical gaps. A 60 nm thick aluminum layer is then deposited using DC sputtering. It is then patterned using wet PAN etchant to form the mask for etching the polyimide, then the polyimide is etched using oxygen RIE to allow anchoring of the disk resonator stem. The aluminum hard mask is then wet stripped, as shown in Figure 8.19 (b). Notably, the chromium layer in the aluminum-chromium-aluminum stack is used as an etch stop to protect the underlying aluminum tracks during the aluminum hard mask stripping step, as the top aluminum in the stack will be attacked during this step in the parts where polyimide was etched, as

Table 8.2: Measured contact resistance for different interface materials

Interface	Contact resistance ($\Omega.\mu m^2$)
Al-SiC	5×10^9
Al-Cr-SiC	2.5×10^9
Al-W-SiC	2×10^7
Al-Ti-SiC	2.5×10^7

shown in Figure 8.19 (b). Afterwards, the disk stack layers are deposited through sputtering: a 60 nm thick aluminum bottom conductive layer, a 10 nm thick layer for contact resistance improvement (titanium (Ti) and tungsten (W) tested, as explained later), below a 2 μm a-SiC structural layer, the same layer of contact resistance improvement, and finally a 60 nm thick layer of aluminum as a top layer. A 1.4 μm photoresist layer is then applied to serve as electrode-disk vertical spacer. The photoresists is then baked on a hot plate at 170 ^{o}C for 30 minutes, in order to survive the subsequent sputtering steps. Then, a hard mask stack of a 600 nm thick chromium layer below a 60 nm thick layer of aluminum is deposited, as shown in Figure 8.19 (c). The aluminum and chromium are wet patterned. Then, the aluminum is used to etch the vertical spacer resist using oxygen RIE stopping on the aluminum top metallization layer. An aluminum wet etch step then follows to etch the top metallization layer as well as strip the aluminum hard mask, as illustrated in Figure 8.19 (d), stopping on the contact resistance enhancement layer. The contact enhancement layer is then etched and then the SiC is etched using RIE in NF_3 utilizing chromium as a hard mask and stopping on the bottom contact resistance enhancement layer, which is then etched, followed by wet etching of the underlying aluminum layer and the chromium hardmask, as shown in Figure 8.19 (e). Next, a 120 nm conformal layer of CVD parylene is deposited to define lateral gaps. Then a 60 nm thick aluminum layer is deposited using DC sputtering, in order to be used as a hard mask for etching the anchors of the second SiC structural layer in parylene and polyimide, as shown in Figure 8.19 (f). The aluminum hard mask is then patterned using wet PAN etchant. Openings are formed through the polymer stack by O_2 RIE to later anchor the electrodes to the substrate and then the aluminum hard mask is stripped, as shown in Figure 8.20 (g). A 2 μm layer of photoresist is spin-coated for planarization prior to subsequent processing, and patterned, as shown in Figure 8.20 (h). The planarization resist layer is then baked on a hot plate at 170 ^{o}C for 30 minutes, in order to survive the subsequent structural SiC sputtering step. The second structural multi-material stack forming the electrodes is then sputtered, which is composed of a 10 nm thick chromium adhesion layer, a 300 nm thick aluminum metallization layer, a 2 μm a-SiC structural layer, a 60 nm thick aluminum top metallization layer, and a 600 nm thick chromium hardmask layer, as shown in Figure 8.20 (i).

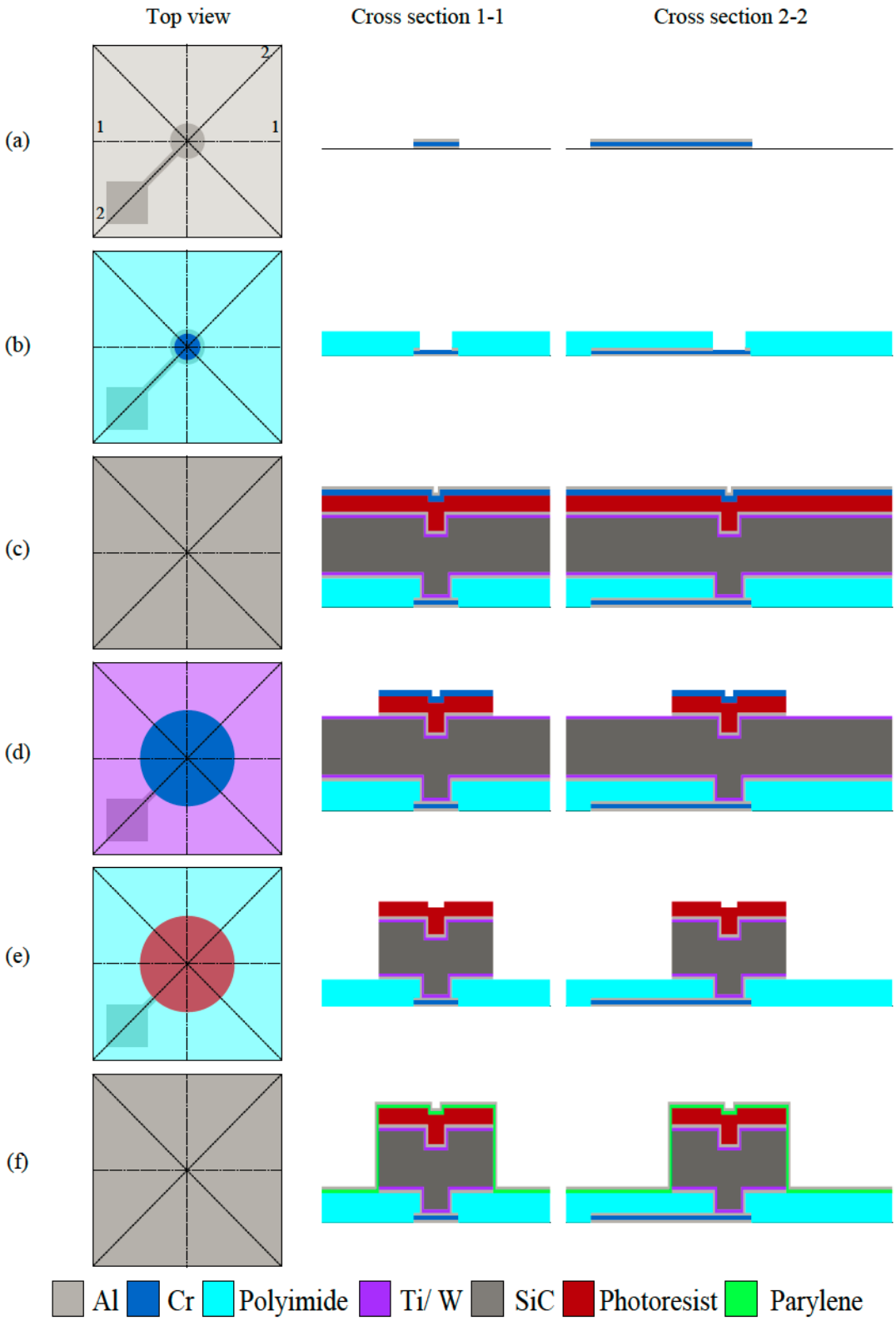

Figure 8.19: Final process flow of the lateral gap SiC process, shown on a disk resonator as an example (part 1).

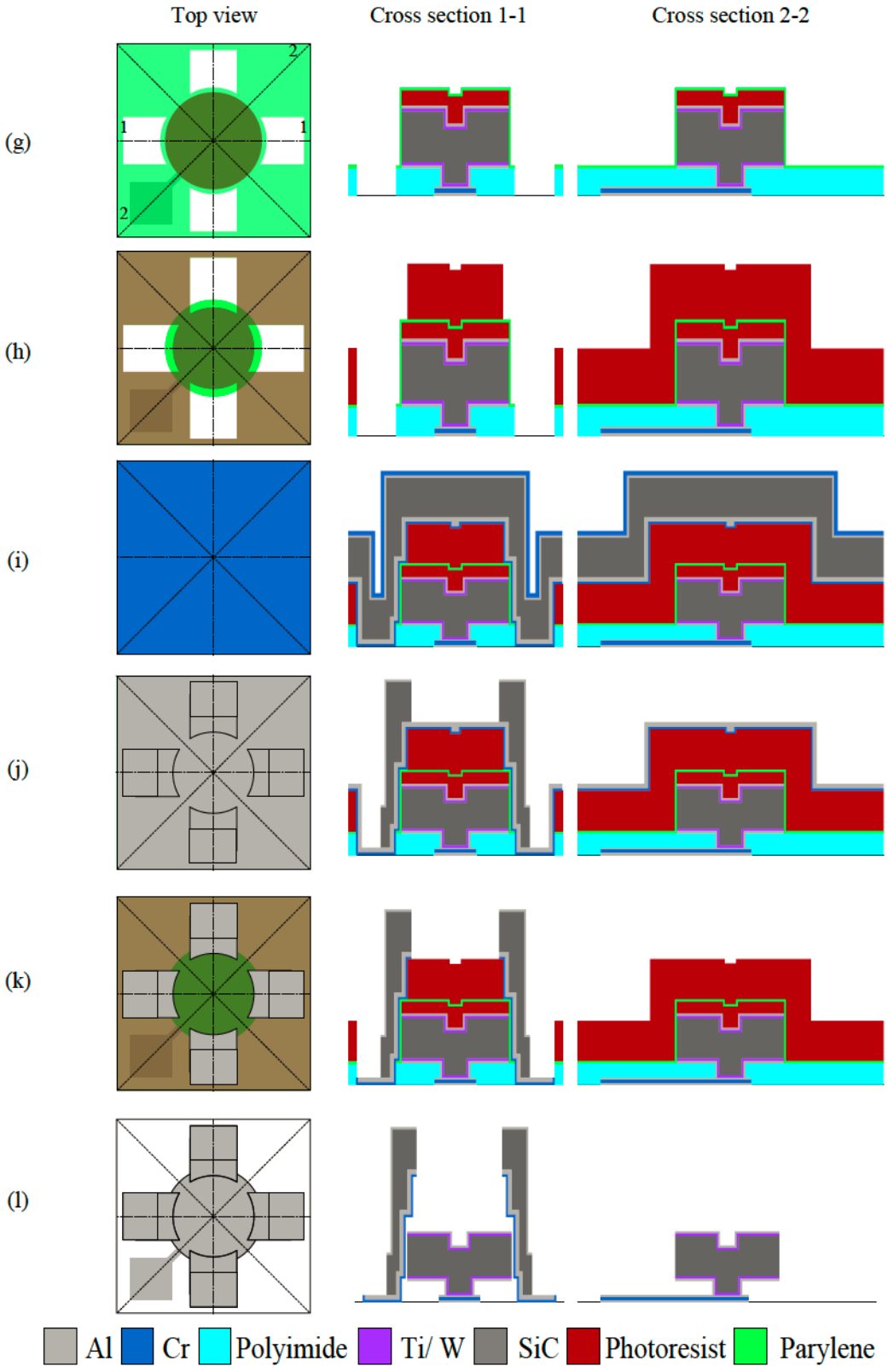

Figure 8.20: Final process flow of the lateral gap SiC process, shown on a disk resonator as an example (part 2).

The top chromium and aluminum layers are patterned using wet chemical etchants. Then, the a-SiC is etched, as previously described, in NF_3 RIE to form the suspended electrodes, with the etch stopping at the aluminum. The chromium hardmask is then wet stripped, as shown in Figure 8.20 (j). Afterwards, aluminum is wet patterned to form electrical interconnects and pads, as shown in Figure 8.20 (k). Finally, the devices are released by O_2 plasma, which clears all the remaining polymers, as shown in Figure 8.20 (l). Several devices were fabricated in the process, including disk resonators and disk gyros. Figure 8.21shows SEM micrographs of examples of fabricated devices.

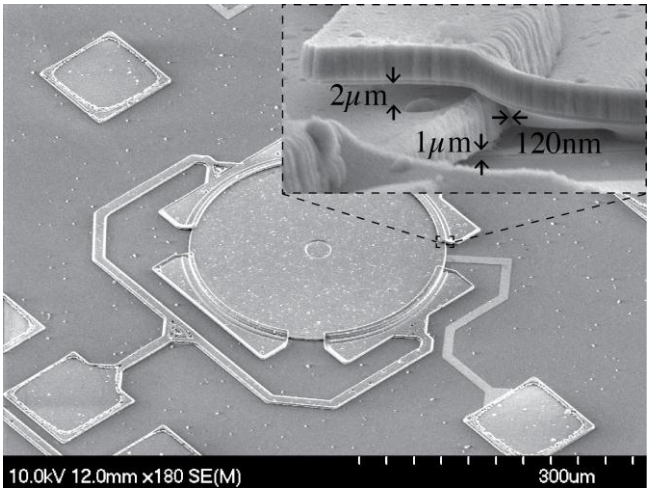

(a)

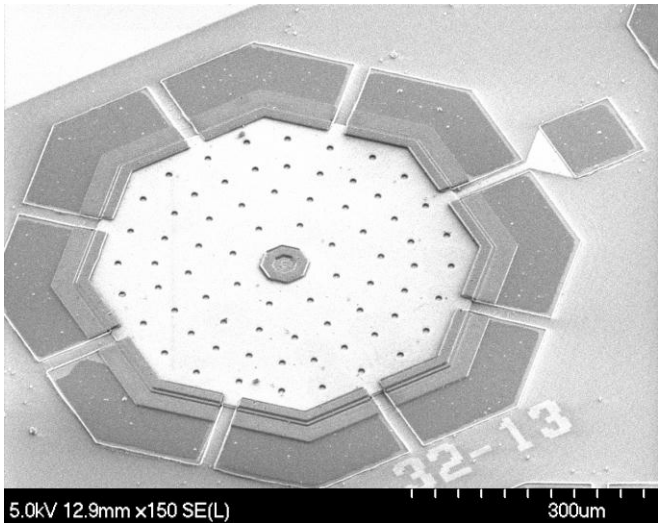

(b)

Figure 8.21: SEM micrographs of example fabricated devices: (a) bulk-mode circular disk resonator, and (b) bulk-mode octagon disk gyroscope.

8.6. Resonance Characterization

8.6.1. Test Setups

The simplest resonance characterization test setup for any resonator is the 1-port setup shown in Figure 8.22, where one of the ports of the vector network analyzer (VNA) is connected to a single port of the device (or to ports with similar polarity) and the other VNA port is connected to the resonating structure itself through a bias tee in order to decouple the AC signal from the DC polarization voltage needed for actuation. In this setup the feed-through capacitance (C_{ft}) between the electrode and the resonator structure appears in parallel with the motional R-L-C model of the resonator and therefore affects the resonance transmission characteristics leading to observing very small peaks and preventing the deduction of resonance parameters (e.g., quality factor).

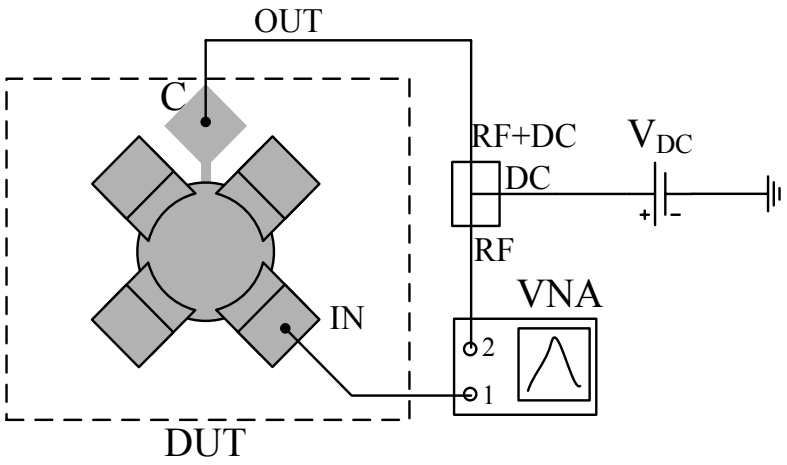

(a)

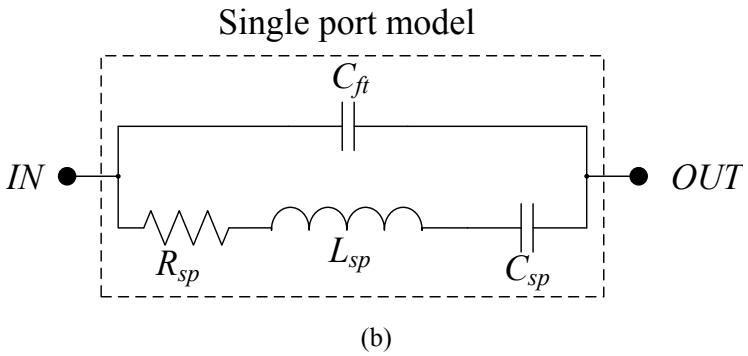

(b)

Figure 8.22: 1-port test setup: (a) connection schematic, and (b) electrical model.

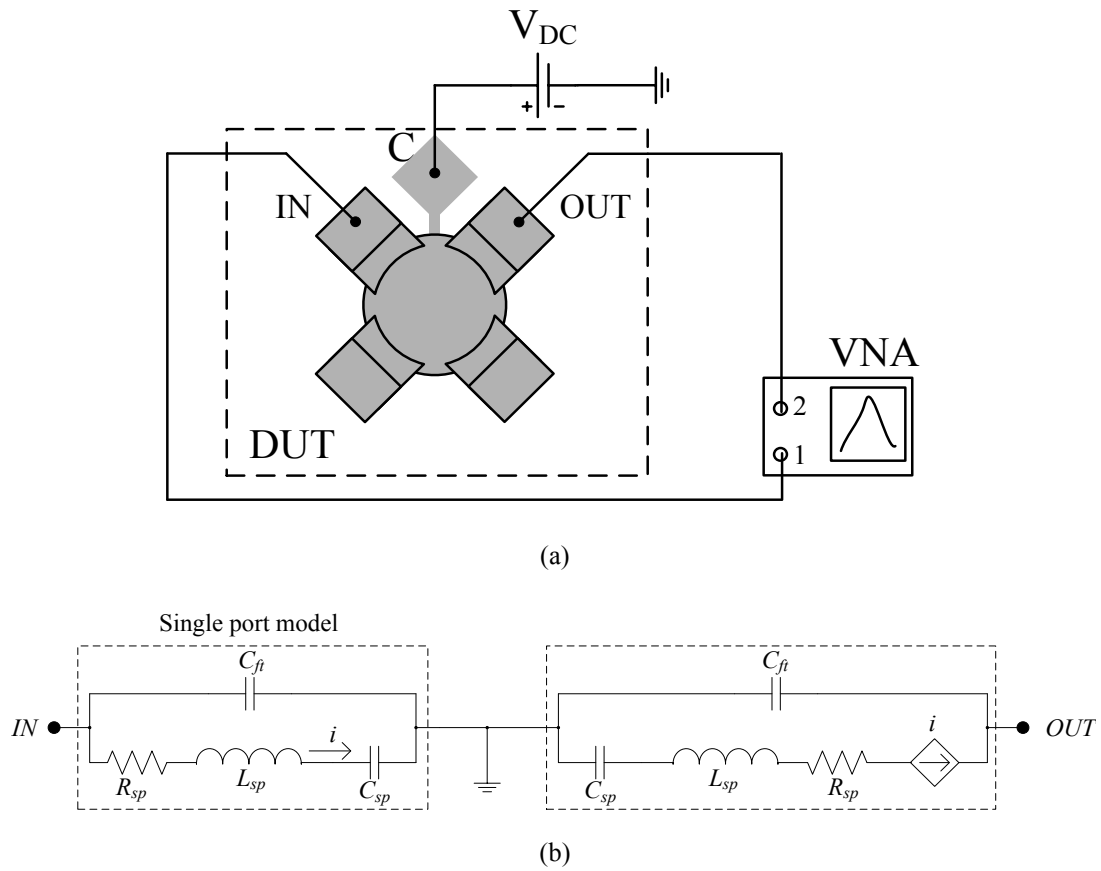

Figure 8.23: 2-port test setup: (a) connection schematic, and (b) electrical model.

One way of solving this issue is to use another setup, namely the 2-port setup, where one of the ports of the VNA is connected to a single port of the device (or to ports with similar polarity) and the other VNA port is connected to another port of the device (or to ports with similar polarity). The DC polarization voltage is connected directly to the resonating structure, as shown in Figure 8.23. The polarization voltage node is considered a virtual ground for AC signals. This should turn all floating feed-though capacitances to grounded capacitance and therefore should reduce their impact on the transmission characteristics. Figure 8.24 shows ADS simulation results using the electrical models of the two setups for an arbitrary resonator to illustrate the advantage of the 2-port setup. It is worth mentioning that this works if the path between the resonator structure and the DC polarization voltage source is a low resistance path, so that the structure becomes grounded for AC signals.

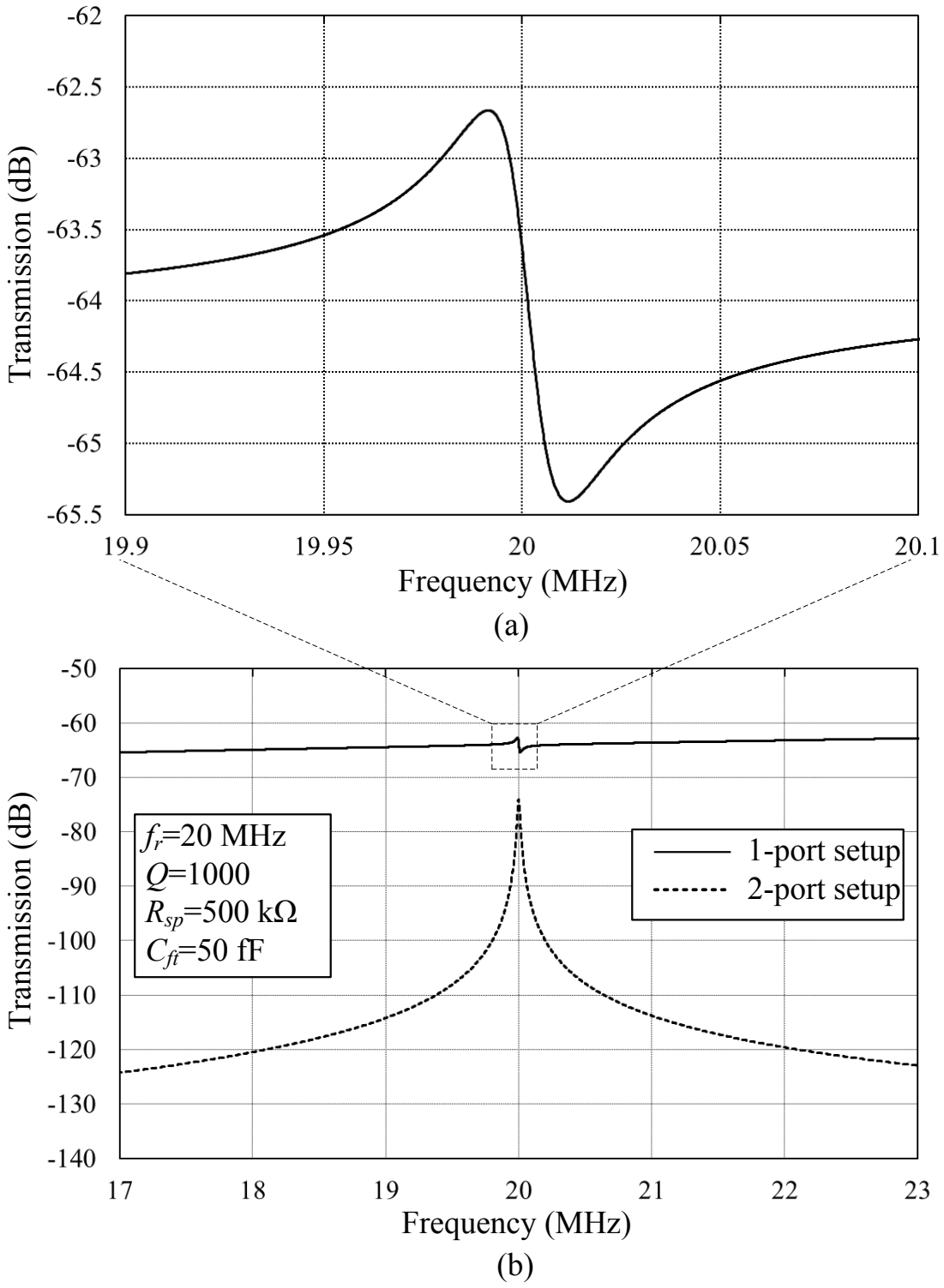

Figure 8.24: ADS simulation results for the transmission (S_{21}) of an arbitrary resonator: (a) Zoomed-in image for the response using a 1-port test setup, and (b) 1-port and 2-port setup responses shown on the same graph for comparison.

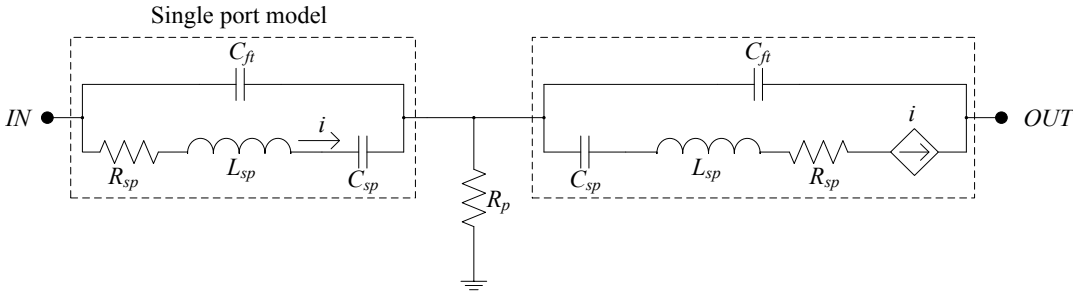

Figure 8.25: Electrical model of the 2-port resonator test setup including the parasitic resistance between the structure and AC ground.

The silicon carbide utilized for our technology has a relatively high resistivity around 4.2 Ω.m, and due to the contact resistance between the silicon carbide and the underlying metal as explained in section 8.4.4, an unintentional parasitic resistance (R_p) appears in the path, as illustrated in Figure 8.25. Therefore, the structure is not grounded properly, and consequently the feed-through capacitances are still in-effect, as illustrated by the ADS simulation results shown in Figure 8.26 illustrating the resonator transmission (S_{21}) for various values of R_p. As R_P increases, the floor of the transmission curve increases due to the effect of the feed-through capacitance and the resonance peak becomes smaller.

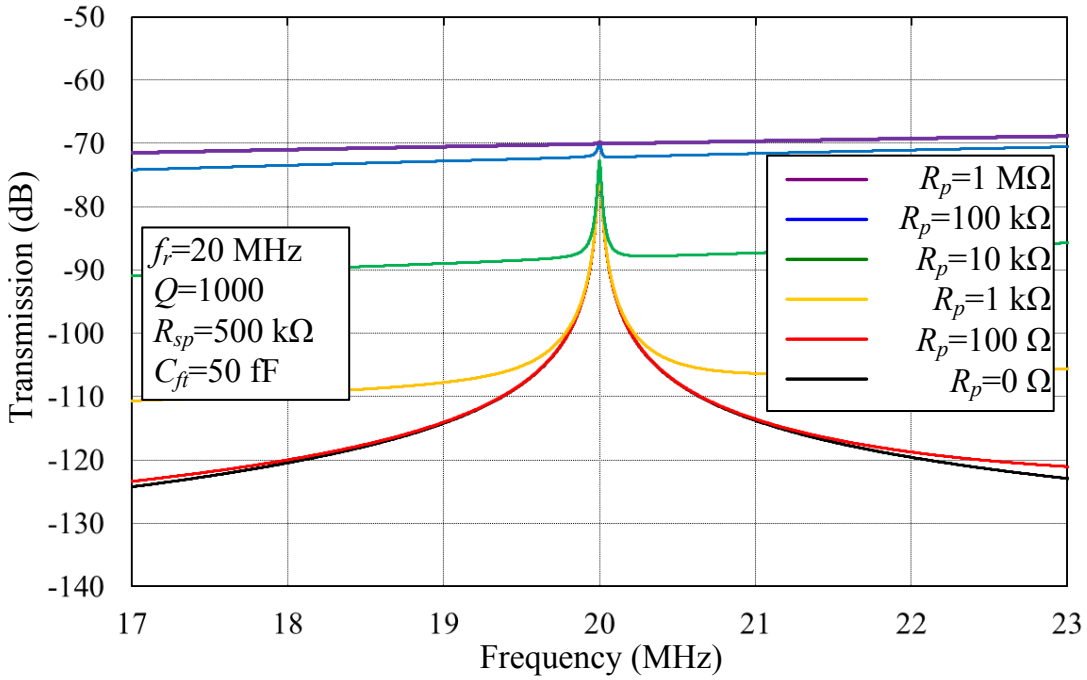

Figure 8.26: ADS simulation for the resonator transmission for different values of the parasitic resistance in the 2-port setup.

The curve then approaches the 1-port setup result shown in Figure 8.24 (a), where the peak is so small to the extent that the resonance characteristics (e.g., quality factor) cannot be deduced accurately.

In order to get rid of the effect of this parasitic resistance, a differential setup is used, similar to the setup used in [14, 21], as shown in Figure 8.27, where a single-ended to differential converter (balun) is utilized at the input to convert the source AC signal (VNA output) to differential signals. Since the ports are symmetric, a virtual ground is formed on the structure. Therefore, no motional current passes in the parasitic resistor and the feed-through capacitances become grounded, as desired. At the output, a differential to single-ended converter to turn the signal back to single-ended to be connected to the second port of the VNA. Figure 8.28 shows ADS simulation results for the transmission (S_{21}) of a resonator using the differential test setup. The curve with high parasitic resistance coincides

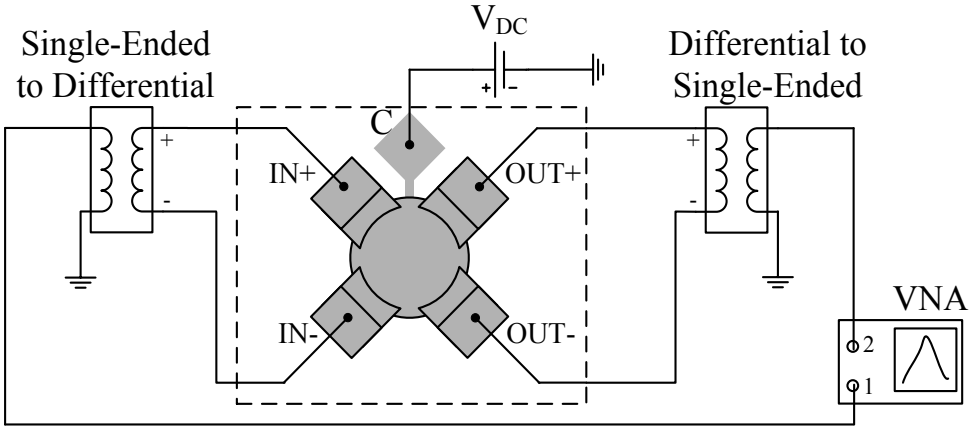

(a)

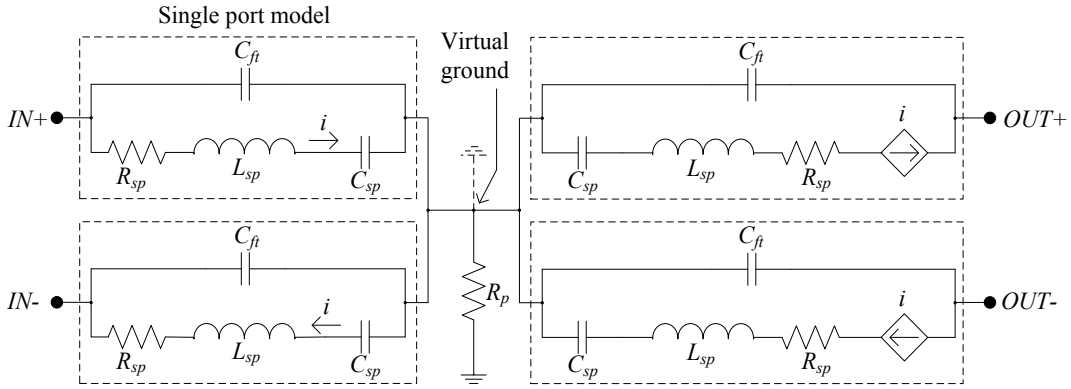

(b)

Figure 8.27: Differential test setup: (a) connection schematic, and (b) electrical model.

exactly with the curve without resistance illustrating that the effect of the parasitic resistance and the feed-through capacitances are totally cancelled out thought the differential setup. Therefore, the differential setup was selected for the characterization of the silicon carbide devices fabricated in the technology presented.

Devices are tested by direct probing using a probe station, utilizing four GSG probes for the input and output AC signals as shown in Figure 8.29. Also, a DC probe is used to connect the necessary polarization voltage to the resonator structure. Alternatively, to test the devices in vacuum, a printed circuit board (PCB) is used where the chip with the device under test is wire bonded directly (without any package), in order to minimize the parasitic capacitances and make sure that the values of the feed-though capacitances of the different ports are as close as possible so that the differential test setup concept (exact matching between the ports) is valid, and consequently a virtual ground potential at the resonator structure is created. A picture of the PCB is shown in Figure 8.30. The board can then be placed in a vacuum chamber for testing of the devices in vacuum.

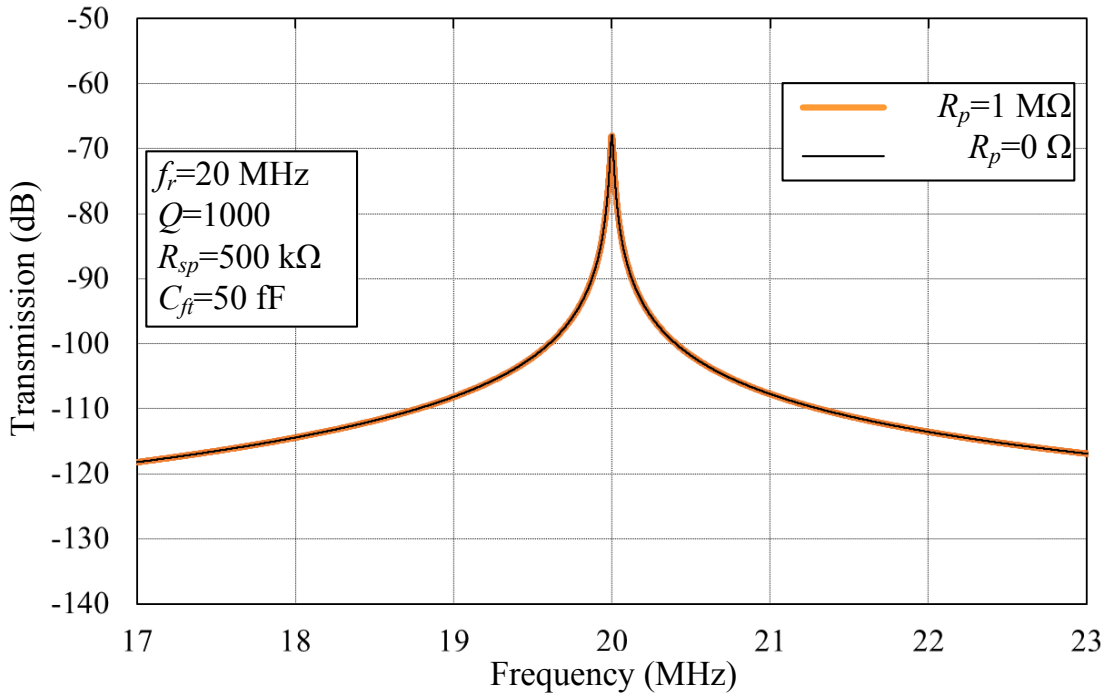

Figure 8.28: ADS simulation for the resonator transmission for different values of the parasitic resistance in the differential setup.

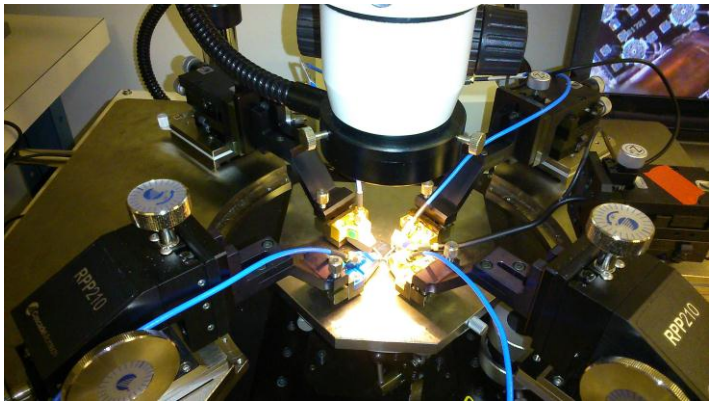

(a)

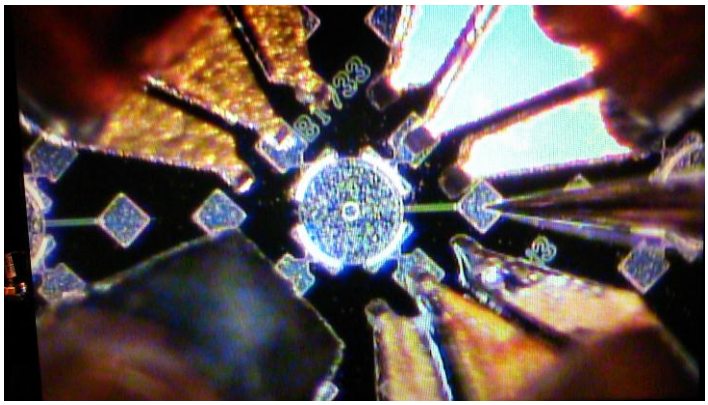

(b)

Figure 8.29: Differential test setup using a probe station: (a) photo of the setup, and (b) microscope image of a tested device and the different probe connections.

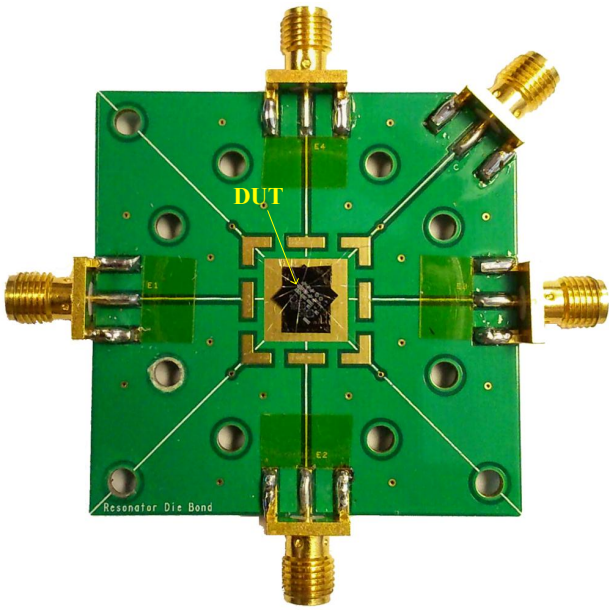

Figure 8.30: PCB with device die directly wire bonded to minimize the parasitic capacitances.

8.6.2. Measurement Results

The measured transmission curve of one of our fabricated resonators using the 1-port test setup shown in Figure 8.22 is shown in Figure 8.31. This device resonates at ~ 20.74 MHz. The quality factor could not be extracted from the measured curve, as the peak is very small (< 3 dB), due to the excessive parasitic resistance between the DC voltage and the disk, which increases the effect of the feed-through capacitance, as explained earlier in section 8.6.1.

In order to mitigate the effect of the parasitic resistance and feed-through, the differential setup, explained in section 8.6.1 is used. Figure 8.32 illustrates the measured transmission curve for a fabricated device without a contact resistance improvement layer for different DC polarization voltages. This resonator exhibits a resonance frequency of ~25.9 MHz, a quality factor of ~1000, and a signal transmission of ~ -104 dB at resonance for a 20 V polarization voltage. This loss level corresponds to an equivalent resistance of ~16 MΩ. The resistance is very high as a result of the silicon carbide to aluminum contact resistance, as detailed in section 8.4.4.

After adding a contact resistance improvement layer (results for titanium and tungsten are presented), the loss and consequently the contact resistance are reduced, as

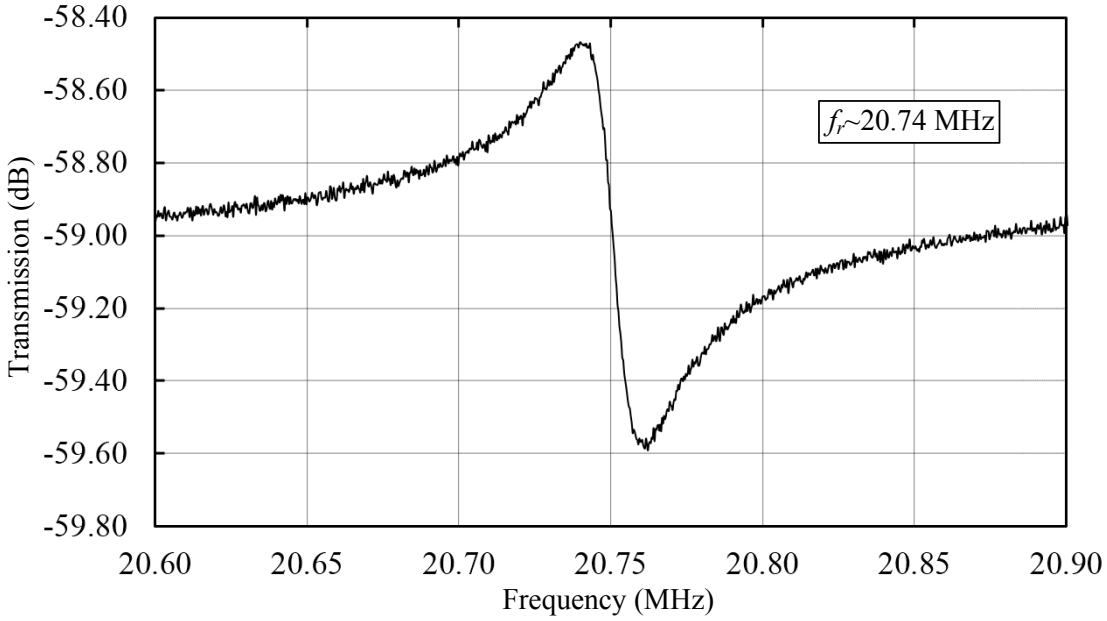

Figure 8.31: Measured transmission curve for a fabricated device using the 1-port setup.

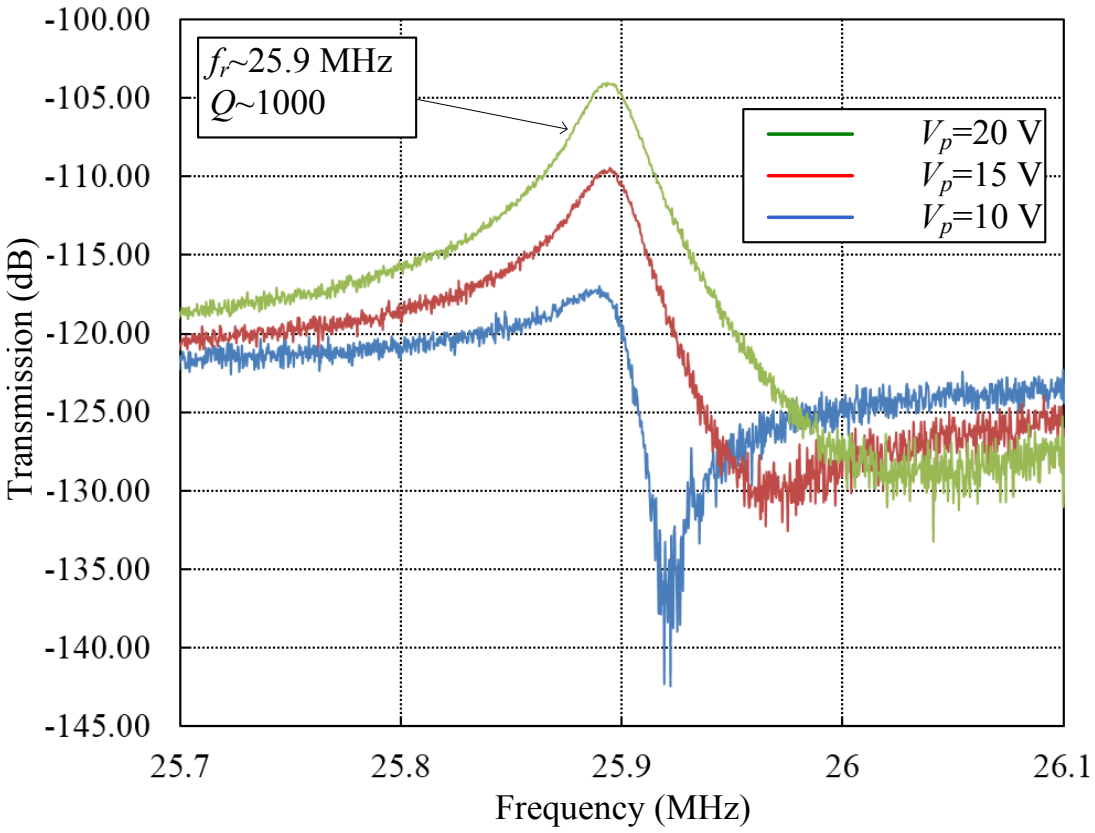

Figure 8.32: Transmission curve of a fabricated resonator without a contact resistance improvement layer using the differential test setup for different DC polarization voltages.

shown in Figure 8.33. The quality factor is reduced compared to the resonators without the contact improvement layer, as this added layer results in more damping and consequently reduces the quality factor. The signal loss at resonance is reduced to ~ 87 dB and ~ 82 dB for titanium and tungsten, respectively. This corresponds to an improvement in the resonator equivalent resistance by factors of 7 and 12.6 for both materials, respectively. These factors of improvement are lower than the ones reported in section 8.4.4. The reason for this discrepancy is still under investigation.

Cross sections of some of the fabricated devices were checked. First, the sample was coated with epoxy and then the cross section was polished till the desired section was reached, as shown in Figure 8.34. The epoxy is used to hold the released structures in-place without collapsing. Figure 8.35 shows microscope images and SEM micrographs for the cross sections of devices with 100 nm and 300 nm lateral gap thickness. It is clear from the figure that the structures are released successfully. However, it is clear that the electrode

structures suffer from notching effect during the etch of the second structural layer. This results in thinning of the electrodes at some of the electrode structure corners. Consequently, the stiffness of the electrode structures is significantly reduced resulting in vibration of the electrodes while exciting the main resonator structure. This motion acts as

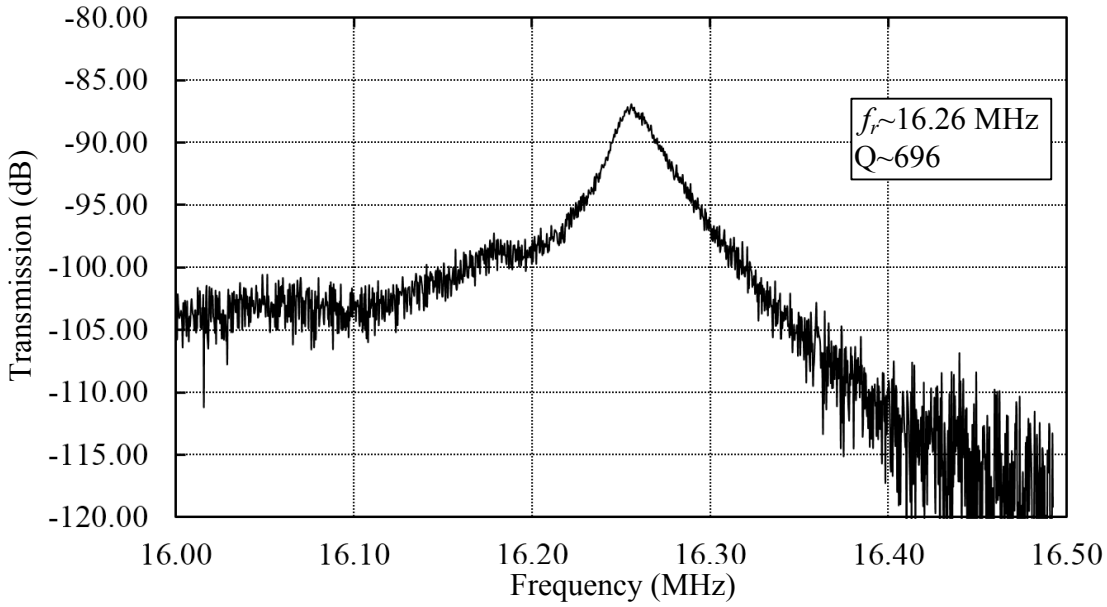

(a)

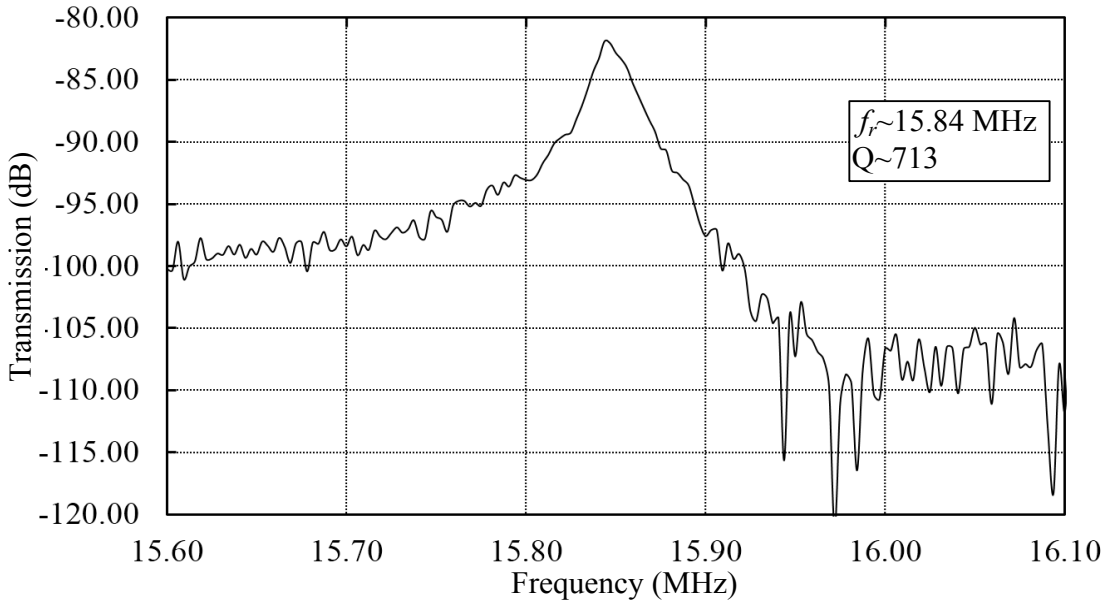

(b)

Figure 8.33: Transmission curves of fabricated resonators using different contact resistance improvement layers: (a) titanium, and (b) tungsten.

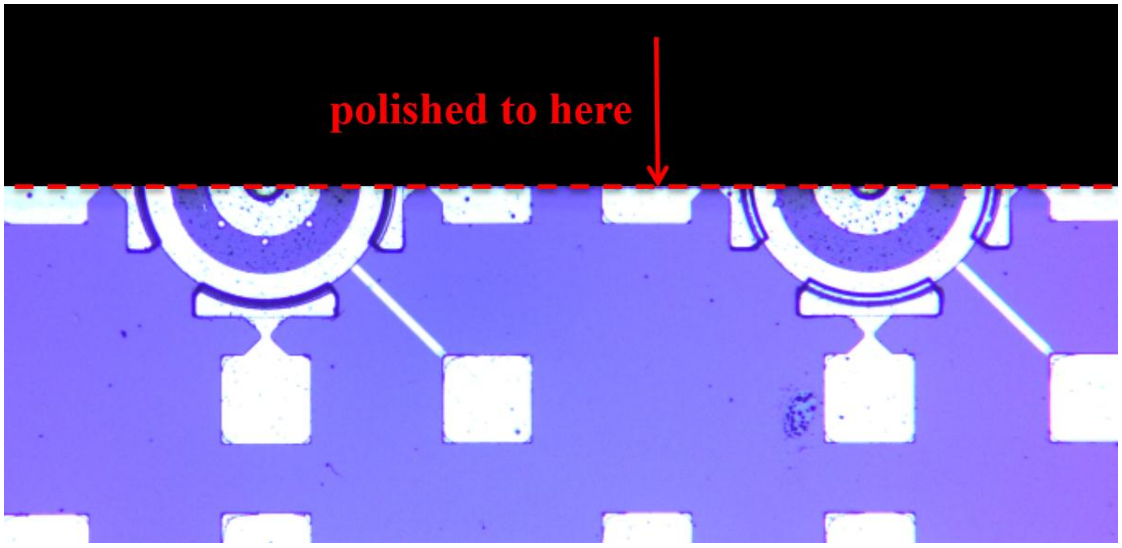

Figure 8.34: Top view sample illustrating the polishing process.

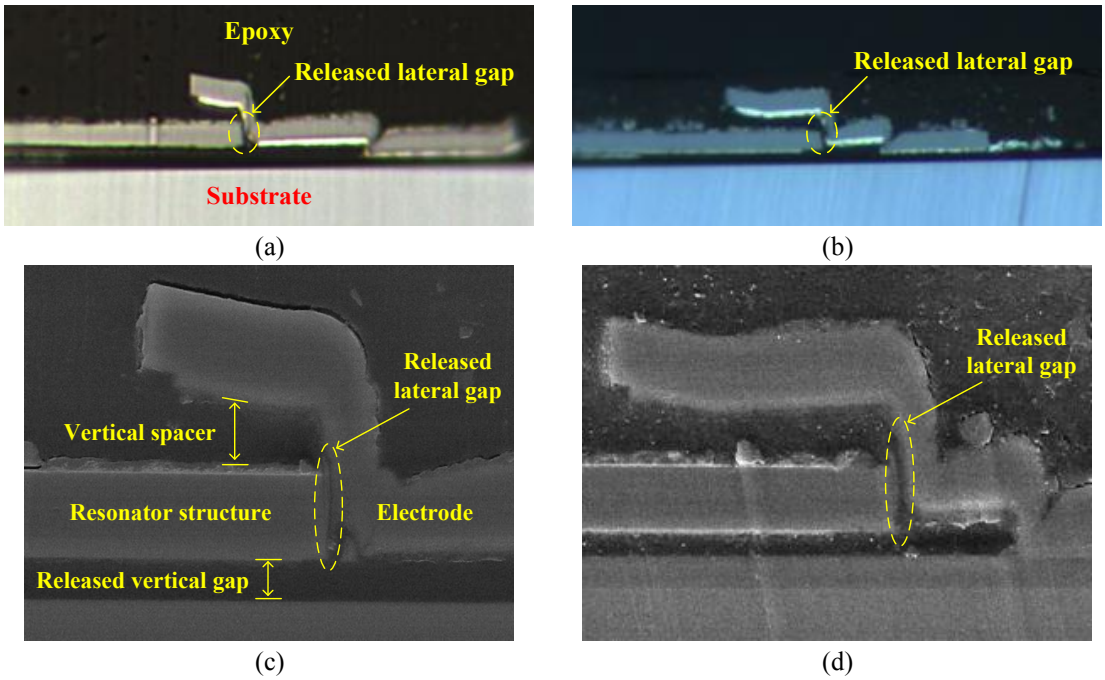

Figure 8.35: Microscope images of device cross-sections with parylene thickness of: (a) 100 nm, (b) 300 nm, and SEM micrographs with parylene thickness of: (c) 100 nm, (d) 300 nm.

a path for energy loss and is probably the main reason for the lower quality factor and higher motional resistance measured. For this issue to be solved, the electrodes need to be made thicker in order to increase their stiffness. Also, other materials need to be investigated for contact improvement in order to get better quality factor by reducing the damping effect of this layer on the whole structure. Alternatively, if the SiC structural layer

could be doped in order to reduce its resistivity as well as improve its direct contact to aluminum, this would be ideal. As, in this case the top and bottom aluminum of the structural layer stack, as well as the contact enhancement layers can be omitted, and consequently the devices will be capable of achieving better quality factors as a result of reduced damping. Lower signal loss will also be achievable as the added electrical parasitic resistances will be minimized and the loss will just depend on the motional resistance of the resonator.

8.7. Conclusion

In this chapter, the first surface micromachining technology based on amorphous silicon carbide (a-SiC) targeting above-IC integration of capacitive devices was presented. The process features submicron lateral and vertical transduction gaps of independently controlled thicknesses which makes it ideal for realizing bulk mode electrostatic devices. Processing is optimized for full compatibility with commercial CMOS processes, with the lowest reported fabrication temperature amongst comparable technologies. Amorphous silicon carbide structural layers, combining high stiffness and fracture strength, are used. Two polymer-based sacrificial layers define the vertical gaps and sub-micron lateral gaps, without requiring high resolution photolithography, and are ultimately dry released to prevent stiction, a challenging issue with wet release methods. The process utilizes surface micromachining, as it allows for more fabrication flexibility, especially for integrating micromachined devices with electronic circuits. This is very advantageous in order to reduce parasitics between the devices and their interface circuitry, compared to side-by-side co-fabrication approaches. This consequently would allow for improved performance. Multiple devices including disk resonators and disk gyroscopes were fabricated and resonance frequencies as high as ~25 MHz with quality factors as high as ~1,200 were measured. The quality factor and signal loss are degraded compared to the expected performance. This is primarily due to the contact resistance to the silicon carbide resonating structures. A contact resistance improvement layer was introduced between aluminum and silicon carbide to enhance the contact. Titanium and tungsten were found promising. They were measured to improve the contact resistance by at least an order of magnitude and consequently led to significant improvement in the signal loss. Other paths were identified

for further improvement of the loss and quality factor. More materials need to be investigated for contact improvement in order to get better quality factor by reducing the damping effect of these layers on the whole structure. Alternatively, if the SiC structural layer could be doped in order to reduce its resistivity as well as improve its direct contact to aluminum, this would be ideal. As, in this case the top and bottom aluminum of the structural layer stack, as well as the contact enhancement layers can be omitted, and consequently the devices will be capable of achieving better quality factors as a result of reduced damping. Lower signal losses will also be achievable as the added electrical parasitic resistances will be minimized and the loss will depend solely on the motional resistance of the resonator structure itself. Also, the electrodes need to be made thicker in order to increase their stiffness and minimize the energy losses resulting from their vibration with the main device structure.

8.8. References

[1] A. Ajayakumar, S. Maruthoor, T. Fuchs, F. Rohlfing, O. Jakovlev, J. Wilde, and H. Reinecke, "Improvement of Process Parameters for Polycrystalline Silicon Carbide Low Pressure Chemical Vapor Deposition on 150 mm Silicon Substrate Using Monomethylsilane as Precursor," *Journal of Thin Solid Films*, vol. 536, pp. 94-98, April 2013.

[2] S. Maruthoor, A. Ajayakumar, T. Fuchs, O. Jakovlev, H. Reinecke, and J. Wilde, "Mechanical Characterization of Polycrystalline and Amorphous Silicon Carbide Thin Films Using Bulge Test," *Journal of Microelectromechanical Systems*, vol. 22, no. 1, pp. 140-146, February 2013.

[3] A. Scheurle et al., "A 10 μm Thick Poly-SiGe Gyroscope Processed Above 0.35 μm CMOS," *Proceedings of the IEEE International Conference on Microelectromechanical Systems*, pp. 39-42, January 2007.

[4] "Design and Technology Solutions for Development of SiGe MEMS devices", IMEC-Coventor.

[5] W. -H. Chuang, T. Luger, R. Fettig, and R. Ghoddsi, "Mechanical Property Characterization of LPCVD Silicon Nitride Thin Films at Cryogenic Temperatures,"

Journal of Microelectromechanical Systems, vol. 13, no. 5, pp. 870-879, October 2004.

[6] "LPCVD Low Stress Nitride Characterization," Cornell NanoScale Science and Technology Facility (CNF), available at: http://www.cnf.cornell.edu/cnf_process_tf_cvd.html, 2004.

[7] H. Huang, K. Winchester, A. Suvorova, B. Lawn, Y. Liu, X. Hu, J. Dell, and L. Faraone, "Effect of Deposition Conditions on Mechanical Properties of Low-Temperature PECVD Silicon Nitride Films," *Journal of Materials Science and Engineering A*, pp. 453-459, 2006.

[8] L. Liu, W. -G. Liu, N. Cao, and C. -L, Cai, "Study on the Performance of PECVD Silicon Nitride Thin Films," *Journal of Defence Technology*, vol. 9, pp. 121-126, November 2013.

[9] F. Nabki, T. Dusatko, S. Vengallatore, and M. El-Gamal, "Low-Temperature (<300°C) Low-Stress Silicon Carbide Surface Micromachining Fabrication Technology," *Technical Digest of the Hilton Head Solid-State Sensors, Actuators and Microsystems Workshop*, pp. 216 - 219, June 2008.

[10] F. Nabki, T. Dusatko, S. Vengallatore, and M. El-Gamal, "Low Stress CMOS-Compatible Silicon Carbide Surface-Micromachining Technology - Part I: Process Development and Characterization," *Journal of Microelectromechanical Systems*, vol. 20, no. 3, pp. 720-729, June 2011.

[11] F. Nabki, P. Cicek, T. Dusatko, and M. El-Gamal, "Low Stress CMOS-Compatible Silicon Carbide Surface-Micromachining Technology - Part II: Beam Resonators for MEMS above IC," *Journal of Microelectromechanical Systems*, vol. 20, no. 3, pp. 730-744, June 2011.

[12] Y. Xie, S. Li, Y. Lin, Z. Ren, and C. Nguyen, "1.52-GHz Micromechanical Extensional Wine-Glass Mode Ring Resonators", *IEEE Transactions on Ultrasonics, Ferroelectrics and Frequency Control*, vol. 55, no. 4, pp. 890-907, May 2008.

[13] J. Wang, J. Butler, T. Feygelson, and C. Nguyen, "1.51-GHz Nanocrystalline Diamond Micromechanical Disk Resonator with Material Mismatched Isolating Support", *Proceedings of the IEEE International Conference on Microelectromechanical Systems*, pp. 641-644, 2004.

[14] S. Bhave, D. Gao, R. Maboudian, and R. Howe, "Fully-Differential Poly-SiC Lamé Mode Resonator and Checkerboard Filter", *Proceedings of the IEEE International Conference on Microelectromechanical Systems*, pp. 223-226, January 2005.

[15] F. Ayazi and K. Najafi, "High Aspect Ratio Combined Poly and Single-Crystal Silicon (HARPSS) MEMS Technology", *Journal of Microelectromechanical Systems*, vol. 9, no. 3, pp. 288-294, September 2000.

[16] H. Johari and F. Ayazi, "Capacitive Bulk Acoustic Wave Silicon Disk Gyroscopes," *Technical Digest of the IEEE Electron Devices Meeting*, pp. 1-4, December 2006.

[17] W. Sung, M. Dalal, and F. Ayazi, "A 3 MHz Spoke Gyroscope with Wide Bandwidth and Large Dynamic Range," *Proceedings of the IEEE International Conference on Microelectromechanical Systems*, pp. 104-107, January 2010.

[18] W.-L. Huang, S. -S. Li, Z. Ren, and C. Nguyen, "UHF Nickel Micromechanical Spoke-Supported Ring Resonators", *Proceedings of the IEEE International Conference on Solid-State Sensors, Actuators, and Microsystems*, pp. 323-326, June 2007.

[19] S. Kazmi, T. Aarnink, C. Salm, and J. Schmitz, "CMOS-MEMS Post Processing Compatible Capacitively Transduced GeSi Resonators, " *Proceedings of the IEEE International Frequency Control Symposium*, pp. 1-4, May 2012.

[20] S. D. Senturia, "*Microsystem Design*," Springer, 2001.

[21] M. Ziaei-Moayyed, D. Elata, E. Quévy, and R. Howe, "Differential Internal Dielectric Transduction of a Lamé-Mode Resonator," Journal of Micromechanics and Microengineering, vol. 20, no. 11, pp. 115036-115051, October 2010.

Chapter 9 Conclusion

This chapter concludes the thesis by first presenting a summary highlighting the major contributions. Then, possible future developments are discussed as means for further improving the presented work.

9.1. Summary

This thesis explained in details the novel architectures we devised to enhance the performance of different types of MEMS devices, and finally presented the surface micromachining fabrication technology we developed targeting above-IC integration of bulk mode MEMS resonators and sensors. Part I (chapters 2 and 3) focused on MEMS gyroscopes. Chapter 2 comprised an overview about different types of gyroscopes, then focused on MEMS gyroscopes including their types, applications, and operation principles. Chapter 3 detailed a technique we devised for enhancing the sensitivity of bulk mode devices by introducing combs at the points exhibiting the maximum vibration amplitude and adjusting the stiffness of the comb structures. The chapter also presented the fabricated prototype, and the measurement results highlighting the performance enhancement achieved. Part II (chapters 4 and 5) concentrated on MEMS magnetometers. An overview about this type of devices was presented in chapter 4. Chapter 5 detailed our combined magnetometer/ accelerometer sensor. The architecture is based on electrical current switching between orthogonal directions on the device structures in order to obtain magnetic field measurements along the different axes based on the Lorentz force. The acceleration can also be measured accurately when the current is switched off, and its effect can be cancelled out from the magnetic field measurements. Therefore, the sensor is capable of achieving accurate measurements of both magnetic field and acceleration. The fabrication process was presented as well as the measurement results of the fabricated prototypes. Part III (chapters 6 and 7) was focused on resonators. Chapter 6 presented a brief introduction about them including their different types, transduction methods, recent

advancements, and challenges. Chapter 7 presented our novel design for a wine-glass disk resonator with transverse piezoelectric actuation and capacitive frequency tuning fabricated in a commercial of-the-shelf technology. The chapter also detailed the test setups and device characterization results. Part IV (chapter 8) focused on the fabrication technology. It first described state-of-the-art advancements in the fabrication technologies used for realizing bulk mode devices. Then, it presented the low temperature (<200 ^{o}C) surface micromachining technology developed through this work, targeting above-IC integration. The technology features independently controlled vertical and lateral gaps with thicknesses that can range from 50 nm to few microns. All processing steps were optimized to be suitable for post-processing standard CMOS wafers.

The resulting major contributions can be summarized, as described in chapter 1: (*i*) a novel architecture for enhancing the sensitivity of bulk mode devices, (*ii*) a combined magnetometer/ accelerometer sensor based on a novel current switching technique, (*iii*) a bulk mode disk resonator with transverse piezoelectric actuation and electrostatic tuning, and (*iv*) an above-IC compatible silicon carbide technology with sub-micron lateral gaps.

9.2. Future Developments

Many different aspects of the work can still be improved upon. These are mainly related to the MEMS lateral gap fabrication technology, realizing the novel sensitivity enhancement technique for bulk mode devices presented in chapter 3 in our lateral gap silicon carbide technology, augmenting our novel combined magnetometer/ accelerometer device presented in chapter 5 to create a full 3D magnetometer/ accelerometer, and optimizing the support dimensions for the piezoelectric resonator presented in chapter 7, in order to achieve the highest possible quality factor.

9.2.1. Lateral Gap Fabrication Technology Improvements

Part IV presented the silicon carbide fabrication technology developed in this work, featuring independently controllable vertical and lateral gaps. Devices were found to resonate at frequencies close to the desired designed values. However, the quality factor

and signal loss were found degraded compared to the expected performance. This is primarily due to the contact resistance to the silicon carbide resonating structures and the increased damping due to the loading effect of the metal layers above and below the structures. A contact resistance improvement layer was introduced between aluminum and silicon carbide to enhance the contact. Titanium and tungsten were found promising. They were measured to improve the contact resistance by at least an order of magnitude.

This factor is lower than that expected in section 8.4.4. The reason is primarily attributed to the low stiffness of the electrode structures which vibrate during the excitation of the main resonator structure and therefore this introduces an additional path for energy loss which increases the damping and results in lower quality factor and higher motional resistance. This can be solved by increasing the thickness of the second structural SiC layer forming the electrodes.

Also, other materials need to be investigated for contact improvement in order to get better quality factor by reducing the damping effect of this layer on the whole structure and also to further improve the contact resistance. Alternatively, if the SiC structural layer can be doped in order to reduce its resistivity as well as improve its direct contact to aluminum, this will be ideal. As in this case, the top and bottom aluminum of the structural layer stack, as well as the contact enhancement layers can be omitted, and consequently the devices will be capable of achieving better quality factors as a result of reduced damping. Lower signal loss will also be achievable as the added electrical parasitic resistances will be minimized and the loss will depend solely on the motional resistance of the resonating structure.

9.2.2. Implementing the Bulk-Mode Device's Sensitivity Enhancement Technique in the Lateral Gap SiC Technology

After optimizing the fabrication process, the next step would be to implement the sensitivity enhancement technique presented in chapter 3 to create superior performance bulk-mode resonators and gyros. Full systems (e.g., oscillators, phase lock loops, sensory systems), including mechanical parts and electronic circuits can then be implemented on the same chip by utilizing our low temperature surface micromachining technology.

9.2.3. Augmenting the Novel Combined Magnetometer/ Accelerometer Device to Create a Full 3D Magnetometer/ Accelerometer

Regarding the combined magnetometer/ accelerometer presented in chapter 5, the next step would be to augment the device to achieve 3D sensing functionality by adding electrodes surrounding the main structure utilizing the lateral gap technology. This will create a 6-axis IMU using the 3D magnetometer and the 3D accelerometer built using a single compact device based on the current switching technique. The readings of the accelerometer and magnetometer can then be combined using software to estimate the 3D angular rate measurements and achieve a 3D emulated gyroscope similar to [1]. Thus, our technique is capable of creating a full 9-axis IMU using a single micromachined structure.

9.2.4. Support Dimension Optimization for the Piezoelectric Resonator

As discussed in chapter 7, the quality factor of the resonator presented here is limited by anchor loss due to the support width imposed by the fabrication technology. Two approaches can be investigated to optimize the support dimensions. The first path is that, the support width could be narrowed by a post-process timed isotropic etch. Xenon di-fluoride (XeF_2) vapor is a promising candidate to perform this etch, as it has already been successfully used in to release MEMS structures (e.g. [2]) and is highly selective to silicon. The other is to optimize the support length to achieve quarter wavelength matching and minimize the energy loss through the anchors, as suggested in [3-4].

9.3. References

[1] "*KMX61G Mag-Accel Combo*," Kionix, available at: http:// www.kionix.com, 2013.

[2] Li. -W. Hung and C. Nguyen, "Capacitive-Piezoelectric AlN Resonators with Q>12,000," *Proceedings of the IEEE International Conference on Microelectromechanical Systems*, pp. 173-1766, January 2011.

[3] Y. Xie, S. Li, Y. Lin, Z. Ren, and C. Nguyen, "1.52-GHz Micromechanical Extensional Wine-Glass Mode Ring Resonators", *IEEE Transactions on Ultrasonics, Ferroelectrics and Frequency Control*, vol. 55, no. 4, pp. 890-907, May 2008.

[4] M. U. Demirci and C. Nguyen, "Higher-Mode Free-Free Beam Micromechanical Resonators," *Proceedings of the IEEE International Frequency Control Symposium*, pp. 810-818, May 2003.